Dynamics of electron acceleration in laser-driven wakefields: Acceleration limits and asymmetric plasma waves

Antonia Popp

Dynamics of electron acceleration in laser-driven wakefields: Acceleration limits and asymmetric plasma waves

Dissertation
an der Fakultät für Physik
der Ludwig-Maximilians-Universität in München

von

Antonia Popp
aus Bamberg

Erstgutachter: Prof. Dr. Stefan Karsch
Zweitgutachter: Prof. Dr. Malte Kaluza

Tag der mündlichen Prüfung: 16. Dezember 2011

Hofstadter's Law:
It always takes longer than you expect,
even when you take into account
Hofstadter's Law

Douglas Hofstadter, *Gödel, Escher,*
Bach: An Eternal Golden Braid

Zusammenfassung

Die Experimente dieser Doktorarbeit untersuchen verschiedene Aspekte der Elektronenbeschleunigung in laser-getriebenen Plasmawellen. Hoch-intensive Laserpulse können effizient eine Plasmawelle treiben, die elektrische Felder von 100 GV/m aufrecht erhalten kann. Da diese Felder 3-4 Größenordnungen stärker sind als in Radiofrequenz-Beschleunigern, kann die benötigte Beschleungiungsstrecke um den gleichen Faktor reduziert werden, wodurch die sogenannte *Laser-Wakefield Acceleration* (LWFA) zu einer vielversprechenden platzsparenden, und eventuell auch billigeren, Alternative wird. Die vorliegende Arbeit soll zu einem besseren Verständnis des Beschleunigungsprozesses beitragen und helfen, die Elektronenparameter zu optimieren.

Die Pulse des *ATLAS*-Lasers (25 fs, 1.8 J) am Max-Planck-Institut für Quantenoptik wurden in eine Gaszelle mit turbulenzfreiem, stationärem Gasfluss fokussiert. Aufgrund der guten Repoduzierbarkeit dieses Gastargets konnten Elektronenpulse sehr stabil beschleunigt werden. Es war daher möglich, die Empfindlichkeit der Elektronenparameter auf kleine Änderungen im Aufbau mit aussagekräftiger Statistik zu untersuchen. Mit optimierten Parametern wurden Elektronenpulse mit $\approx$ 50 pC Ladung und einer Divergenz von $\approx$ 2 mrad FWHM auf Energien von bis zu 450 MeV beschleunigt.

Da die Länge der Gaszelle von 2 bis 14 mm variiert werden kann, war es möglich, die Energie der Elektronenpulse nach verschiedenen Beschleunigungsstrecken zu bestimmen und aus deren Evolution wichtige Parameter des Beschleunigungsprozesses zu entnehmen. Bei einer Elektronendichte von $6,43 \cdot 10^{18}$ cm^{-3} wurde ein maximales elektrisches Feld von $\approx$ 160 GV/m in der Plasmawelle bestimmt. Die Strecke, nach der die Elektronen von der beschleunigenden in die bremsende Phase des elektrischen Felds wechseln, - die Dephasinglänge - betrug 4.9 mm. Beide Werte stimmen gut mit der Theorie überein. Zusätzlich wurde bestimmt, welche Faktoren, bei unseren Laserparametern, die Beschleunigungsstrecke bei verschiedenen Dichten limitieren. Bei niedriger Hintergrunddichte,im Prinzip ideal um höchste Energien zu erreichen, endet die Beschleunigung sogar noch vor dem Erreichen der Dephasinglänge, weil der Laserpuls defokusiert. Diese Messung ist der erste Längenscan, der einen großen Bereich abdeckt, sogar über die Dephasinglänge hinaus, was eine zuverlässige Bestimmung der Beschleunigungsparameter zulässt. Mit diesem Wissen können Gaszellenlänge und Elektronendichte für gegebene Laserparameter optimiert werden.

In einem zweiten Experiment wurde der Einfluss einer gekippten Intensitätsfront des Lasers auf LWFA untersucht. Diese Verkippung kann ausgenutzt werden, um asymmetrische Plasmawellen anzuregen, die die Elektronenpulse von der ursprünglichen Propagationsachse ablenken und damit eine rein optische Kontrolle der Elektronenflugrichtung ermöglichen (bei uns innerhalb eines Öffnungswinkels von 8 mrad). Ebenso muss die aus dem Laser stammende Pulsfrontverkippung sorgfältig überwacht werden, wenn dieser Effekt vermieden werden soll. Desweiteren wurden Hinweise auf kollektive Betatronoszillationen der Elektronen beobachtet, die aufgrund der Asymmetrie außerhalb der optischen Achse in die Plasmawelle injiziert wurden. Da die Stärke der Verkippung die Asymmetrie, und damit die Entfernung des Injektionspunktes zur Achse, bestimmt, kann auf diese Weise eventuell die Wellenlänge der Betatronstrahlung verändert werden.

Alle Ergebnisse werden durch 3D-Particle-in-Cell-Simulationen unterstützt.

Abstract

The experiments presented in this thesis study several aspects of electron acceleration in a laser-driven plasma wave. High-intensity lasers can efficiently drive a plasma wave that sustains electric fields on the order of 100 GV/m. Electrons that are trapped in this plasma wave can be accelerated to GeV-scale energies. As the accelerating fields in this scheme are $3-4$ orders of magnitude higher than in conventional radio-frequency accelerators, the necessary acceleration distance can be reduced by the same factor, turning laser-wakefield acceleration (LWFA) into a promising compact, and potentially cheaper, alternative. However, laser-accelerated electron bunches have not yet reached the parameter standards of conventional accelerators. This work will help to gain better insight into the acceleration process and to optimize the electron bunch properties.

The 25 fs, 1.8 J-pulses of the *ATLAS* laser at the Max-Planck-Institute of Quantum Optics were focused into a steady-state flow gas cell. This very reproducible and turbulence-free gas target allows for stable acceleration of electron bunches. Thus the sensitivity of electron parameters to subtle changes of the experimental setup could be determined with meaningful statistics. At optimized experimental parameters, electron bunches of $\approx$ 50 pC total charge were accelerated to energies up to 450 MeV with a divergence of $\approx$ 2 mrad FWHM.

As, in a new design of the gas cell, its length can be varied from 2 to 14 mm, the electron bunch energy could be evaluated after different acceleration distances, at two different electron densities. From this evolution important acceleration parameters could be extracted. At an electron density of $6.43 \cdot 10^{18}$ cm^{-3} the maximum electric field strength in the plasma wave was determined to be $\approx$ 160 GV/m. The length after which the relativistic electrons outrun the accelerating phase of the electric field and are decelerated again, the so-called dephasing length, was found to be 4.9 mm. Both values are in good agreement with theory. In addition, for our laser parameters, the factors that limit the acceleration distance at the different densities were identified. In the desirable low-density case, where in principle the highest energies can be reached, diffraction of the driver pulse stops the acceleration even before the dephasing length is reached. While plasma-length scans have been performed by other groups, e.g. [1], this is the first comprehensive scan that covers a wide range of lengths, even beyond the dephasing length, thus allowing for a reliable determination of acceleration parameters. Only with this knowledge the gas target length and electron density can be optimized for given laser parameters.

In a second experiment, the influence of a tilted laser-pulse-intensity front on laser-wakefield acceleration was investigated. Such a tilt may be used to excite asymmetric plasma wakes, which can steer electron bunches away from the initial laser axis and thus allow for all-optical control of the electron-pointing direction, in our setup within an 8 mrad opening window. This also implies that the pulse front tilt (PFT) originating in the laser system needs to be carefully monitored if one wants to avoid this effect. We also discovered evidence of collective electron-betatron oscillations due to off-axis electron injection into the wakefield induced by a pulse-front tilt. This is a potential knob to tune the X-ray radiation wavelength, as the strength of PFT changes the off-axis distances for injection . All experimental results are support by full-scale three-dimensional Particle-in-Cell simulations.

Contents

Chapter I

Introduction

I.1. Motivation

Since the first detection of X-rays by Wilhelm Röntgen in 1895 [2] this high-energy radiation became indispensable both in diagnostics of biological and medical samples and in material science or condensed matter physics. Nowadays, over one decade after the first cathode-ray experiments, X-ray sources are available for research applications that offer directed high-quality X-ray beams with outstanding characteristics in photon numbers, spatial coherence and wavelength accuracy. These are synchrotron sources, where, in early days, the X-rays were only a by-product of the electron acceleration on a circular path, in later generations, however, dedicated insertion devices, such as bending magnets, wigglers or undulators are used for controlled X-ray generation. Such facilities can be found all over the world, e.g. *DESY* (Hamburg, Germany), *BESSY* (Berlin, Germany), *ESRF* (Grenoble, France), *LBNL* (Berkeley, USA), *SOLEIL* (Paris, France). Their light is used to investigate the atomic structure of biomolecules, e.g. for drug development, or of promising new materials. But even the most original application of X-rays, the imaging of inner details of the human body, could still be improved by means of these brilliant X-ray sources. Instead of observing the variations in intensity of the transmitted X-rays, the phase of these spatially coherent beams can be evaluated, which contains more detailed information despite lower required dose deposition. For example, cancer patients could benefit from phase contrast imaging [3] as the high resolution might allow the discovery of tumors before they metastasize. However, especially this last application of synchrotron radiation immediately illustrates the large disadvantage of these sources. They are large-scale, cost-intensive facilities that are operated, funded and used by international collaborations. Small-scale laboratories or even hospitals cannot afford their own synchrotron sources due to both spatial and monetary restrictions. The crucial part of synchrotrons in this context is the electron accelerator. The maximum achievable accelerating fields in radio-frequency cavities are limited to several 10 MV/m which results in kilometers of acceleration distance in order to reach GeV-scale electron energies.

However, the concept of electron acceleration in plasma waves can potentially overcome these problems. Plasma waves can sustain longitudinal electric fields exceeding

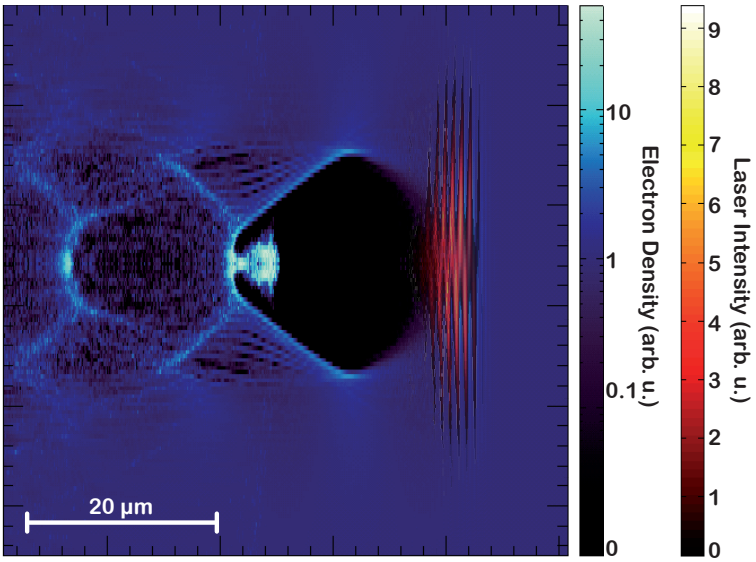

Figure I.1.: *Concept of laser-wakefield acceleration in the non-linear bubble regime. In red, the intensity distribution of the laser pulse is shown, the blue color scale encodes the electron density.*

100 GV/m, which allows for a reduction of acceleration length by up to four orders of magnitude. Such plasma waves can be excited by a high-intensity laser pulse and electrons of sufficient initial momentum may be trapped inside this wake and efficiently accelerated to ultra-relativistic energies. Thus so-called laser-wakefield acceleration (LWFA) might become a key feature in future electron accelerators, especially if size and costs play an increasingly important role.

I.2. Concept and State-of-the-Art

Figure I.1 sketches the very basic principle of electron acceleration in the so-called bubble regime (III.5), where the plasma wave is extremely non-linear due to the high intensity of the driver pulse. By the ponderomotive force of the laser pulse electrons of the plasma are expelled from the high-intensity regions. Behind the laser pulse a cavity void of electrons forms (”bubble” or ”blow-out region”). Due to the restoring force of the undisturbed ions a part of the expelled electrons come back to the laser axis roughly after one plasma wavelength (on the order of several 10 μm). From the high-density point where the trajectories of the deflected electrons cross, electrons with sufficient momentum can be trapped III.3.1 in the blow-out region and subsequently accelerated. In this picture, another large advantage of laser-plasma accelerators, apart from the compact size, can be directly seen: Due to the small scales of the accelerating structure the duration of the trapped electron bunch is inherently extremely short. Pulse durations of several femtoseconds have been measured [4, 5, 6]. As, with most X-ray generation methods, this pulse duration is transferred to the X-ray pulses, these can then be used to probe ultra-fast processes with both high temporal and high spatial resolution.

The idea to accelerate electrons to relativistic energies in a laser-driven plasma wave has been first brought up by Tajima and Dawson [7] in 1979. The development of chirped-pulse-amplification [8] (also II.2) in 1985 has then lead to a leap in laser intensity that made first experimental studies possible. For the first time, laser-driven wakefield acceleration was successfully demonstrated in 1993 by Clayton et al. [9] with an externally injected electron bunch of 1.5 MeV. In the following years several groups managed to accelerate electrons to energies above 100 MeV within only a millimeter (e.g. [10] and references therein). The acceleration regime that could be accessed with lasers of that time with picosecond pulse durations is called self-modulated laser-wakefield acceleration (SM-LWFA) . The advantage over earlier experiments was, that electrons from the plasma background were self-injected into the plasma wave, but only thermal broadband energy spectra could be achieved. In 2002 Pukhov and Meyer-ter-Vehn [11] predicted a highly non-linear regime, that -in simulations- lead to mono-energetic electron bunches. This so-called bubble regime may be accessed when the driving laser-pulse length is comparable to half the plasma wavelength and the a normalized vector potential of the pulse is $a_0 > 1$. The advance in high-power ultra-short-pulse lasers allowed for the first experimental generation of laser-driven quasi-monoenergetic electron bunches in 2004. Faure et al. [12], Geddes et al. [13] and Mangles et al. [14] independently demonstrated laser-accelerated 100 MeV-electron bunches with a relative energy spread of only a few percent and 100 pC of charge. This great breakthrough triggered a broad range of technological improvements to the acceleration scheme. Among other an external guiding channel could push electron energies to 1 GeV energies [15, 16], and sophisticated injection methods helped to further reduce the energy spread. For example, Rechatin et al. [17] achieved 10 pC electron bunches at 200 MeV with a 1% FWHM relative energy spread by injecting the electrons with a counter-propagating colliding pulse. Also the stability of the acceleration process and the shot-to-shot reproducibility was massively enhanced, due to advances in laser technology and improved gas targets [18], but also due to an increased awareness of the influences of the different experimental parameters on the electron beam quality. The experiments done in the frame of this thesis use a steady-state flow gas cell, that delivers extremely reproducible electron bunches, to study some of these influences. More information on the current state of experimental and theoretical research can be found in the first part of the thesis where the basics of laser-wakefield acceleration are discussed in detail.

I.3. Methods for X-ray Generation

While some projects aim at an electron-positron collider based on laser-wakefield acceleration (similar to the planned *ILC* [19]), the more near-term application of this principle will be found in the generation of high-energy radiation from the UV- to the gamma-ray range. The following possible techniques for X-ray generation should be kept in mind as

an application of the electron bunches described in this work:

- X-ray radiation from betatron oscillations of the electrons in the focusing fields of the bubble is a by-product of the acceleration process (cf. section III.5.4). No further setup is needed. "Bubbletron" radiation has been measured and characterized e.g. by [20].

- Alternatively, an undulator can be used for the generation of bright X-rays. An undulator consists of alternating magnets, that force the electrons on an oscillatory path. The electrons emit radiation at a wavelength that is mainly determined by the undulator period shortened by a factor of $1/\gamma^2$ ($E = \gamma mc^2$ is the electron energy). First proof-of-principle experiments have been conducted with our setup [21] where soft-X-ray radiation down to 7 nm was detected from 210 MeV electron bunches.

- In a next step one can think about building a table-top X-ray FEL with a laser-driven electron source [22]. However, for this ambitious goal, the electron bunch quality still has to be drastically improved (also see chapter VIII).

- A last possibility to generate X-rays is via Thomson scattering [23, 24]. In this scheme as laser pulse is scattered from the relativistic electron bunch. Thereby the photon energy is up-shifted by a factor of γ^2. The formalism describing this process is very similar to the generation of undulator radiation. However, in Thomson scattering, the basic length scale that determines the final X-ray wavelength is the laser wavelength ($\sim 1\ \mu$m) which is significantly smaller than the undulator period (0.5 – 2 cm). Thus, with moderate electron energies, extremely high-energy X-rays or even gamma-rays can be generated.

X-ray radiation from all these sources, just as from conventional synchrotrons, is extremely directed (opening cone $\sim 1/\gamma$) and to a certain degree spatially coherent.

I.4. Structure of this work

The experiments described in this work help to understand some basic dynamics of laser-wakefield acceleration. This is important to be able to improve the electron bunch parameters and their reproducibility. One presented measurement uses a variable-length gas cell to scan the evolution of the electron properties during the acceleration process. Basic parameters such as the dephasing length and accelerating field strength are extracted. In the second experiment a laser pulse with tilted intensity front is used to excite the wakefield. It is demonstrated that this asymmetry leads to a deflection of the electron bunch from the original propagation axis. Furthermore, simulations show that in this case electrons are injected into the bubble at an off-axis position, probably leading to enhanced betatron oscillations.

The structure of this work is as follows:

- First the basic properties of a typical high-intensity laser pulse as it is used for LWFA are explained. A special focus lies on spatio-temporal distortions of the pulse, as those will be important for one of the experiments (section II.1).
- Subsequently, a brief overview over the practical generation of ultra-short laser pulses is given (section II.2).
- The next part discusses the theory of laser-wakefield acceleration. Starting from the very basic interaction of a single electron with a plane light wave, the ponderomotive force of a laser pulse is derived, which eventually can lead to the excitation of plasma waves. The analytical 1D wakefield theory and its consequences are detailed. Some limitations and scalings for the 3D non-linear regime are cited that were deduced from PIC-simulations (chapter III).
- After the theoretical discussion of the underlying physical processes, the experimental setup is described in detail (chapter V).
- With this setup two experiments were conducted. Both measurements are supported by simulations. Thus the last two parts of this work consist each of the description of the experiment, the results and subsequently the simulations and their interpretation (chapter VI and chapter VII).

Chapter II

High-Intensity Ultra-Short Laser Pulses

Laser-wakefield acceleration is driven by ultra-short high-intensity laser pulses. As an example the laser facility used for the presented experiments generates $\approx$ 23 fs pulses with $\approx$ 1.7 J energy (75 TW peak power), resulting in focused peak intensities of $\approx 1 \cdot 10^{19}$ W/cm^2 (for $f/22$ focusing optics). The electric field strength of these pulses is on the order of 10 TV/m and electrons wiggling in these fields reach relativistic energies. In the following, the basic characteristics and generation methods of ultra-short high-intensity laser pulses will be described. The objective of the experiments in chapter VII is to analyze the influence of a driver pulse with a tilted intensity front. Therefore a special focus in the description below lies on possible spatio-temporal distortions (such as pulse-front tilt) and their occurrence during the laser pulse generation.

II.1. Mathematical Description

The concepts compiled in this chapter and additional information can be found in e.g. Jackson [25], Rulliere [26], Pretzler [27] and Wollenhaupt et al. [28].
In the following descriptions, vector quantities are indicated by bold characters.

II.1.1 General Characterization

II.1.1.1 Fields

A laser pulse can be described in the space-time domain by an electro-magnetic field $\boldsymbol{E}$, $\boldsymbol{B}$ oscillating with the carrier angular frequency ω_0 multiplied by a spatially and temporally confined envelope $\boldsymbol{E}_A$,$\boldsymbol{B}_A$.

$$\begin{aligned} \boldsymbol{E}(\boldsymbol{x},t) &= \boldsymbol{E}_A(\boldsymbol{x},t)\cos\left(\omega_0 t - \boldsymbol{k}\boldsymbol{x} + \varphi_0\right) \\ \boldsymbol{B}(\boldsymbol{x},t) &= \boldsymbol{B}_A(\boldsymbol{x},t)\cos\left(\omega_0 t - \boldsymbol{k}\boldsymbol{x} + \varphi_0\right) \end{aligned} \tag{II.1}$$

Here, $\boldsymbol{E_A}$ and $\boldsymbol{B_A}$ define the respective polarization direction and amplitude, and the wave vector $\boldsymbol{k}$, with $k = \omega/c$, the propagation direction, c denotes the speed of light in vacuum.

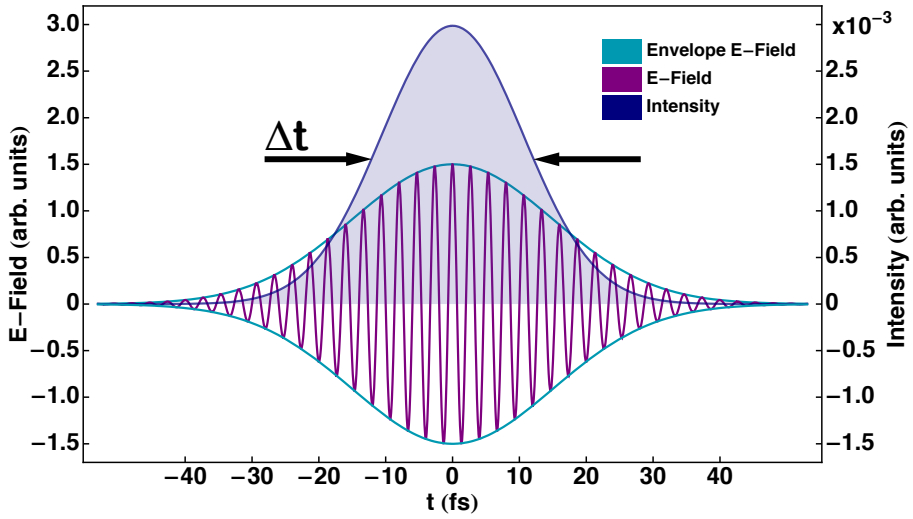

Figure II.1.: *Oscillating electric field and Gaussian envelopes and intensity envelope of a laser pulse with a carrier wavelength of* $\lambda_0 = 800$ nm*, a pulse duration of* $\Delta t = 25$ fs *FWHM (defined by the intensity envelope) and* $\varphi(t) = 0$*.*

φ_0 represents an absolute phase. In vacuum, the $\boldsymbol{E}$- and $\boldsymbol{B}$-field oscillate in phase and $\boldsymbol{E} \perp \boldsymbol{B}$, $\boldsymbol{E} \perp \boldsymbol{k}$, $\boldsymbol{B} \perp \boldsymbol{k}$ and $B_A = E_A/c$. Furthermore, the angular frequency ω_0 of the field oscillation is related to its wavelength λ_0 via $\omega_0 = 2\pi c/\lambda_0$.
The intensity I, which is defined as the modulus of the energy flux density averaged over the time T of one oscillation period, can be measured more easily than the field itself, and is the physically important parameter in many processes.

$$I = \epsilon_0 c \langle E^2 \rangle_T \qquad [I] = \mathrm{W/m^2} \tag{II.2}$$

Figure II.1 shows the temporal dependence of the electric field and the intensity of a pulse with a Gaussian envelope

$$E_A(t) = E_0 \cdot e^{-t^2/\tau_0^2} \tag{II.3}$$

Here τ_0 represents the pulse duration given as the $1/e$ half-width of the Gaussian envelope of the electric field. Details on the different pulse length and width definitions of a Gaussian pulse are found in appendix A. The complete 3-dimensional envelope is often assumed to be Gaussian in all dimensions:

$$\boldsymbol{E}_A(\boldsymbol{x}, t) = E_0 \cdot e^{-t^2/\tau_0^2} \cdot e^{-x^2/w_{x,0}^2} \cdot e^{-y^2/w_{y,0}^2} \tag{II.4}$$

Here, $\boldsymbol{x} = (x, y, z)$ and the pulse propagates along $z = ct$. $w_{x,0}$ ($w_{y,0}$) determines the $1/e$ beam size in x (y)-direction (appendix A) and E_0 is the maximum field amplitude.

In vacuum, i.e. in the absence of any charge and currents, these fields (II.1) fulfill the

Maxwell equations

$$\nabla \cdot \boldsymbol{E} = 0 \qquad \nabla \times \boldsymbol{B} = \frac{1}{c^2}\frac{\partial \boldsymbol{E}}{\partial t} \tag{II.5}$$

$$\nabla \times \boldsymbol{E} = -\frac{\partial \boldsymbol{B}}{\partial t} \qquad \nabla \cdot \boldsymbol{B} = 0 \tag{II.6}$$

and the wave equation:

$$\left(\frac{\partial^2}{\partial t^2} - v^2\nabla^2\right)\Xi(\boldsymbol{x}, t) = 0 \tag{II.7}$$

where v is the propagation velocity of the wave. This equation is satisfied by the $\boldsymbol{E}$- and $\boldsymbol{B}$-field ($\Xi \in [\boldsymbol{E}, \boldsymbol{B}]$), if

$$k = \frac{\omega}{v} = \frac{\omega\eta}{c} \tag{II.8}$$

where η is the refractive index of the medium. In vacuum by definition $\eta = 1$ and $v = c$. The fields of an electro-magnetic wave can also be described by associated potentials $\boldsymbol{A}, \Phi$ (see next paragraph). These must also satisfy the wave equation ($\Xi \in [\boldsymbol{A}, \Phi]$).

II.1.1.2 Potentials

A light pulse can also be described by a vector potential $\boldsymbol{A}$ and a scalar potential Φ that are related to the fields (II.1) by

$$\begin{aligned} \boldsymbol{E} &= -\frac{\partial}{\partial t}\boldsymbol{A} - \nabla\Phi \\ \boldsymbol{B} &= \nabla \times \boldsymbol{A} \end{aligned} \tag{II.9}$$

Two of the Maxwell equations (II.6) are automatically satisfied by this definition [1]. The other two Maxwell equations (II.5) with the fields substituted by the potentials as in (II.9) give a new complete set of two equations that is equivalent to the four equations for the fields. For the potentials there exists a gauge freedom, i.e. different potentials connected by a scalar function $f(\boldsymbol{x}, t)$ can lead to the same fields.
If $\boldsymbol{A}$ and Φ fulfill the Lorentz gauge condition, they also solve the wave equation (II.7),

$$\nabla \cdot \boldsymbol{A} + \epsilon_0\frac{\partial}{\partial t}\Phi = 0 \tag{II.10}$$

A solution to this set of equations in the absence of charge and current is:

$$\begin{aligned} \boldsymbol{A}(\boldsymbol{x}, t) &= -\boldsymbol{A}_A \sin\left(\omega_0 t - \boldsymbol{k}\boldsymbol{x} + \varphi_0\right) \\ \Phi(\boldsymbol{x}, t) &\equiv 0 \end{aligned} \tag{II.11}$$

where

$$A_A = \frac{1}{\omega_0}E_A = \frac{c}{\omega_0}B_A \tag{II.12}$$

[1] These are the homogeneous Maxwell equations, if the general expressions with currents and charges present is considered.

II.1.2 Spectrum

As the light pulse can be described as a product of a pure sinusoidal ('oscillating') term and an envelope, the spectrum is given by the convolution of the Fourier transform of each. The oscillating term only fixes the central frequency ω_0, whereas the envelope determines the shape and the width of the spectrum. For a Gaussian envelope, the Fourier transform is again Gaussian with a spectral width $\Delta\omega$ that is larger for shorter pulse durations Δt. Changing to a complex description of the light pulse facilitates the Fourier transform.

$$\begin{aligned} \boldsymbol{E}(t) &= \boldsymbol{E}_A(t)\cos(\omega_0 t + \varphi_0) \\ &= \frac{1}{2}\left[\tilde{E}(t) + \tilde{E}^*(t)\right] \qquad \text{with} \quad \tilde{E}(t) = E_A(t)e^{i(\omega_0 t+\varphi_0)} \end{aligned} \tag{II.13}$$

The E-field can then be described as the integral over its Fourier components:

$$\tilde{E}(t) = \frac{1}{\sqrt{2\pi}}\int_{-\infty}^{+\infty}\tilde{E}(\omega)e^{i\omega t}\,d\omega \qquad \text{and} \qquad \tilde{E}(\omega) = \frac{1}{\sqrt{2\pi}}\int_{-\infty}^{+\infty}\tilde{E}(t)e^{-i\omega t}\,dt \tag{II.14}$$

Still, the real physical conditions, the real temporal evolution and spectral content and shape of the pulse, are depicted by the real part of both $\tilde{E}(t)$ and $\tilde{E}(\omega)$.

For the fields given above, where there are no higher order time dependencies in the oscillating term, the pulse is called transform-limited. In this case the time-bandwidth product is smallest: $\tau_0 \cdot \sigma_\omega = 2$ (if τ_0 and σ_ω are the Gaussian widths of the envelopes of the electric field) or $\Delta t \cdot \Delta\omega = 2.77$ (for FWHM quantities Δt, $\Delta\omega$ of a Gaussian intensity envelope). If there are higher order phase terms, leading to a time-dependent instantaneous frequency, the pulse is called "chirped". The pulse duration and thus the time-bandwidth product of a chirped pulse is larger than in the transform-limited case.

II.1.3 Gaussian Beams

Laser pulses are often approximated by a Gaussian beam profile

$$E(\boldsymbol{x}) = E_0 \cdot \frac{\exp(-ikz - \varphi(z))}{w(z)}\exp\left(-\frac{x^2+y^2}{w(z)^2} - i\frac{\pi}{\lambda}\frac{x^2+y^2}{R(z)}\right) \tag{II.15}$$

Here, $\varphi(z)$ denotes a phase shift (Guoy shift), $R(z)$ is the beam radius of curvature, and $w(z)$ is the transverse spot size at a position z along the beam path. A Gaussian beam propagating in free space has exactly one waist w_0, where the spot size is smallest and is fully characterized by λ and w_0. The distance after which the transverse beam area has doubled in size is called the Rayleigh length and is given by

$$l_r = \frac{\pi w_0^2}{\lambda} \tag{II.16}$$

which determines all other parameters

$$w(z) = w_0\sqrt{1+\left(\frac{z}{l_r}\right)^2} \qquad R(z) = z + \frac{l_r^2}{z} \qquad \varphi(z) = \arctan\frac{z}{l_r}$$

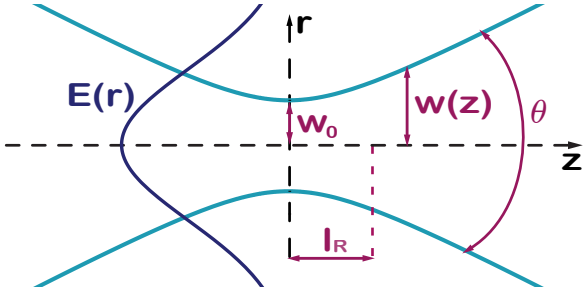

Figure II.2.: *Schematic of a Gaussian beam with Rayleigh length l_R, waist w_0 and divergence angle θ*

The depth of focus of the beam, also called the ”confocal parameter” is defined as twice the Rayleigh length. The Gaussian waist width w_0 and the FWHM spot size Δx are connected by $\Delta x = \sqrt{2\ln(2)}w_0$ (note that Δx is defined by the intensity envelope and w_0 by the field envelope), see also appendix A.

II.1.4 Spatio-Temporal Phenomena

In one of the experiments presented in this work the influence of laser pulses with a tilted intensity front on the acceleration process is studied. Although the phase fronts are perpendicular to the propagation direction, the intensity front is tilted, i.e. the peaks of every longitudinal lineout through the intensity envelope arrive at different temporal delays (see figure II.3). The ”pulse front tilt” belongs to the class of spatio-temporal pulse distortions, which therefore will be described in detail in this section. The three types, angular and spatial chirp and pulse front tilt, are closely connected.
Up to now, it was assumed that the temporal amplitude $E_t(t)$ and the spatial amplitude $E_x(\boldsymbol{x})$ are completely separable and functions of one variable. The same holds for the corresponding amplitudes in the Fourier space: the spectral amplitude $E_\omega(\omega) = \mathscr{F}(E_t(t))$ and $E_{k_x}(\boldsymbol{k_x}) = \mathscr{F}(E_x(\boldsymbol{x}))$.
If there are spatio-temporal distortions present, the combined amplitudes $E(\boldsymbol{x}, t)$, $E(\boldsymbol{k_x}, \omega)$, $E(\boldsymbol{x}, \omega)$ become inseparable functions of two variables, where the spatial and spectral dimension is coupled [29]

$$E(\boldsymbol{x},t) = E_x(\boldsymbol{x}) \cdot E_t(t + \frac{dt_0}{dx}(x - x_0)) \quad \text{Pulse front tilt} \quad \text{(II.17a)}$$

$$E(\boldsymbol{k_x},\omega) = E_{k_x}(k_x + \frac{dk_{x_0}}{d\omega}(\omega - \omega_0), k_y, k_z) \cdot E_\omega(\omega) \quad \text{Angular chirp} \quad \text{(II.17b)}$$

$$E(\boldsymbol{x},\omega) = E_x(x + \frac{dx_0}{d\omega}(\omega - \omega_0), y, z) \cdot E_\omega(\omega) \quad \text{Spatial chirp} \quad \text{(II.17c)}$$

For the sake of simplicity only one transverse spatial dimension (x) is affected and the small influences on the longitudinal dimension are neglected.
All of these effects can easily occur in a short laser pulse (see section II.2) and are usually unwanted as they deteriorate the pulse quality by increasing the pulse duration and the transverse spot size.

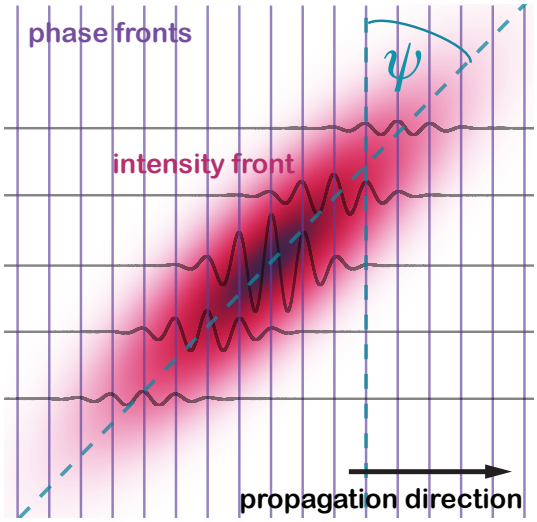

Figure II.3.: *Schematic of a tilted pulse front.*

II.1.4.1 Spatial Chirp

Equation (II.17c) describes a spatial separation of the different frequencies transverse to the propagation direction. Quantitatively, the spatial chirp is characterized by either the spatial dispersion $\xi = dx_0/d\omega$ [30] or the frequency gradient $\upsilon = d\omega_0/dx$:
If $E_x(x)$ and $E_\omega(\omega)$ are two Gaussian functions with a Gaussian width of w_0 and σ_ω (cf. appendix A), respectively, then the frequency gradient is given by [30]:

$$\upsilon = \frac{\xi}{\xi^2 + (\frac{w_0}{\sigma_\omega})^2} \tag{II.18}$$

It has to be noted that υ and ξ are not simply inverse functions. Whereas ξ is only determined by the optical system itself (gratings, imaging, see section II.2), υ additionally depends on the properties of the input pulse (w_0,σ_ω). This description is analogous in the case of a temporal chirp where the respective relations are between time and frequency domain.
The presence of a spatial chirp in an ultra-short laser pulse causes a local reduction in bandwidth ($\sigma_\omega \rightarrow \sigma'_\omega$), leading to an increased pulse duration. Also the transverse spot size is enlarged ($w_0 \rightarrow w'_0$) due to the spatial separation of the different frequencies. The new quantities are given as:

$$\sigma'_\omega = \left[\frac{1}{(\sigma_\omega)^2} + \frac{\xi^2}{(w_0)^2}\right]^{-\frac{1}{2}} \tag{II.19}$$

$$w'_0 = \left[\frac{1}{(w_0)^2} + \frac{\upsilon^2}{(\sigma_\omega)^2}\right]^{-\frac{1}{2}} \tag{II.20}$$

II.1.4.2 Angular Chirp and Pulse Front Tilt

Equation (II.17b) describes an angular chirp (AC) implying that the virtual (!) phase fronts of different frequencies propagate under different angles (figure II.4). This happens

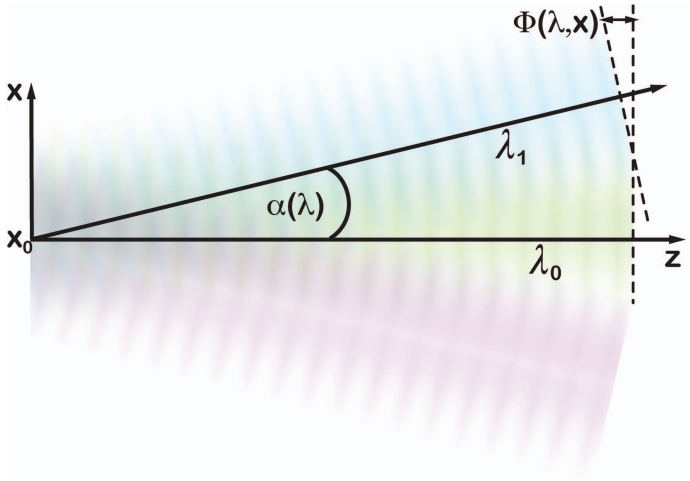

Figure II.4.: *Schematic of an angular chirp. Different colors propagate under different angles.*

for example if a short laser pulse hits a diffraction grating or a prism. In a chirped-pulse-amplification laser system these are essential components (see section II.2) and therefore an angular chirp can easily occur if the alignment is not perfect.
The angular chirp is usually not expressed by $\mathrm{d}k_x/\mathrm{d}\omega$ as in (II.17b) but more intuitively as $\mathrm{d}\alpha/\mathrm{d}\lambda$, where α is the angle between the propagation direction of the whole pulse and the direction of the virtual phase front of a certain wavelength component (see e.g. [31, 32]). The angular chirp introduced by a single grating with groove spacing s, diffraction angle β and diffraction order m is [33]:

$$\frac{\mathrm{d}\alpha}{\mathrm{d}\lambda} = \frac{c \cdot g}{\lambda_0} \qquad \text{with } g = \frac{dk_x}{d\omega} = \frac{m\lambda_0^2}{c \cdot s\cos\beta} \tag{II.21}$$

A pulse front tilt (PFT) is a tilt of the intensity envelope relative to the optical axis as can be seen in fig. II.3. The phase front, however, remains unaltered, perpendicular to the propagation direction.
Considering expressions (II.17a) and (II.17b) representing a pulse front tilt or an angular chirp , respectively, it can easily be shown, that in most cases both descriptions are equivalent and only two different aspects of the same effect.
(II.17b) is the double Fourier transform of (II.17a) with $\omega \to t$ and $\boldsymbol{k}_x \to \boldsymbol{x}$. As the distortion term $dk_{x_0}/d\omega$ in (II.17b) includes both coordinates, it is involved in both steps of the Fourier transform. According to the shift theorem [2] (e.g. [34]) the frequency-dependent "shift" in the spatial wave vector (=angular chirp) turns into a phase in the $x-\omega$ domain, which again - with the second Fourier transform - is converted into a time-dependent shift in space (=pulse front tilt).

[2] If $G(\omega) = \mathscr{F}(g(t))$, then $\mathscr{F}(g(t-a)) = G(\omega)e^{-ia\omega}$, where $\mathscr{F}$ means taking the Fourier transform.

Not-affected coordinates are neglected:

$$\begin{aligned}\hat{\tilde{E}}(k_x,\omega) &= &&= \hat{\tilde{E}}_0(k_x + g(\omega-\omega_0),\omega)\\ \tilde{E}(x,\omega) &= \mathscr{F}^{-1}(\hat{\tilde{E}}(k_x,\omega)_{k_x\to x} &&= \tilde{E}_0(x,\omega)e^{ig(\omega-\omega_0)x}\\ E(x,t) &= \mathscr{F}^{-1}(\tilde{E}(x,\omega))_{\omega\to t} &&= E(x,t+gx)\end{aligned} \tag{II.22}$$

The simple argument as it is given above is only valid if there are no other effects present that couple the different coordinates. A spatial chirp, for example, couples x and ω as seen in (II.17c). The Fourier transform can then not be calculated in the shown way. As a consequence, an angular chirp indeed always causes a pulse front tilt, but a pulse front tilt can not only be created by an angular chirp. Also a combination of spatial and temporal chirp can have the same effect.

Another way to look at the AC-PFT equivalence is to consider the difference in spectral phase $\phi(x,\lambda)$ that an angular chirp introduces (cf. [31]). As can be deducted from figure II.4

$$\Delta\phi(x,\lambda) \approx \frac{2\pi}{\lambda}\alpha(\lambda)(x-x_0) \tag{II.23}$$

and therefore a linear phase chirp component

$$\left.\frac{d\phi}{d\lambda}\right|_{\lambda_0} = \frac{2\pi}{\lambda_0}\left.\frac{d\alpha}{d\lambda}\right|_{\lambda_0}(x-x_0) \tag{II.24}$$

depends on the spatial position $x - x_0$. Consequently, also the group delay $D_g(\omega)$ varies with the transverse position:

$$D_g(\omega) = \frac{\lambda_0}{c}\left.\frac{d\alpha}{d\lambda}\right|_{\lambda_0}(x-x_0) \tag{II.25}$$

If the group delay of the pulse linearly increases with the transverse positions, it means that the intensity envelope is tilted relative to the propagation direction.
The PFT angle in the near field of the beam ψ is then given by [35]

$$\tan\psi = \lambda_0\,\mathrm{d}\alpha/\mathrm{d}\lambda \tag{II.26}$$

One important fact to notice is that the spatio-temporal distortions angular chirp $d\alpha/d\omega$ and spatial chirp $dx/d\omega$ are characteristics of the optical system and independent of the input pulse. The chirps define a differential angular or spatial offset between different frequencies that is imposed on an input pulse by an optical system. However, for example, the pulse duration of the output pulse depends on the frequency content and pulse duration of the input pulse. The pulse front tilt as introduced by e.g. a diffraction grating depends on the central wavelength but is in principle independent of beam characteristics such as size and pulse length (see (II.26)). However, the angle might change after propagation through further optical elements if subsequently the pulse duration and beam size are

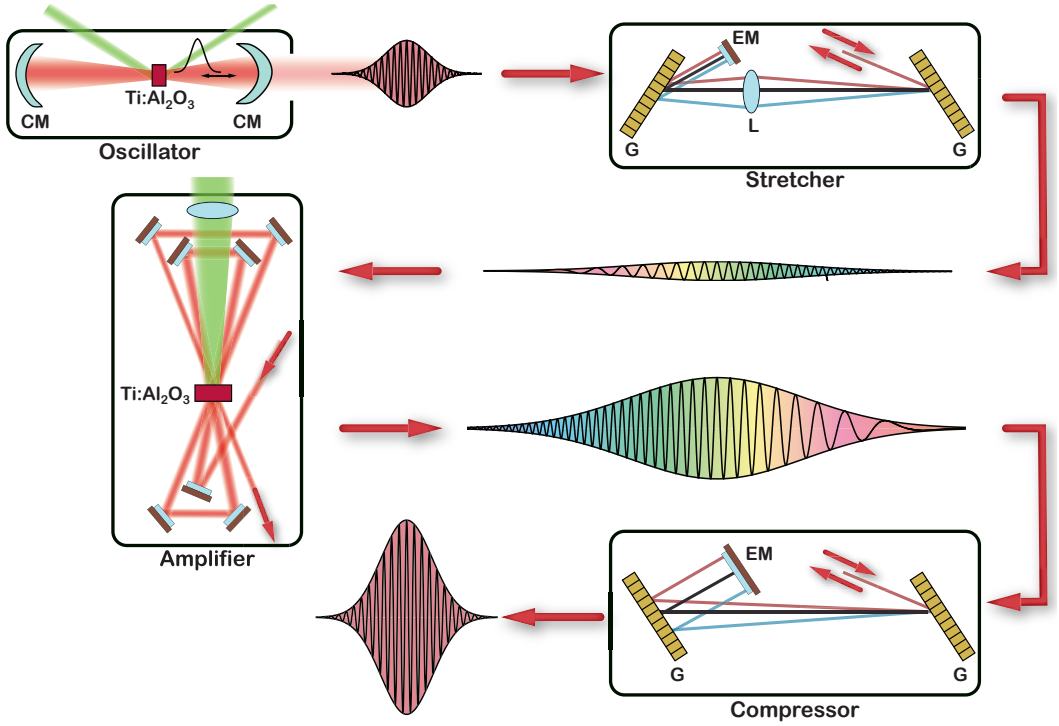

Figure II.5.: *Scheme of a high-intensity CPA laser chain. CM: chirped mirror, G: diffraction grating, EM: end mirror*

changed. For strong angular chirps even free space propagation can change the pulse front tilt angle [32], as the transverse separation of frequencies leads to a considerable increase of beam size and pulse duration.
More details, also about the evolution of a pulse with tilted intensity front, can be found in chapter VII and appendix E.

II.2. Generation

II.2.1 General Concept of High-Intensity Short-Pulse Lasers

High-intensity short pulse lasers rely on the concept of ”chirped-pulse amplification” (CPA) [8]. A low-energy sub-20 fs-pulse train (”seed”) from a passively mode-locked Titanium:Sapphire oscillator is amplified in a subsequent amplifier chain. As, in principle, already during the amplification process the intensity can easily reach the damage threshold of the optics in the amplifiers, one has to ensure a low enough intensity on the optics either by increasing the area of the beam or the pulse duration. Although it is simple to increase the area, it is only practicable up to a certain size, as Ti:Sapphire crystals can only be grown to a limited size, other optics get expensive and the geometry of e.g. multi-pass amplifiers would consume a lot of space. Hence in order to realize a high-intensity laser the pulses are temporally stretched, amplified and subsequently compressed again

(fig. II.5). The stretching/compression is done by introducing a positive/negative chirp in a controlled way (→ chirped-pulse amplification), either via a pair of parallel gratings (see section II.2.1.1) or a set of prisms.
The amplification is typically achieved by pumping a Ti:Sapphire crystal with 532 nm-light (usually from a frequency doubled Nd:YAG laser) and sending the seed pulse several times through the excited crystal. For this there exist two different geometries:

regenerative amplifier: The seed pulse is coupled into a resonator by a Pockels cell, bounces back and forth through the pumped crystal and is coupled out again after a certain amount of round-trips. Advantages are the high energy boost within one amplification stage and the improvement of the transverse beam profile. Only light that matches the eigenmode of the resonator will be amplified and the cavity works as a spatial filter. The disadvantage is the high probability of amplification of spontaneous emission (ASE). This leads to a large pedestal on the timescale of the length of the pump pulse and thus bad contrast between main pulse and background.
multi-pass amplifier: The seed pulse passes through the crystal a few times in bow-tie like geometry (see fig. II.5), no cavity is involved. Advantage: less ASE, no transmissive optics as Pockels cells or polarizers necessary, disadvantage: space consuming, geometrically limited number of passes.

II.2.1.1 Grating Compressor

The key parts in a CPA system are stretcher and compressor, which are based on optical setups with dispersive elements (e.g. gratings or prisms). In the complementary stretcher and compressor arrangements different spectral components of the incident pulse travel different distances leading to a positive or negative chirp of the pulse. Details on different stretcher/compressor versions can be found e.g. in Diels and Rudolph [36] or Pretzler [27]. In a grating-based system, as used in the *ATLAS* facility, the stretcher introduces a positive chirp, just as most transmissive optical elements in the laser chain do, and the compressor imposes a negative phase on the pulse. The compressor has to eliminate the combined spectral dispersion introduced by the strechter and the material in the amplifier chain .
A grating compressor consists of two identical parallel diffraction gratings and an end mirror (fig. II.6). The colors of an incoming unchirped broadband laser pulse are diffracted to different angles on the first grating, which corresponds to an angular chirp. After the second grating that has the same diffractive properties as the first one, all colors have traveled different distances, but are parallel again, although spatially separated (”spatial chirp”). The plane end mirror reflects that beam again on the exact same path backwards through the double-grating setup. All colors end up spatially confined again, the spatial chirp has been removed. But due to the different path lengths that different colors traveled through the setup, the pulse is then temporally chirped. In reality the end mirror is a 90° roof mirror, that shifts the beam in height, but does not change the direction, allowing for a spatial separation of the incoming and outgoing beam. Obviously, if one enters a compressor setup with a temporally (positively) chirped pulse it will be compressed. The total spectral phase that is introduced during the propagation in the compressor (back and

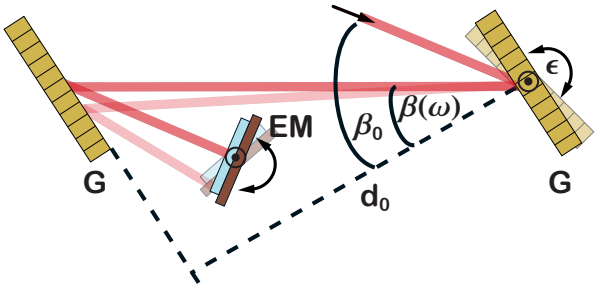

Figure II.6.: *Grating compressor setup, G: Grating, EM: End Mirror, β_0: angle of incidence, $\beta(\omega)$ diffraction angle*

forth, two hits on each grating) is

$$\phi(\omega) = 2\frac{\omega}{c} d_0 \cos\left(\beta_0 - \beta(\omega)\right) \tag{II.27}$$

where d_0 denotes the grating separation (see fig. II.6).
A corresponding stretcher setup has to introduce a spectral phase corresponding to the compressor phase minus the phase introduced by the material dispersion, with the inverse sign. The basic geometry incorporates two exactly anti-parallel identical gratings, an imaging lens that produces a 1:1 (virtual) image of the first grating and an end mirror (cf. sketch of "stretcher" in fig. II.5). Possible extensions of this principle include a mirror instead of the lens or a folding mirror to save one grating and reduce the size of the setup. Furthermore a roof mirror that offsets the beam horizontally or vertically can allow for more than one pass through the setup in order to introduce more dispersion.

II.2.1.2 Acousto Optic Programmable Dispersive Filter

The stretcher and compressor in a laser chain are matched as closely as possible to the material dispersion in the amplifier chain. The residue, especially higher order dispersion components, are taken out by an acousto-optic programmable dispersive filter (AOPDF) or *DAZZLER* [37, 38] can be used. A chirped acoustic wave is coupled into a birefringent uniaxial crystal co-propagating collinearly with the chirped optical wave. As the refractive index of the crystal is modulated by the acoustic wave phase-matching of the ordinary and extraordinary axes can be achieved for certain frequencies causing those frequencies to be scattered from the ordinary to the extraordinary axis. As the velocity of optical waves is much larger than that of the acoustic wave, and because we assume short optical pulses they will see a fixed spatial refractive index variation along the propagation direction. Thus different frequencies of the optical pulse are scattered from the ordinary into the extraordinary axis at different longitudinal positions during the propagation through the crystal. As the indices of refraction and thus the velocities of light in both axes differ, different colors covering different distances within the respective axes are delayed with respect to each other. By controlling the chirp of the acoustic wave an accurate, high-order chirp can be imposed onto the optical pulse. The *DAZZLER* usually sits in the beginning of the laser chain where the seed pulse is still small and pre-compensates dispersion that is introduced during amplification.

	power (TW)	Δt	energy (on target)
ATLAS 25	27	37 fs	0.85 J
ATLAS 40	42	26 fs	1.1 J
ATLAS 80	74	23 fs	1.7 J

Table II.1.: *Pulse parameters of the different ATLAS stages. The transmission of the compressor plus the beamline to the target chamber was measured to be* 65 % *(ATLAS 40/80) or* 50 % *(ATLAS 25), respectively.*

II.2.2 The *ATLAS* facility

The presented experiments were conducted at the **A**dvanced **T**itanium:Sapphire **LAS**er (*ATLAS*) facility. During the course of this work the parameters of ATLAS changed as two major upgrades were implemented. Table II.1 shows the pulse parameters for the different development stages. The *ATLAS* facility is a Ti:Sapphire CPA system with a grating stretcher/compressor + *DAZZLER* setup and 10 or 5 Hertz repetition rate (*ATLAS 25* or *ATLAS 40/80*, respectively.) The *ATLAS 25* setup is described and characterized in depth in [39] and [40]. Pulses (0.5 nJ) from the oscillator were pre-amplified to 1 μJ and subsequently stretched to 350 ps. The 12-pass regenerative amplifier then boosted the energy to 18 mJ. Two multi-pass power amplifiers then reached 0.5 J and eventually 1.7 J. After compression and propagation through the beamline a 37 fs pulse with 850 mJ total energy reached the target. The energy could be confined to the central focal spot with a Strehl ratio[3] of ~ 0.7.
The front-end of *ATLAS 40/70* incorporates as the new key part a *MAZZLER*[4] within the regenerative amplifier in order to counter-act gain narrowing in the power amplifiers and therefore guarantee a larger amplified bandwidth. Thus a bandwidth 50 *nm* can be sustained through the entire amplification chain. Subsequently, two (*ATLAS 40*) or three (*ATLAS 70*) bow-tie-geometry multi-pass amplifiers boost the pulse to the final maximum energy of 3 J before compression (2.6 J on a daily basis). The ASE contrast[5] is 10^{-8} at 20 ps before the main pulse.

[3] The Strehl ratio characterizes the focusability of a laser beam. It defines the ratio of energy that is contained in the central Airy disc of the focused beam to the energy that should be collected there if the beam profile was perfect. A Strehl ratio of 1 therefore defines a flat wavefront with a top-hat intensity distribution or if applied to characterize optical systems a completely aberration-free imaging [41].

[4] A *MAZZLER* is the same device as a *DAZZLER* (see section II.2.1.2) only that the transmitted beam from the ordinary crystal axis is used. The *MAZZLER* can pre-shape the spectrum of the seed pulse with a dip in spectral regions where amplification is highest. If positioned in a regenerative amplifier this leads to a uniform amplification of a broad spectral range.

[5] The ratio between the ASE pedestal and the main peak.

Chapter III

Laser-Matter-Interaction

In the following sections a basic understanding of high-intensity laser-matter interactions will be established, ranging from the behavior of a single electron in an intense electromagnetic wave to the collective dynamics a plasma wave excited by a laser pulse. Furthermore, the propagation of a high-intensity laser pulse in plasma is analyzed, including non-linear effects such as self-focusing. Eventually, the characteristics of laser-wakefield acceleration (LWFA) are discussed. By this mechanism electrons are efficiently accelerated to relativistic energies in the electric field prevailing between the electron density peaks of a plasma wave.

III.1. Plane Wave and Single Electron

The basics of plasma physics and laser-matter interaction explained in the following sections are composed from e.g. Goldston and Rutherford [42], Gibbon [43], Kruer [44] and Meyer-ter-Vehn and Pukhov [45].

III.1.1 Basic Interaction of Light Fields with Particles

The motion of a charged particle in an electro-magnetic field is determined by the Lorentz force:

$$\frac{\mathrm{d}\boldsymbol{p}}{\mathrm{d}t} = q(\boldsymbol{E} + \boldsymbol{v_e} \times \boldsymbol{B}) \tag{III.1}$$

In the non-relativistic case $v \ll c$ this reduces to $d\boldsymbol{p}/dt = q\boldsymbol{E}$, as $B = E/c \ll E$ and thus the second term can be neglected. By integrating this equation one can obtain the maximum velocity an electron can achieve in an E-field as described in II.1: $v_{e,quiv} = eE_A/(\omega_0 m)$. $v_{e,quiv}$ is also called quiver velocity. If this velocity approaches c, neglecting the $\boldsymbol{v} \times \boldsymbol{B}$-term is not justified anymore.
In terms of the vector potential $\boldsymbol{A}$ the equation of motion has the form:

$$\frac{\partial \boldsymbol{p}}{\partial t} + (\boldsymbol{v} \cdot \nabla)\boldsymbol{p} = e\left(\frac{\partial \boldsymbol{A}}{\partial t} - \boldsymbol{v} \times \nabla \times \boldsymbol{A}\right) \tag{III.2}$$

Here, the Coulomb gauge $\nabla \boldsymbol{A} = 0$ was used and the identity $d/dt = \partial/\partial t + \boldsymbol{v} \times \nabla$.
The normalized laser vector potential $a_0 \equiv eA/m_e c < 1$ is considered as a rough distinction between the classical $a_0 < 1$ and the relativistic regime $a_0 > 1$. With $a_0 = 1$, a classical calculation would lead to $v_{e,quiv} = c$. From (II.12) it also follows

$$a_0 = \frac{eA}{mc} = \frac{\lambda}{2\pi} \frac{eE}{m_e c^2} \tag{III.3}$$

which illustrates that the energy an electron can gain from the electric field of the laser pulse equals the rest energy of an electron for $a_0 = 1$.

III.1.1.1 A Single Electron in a Plane Wave

Although this is the most basic light-particle interaction, all other effects such as the ponderomotive force, self-focusing or driving a plasma wave are in the end based on the behavior of each single electron in a light wave with relativistic intensities. For a comprehensive understanding of these collective processes, the basic characteristics of this simple single-electron motion will be discussed.

According to the Noether theorem [1] the two symmetries of a plane wave (two-dimensional structure and invariance under $t \rightarrow t - \boldsymbol{x}/c$) correspond to two conservation laws for the electron motion:

- The transverse momentum $\boldsymbol{p}_\perp$ is always conserved.

$$\boxed{\boldsymbol{p}_\perp + q\boldsymbol{A}_\perp = const1} \text{ for an initial } p_0 = 0 \rightarrow const1 = 0 \tag{III.4}$$

  It follows $p_\perp/mc = a$ and thus [2]

$$\gamma_\perp = \left(1 + a^2\right)^{1/2} \tag{III.5}$$

- For the longitudinal momentum $\boldsymbol{p}_\parallel$ it holds

$$\boxed{E - cp_\parallel = const2} \text{ for an initial } p_0 = 0 \rightarrow const2 = mc^2 \tag{III.6}$$

The energy of a relativistic electron in the coordinate system of the laser pulse can be written as:

$$E = \gamma mc^2 = \sqrt{(mc^2)^2 + p_\parallel^2 c^2 + p_\perp^2 c^2} \tag{III.7}$$

[1] Noether's theorem: Every differentiable symmetry of the action of a physical system has a corresponding conservation law. The action of a physical system is the time-integral over the Lagrangian. Symmetry under a time shift gives conservation of energy, symmetry under translation in space gives conservation of momentum and rotation symmetry gives conservation of angular momentum.

[2] The relativistic γ is defined as:

$$\gamma = \frac{1}{\sqrt{1 - \beta^2}} = \sqrt{1 + \left(\frac{\boldsymbol{p}}{m_e c}\right)^2} \qquad \text{and} \qquad \boldsymbol{\beta} = \frac{\boldsymbol{v}}{c}$$

and with equations (III.4) and (III.6) it follows

$$E_{kin} = mc^2(\gamma - 1) = p_{\parallel}c = \frac{p_{\perp}^2}{2m} = \frac{e^2 A_{\perp}^2}{2m} \tag{III.8}$$

With the definition of the normalized vector potential (III.3) and regarding the fact that $\boldsymbol{a} = \boldsymbol{a}_{\perp} = (a_x, a_y, 0)$ it follows

$$\gamma = 1 + \frac{a^2}{2} \tag{III.9}$$

With the aid of the derived constants of motion the integration of the equation of motion (III.1) is easily done and the trajectory of a single electron in a light field (linear polarization in x-direction) is obtained as follows:

$$\begin{aligned} x(\tau) &= \frac{ca_0}{\omega}\sin(\omega\tau) \qquad\qquad \text{with } \tau = t - \frac{z(\tau)}{c} \\ y(\tau) &= 0 \\ z(\tau) &= \frac{ca_0^2}{4}\left[\tau + \frac{1}{2\omega}\sin(2\omega\tau)\right] \end{aligned} \tag{III.10}$$

This trajectory consists of a drift in the light-propagation direction $z_{drift}(t) = a_0^2(a_0^2+4)^{-1}ct$ and a figure-8 motion in this drift frame $x = a_0 c\omega^{-1}\sin(\omega\tau)$, $z - z_{drift} = a_0 c(8\omega)^{-1}\sin(2\omega\tau)$. The electron can only gain energy from the transverse electric field. For $\boldsymbol{v} \approx c$ the $\boldsymbol{v} \times \boldsymbol{B}$-force directs this motion in the propagation direction of the laser. Still, if one imposes a symmetric temporal envelope on the electric field, the electron is at rest again after the pulse has passed. No energy is transferred. However, if this assumption of spatially uniform light fields with a slowly varying temporal envelope is violated, the electron can indeed gain energy. For example tightly focused laser beams with strong intensity gradients can "repel" electrons from the high-intensity regions. The corresponding force is described in detail in the next section. It could be experimentally verified [46] that the angle θ under which electrons are scattered out of an intense laser focus is the same angle under which an electron moves in a plane wave (with (III.8)):

$$\tan\theta = \frac{p_{\perp}}{p_{\parallel}} = \sqrt{\frac{2}{\gamma - 1}} \tag{III.11}$$

III.1.1.2 Ponderomotive Force

The interaction of a single electron with an electro-magnetic wave becomes more interesting, if, instead of a plane wave, one considers a spatially and temporally limited pulse e.g. with a Gaussian envelope as (II.4). As will be seen, although in principle following the electric field (quiver motion), electrons drift away from regions of higher intensity.
In the limit $v \ll c$ the equation of motion (III.1) for an electron in a light wave polarized along the x-direction and propagation along z reduces to

$$\frac{\partial v_x}{\partial t} = -\frac{e}{m}E_x(\boldsymbol{x}) \tag{III.12}$$

The Taylor expansion of an electric field as in (II.1) gives

$$E_x(\boldsymbol{x}, t) = E_{x,A}(x, t)\cos(\varphi) + x\frac{\partial E_{x,A}(x, t)}{\partial x}\cos(\varphi) + \dots \tag{III.13}$$

with $\varphi = \omega_0 t - k_z z$. To the lowest order the electron directly follows the field and moves with the quiver velocity $v_{e,quiv}$ as defined before. However, from the cycle-averaged equation of motion for the second order field

$$\left\langle \frac{\partial v_x^{(2)}}{\partial t} \right\rangle_T = \left\langle \frac{e^2}{m^2\omega^2c^2} E_{x,A}\frac{\partial E_{x,A}(x, t)}{\partial x}\cos(\varphi)^2 \right\rangle_T = \frac{e^2}{4m^2\omega^2}\frac{\partial E_{x,A}^2}{\partial x} \tag{III.14}$$

the non-relativistic ponderomotive force $F_p = m\langle \partial v_x/\partial t\rangle$ can be determined (here already for the general 3D case):

$$\boldsymbol{F}_p = -\frac{e^2}{4m\omega_0^2}\nabla E_A^2 \tag{III.15}$$

It is obvious that the ponderomotive force is proportional to the gradient of the intensity $I \propto E_A^2$. Furthermore the ponderomotive force is a conservative force that can be derived from a potential U_p via $F_p = -\nabla U_p$ with

$$U_p = \frac{e^2}{4m\omega_0^2}E_A^2 \tag{III.16}$$

It should be noticed that the ponderomotive potential is not only proportional to the intensity but to $I\lambda_0^2$.
In the relativistic case $v \approx c$ the equation of motion is best used in the form of (III.2). Assuming that again the motion can be separated into a fast oscillating part, that directly follows the vector potential $\boldsymbol{p} = e\boldsymbol{A}$ (III.4) and a slow component, the relativistic ponderomotive force can be determined (with $\gamma = (1 + (p/mc)^2)^{1/2}$ (III.5)):

$$\boldsymbol{F}_{p,rel} = -\frac{e^2 m}{2\gamma}\nabla A^2 = -mc^2\nabla\gamma \tag{III.17}$$

For a detailed derivation of the relativistic ponderomotive force see e.g. [47].

III.2. Laser Pulse and Plasma

III.2.1 Ionization

In the case of high-intensity laser pulses it is valid to reduce the description of laser-*matter* interaction laser-*plasma* interaction. By the mechanisms explained in the following section, matter is at least partially ionized already by the pre-pulses or the rising edge of the main pulse.
The electric potential of a high-intensity laser pulse is comparable to the potentials binding inner-shell electrons of heavy atoms to their cores. For light atoms, e.g. hydrogen

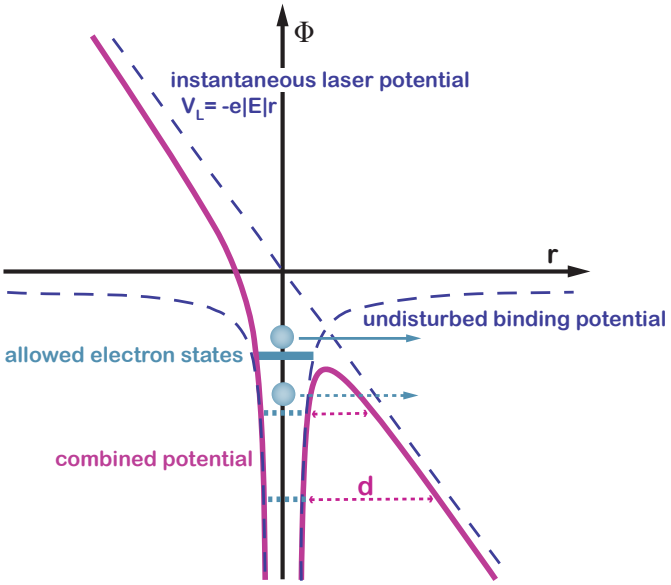

Figure III.1.: *Scheme of barrier suppression ionization (highest electron state, continuous line) and tunnel ionization (lower two states, dashed lines). The instantaneous laser potential on the time-scale of ionization can be approximated to be linear in space.*

a laser pulse intensity of $1.4 \cdot 10^{14}$ Wcm^{-2}, corresponding to an electric field strength of $2.4 \cdot 10^{9} Vm^{-1}$, deforms the potential well that binds the electron to the proton so heavily that the electron is immediately set free (see fig. III.1, highest electron state, continuous line). This effect is called barrier suppression ionization. If the light field is not strong enough to suppress the binding field completely below the respective occupied state still tunnel ionization can occur. The electrons can tunnel through the finite barrier with a probability that is inversely proportional to the barrier width d (see fig. III.1, lower two electron states, dashed line). Both regimes are quantitatively characterized by the ADK-model described in Ammosov et al. [48] and Delone and Krainov [49].
For even lower light intensities this semi-classical picture is not valid anymore and the ionization mechanism changes to multi-photon ionization [50]. If the energy of one photon (Ti:Sapph laser with $\lambda_L = 800$ nm $\rightarrow$ $E_L = \hbar\omega = 1.5$ eV) is not enough for direct photo-ionization (ionization energy for hydrogen $E_i = 13.6$ eV) the summed up energy of $n = \lfloor E_i/E_L \rfloor$ simultaneously incident photons can cause multi-photon ionization of the atom. "Simultaneously" in this case means that the $n + 1^{\text{st}}$ photon has to arrive within the lifetime of the n^{th} virtual excited state, which usually is on the order of 10^{-14} s [51] and easily fulfilled with a finite probability for high-intensity laser pulses that deliver Joules of energy within several ten femtoseconds (1 J $= 6.2 \cdot 10^{18}$ eV $\approx 4 \cdot 10^{18}$ photons at $\lambda_L = 800$ nm).
In conclusion, it becomes clear that for focused laser intensities of $> 10^{18}$ Wcm^{-2} interacting atoms will be ionized at least four to five orders of magnitude below the peak intensity. In the case of hydrogen which is used in the experiments of this work it is even justified to assume a fully ionized plasma, when the main interaction takes place.

III.2.2 Plasma Properties

A plasma is a mixture of neutral and charged particles or, in the case of a fully ionized plasma, only of positively and negatively charged particles. The formal definition of a plasma requests two characteristics to be fulfilled:

1. The distance over which the charge of a test particle that is inserted into the plasma is shielded out must be much smaller than the plasma size. This distance, called Debye length, is:

$$\lambda_D \equiv \sqrt{\frac{\epsilon_0 k_B T_e}{n_e e^2 (1 + Z T_e / T_i)}} \tag{III.18}$$

   where k_B is the Boltzmann-factor, T_e the electron temperature, T_i the ion temperature and n_e the electron density. This expression is only valid, if electrons and ions each are in a thermal equilibrium among themselves. However, electrons and ions do not necessarily have to be in a thermal equilibrium with each other.
   This condition can also be regarded as quasi-neutrality, i.e. on a length scale $> \lambda_D$ the plasma appears to be electrically neutral.

2. There must be $\gg 1$ particles within a Debye sphere of radius λ_D:

$$n_e \cdot \frac{4}{3}\pi\lambda_D^3 \gg 1 \tag{III.19}$$

   If the Debye sphere is densely populated, the plasma is called weakly coupled; the plasma then is hot and diffuse and collective effects can occur as Coulomb scattering between particles is rare. For strongly coupled plasmas a different formalism has to be applied.

In laser-wakefield acceleration of electrons the plasma before the laser arrival is assumed to be weakly-coupled and quasi-neutral. During the interaction of the laser with the plasma only electrons are affected. The heavier protons and ions form an immobile background, as the normalized vector potential for protons is $a_{0,p} = eA(m_p c)^{-1} \ll 1$
It has to be noted that the interaction with a femtosecond laser pulse happens on a time scale τ_{int} that is much smaller than the mean free time between collisions τ_c in such a plasma. Even for solid state plasma densities $\tau_c/\tau_{int} \approx 40$ [52]. Consequently, collisions can be neglected when treating relativistic interactions between ultra-short laser pulses and plasma. On the other hand the electron population cannot be in a thermal equilibrium during the interaction. Applicable simulation codes account for both conditions (see appendix B).

III.2.3 Plasma Waves

If electrons in an unmagnetized plasma are dislocated from their equilibrium position by a force that is not strong enough to influence the heavier ions a so-called Langmuir oscillation is initiated. The displaced electrons are pulled back towards the stationary ions, but overshoot due to their inertia and build up a new charge density peak on the

other side. On the time scale of this oscillation the ion background does not respond to the generated electric fields as its inertia is too high. The oscillation frequency ω_p of a cold plasma is governed by the restoring force and thus dependent on the electron density:

$$\omega_p = \sqrt{\frac{n_e e^2}{\epsilon_0 m}} \tag{III.20}$$

and the plasma wavelength is $\lambda_p = 2\pi c/\omega_p$. m is the electron mass.
For general Langmuir waves in a warm plasma the "Bohm-Gross dispersion relation" is valid:

$$\omega_L^2 = \omega_p^2 + 3\frac{k_B T_e}{m} k_L^2 \tag{III.21}$$

where T is the plasma temperature and $\boldsymbol{k}_L = c/\omega_L$ the wave vector of the Langmuir wave. At low temperature or long wavelength (low k) the phase velocity ω_L/k_L can grow arbitrarily large, but the group velocity $\partial\omega/\partial k$ approaches zero, so no energy or information can propagate. At short wavelengths (large k) or high temperatures, however, group and phase velocity both converge to $\sqrt{3k_B T/m}$ and the wave propagates forward. This is very important for the subject of laser-wakefield acceleration as energy transfer is possible between propagating plasma waves and charged particles that move at velocities close to the wave phase velocity (Landau damping). If the plasma wave is driven by a laser pulse, the phase velocity of the plasma wave corresponds to the group velocity of the laser pulse (see section III.2.4)
Langmuir waves are purely longitudinal, electrostatic waves. Only if the wave has transverse components also magnetic fields can oscillate. If the wave is excited by a high-intensity few-cycle laser pulse, electrons are displaced both longitudinally and transversely relative to the laser propagation axis and the resulting electromagnetic oscillation incorporates a complex three-dimensional structure (see section III.5).

III.2.4 Laser-Propagation in Plasma

The characteristics of plasma-light interactions differ depending on the ratio of ω_p/ω_l (where ω_l is the frequency of the incident light). If $\omega_p < \omega_l$ the light can propagate through the plasma. Then the plasma is called undercritical or underdense (as $\omega_p \propto \sqrt{n_e}$). If $\omega_p > \omega_l$ the light is reflected and enters the plasma only to the skin depth on the order of c/ω_p. In the overcritical case the resonance frequency of the plasma electrons is higher than the frequency of the driving electric field of the laser and they can easily follow the oscillation. The driving laser field is damped and the secondary dipole emission of the oscillating electrons is reflected back.
For a Ti:Sapphire laser with $\lambda_0 = 800$ nm the critical density n_c at which $\omega_p = \omega_0$ is $1.74 \cdot 10^{21}$ cm^{-3}

The dispersion relation for the propagation of light in plasma is:

$$\omega_l^2 = \omega_p^2 + c^2 k_l^2 \tag{III.22}$$

which determines the refractive index of plasma for laser frequency ω_l

$$\eta = \sqrt{1 - \left(\frac{\omega_p}{\omega_l}\right)^2} = \sqrt{1 - \frac{n_e}{n_c}} < 1 \tag{III.23}$$

In the case of high laser intensities $a_0 \geq 1$ the plasma electrons gain significant energy during the interaction with the laser. As the dispersion relation for the laser propagation in plasma is mainly determined by the electron response, this energy change must be considered. According to [53] this can be accounted for by substituting ω_p^2 by $\hat{\omega_p^2} = \omega_p^2/\gamma$. Due to the reduced effective plasma frequency laser pulses can then even propagate in moderately overdense plasmas. The effect is called self-induced relativistic transparency. The phase velocity of a laser pulse traveling in plasma is $v_{l,ph} = c/\eta$ and the group velocity is $v_{l,gr} = \eta c$. With (III.22) this gives a relativistic laser group velocity of $v_{l,gr} = c(1 - \omega_p^2/(\gamma^2\omega_0^2))^{1/2}$. The phase velocity of a plasma wave excited by a laser pulse is equal to the group velocity of the laser. Hence, the $\gamma_{p,ph}$ of the plasma electrons can be determined to

$$\gamma_{p,ph} = \frac{1}{\sqrt{1 - \frac{v_{l,gr}}{c}}} = \frac{\omega_0}{\omega_p}\gamma \tag{III.24}$$

III.2.4.1 Self-Focusing

As a laser pulse with $a_0 \geq 1$ propagates through an underdense plasma background, electrons quiver with relativistic relativistic and the instantaneous energy $E = \gamma mc^2$ depends on the laser intensity. As γ directly enters into the refractive index (III.23), this leads to a reduced phase velocity in regions of high laser intensities. In addition, the ponderomotive force (III.17) of the laser pulse is directed along the intensity gradient and thus expels electrons from the central high intensity zone. This generates a density gradient, with lower densities, meaning higher refractive index, in regions of higher laser intensity.
Both effects lead to a transverse plasma profile with high refractive index on the optical axis and lower η off-axis that is generated by the very front part of the laser pulse and acts as a lens for the main part. The effect is even enhanced during propagation as focusing of the pulse increases the focal power of the ”lens”. This so-called self-focusing counteracts the beam diffraction and can lead to self-guiding of the laser pulse over several Rayleigh lengths. Of course, also external guiding channels can be formed by e.g. additional laser pulses or an electric discharge.
If no external guiding channel is used, self-guiding is desirable as the interaction length with high laser intensities, that are only available in the focal spot, can be extended beyond the Rayleigh length.
Longitudinal/temporal self-modifications due to intensity-dependent changes in the index of refraction will be discussed in the next section. In order to achieve proper guiding of a Gaussian beam with waist w_0, the plasma channel must exhibit a parabolic transverse profile of depth $\delta n_{ch} = (\pi r_e w_0^2)^{-1}$ (e.g. [54]) or normalized to the initial plasma density

$$\delta n_{ch}/n_e \approx 4/(k_p w_0)^2 \tag{III.25}$$

$r_e = 1/(4\pi\epsilon_0)e^2/(mc^2)$ is the classical radius of an electron. In general the index of refraction in a plasma with a spatially slightly varying density $\tilde{n_e}$ is given by

$$\eta(r,z) = \sqrt{1 - \frac{\omega_p^2}{\omega_0^2}\frac{\tilde{n_e}(r,z)}{n_e\gamma(r,z)}} \tag{III.26}$$

If $\tilde{n_e}$ is small, then η can be expanded around $\delta n_e = \tilde{n_e} - n_e$ ([55, 56, 57, 58])[3]:

$$\eta(r,z) = 1 - \frac{1}{2}\left(\frac{\omega_p}{\omega_0}\right)^2\left(1 - \frac{a_0^2}{8} + \frac{\delta n_e}{n_e} + \frac{\Delta n_{ext}}{n_e}\right) \tag{III.27}$$

Here, the term $a_0/8$ causes the change of γ of the background electrons (relativistic self-focusing), δn_e is the density depletion due to the transverse ponderomotive force (ponderomotive self-focusing), and Δn_{ext} is a possibly preformed external plasma channel.
If there is no external guiding channel ($\Delta n_{ext} = 0$), the dominant effect is the relativistic mass correction. Therefore, commonly a critical laser power P_c for self-focusing is deduced only from this term. Ponderomotive effects (see below) and external channels reduce P_c [59].
A guiding profile (III.25) is generated by the relativistic mass correction term if

$$\frac{a_0^2}{8} \geq \frac{4}{(k_p w_0)^2} \tag{III.28}$$

Condition (III.28) for relativistic self-focusing can also be expressed in terms of laser power. In order to achieve self-guiding the power P must be larger than a critical power P_c (for linear polarization):

$$\frac{P}{P_c} \geq \frac{a_0^2 k_p^2 w_0^2}{32} \tag{III.29}$$

with

$$P_c = 2c\left(\frac{e^2}{r_e^2}\right)^2\left(\frac{\omega_0}{\omega_p^2}\right)^2 = 17.4\frac{\omega_0^2}{\omega_p^2}[GW] \tag{III.30}$$

For $P < P_c$ diffraction dominates, for $P > P_c$ the pulse is focused down until higher-order non-linearities that are not included in this simple derivation will balance the focusing force. If $P = P_c$ the pulse is guided with the original spot size.
[60] gives an expression for the evolution of the focal spot $w(z)$ size during self-focussing (with $dw/dz = 0$ at $z = 0$):

$$\frac{w(z)}{w_0} = 1 + \left(1 - \frac{P}{P_c}\right)\frac{z^2}{l_r^2} \tag{III.31}$$

[3]The formality to handle a paraxial wave propagating in a such a refractive index distribution is similar to non-linear optics, where the Schrödinger equation is solved with a third-order non-linearity. The index of refraction n of a material has a weak dependence on the intensity I of the propagating light: $n = n_0 + \Delta n(I) = n_0 + \frac{1}{2}n_2 I + \ldots$ As n_2 is on the order of 10^{-20} m^2/W, it only plays a role for high-intensity pulses. For those pulses a non-linear phase contribution $\Delta\phi = \frac{x}{c}\omega n_2 I$ can be observed that is varying with the intensity envelope. As a consequence, the phase velocity v_{ph} differs at different points in the pulse, both in time and in space, evoking the two phenomena: self-phase-modulation and self-focusing.

The density variation δn_e due to the ponderomotive force can be estimated from the fact that the ponderomotive force must be balanced by the space charge force as the resulting force should be a steady-state radial force. This means that (with (III.17)) $\nabla_\perp \gamma_\perp = \nabla_\perp \Phi$, where $\gamma_\perp = (1 + a^2)^{1/2}$ ((III.5)), and with the Poisson equation ($\nabla_\perp^2 \Phi = k_p^2 \delta n_e / n_e$) follows:

$$\frac{\delta n_e}{n_e} = \frac{\nabla_\perp^2 (1 + a^2)^{1/2}}{k_p^2} \tag{III.32}$$

assuming that $\delta n_e / n_e \leq 1$. For a Gaussian laser pulse $a^2 = a_0^2 \exp(-2r^2/w_0^2)$ and $a < 1$ this yields a density variation

$$\delta n_e = -\delta n_e(0) \left(1 - 2\frac{r^2}{w_0^2}\right) \exp(-2r^2/w_0^2) \tag{III.33}$$

where the on-axis channel depth is

$$\delta n_e(0) = a_0^2 \frac{1}{\pi r_e w_0^2} = a_0^2 \delta n_{ch} \tag{III.34}$$

This shows already that for $a_0 < 1$ self-guiding can not be established merely due to density variations caused by the ponderomotive force. For laser powers that approach the critical power P_c relativistic self-focusing will dominate. Sun et al. [61] and Hafizi et al. [62] show that the ponderomotive force can enhance the effect by slightly decreasing the threshold power for self-focusing to

$$P_{c,r+p} = 16.2 \frac{\omega_0^2}{\omega_p^2} [GW] \tag{III.35}$$

However, the density response term δn_e in the refractive index (III.27) becomes important to the effectiveness of self-guiding for ultra-short pulses with $L = c\Delta t < \lambda_p$. Due to the temporal/longitudinal intensity gradient of the laser pulse, the ponderomotive force at the front of the pulse also accelerates electrons in longitudinal direction, "pushes them forward". This leads to a density bump in the front region of the pulse (see also fig.III.2(b)), and thus a decrease in refractive index which almost entirely cancels the increase due to relativistic mass effects. Hence, the leading edge of a pulse always diffracts. As the time scale for the channel formation is determined by the time scale $\sim \omega_p^{-1}$ on which collective plasma dynamics take place, laser pulses that are shorter than a plasma wavelength $L < \lambda_p$ can not be guided efficiently, even if $P/P_c > 1$. However, a degree of self-guiding also for ultra-short pulses has been observed under certain circumstances.

Decker et al. [63] showed that self-guiding of short pulses is possible for $P/P_c \gg 1$. Electrons in the leading edge of the pulse are accelerated forward with a momentum $p_\parallel = mca_0^2/2$. If $a_0^2 \gg 1$ the electrons keep up with the leading edge of the laser pulse and constantly extract energy. This leads to 100% local energy depletion of the front part before it can diffract and to an electron-free ion channel right behind which can guide the back of the pulse (also see section III.5).

Furthermore Thomas et al. [64] have shown experimentally, that pulses with $L \approx \lambda_p$ are

still self-guided, as long as their transverse focal spot size $w_0 \geq \lambda_p$. If the so-called blow-out radius, the transverse size of the wakefield structure determined by the laser focal spot size, is too small, then the expelled electrons turn back to the laser axis within the length of the laser pulse. The resulting density variations along the laser pulse again cause modulations in the pulse which can lead to instabilities or even cause the pulse to break up into several filaments.

For $a_0 \geq 1$ another aspect has to be considered: The laser will drive a (non-linear) plasma wave and lose energy to the plasma (pump depletion). Therefore the guiding condition $P = P_{cr}$ can only be fulfilled for a limited distance (see depletion length, paragraph III.2.4.4), as with the pump depletion the available power decreases and for $P < P_{cr}$ diffraction dominates. If one starts with $P > P_{cr}$ to obviate the energy/power loss or because it is necessary for the desired interaction, self-focussing will set in and the beam diameter will decrease indefinitely (in first order theory). One possibility to achieve stable self-guiding in the case of strong plasma wave excitation is to go to configurations where the on-axis density becomes zero due to ponderomotive expulsion of electrons from regions of high laser intensity. This means that the on-axis density deviation (III.34) should correspond to the initial density $\delta n_e(0) = n_e$. With $k_p^2 = n_e e^2/(mc^2\epsilon_0)$ this conditions shortens to $w_0 k_p = 2a_0$, which is valid for $a_0 < 1$. In the non-linear $a_0 > 1$ case the cavitation condition reads (e.g. [60]):

$$w_0 k_p = 2\sqrt{a_0} \tag{III.36}$$

With such a combination of laser pulse and plasma parameters a stable guiding channel is formed, where relativistic self-focussing is suppressed even if $P > P_{cr}$, merely due to the lack of electrons in the center [65], [66]. Since further focusing cannot occur, stable guiding can take place inside the resultant cavitated channel. This regime also corresponds to the bubble or blowout regime of laser-wakefield-acceleration (section III.5). Additional automatic self-channeling of the laser is a welcome side-effect of the bubble regime as the electron acceleration length is not limited by diffraction.
For electron acceleration the important length is the dephasing length L_{deph} (see details in section III.2.4.4). It has been shown in simulation [58] (also section III.5.2) and experiment [67] that the initial power that is necessary to self-guide a laser pulse that is driving a plasma wave (and thus continuously losing energy) over L_{deph} is

$$P_0 \geq \frac{1}{8}\frac{\omega_0}{\omega_P}^{6/5} P_c \tag{III.37}$$

As mentioned before, it is also possible to create the plasma density profile necessary for guiding (see (III.25)) externally. Established approaches include an electrical discharge [68] or two additional laser pulses - an ionizing "ignitor" pulse (< 100 fs) and a heater pulse (~ 200 fs) [69].

III.2.4.2 Temporal pulse modifications due to collective plasma dynamics

The same modulations in the refractive index responsible for self-focusing also occur longitudinally along the laser pulse. The locally varying group velocity $v_{l,gr} = \eta c$ can cause a compression of the pulse accompanied by the generation of new frequencies in the laser spectrum (self-phase modulation). For details see e.g. [70]. This pulse shortening effect can be especially useful if the initial laser pulse is too long to resonantly drive a wakefield [71]. Faure et al. [72] measured a pulse compression from 38 fs to 10 – 14 fs. Schreiber et al. [73] characterized the complete temporal pulse shape including pulse steepening at the front or rear side, respectively, depending on the position in the plasma wave.

III.2.4.3 Analytical Approaches to LWFA

In the wake of the invention of high-power short-pulse lasers an analytical description of laser-driven highly non-linear plasma waves was developed. A comprehensive derivation can be found in e.g. [39]. It concludes work done by Tsytovich et al. [74], Berezhiani and Murusidze [75], Bulanov et al. [76] and Sprangle et al. [77], who managed to formulate a theory with the assumption that the group velocity of the laser equals the speed of light in vacuum ($v_{l,gr} = c$). This restriction could be released later on as can be seen in the extended work of Dalla and Lontano [78], Esarey et al. [79], Kingham and Bell [80] and Mori [56].
This fully relativistic one-dimensional plasma wakefield theory outlined below is based on the following assumptions:

- Collisions can be neglected.
- Ionization and recombination do not a play a role.
- Thermal plasma effects can be ignored.
- Arbitrary laser amplitudes a_0 are allowed.
- Arbitrary group velocities of the laser pulse $\beta_{l,gr} = v_{l,gr}c^{-1}$ are supported.
- The driver pulse is linearly polarized (and travels along the z-direction).

As seen before, collisions take place on a much longer time scale than the laser-particle interaction. Consequently, also recombination can be neglected. Due to the high field strength total ionization of the relevant plasma volume occurs in reality already with prepulses or the raising edge of the main pulse (see section III.2.1). Furthermore the quiver energy that the electrons gain from the laser field is much larger than their thermal energy.

Basically, a closed set of differential equations to gain expressions for the different plasma wave properties is derived as follows:

In the following normalized quantities are used: normalized vector potential $a_0 = eA(mc)^{-1}$ *of the laser pulse, normalized scalar potential* $\Phi_0 = e\Phi(mc^2)^{-1}$ *of the plasma*

charge distribution, normalized electric field $\epsilon_0 = eE/(mc\omega_p)$, normalized electron/plasma wave velocities $\boldsymbol{\beta} = \boldsymbol{v}c^{-1}$, normalized electron density $n_0(z) = n_e(z)(Zn_i)^{-1}$ (here Z is the charge number, n_i is the ion density, Zn_i therefore is the initial homogeneous electron density). Indices e,p and l denote electron, plasma and laser quantities, respectively.

- The motion of the electrons is determined by (III.1). In transverse direction only the laser fields have to be considered. In longitudinal direction both the magnetic field of the laser and electric field of the plasma wave influence the electron motion.
- The electron density distribution can be extracted from the continuity equation

$$\frac{\partial n_0}{\partial t} + c\frac{\partial}{\partial z}(n_0\beta_{e,z}) = 0 \tag{III.38}$$

- The wave equation for the vector potential $\boldsymbol{a_0}$ of a general electro-magnetic wave connects fields (cf. (II.9)) to the charge density distribution

$$\frac{\partial^2 a_0}{\partial t^2} - c^2\nabla^2 a_0 = -\omega_p^2\frac{n_0 a_0}{\gamma} \tag{III.39}$$

- The scalar potential that is generated by the charge separation in the plasma wave can be calculated by means of the Poisson equation

$$\frac{\partial^2\Phi_0}{\partial z^2} = \frac{\omega_p^2}{c^2}(n_0 - 1) \tag{III.40}$$

- The normalized longitudinal electric field is then defined as

$$\epsilon_0 = \frac{c}{\omega_p}\frac{\partial\Phi_0}{\partial\zeta} \tag{III.41}$$

The final set of differential equations and their solutions are easier to obtain in a frame that is co-moving with the laser pulse at its group velocity $v_{l,gr}$: $\zeta = z - v_{l,gr}t$. Furthermore the quasi-static approximation [79] is applied assuming that the envelope of the laser pulse is not evolving in the co-moving frame. Thus the laser pulse duration Δt must be much shorter than the typical diffraction time on the order of $z_r c^{-1}$.
A differential equation for the potential is obtained

$$\frac{\partial^2\Phi_0}{\partial\zeta^2} = \frac{\omega_p^2}{2c^2}\left[\frac{1 + a_0^2}{(1 + \Phi_0)^2} - 1\right]$$

and an expression for the density distribution (with $\gamma_{l,gr} \equiv (1 - \beta_{l,gr}^2)^{-1/2}$)

$$n_0 = \gamma_{l,gr}^2\beta_{l,gr}\left(\frac{1}{\Omega} - \beta_{l,gr}\right) \qquad \text{with } \Omega = \sqrt{1 - \frac{1 + a_0^2}{\gamma_{l,gr}^2(1 + \Phi_0)^2}} \tag{III.42}$$

The total electric field in the plasma wave can be calculated from (III.41).
Under the assumption of $\beta_{l,gr} \rightarrow 1$ Berezhiani and Murusidze [75] deducted scaling laws for the respective maxima:

$$\Phi_{0,max} \propto a_0^2 \tag{III.43}$$

$$\epsilon_{0,max} \propto \frac{a_0^2}{\sqrt{a_0^2 + 1}} \tag{III.44}$$

$$p_{0,max} \propto \frac{1 + \frac{1}{1}a_0^2}{1 + a_0^{-2}} \qquad \text{with } p_0 = \frac{p_z}{mc} \tag{III.45}$$

Fig. III.2 shows normalized plasma wave properties in the case of $\beta_{l,gr} \rightarrow 1$. The spatial coordinate ζ in the co-moving frame is normalized to the non-relativistic plasma wavelength λ_p. From figure III.2(a) it becomes clear, that for increasing driver pulse intensity the plasma wave becomes highly non-linear. High density peaks are formed behind a region of extremely low electron density. The total wavelength of these plasma oscillations increases with greater a_0.

Figure III.2(b) displays the electric potential and field for the $a_0 = 3$ case. Between the density peaks the electric field increases almost linearly. An electron that is inserted at the rear part of one oscillation (e.g. at $\zeta/\lambda_p \approx 3.8$ in figure III.2(b)) can be accelerated efficiently. Relativistic electrons are traveling almost at c, but in plasma the group velocity of the driver pulse and thus the phase velocity of the plasma wave is $v_{l,gr} = v_{p,ph} < c$. Due to this difference in velocity, the accelerated electrons move forward in the wave bucket and are decelerated again when the sign of the electric field changes ($\zeta/\lambda_p \approx 4.4$ in figure III.2(b)).

It should also be noted that a plasma wave is driven most efficiently if the laser pulse roughly is shorter than half the non-relativistic plasma wavelength. Within the scope of this one-dimensional model the optimal pulse duration for a resonant wave excitation is $L_{res} = c\Delta t = 0.14\lambda_p$ in the case of a Gaussian driver pulse with $a_0 \simeq 1$ and $L_{res} = c\Delta t = 0.5\lambda_p$ for a rectangular pulse. For higher a_0 this value even decreases slightly, but the overall influence of the pulse duration also decreases.

Based on the potential obtained from the differential equation (III.42) a Hamiltonian can be defined for the system [81]:

$$H(\zeta, p_0) = \sqrt{1 + p_0^2 + a_0^2(\zeta)}\Phi_0(\zeta)\beta_{p,ph}p_0 = h_0 \tag{III.46}$$

h_0 is the total energy, composed of potential and kinetic energy, of a single electron.
Figure III.3 shows the electron momentum phase-space in a co-moving frame as deduced from this Hamiltonian. The contour lines represent possible electron trajectories $(\zeta(t), p_0(t))$ with a certain constant total energy h_0. The lower blue dashed line (path b) shows one possible trajectory for low-momentum background electrons that constitute the plasma wave itself. The pink dashed lines, the separatrices, define the border between

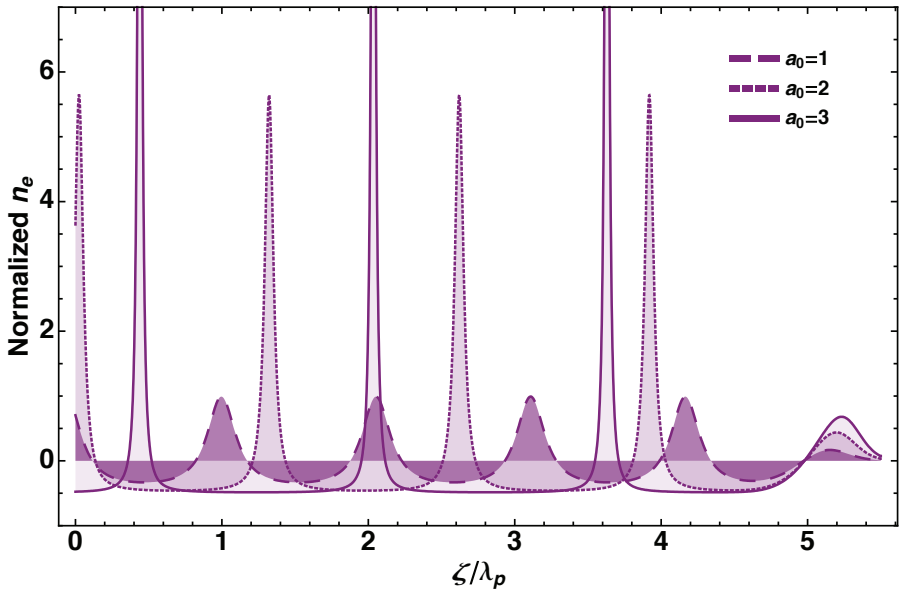

(a) wakefield n_e $a_0 = 1, 2, 3$

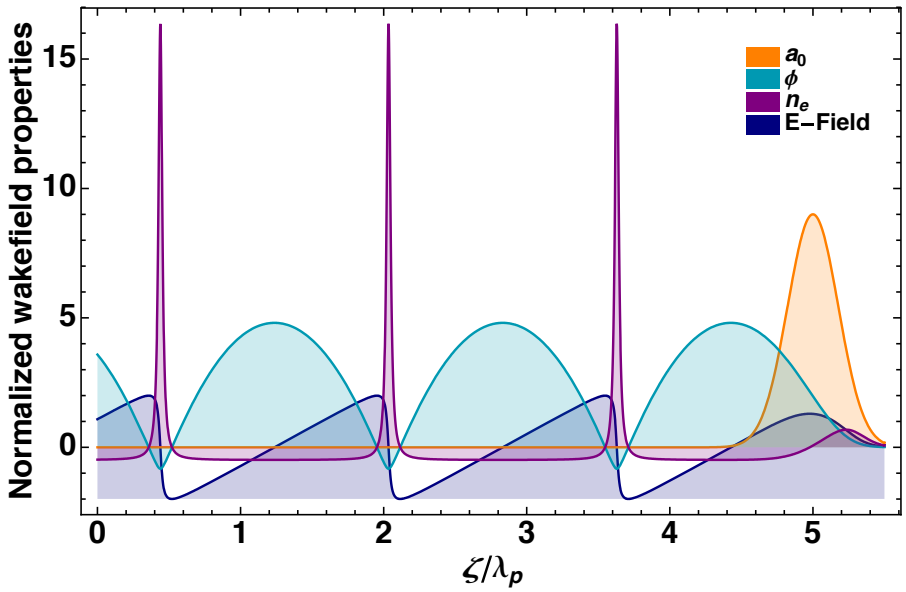

(b) wakefield properties $a_0 = 3$

Figure III.2.: *Normalized wakefield properties*

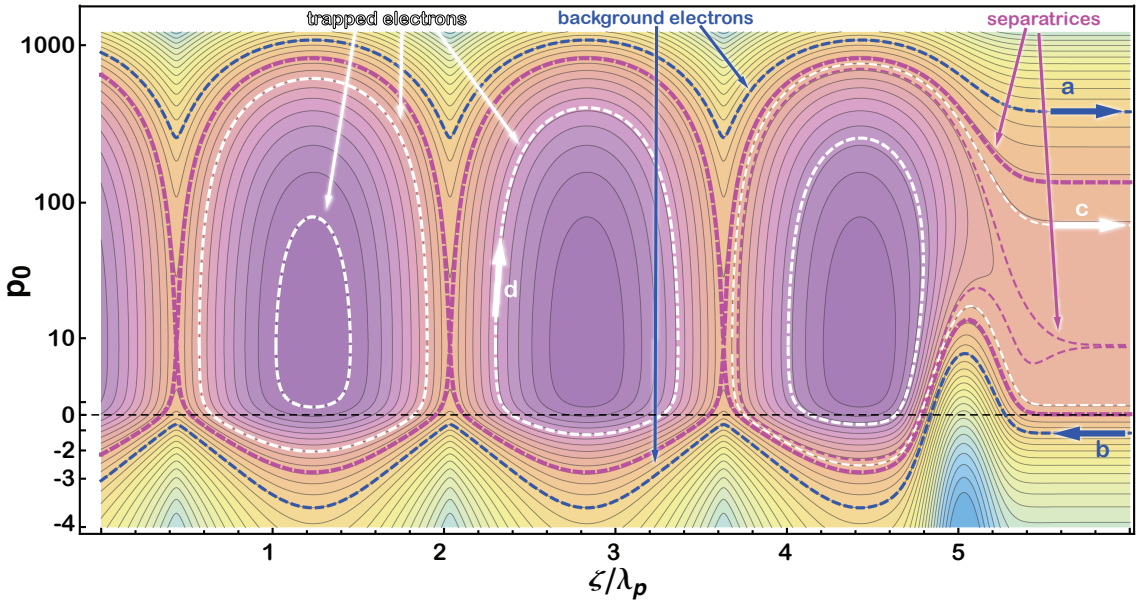

Figure III.3.: *Phase space of a plasma wave in a co-moving frame with parameters as in fig. III.2 (top,* $a_0 = 3$*), but* $\beta_{p,ph} = 0.993$*. The laser pulse sits at* $\chi/\lambda_p = 5$

trapped and untrapped paths, i.e. trajectories on which the electrons can gain kinetic energy or not. For the second and third bucket ($\zeta/\lambda_p \approx 0 - 3.6$), there is a clear separation and the closed white curves (d) exemplify trapped orbits of electrons that can be significantly accelerated (or decelerated) by the electric fields of the plasma wave. In the first bucket behind the driver laser ($\zeta/\lambda_p \approx 3.6 - 5$) the direct presence of the laser modifies the potential of the wake and thus the electron trajectories. Here, the inner thin pink line encloses the truly confined orbits, that are similar to case d. The outer pink separatrix marks the transition to untrapped electron paths. In the phase-space region between the two separatrices of the first wave bucket electrons can also be efficiently accelerated by the waves potential but then leave the wave trough and overtake the laser (path c), as the laser potential inhibits deceleration. The upper blue line (path a) describes the path of an electron that already initially has a much higher kinetic energy than the wave itself, therefore cannot be trapped and overtakes the wave.

III.2.4.4 Limitations

Electron Dephasing

The maximum distance L_{deph} that an electron can travel in the laboratory frame, until it hits the zero-crossing of the electric field and starts losing energy again, can easily be

estimated by

$$(c - v_{l,gr})\frac{L_{deph}}{c} = \frac{\lambda_p}{2} \tag{III.47}$$

$$L_{deph} = \frac{\lambda_p^3}{\lambda_0^2} \propto \frac{1}{n_e^{3/2}} \tag{III.48}$$

Here, it was assumed that the electrons travel approximately with the vacuum speed of light c and the phase velocity of the plasma wave is given by the group velocity $v_{l,gr}$ of the driving laser pulse (central wavelength λ_0). This approximation is only valid if $a_0 \approx 1$ as for $a_0 \gg 1$ the effective plasma wavelength increases. Esarey et al. [82] give a more elaborate analysis based on the presented one-dimensional non-linear theory that considers both regimes:

$$L_{deph} \approx \left(\frac{\omega}{\omega_p}\right)^2 \lambda_p \begin{cases} 1 & \text{if } a_0 \ll 1 \\ (\sqrt{2}/\pi)a_0 & \text{if } a_0 \gg 1 \end{cases} \tag{III.49}$$

Again it can be seen that the dephasing length increases with lower background electron density as for all intensities $L_{deph} \propto n^{-3/2}$. If one accounts for the fact that in linear plasma waves the accelerating and transversely focusing fields are phase-shifted by $\pi/2$ (section III.5.4) the effectively usable acceleration length is halved compared to (III.49).

Laser Energy Depletion

Another important factor that limits the maximum energy gain of an electron is the energy depletion of the driver laser. By driving the plasma wave energy from the laser pulse is coupled into the wake potential. The acceleration ends at the latest when the laser energy is approaching zero. Obviously, this energy depletion length L_{ed} ([83],[84],[85]) ideally should match the dephasing length. Again it is possible to deduce an estimate for L_{ed} from the 1D model: The depletion length can be deduced by equating the energy contained in the driving laser pulse with the energy left behind in the wakefield. It is assumed that the laser pulse has the optimum length L_{res} to resonantly drive a non-linear wakefield.

$$L_{ed}\left\langle E_z^2\right\rangle = L_{res}a_0^2 \tag{III.50}$$

where $\left\langle E_z^2\right\rangle$ is the longitudinal electric field averaged over a period of the wakefield.

If a_0 is small the maximum potential in the wake and thus the efficiency for coupling energy from the laser to the wakefield scales $\propto a_0^2$ as given in (III.43). Therefore L_{ed} decreases with increasing a_0. For large intensities $a_0 \gg 1$, however, the coupling efficiency decreases with increasing a_0 and thus L_{ed} increases. This behavior can be understood since both the maximum electric field as given in (III.44) scales $\propto a_0$ ($a_0 \gg 1$) and the resonant laser pulse length $L_{res} \approx a_0/\pi\lambda_p \propto a_0$ [83]. An absolute value of the depletion length is approximated by [82]:

$$L_{ed} \approx \left(\frac{\omega_0}{\omega_p}\right)^2 \lambda_p \begin{cases} 2a_0^{-2} & \text{if } a_0 \ll 1 \\ (\sqrt{2}/\pi)a_0 & \text{if } a_0 \gg 1 \end{cases} \tag{III.51}$$

Within the scope of this theory, the dephasing length and the energy depletion length are approximately equal for linear wakefields $a_0 \simeq 1$ (ignoring the fact that the transverse fields might not be focusing over the entire acceleration distance) or $a_0 \gg 1$.
However, the linear scaling of the depletion length with a_0 in the non-linear case is only owed to the fact that a resonant flat-top driver is assumed and in this case the resonance length increases with increasing a_0. Yet, for a Gaussian driver pulse it can be shown that the excitation of the plasma wave has a broad resonance and the resonance length thus is approximately independent of a_0 [86]. For a Gaussian driver also the exact value of the maximum electric field changes which also leads to a proportionality factor different from (III.51). All together this gives the depletion length for a Gaussian driver pulse [86]:

$$L_{ed} \approx 8.7 \left(\frac{\omega_0}{\omega_p}\right)^2 \lambda_p \begin{cases} 2a_0^{-2} & \text{if } a_0 \ll 1 \\ 1 & \text{if } a_0 \gg 1 \end{cases} \tag{III.52}$$

For the calculation of the dephasing length the shape of driver is of minor importance[4]. Thus for $a_0 < 19$ the depletion length of a Gaussian driver is nominally longer than the dephasing length. However, Shadwick et al. [86] also show, that this analytical expression (III.52) overestimates the fractional depletion as the energy deposition is not linear during the wake excitation process. But it can be seen from their simulations (also in [82]) that for $a_0 \geq 1$[5] after propagating the dephasing length there is approximately still fifty percent of the initial energy left in the driver pulse.
This percentage of energy deposition is already much more efficient than in the linear case, where almost no energy transfer takes place. Yet, with regard to the experiments described in chapter VI it must must be noted that for common experimental parameters a laser pulse that has lost half its energy can still drive a wakefield. Thus, electrons might again lose energy if the plasma (gas cell) length is not exactly adapted to the dephasing length.

Laser Diffraction

Another limitation for the total acceleration length is the diffraction of the laser. The diffraction length L_{diff} is governed by the Rayleigh length l_r (section II.1.3): $L_{diff} = 2l_r$. Assuming a focal spot size $w_0 \approx \lambda_p$, $a_0 \geq 1$ and $\omega_p/\omega_0 \ll 1$, then $L_{diff} \approx 2\pi(\omega_0/\omega_p)\lambda_p \ll L_{ed} \simeq L_{deph}$. From this it becomes clear that either an external guiding channel is needed to maintain the acceleration over a maximum possible distance or it must be ensured that the laser power exceeds the self-focusing threshold for the respective density.

III.3. Electron Injection

From the previous evaluations it is clear that a non-linear wakefield can constitute an efficient compact accelerator for electron bunches. However, injecting an electron bunch into the small ($\sim \lambda_p \approx 10 - 100\mu$m) acceleration structure at the proper phase with an

[4] the scaling for $a_0 \gg 1$ is mainly caused by the relativistic elongation of the plasma wavelength
[5] In [82] simulations up to $a_0 = 2.5$ are shown.

adapted initial momentum and a pulse length that is smaller than the plasma wavelength is not trivial. If the electron bunch length is not small enough and the phase is not matched correctly the final energy spread will be large. If the initial electron momentum is too small it can not be accelerated efficiently.
The dynamics of an electron in the presence of a laser excited plasma wave is given by the phase-space trajectories corresponding to a constant total energy of the Hamiltonian (III.46) as depicted in figure III.3. Only if the orbit of an electron coincides with an orbit within the separatrix, the electron is trapped and can be accelerated by the wave's electric field. The minimum initial momentum that an electron needs to be trapped is [87]

$$p_{0,t} = \gamma_{p,ph}\beta_{p,ph}(1 - \gamma_{p,ph}\Phi_{0,min}) - \gamma_{p,ph}[(1 - \gamma_{p,ph}\Phi_{0,min})^2 - 1]^{1/2} \tag{III.53}$$

This is valid for electrons in a warm plasma right behind the driver laser. Φ_{min} is the minimum of the wake potential with

$$\Phi_{0,max/min} = \epsilon_{0,max}^2/2 \pm \beta_{p,ph}\epsilon_{0,max}(1 + \epsilon_{0,max}^2/4)^{1/2} \tag{III.54}$$

and $\epsilon_{0,max}$ being the maximum electric field in the wake as in (III.44). The threshold momentum necessary for trapping decreases for a larger plasma wave amplitude (larger $\epsilon_{0,max}$, larger a_0) and for a lower plasma wave phase velocity $\beta_{p,ph}$ (higher plasma density).

As conventional injector technology so far does not fulfill the high requirements for laser-wakefield acceleration especially in timing accuracy and duration of the generated electron bunch several different techniques for electron injection into a plasma wakefield structure are explored. For all approaches it is desirable that electron injection is localized in space and time such that all electrons are exposed to the same acceleration field over the same acceleration distance. Thus the initial low absolute energy spread ΔE is preserved which results in a low relative energy spread $\Delta E/E_f$ after acceleration to the final energy E_f. Furthermore, if not an external electron beam is injected, but electrons from the plasma background should be trapped they need to be "pre-accelerated" to $p_{0,t}$ (III.53).

III.3.1 Wave Breaking and Self-Injection

The injection method that requires the least complex experimental setup, but also lacks extensive control over the injection and acceleration process, is self-injection via wave breaking. The wave structure derived from the 1D non-linear theory exists only if the maximum velocity of the plasma electrons β_m is smaller than the phase velocity of the wake $\beta_{p,ph}$. If $\beta_m > \beta_{p,ph}$ then electrons in the density peaks move faster than the wave itself and "re-phase" into the accelerating phase of the wakefield. Formally, this regime is called wave breaking and can not be described by fluid dynamics anymore. The maximum electric field in a plasma wave that can be achieved before wave breaking is

$$E_{wb} = \frac{mc\omega_p}{e}\sqrt{2(\gamma_{p,ph} - 1)} \tag{III.55}$$

This 1D limit holds for low temperature plane plasma waves. Thermal effects can reduce that maximum field. In the non-relativistic limit ($\gamma_{p,ph} - 1 \approx \beta_{p,ph}^2/2$) the wave breaking

field reduces to

$$E_{wb} = m\omega_p v_{p,ph}/e \tag{III.56}$$

In 2D and 3D plasma waves excited by a finite-width driver pulse have curved, horseshoe-like wave fronts (cf. also upper part of figure III.4). Those waves first break near the wave axis and for lower values than the plane-wave limit. In addition to the 1D, longitudinal wave breaking transverse wave breaking can occur [88] if the radius of curvature of the plasma wave front becomes comparable to the electron displacement. For highly non-linear wakefields as described in depth in the next section the 3D wavebucket can be even approximated by a sphere. Electrons that are "blown away" by the laser pulse, follow a roughly semi-circular path and cross the laser-propagation axis again after approximately one plasma wavelength. The larger the "blow-out" radius, the larger the momentum in forward direction that the electrons have at that point. Furthermore, at the rear of the bucket, where the electron trajectories intersect, the density is highest and Coulomb repulsion additionally increases the momentum in forward direction. Hence, according to Lu et al. [58] a blowout radius R as low as $R \sim 0.64\lambda_p$ leads to a longitudinal momentum that is high enough for the electrons to get trapped (for a laser wavelength of 800 *nm* and in the range of plasma densities of interest).
The big advantage of self-injection is the simplicity of the setup. One drawback is the inevitable non-linearity of the process which can amplify fluctuations in the initial laser and plasma conditions. Furthermore, self-injection is not necessarily temporally limited which would either entirely inhibit the formation of a spectral peak or at least lead to a substantial low energy background. Under suboptimal circumstances injection can continue until the space-charge fields of the trapped electrons massively disturbs the accelerating fields and deforms the wakefield structure (also see section III.4).
If more control over the injection process is desired in order to improve or vary the electron bunch parameters an external injection methods needs to be employed. In the following several known injection schemes are presented.

III.3.2 Ponderomotive Injection

Here, the basic idea is to use two laser pulses, one to drive the wakefield and a second one that intersects the wave bucket to inject electrons at some distance behind the driver pulse. The injection pulse accelerates a fraction of the background electrons to $p_{0,t}$ due to its ponderomotive force. In order to inject only into one wave bucket the injection pulse has to be temporally ($c\tau_0$) and spatially (w_0) small compared to the plasma wavelength λ_p. In order to transfer an initial momentum large enough for trapping to the plasma electrons the injection laser requires an intensity comparable to the driver laser. Umstadter et al. [89] performed simulations with two laser pulses propagating perpendicular to each other both with $a_0 \approx 2$ which resulted in a 21 MeV electron bunch with a 6% energy spread. The disadvantage of this approach is the need for two high-intensity laser beams which can be overcome by a slight modification of the concept as will be described in the next section.

III.3.3 Beat Wave Injection

Beat wave injection is a variation of ponderomotive injection, where two counter-propagating laser pulses are used to generate a standing wave that is confined in space and time. The advantage is that in the case of a standing wave the intensity gradient is determined by the laser wavelength instead of the intensity envelope. Hence even low intensity injection pulses can generate the ponderomotive force necessary to pre-accelerate plasma electrons for efficient trapping. The original scheme [90] employed three laser pulses, one intense pulse for wakefield excitation and two low-intensity pulses to generate the beat wave. The configuration currently under investigation (e.g. [91]) uses one pulse to drive the wakefield and a second low-intensity counter-propagating pulse that generates the beat wave with the driver pulse. The great advantage of colliding pulse injection is that it provides extensive control over several electron beam parameters. By changing the delay between the two pulses the final electron energy can be varied as the injection point is shifted longitudinally and thus the effective acceleration distance changes. The strength of the injection pulse and relative polarization determines the phase-space volume of the injected particles and thus the bunch charge and energy spread. Thus Rechatin et al. [17] were able to optimize beamloading and achieve 10 pC electron bunches at 200 MeV with a 1% relative energy spread at FWHM.
The disadvantage of the counter-propagating pulse injection is the necessity of a second laser pulse which increases the experimental complexity. Also, the experiments mentioned above were conducted with a small angle between the counter-propagating pulses, which facilitates the setup geometry and prevents the beams from propagating backwards through the laser amplifier chain. If a longer acceleration distance is used in order to generate GeV-level electron bunches an external guiding channel might be indispensable. In this case a strict 180°-geometry is necessary which requires elaborate laser protection.

III.3.4 Density Transitions

One concept that does not depend on additional laser beams instead requires more refined gas target engineering. Electron injection into the wakefield takes place in an electron density transition from high to low density. The injected bunch is then further accelerated in a low density channel (below the self-injection threshold, see section III.3.1). If the density transition is a downramp that is long compared to the plasma wavelength, plasma electrons get trapped, because the local phase velocity of the plasma wave in the downramp is slowed down until it equals the fluid velocity of the plasma electrons. The effective local phase velocity of the wake is given by (e.g. [60])

$$v_{p,ph} = c\left(1 + \frac{\zeta}{k_p}\frac{dk_p}{dz}\right)^{-1} \tag{III.57}$$

where $\zeta = z - ct$ is the spatial coordinate relative to the driver pulse, which here is assumed to propagate with $v_{l,gr} = c$. $v_{p,ph}$ decreases for decreasing density $dn_e/dz < 0$.
If the density transition is a step function with a scale length $< \lambda_p$, as for instance at a shockfront, the mechanism is slightly different. At the density transition, the plasma wavelength increases abruptly which causes a rephasing of a sizable fraction of the plasma

electrons into the accelerating phase of the plasma wave. In this case, the plasma wave is fully loaded at once. This injection scheme has been investigated theoretically by e.g. Suk et al. [92]. An experimental implementation was demonstrated by Schmid et al. [93] who position a razor blade in a gas jet to generate a shockfront.

III.4. Beamloading

An estimate of how much charge can be loaded into one wakefield cavity is obtained by superimposing the wakefield produced by the trapped electron bunch over the wakefield generated by the laser pulse. Beamloading is reached if the summed up accelerating electric field is flat within the electron bunch. In principle, this is the ideal acceleration situation, as all electrons in the bunch see the same accelerating field and the initial (small) energy spread is maintained during acceleration. If the bunch charge is lower or higher, electrons in different longitudinal positions will be accelerated differently. In linear wakefields also transverse beamloading poses a problem as the acceleration field (also without beamloading) also changes within one transverse slice of the wake. Beamloading of linear plasma waves was studied by Katsouleas et al. [94]. As will be seen in the next chapter, in the highly non-linear blowout regime transverse beamloading can be neglected as the longitudinal electric field does not vary along transverse slices. Tzoufras et al. [95] analyzed beamloading in non-linear wakefields in depth. More details can also be found in the next chapter after a general description of the blowout regime (section III.5.3).

III.5. The Bubble Regime

Making the transition to a comprehensive three-dimensional characterization of the laser-driven wakefield analytical theories fail to include all occurring effects. One has to rely on complex simulations. The code type of choice to model the interaction of ultra-short laser pulses with plasma is the so-called "Particle-in-Cell" (PIC) code. Details on PIC-codes in general and the OSIRIS *implementation employed in this work can be found in the appendix B. Most of the insights given below are based on such simulations.*

III.5.1 General Description

Pukhov and Meyer-ter-Vehn [11] were the first to identify a highly non-linear broken-wave regime in which the wakefield takes the shape of a solitary three-dimensional cavity right behind the driver laser. This cavity is completely void of electrons and there is no downstream structure. Background electrons are continuously trapped. Due to the spherical shape of the cavity, the injected electrons see an almost linear accelerating electric field and a similarly large transverse focusing field. This regime occurs for high intensities ($a_0 \geq 4$ [58]) if $c\tau_0 < \lambda_0$ and is called "bubble" or "blowout" regime. It can be shown that if the relation between the experimental parameters (laser intensity, spot size, pulse length

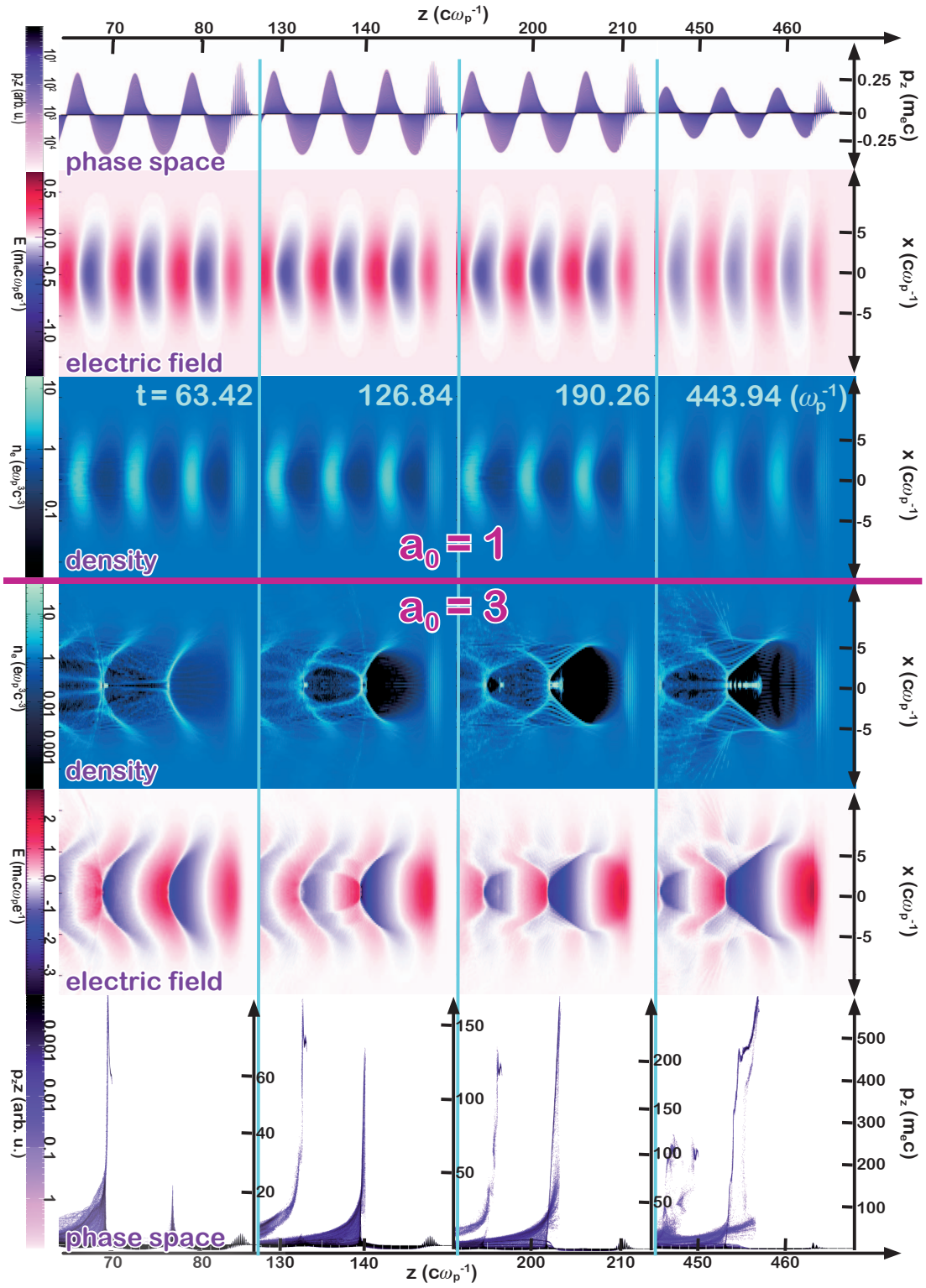

Figure III.4.: *Charge density, longitudinal electric field and longitudinal phase space of a linear ($a_0 = 1$) and a non-linear ($a_0 = 3$) wakefield. For a laser pulse with $\lambda_p = 800$ nm, the simulation parameters are: $n_e = 2 \cdot 10^{18}$ cm^{-3}, $\Delta\tau = 15$ fs, $\Delta x = 8$ μm (central planes of a 3D-simulation)*

and plasma wavelength) is chosen carefully, the bubble structure is stable over the whole acceleration distance and simultaneously the laser is self-guided (see section III.5.2). Figure III.4 shows the central plane of a 3D-PIC simulation of a linear wakefield ($a_0 = 1$) and the blowout regime ($a_0 = 3$). For $a_0 = 3$ there is self-injection and the downstream wave structure is distorted as soon as electron trapping starts. For higher a_0 the complete blowout will occur right from the beginning. In the last frame of the phase space plot the onset of a spectral peak can be observed. This happens when beamloading starts i.e. when the total charge of the injected high-density bunch equals he charge expelled from the cavity. Due to the electric field of the trapped electrons the bubble structure elongates and front and rear side of the cavity move at different speed. The injection point then lags behind and as the cavity elongates the potential maximum and dephasing point shifts "backwards" to the bunch head. The electric field, i.e. the gradient of the potential, decreases and the head of the electron bunch is accelerated less or even decelerated. This produces the horizontal feature in the phase-space plot and a quasi-monoenergetic peak in the energy spectrum.

Figure III.5 shows the longitudinal and transverse electric fields in the accelerating structure of the same simulation. In the non-linear wakefield the longitudinal electric field is almost linear and considerably larger than in the linear case. The transverse electric field is of the same order of magnitude and acts as a focusing force for electrons. Figure III.6 shows the longitudinal field of the wakefield structure (longitudinal and transverse variation of the *longitudinal* field) in a 3D simulation done with parameters as used in the experiments described in the second part of this work (simulation details see appendix C, *ATLAS* 100-run). In both cases the head of the trapped electron bunch is close to dephasing. Within one transverse slice the accelerating field is relative constant over a wide range of the bubble, which if the electrons are focused to that region by the transverse electric fields, allows for low energy spread electron bunches, as all electrons see the same acceleration field independent of their transverse position in the bunch.

In conclusion, the blowout regime provides a stable self-guided acceleration structure for electrons with both longitudinal and transverse electric field strengths on the order of 100 GV/m. Within the dephasing length the electron bunch can reach highly relativistic energies on the GeV-scale. The electron bunch must have a spatial extent that is in all dimensions much smaller than the bubble size determined by the plasma wavelength (a reasonable background electron density of $n_e = 10^{18}$ cm^{-3} corresponds to $\lambda_p = 30\ \mu$m). This means that the source size and the electron bunch length is on the order of a few microns, which is hard to achieve for conventional accelerators. If one assumes that the maximum charge in the bunch in roughly limited by the total expelled charge of the cavity, a spherical bubble with radius $\lambda_p/2$ at a background density of $n_e = 10^{18}$ cm^{-3} would allow for a total bunch charge of 2.3 nC.

The first experimental demonstration of laser-wakefield acceleration in the bubble regime was done by three groups independently in a gas jet ([12, 13, 14]) generating quasi-monoenergetic electron spectra around 100 MeV with an energy spread of a few percent. Since these proof-of-concept experiments a lot of optimization has taken place. Leemans et al. [15] were able to increase the peak energy to 1 GeV by means of an external

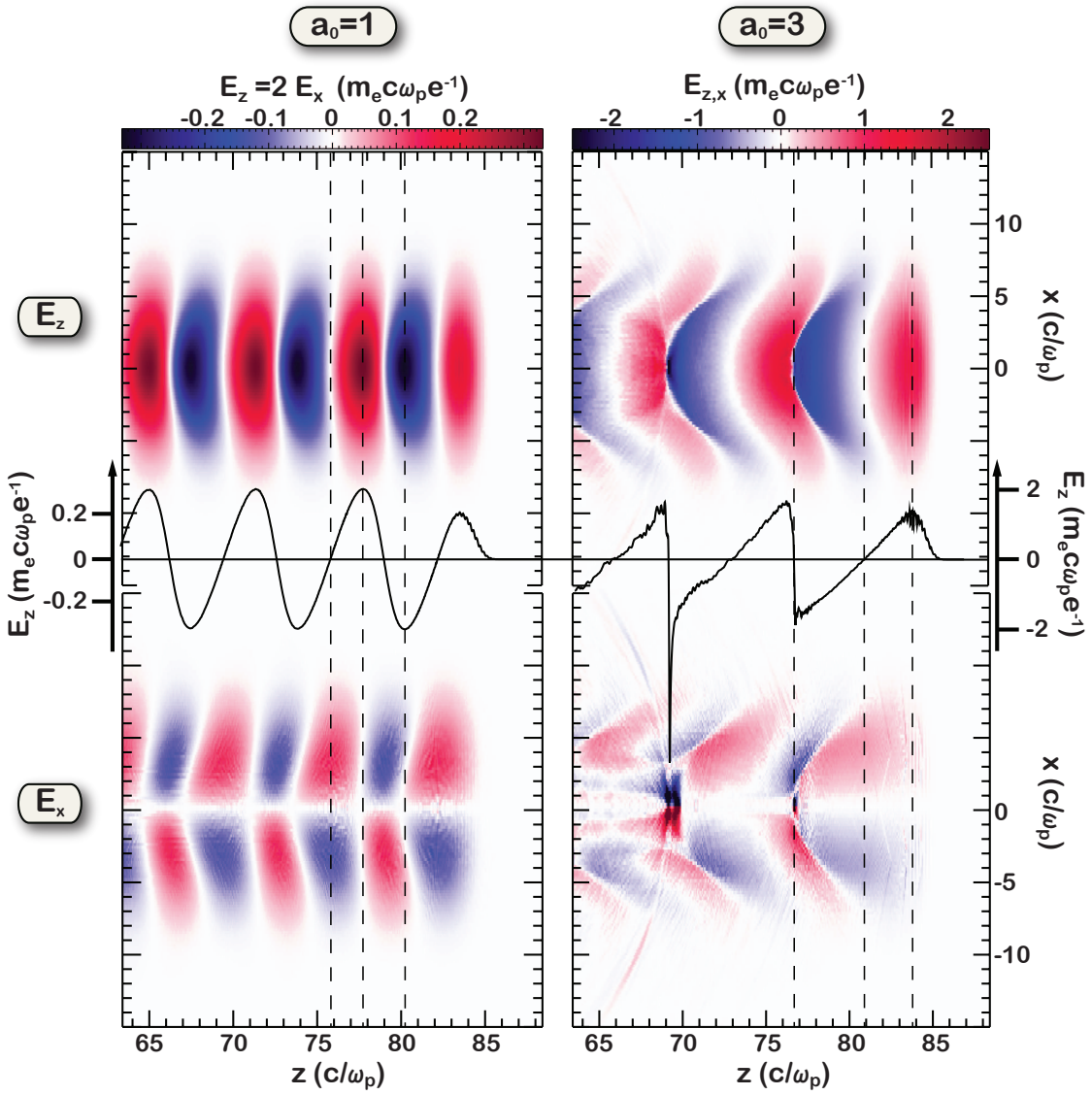

Figure III.5.: *Longitudinal and transverse electric field strength in linear ($a_0 = 1$) and a non-linear ($a_0 = 3$) wakefield, respectively (same simulation as in fig. III.4, first shown timestep $t = 63.42\ \omega_p^{-1}$*

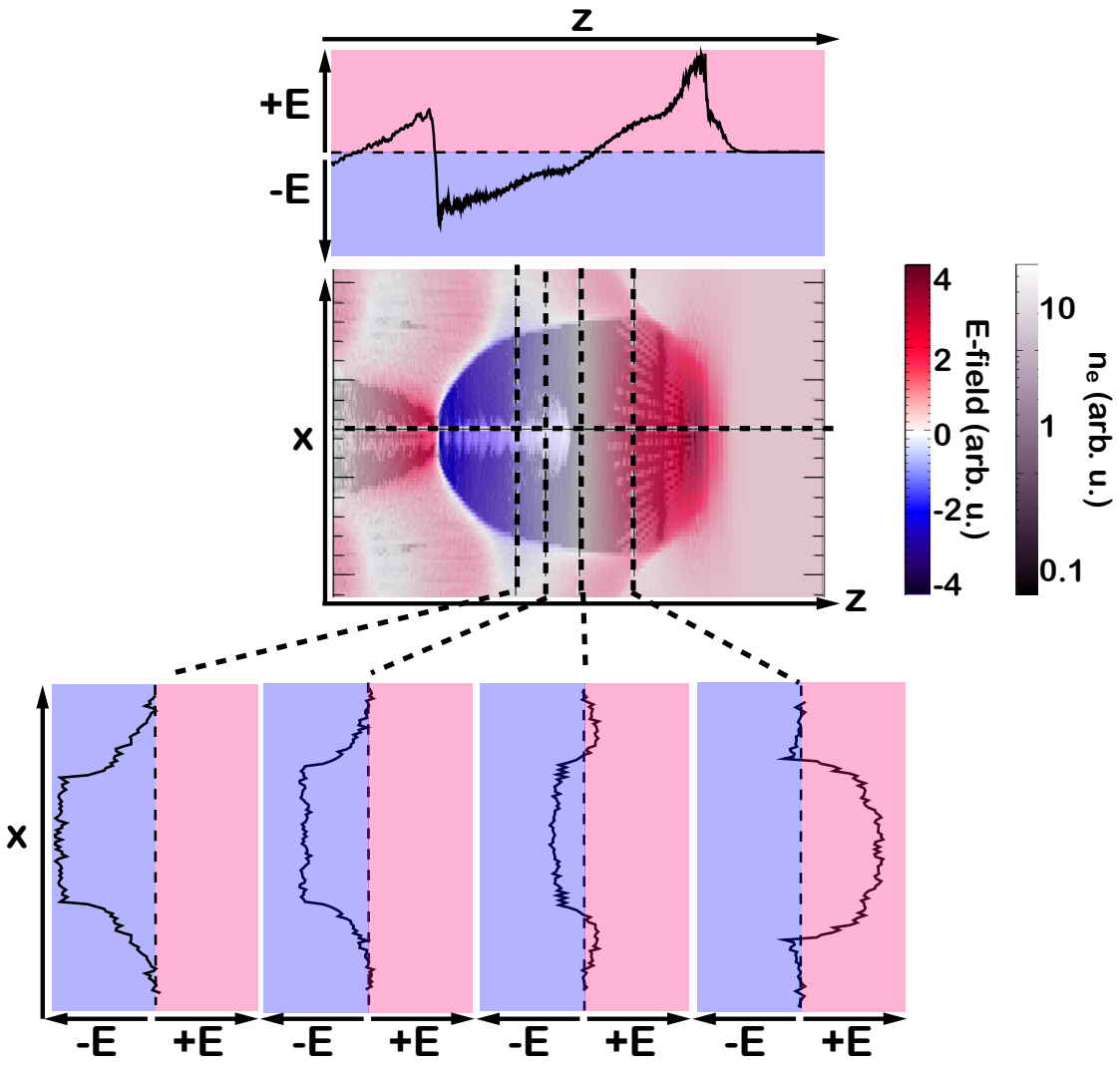

Figure III.6.: *Longitudinal electric field with lineouts in a bubble with injected electrons, ATLAS 100 (longitudinal and transverse variation of the* longitudinal *field)*

guiding channel which extended the acceleration length to the centimeter-scale. Using a steady-state-flow gas cell our group [18] improved the shot-to-shot stability in pointing (1.4 mrad), energy peak position (2.5% RMS) and bunch charge (~ 16% RMS). Furthermore we demonstrated low divergences of 1 mrad RMS and relative energy spreads of ~ 1% RMS for electron bunches accelerated in the self-trapping bubble regime.

III.5.2 Scaling Theory

There is ample theoretical and experimental work that tries to predict the behavior of different electron bunch characteristics depending on scalings of laser pulse and plasma properties. Examples are Esarey et al. [82], Masuda et al. [96] and Maksimchuk et al. [97] who examine electron peak energy dependencies, Reitsma et al. [98], where efficiency of the mechanism and energy spread of the electron bunch are covered or Lotov [99]

who describes a range of different acceleration regimes. In addition, there are two major publications that give a comprehensive scaling theory for the blowout regime based on numerous PIC-simulations. Gordienko and Pukhov [100] and Lu et al. [58] both describe the relations between experimental parameters (plasma wavelength, laser intensity, laser spot size und pulse length) that have to be adhered to in order to

- obtain complete blowout for the first bucket and the spherical bubble shape is maintained over the acceleration distance
- maintain self-guiding over the acceleration distance without significant variations in laser spot size
- achieve self-injection of highly charged electron bunches that eventually stops due to beamloading and thus leads to the formation of a quasi-monoenergetic energy peak
- to match energy depletion of the driver laser to the dephasing length

The derivation of the Gordienko-Pukhov-scaling [100] is based on simulations with $a_0 = 20-80$ and they assume that - in the range where the theory is valid ($a_0 \gg 1$) - the speed of all plasma electrons is close to the speed of light. A single similarity parameter S can be deduced ($S = n_p/(n_c a_0)$) and all electron and plasma parameters scale with some power of S. This can only be valid if the laser parameters (transverse and longitudinal profile and their aspect ratio) stay constant over the whole process. Furthermore, as $v_{p,ph} = c$ is assumed, dephasing is not included in this theory.
Lu et al. [58], on the other hand, conducted simulations starting with $a_0 = 2$ and applied a more phenomenological approach, which allowed for a more flexible theory that also covers experimental parameter sets that are achievable with state-of-the-art technology. Both theories differ in their proposed strategy for the production of highly energetic electron bunches. Lu et al. [58] recommend lower plasma densities and wider spot sizes than the Gordienko-Pukhov-scaling at constant intensities.
In the following the Lu-scaling will be introduced as the corresponding publication cites several current experiments that comply with their scaling theory and because the covered parameter range is comparable to the experiments described in this work.

In the blowout regime the density in the channel should be zero. This is fulfilled if $w_0 k_p = 2\sqrt{a_0}$ (cf. (III.36)). Lu et al. [58] confirmed by simulation that (III.36) holds for $a_0 \geq 4$ and approximately also applies for $a_0 \geq 2$. The laser spot size w_0 also approximately determines the blowout radius R. Furthermore the simulations show that condition (III.36) also supports stable self-guiding of the pulse without significant variations in spot size.
Furthermore the 3D-PIC simulations verify the validity of the 1D energy depletion veloc-

ity $v_{ed} \simeq c\omega_p^2/\omega_0^2$ [63] which leads to an energy depletion length of

$$L_{ed} = \frac{\omega_0^2}{\omega_p^2} c\tau_0 \qquad \text{for} \qquad 2 \leq a_0 \leq 2\sqrt{\frac{n_c}{n_0}} \,^6 \tag{III.58}$$

While exciting the plasma wave, the front of the laser is etched away. In order to stretch the depletion length to the usually longer dephasing length longer laser pulses are necessary. At the same time, of course, they still have to be shorter than the plasma wavelength and intense enough to still be in accordance with the other scaling criteria as (III.36).
As the front of the laser pulse etches backward the resulting phase velocity of the plasma wave is then given by $v_{p,ph} = v_{l,gr} - v_{ed}$ leading to an electron dephasing length of

$$L_{deph} \simeq \frac{c}{c - v_{p,ph}} R \simeq \frac{2}{3}\frac{\omega_0^2}{\omega_p^2} R \qquad \text{for} \qquad 2 \leq a_0 \leq 2\sqrt{\frac{n_c}{n_0}} \,^6 \tag{III.59}$$

where $R \approx w_0$ again is the blowout radius and under the assumption of a spherical blowout region also the distance an electron has to travel from the injection point to the dephasing point in the frame of the bubble. The requirement $L_{ed} \geq L_{deph}$ thus leads to the condition

$$c\tau_0 \geq \frac{2}{3} R \tag{III.60}$$

In reality τ_0 should be larger than $2/3\ Rc^{-1}$ as energy depletion can cause a laser-power-drop below the self-focusing threshold and the laser beam would diffract before reaching dephasing.
The energy gain is given by $\Delta W = qE_{acc}L_{acc}$, where E_{acc} is the average accelerating field of the bubble and L_{acc} is the acceleration distance, ideally determined by L_{deph}. The maximum longitudinal electric field in a spherical bubble as extracted from the 1D theory and confirmed by 3D simulations is (also cf. [101])

$$\frac{eE_{acc}}{mc\omega_p} \simeq \frac{1}{2} R k_p \simeq \sqrt{a_0} \tag{III.61}$$

which leads to (with $E_{average} = 1/2 E_{max}$)

$$\Delta W = \frac{2}{3} mc^2 \left(\frac{\omega_0}{\omega_p}\right)^2 a_0 \tag{III.62}$$

It is important to note, that the final electron energy depends much stronger on the plasma wavelength (as L_{deph} changes) than on the initial laser intensity. But again it must be ensured that for lower plasma densities (leading to higher electron energies) the laser power

[6] For larger a_0 the electrons accelerated directly by the ponderomotive potential of the laser front can move forward faster than the pulse itself, which changes the scaling of the energy transfer. For an underdense plasma with $n_p = 0.003 n_c$ - which is a density as used in the experiments shown later in this work - that upper limit for the given scaling is $a_0 \sim 35$. Beyond that limit the new depletion length is $L'_{ed} = a_0 L_{ed}$ ([58],[100])

still exceeds the critical power for self-focusing. With conditions (III.28) and (III.29), (III.36) can be reformulated to $a_0 = 2(P/P_c)^{1/3}$ and thus

$$\Delta W[GeV] \simeq 3.8 \left(\frac{P}{P_c}\right)^{-2/3} \frac{P[TW]}{100} \tag{III.63}$$

Self-guiding can be sustained over the entire acceleration length if the laser pulse length lost due to pump depletion equals the length of the laser pulse that is lost due to diffraction in each Rayleigh length, i.e. if the laser is etched away as fast as it diffracts. According to Lu et al. [58] this is fulfilled for

$$a_0 \sim \left(\frac{n_c}{n_e}\right)^{1/5} \qquad \text{or} \qquad P/P_c \sim \frac{1}{8}\left(\frac{n_c}{n_e}\right)^{3/5} \tag{III.64}$$

As already described in section III.3.1 efficient self-injection takes place for a blowout-radius of $R \approx 0.64\lambda_p$ or $k_p R \approx 4$.

III.5.3 Beamloading

From the scaling described above the number N of electrons that are accelerated can be deduced as

$$N \approx \frac{1}{30}(k_p R)^3 \frac{1}{k_p r_e} \approx 2.5 \cdot 10^9 \frac{\lambda_0[\mu m]}{0.8} \sqrt{\frac{P[TW]}{100}} \tag{III.65}$$

r_e is the classical electron radius.
This estimate is obtained by balancing the energy stored in the fields in the first bucket, the kinetic energy of the plasma electrons and the energy absorbed by N electrons when propagating through the fields of the bubble. For details see [58].
The efficiency Γ of the process is given $N \cdot \Delta W/\epsilon_L$, where ϵ_L is the total energy in the laser pulse. Assuming (III.60) and (III.36) are fulfilled then $\Gamma \sim 1/a_0$. For the process to be efficient a_0 and thus P/P_c should not be too large. This means that there must be a trade-off in efficiency if one wants to rely on self-focusing over the entire acceleration distance.

III.5.4 Transverse focusing and Betatron Oscillations

Due to the finite width of the driver laser pulse three-dimensional wakefields exhibit also strong transverse electric fields. These fields can be focusing or defocusing for trapped electrons depending on the region in the wakefield. For linear wakefields the part of the wakefield where electrons are both accelerated and focused is about $\lambda_p/4$ long (dephasing/deceleration after $\lambda_p/2$, the transverse fields are phase shifted by $\pi/2$)[102]. This overlap region increases the higher the non-linearity of the wakefield. In the bubble regime (complete blowout) (cf. section III.5) the transverse fields are focusing almost everywhere (also see fig. III.5). This inherent strong focusing (the focusing field is on the order of the accelerating field) leads to electron bunches with extremely small transverse dimensions

(a few microns [103, 104]). Furthermore, it ensures that all trapped electrons see the same acceleration field, as they are concentrated on the axis.
The force on an electron inside a non-evolving sphere with radius R that propagates in z-direction with velocity $v_{p,ph}$ is given by [105]

$$F_x = -\frac{1}{4} m_e \omega_p^2 x(1+\beta_z) \qquad r \leq R \tag{III.66}$$

$$F_y = -\frac{1}{4} m_e \omega_p^2 y(1+\beta_z) \qquad r \leq R \tag{III.67}$$

$$F_z = -\frac{1}{2} m_e \omega_p^2 (\zeta - \beta_x x - \beta_y y) \qquad r \leq R \tag{III.68}$$

and $\boldsymbol{F} = 0$ for $r > R$. The force is expressed in the laboratory frame, but in bubble coordinates $(x, y, \zeta = z - vp, pht)$. If one assumes that in the blowout regime the wakefield structure is perfectly spherical, one can deduce the trajectories of the trapped electrons in the accelerating and focusing fields of the bubble. The arguments explained below are mainly compiled from Thomas [105], but similar considerations can also be found in Lu et al. [101], Lu et al. [58] and Khachatryan et al. [103] .

If one neglects asymmetries that can be introduced by an asymmetric transverse laser pulse shape or due to the linear polarization of the pulse, it is enough to consider the $x-z$-plane. If an electron is trapped with a small initial transverse momentum $p_y \ll p_z$ (therefore $v_z \approx c$) the equation of motion for the transverse oscillation is

$$\frac{d^2 y}{dt^2} = -\frac{1}{\gamma} \omega_p^2 \frac{y}{2} \tag{III.69}$$

If the acceleration time is long, i.e. the change in electron energy within one oscillation period is small, the motion is a harmonic oscillation with the betatron frequency (see also e.g. [106])[7]

$$\omega_\beta = \omega_p \sqrt{\frac{1}{2\gamma}} \tag{III.70}$$

Thomas [105] estimated the initial transverse momentum at injection to be $p_{i,y} = (\pi/4) a_0 m_e c$ (under the assumption that the blowout radius $R = 2\sqrt{a_0} c/\omega_p$). This is result is achieved by solving the equation of motion of an electron moving along the spherical bubble sheath after it was expelled by the laser's ponderomotive force. Using $p_{i,y}$ as a starting condition and solving the equation of motion for the betatron oscillation (III.69) under the assumptions that the oscillations are initiated on-axis at the rear of the bubble (initial phase is zero) and the oscillation amplitude is sufficiently small (such that $2\gamma c^2 \simeq \gamma_p^2 \omega_p^2 (R^2 - \zeta^2)$, from equations (III.62),(III.36),(III.24)), yields (for details see [105])

$$y \simeq \left(\frac{2\gamma_p a_0}{\gamma}\right)^{1/4} \sqrt{\frac{a_0}{\gamma_p}} \frac{c}{\omega_p} \sin\left\{2\gamma_p \left[\arcsin\left(\frac{\zeta}{R}\right) + \frac{\pi}{2}\right]\right\} \tag{III.71}$$

[7] More generally, the betatron frequency is given by $\omega_\beta = \omega_p \sqrt{f\gamma}$ where $f = \partial F_r / \partial r$ is the radial component of the force exerted on the particle in the wakefield. For general wakefield shapes f must be extracted from simulations. For more detailed calculations see Khachatryan et al. [103]

From the argument of the sine-function it can be deduced that the total number of oscillations within R is given by $N_\beta = \gamma_p$. Furthermore, the amplitude of the oscillation scales as $r_\beta \propto (\gamma_i \gamma)^{1/4}$ with γ_i being the initial γ at injection. The minimum amplitude is $r_\beta = 1/2R\gamma_p^{3/4}$ corresponding to the maximum energy gain for the electron in the accelerating field.
In [103] not only the trajectories of single electrons in the wakefield are analyzed but also the behavior of the bunch envelope. The bunch radius oscillates with $2\omega_\beta$ and evolves as $\propto \gamma^{-1/4}$ (see also e.g. [106]). The maximum radius of the envelope oscillation is determined by the strength of the focusing field, whereas the minimum value is dominated by the bunch emittance [8]. In [103] the matched bunch radius is estimated to $\sigma_{m,\beta} = (\lambda_p \epsilon_n/(2\pi))^{1/2}/(f\gamma)^{1/4}$, where σ is the RMS bunch size, ϵ_n the normalized transverse emittance and γ is the mean relativistic factor of the bunch. However, if long electron bunches are accelerated so called longitudinal betatron phase mixing occurs as different parts of the bunch will perform betatron oscillations in a different phase depending on their initial conditions.
A scenario where the betatron oscillation as given by (III.70), (III.71) is destroyed, is depicted by Nemeth et al. [107]. If the tail of the laser pulse and the electron bunch overlap then the electric field of the laser acts as a driving force on the harmonic oscillation which changes the betatron frequency but also increases the oscillation amplitude. This can lead to elliptical bunch shapes with a larger emittance in laser polarization direction.
Khachatryan et al. [103] also consider the case that the electron bunch is injected off-axis into the wakefield bucket. This can happen if a multi-stage acceleration setup is imperfectly aligned or with self-injection if the driver laser and thus the wakefield is asymmetric (cf. chapter VII). "Obviously, when an electron bunch is injected off-axis into the focusing region of a laser wakefield, the bunch, as whole will tend to oscillate around the axis and perform betatron oscillations like a single electron." [103]. However, due to slightly different initial conditions (transverse momentum, position) in the case of a real bunch with finite emittance after some propagation even those bunches will decohere. The analysis of the oscillation of two particles that are injected at two slightly different longitudinal positions ζ_0 and $\zeta_0 + \delta\zeta$ shows that the decoherence time, after which the two particles have moved into opposite oscillation phases, decreases with larger γ_p and with smaller γ_i. Stronger focusing fields also lead to stronger decoherence. This strong decoherence in addition to the above-mentioned betatron phase mixing deteriorates beam parameters as transverse emittance and energy spread. The simulations presented in [103] suggest that the length of an electron bunch that is injected off-axis into a wakefield has to be two orders of magnitude shorter than the plasma wavelength, in order to avoid bunch degradation.

A by-product of these inevitable electron betatron oscillations is the betatron radiation. As an electron undergoes betatron oscillations in a focusing wakefield, it will emit syn-

[8] The emittance ϵ of an electron beam is defined as the area it occupies in phase space ($\boldsymbol{x}$-$\boldsymbol{p}$). It is common to distinguish between longitudinal and transverse emittance, often assuming cylindrical symmetry along the bunch propagation axis. The normalized emittance is $\epsilon_n = \beta\gamma\epsilon$, where β and γ are the mean relativistic parameters of the bunch

chrotron radiation. The wavelength of this radiation depends on the betatron wavelength [106]

$$\lambda_{rad,\beta,n} = \frac{\lambda_\beta}{2n\gamma^2}\left(1 + \frac{K_\beta^2}{2}\right) \tag{III.72}$$

which in the case of $K_\beta^2 \ll 1$ simplifies to

$$\lambda_{rad,\beta} = \frac{\lambda_\beta}{2\gamma^2} \tag{III.73}$$

with the betatron strength parameter being

$$K_\beta = \gamma k_\beta r_\beta \tag{III.74}$$

As before r_β is the amplitude of the electron betatron oscillation and k_β its wavenumber. This process and the corresponding formalism resembles the generation of undulator radiation. For small $K_\beta^2 \ll 1$ light will be emitted mainly with the fundamental wavelength (III.74), whereas for large $K_\beta^2 \gg 1$ all wavelengths $\lambda_{rad,\beta,n}$ will be generated up to critical harmonic number $n_{ch} \simeq 3K_\beta^3/4$ beyond which the intensity quickly drops. In LWFA usually $K_\beta^2 \gg 1$.The line width of a single harmonic is determined by the total number of betatron oscillations $\Delta\omega_n/\omega_n = (nN_\beta)^{-1}$ (remember from above $N_\beta = \gamma_p$ [105]). Furthermore, the betatron radiation is very directed with an opening angle of $\sim 1/\gamma$ or $\sim K_\beta/\gamma$ for large K_β.
However, unlike in the undulator case, the betatron strength parameter K_β depends on γ, which means that for large K_β the γ-dependency of the betatron wavelength cancels out. The betatron wavelength then is mainly determined by the electron oscillation wavenumber and amplitude. Controlled off-axis injection of the electron bunch could thus lead to extremely high harmonic generation up to MeV photon energies (due to large r_β) with the possibility to tune the peak wavelength by varying the transverse injection point.

Chapter IV

Previous Results

The high-intensity laser used for the experiments in this thesis is the *Advanced Titanium-Sapphire LASer* (*ATLAS*) at the Max-Planck-Institut für Quantenoptik in Garching, Germany, as characterized in II.2. This system is well suited for electron acceleration in the blowout regime with self-injection of electrons by wavebreaking. A variety of experiments have been conducted so far covering aspects of electron optimization, application and understanding the underlying processes. The questions that are discussed in the present work arose from previous experiences.

In *'Gev-scale electron acceleration in a gas-filled capillary discharge waveguide.' Karsch, Osterhoff, Popp et al.* [16] (also [39, 108]) it was demonstrated that in a capillary discharge waveguide quasi-monoenergetic electron bunches can be accelerated to up to 500 MeV with the *ATLAS*-laser. Some electron traces even reached up to 1 GeV. The setup was similar to the one employed by Leemans et al. [15], where they could produce 1 GeV electron beams using more energetic laser pulses (1.6 J vs. 0.75 J of *ATLAS*). Further measurements with this gas target setup can also be found in [109].

The gas target for our guiding experiments is a 15 mm-long capillary with an inner diameter of 200 μm (see fig. V.5(a)). Before each laser shot a 20 kV discharge is fired along the axis of the Hydrogen-filled channel. The gas is ionized and the density distribution of the free electrons is determined by the introduced heat gradient: the density increases near the cold capillary walls and decreases on-axis. The resulting radial gradient in the index of refraction turns the plasma channel into an efficient waveguide for high-intensity laser pulses. The external guiding channel extends the acceleration distance beyond the Rayleigh length without the need for self-guiding, thus relieving the demands on the laser power. Although the high electron energies of around 500 MeV document the success of this scheme, the capillary discharge waveguide in this configuration exhibits strong shot-to-shot fluctuations both in peak energy and in pointing. Even in a relatively stable regime at lower energies the peak position varies between 200 and 300 MeV and the beam pointing error is as large as 8 mrad RMS.

While the shot-to-shot fluctuations could be connected to the unstable discharge and varying channel formation, the gas cell itself, without discharge, was established as a very reliable, reproducible gas target.

As shown in *'Generation of Stable, Low-Divergence Electron Beams by Laser-Wakefield*

Acceleration in a Steady-State-Flow Gas Cell' Osterhoff, Popp et al.[18] (also [39, 110]) the steady-state-flow gas cell allows for the generation of electron bunches that exhibit a quasi-monoenergetic peak at 200 MeV with shot-to-shot fluctuations of only 2.5% RMS in energy, 16% RMS in charge and 1.4 mrad RMS in pointing. The divergence is as low as 2.1% FWHM. Injection was observed in almost 100% of the shots. The gas cell is filled with Hydrogen 50 ms before the laser arrives. Within this time a homogeneous density distribution builds up. The unprecedented stability of the electron bunch properties is owed to this lack of spatial fluctuations in the gas profile and the reproducibility of this steady-state. It should be noted that the capillary in this case does not act as any kind of waveguide, as the electron characteristics are independent of the channel diameter.
These high-quality, stable electron bunches from a simple setup enabled several sophisticated measurements. For the first time soft X-ray undulator radiation at down to 7 nm was generated by LWF-accelerated electrons. The experiment described in *'Laser-driven soft-X-ray undulator source'* Fuchs, Weingartner, Popp et al.[21] has a high degree of complexity including miniature quadrupole lenses for electron beam transport, a very narrow-gap undulator and sophisticated X-ray detection. Owing to the ~ 100% injection probability in the wakefield accelerator and the energy and pointing stability of the electron bunches, an undulator radiation signal could be detected in as much as 70% of the driver-laser shots.
Also the two experiments described in this work rely on a high reproducibility of the electron characteristics. The measurements with a tilted laser pulse in chapter VII resulted as a surprising effect when studying the pointing behavior. Variations in the pointing directions are detected that are caused by the subtle asymmetries in the driver laser. This experiment is done with the same 15 mm-long sapphire gas cell target as in all previous experiments. The second experiment, the length scan, presented in chapter VI was the result of a quest to modify the capillary target. The goal was find the optimum acceleration distance by varying the gas cell length. A metal gas cell was fabricated with a variable length of 2 mm-14 mm (see fig. V.5(b)). Owing to the stability of the laser and gas target parameters the dependence of the electron cut-off energy on the acceleration length could be clearly established. Simultaneously, further information about laser dynamics, such as depletion and self-guiding length, could be extracted by varying the electron density.

Chapter V

Basic Experimental Setup

V.1. Overview

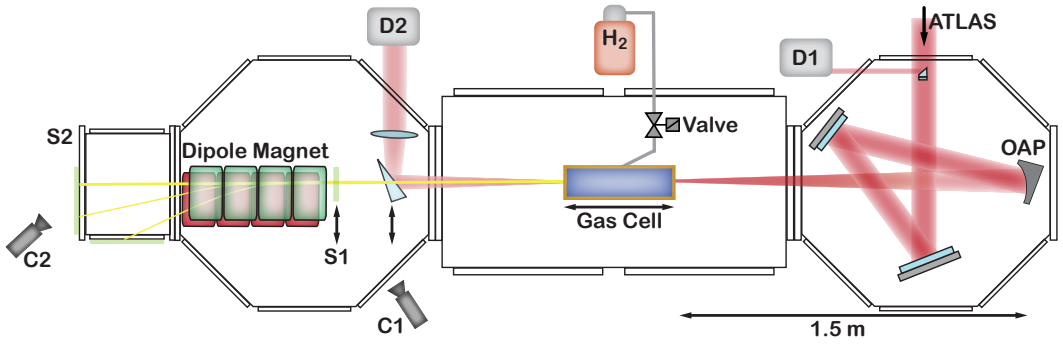

Figure V.1.: *Setup for electron acceleration. OAP: off-axis parabola, D1/D2: laser diagnostics, S1/S2: scintillating screens for electron detection, C1/C2: CCD cameras observing the screens S1 and S2*

The setup for electron acceleration in general evolved from the one described in [39], that was used for all previous measurements.
The high-intensity laser used in the experiments is *ATLAS* as characterized in II.2 with $\approx$ 850 mJ on target (Strehl ratio $>$ 0.7) and a pulse duration of $\Delta t \approx 37$ fs (*ATLAS 25*) or later on *ATLAS 80* with $\Delta t = 26$ fs and an energy of ≈ 1.7 J. Focusing these laser pulses by a 1.5 m focal length off-axis parabola results in a diffraction limited waist of $\Delta x = 22\ \mu$m ($F\# = 22$). The laser polarization in the PFT-experiment (*ATLAS 25*) is parallel to the vacuum chamber floor, meaning perpendicular to the energy dispersion direction of the electron spectrometer (see below). In the length-scan measurement, the polarization is rotated by 90° and thus oriented along the spectrometer dispersion direction due to a rearrangement of the beam transport system.
By means of a 1/2-inch diameter pick-off mirror that is situated close to the center of the collimated beam a part of the incoming pulse can be sent to a *GRENOUILLE*[1]-type

[1] GRating-Eliminated No-nonsense Observation of Ultrafast Incident Laser Light E-fields

FROG[2] device [111, 112] for pulse duration measurements and to an optical spectrometer (D1 in Fig. V.1). The spectrum of the laser light can again be diagnosed after the interaction with the plasma (D2 in Fig. V.1). To this end, a wedged glass plate slides in and out of the beam path to either send the transmitted laser beam to the diagnostics setup or to allow an unhindered propagation of the accelerated electron bunches to the respective electron diagnostics.
The electron bunches are detected on two scintillating screens S1 and S2 (Fig. V.1). Each scintillating screen in the setup is observed by a 12-bit *CCD* camera. In the experiment *CAWO OG 16* [113] intensifying screens are used. These consist of phosphor materials based on rare earths that emit light around 550 nm if hit by energetic X-rays or electrons. The version *OG 16* has the lowest spatial resolution of the series, about 3 line pairs per mm with an MTF[3] of 10%, but provides the highest photon count per incident electron or X-ray (also compared to most other screens, see fig. V.4(a)).
As demonstrated in [114] the number of emitted photons is proportional to the number of electrons if the electron energy is above $\approx$ 5 MeV. Hence, these scintillating screens are suitable to detect both the transverse profile of the electron beam and the charge contained in the bunch (see V.3, [115],[114]). If placed behind a dipole magnet also the energy of the electrons can be determined (S2), since the deviation of the electrons by the magnetic field depends on their energy (see below V.2).
The first scintillating screen (S1) is used to determine the transverse electron beam profile, its divergence and the pointing fluctuations. It has to be removed for accurate electron spectrum measurements as the electrons scatter in the screen and the increased divergence reduces the spectrometer resolution. The drawback clearly is that there is no shot-to-shot knowledge about the electron beam pointing and thus the position at the spectrometer entrance, which adds an error to the energy determination that increases with increasing energy. However, as Osterhoff [39] shows that with pointing fluctuations of $\leq$ 1.4 mrad the error is reasonably small. Furthermore, low fluctuations in the peak/cut-off energy are also an indication for stable electron pointing and raises the trust in the energy evaluation.
The vacuum chamber that contains the entire setup except for the diagnostics D1 and D2 is kept at a pressure of $< 5 \cdot 10^{-4}$ mbar. During the short period when the gas cell is filled with Hydrogen the pressure can briefly increase by one order of magnitude. The screen S1 is attached to the outside of the vacuum chamber. In this region the thickness of the Aluminum door is reduced to 2 mm.

V.2. Electron Spectrometer

For the experimental campaign with an asymmetric driver pulse (chapter VII) the electron spectrometer setup detailed in [39] was used. For the subsequent measurement with the variable-length gas cell (chapter VI) a new dipole magnet was installed and the geometry

[2] Frequency-Resolved Optical Gating
[3] Modulation Transfer Function. In the case of lines with a sinusoidal intensity profile, the MTF corresponds to the contrast with which these lines are reproduced at a given spatial frequency.

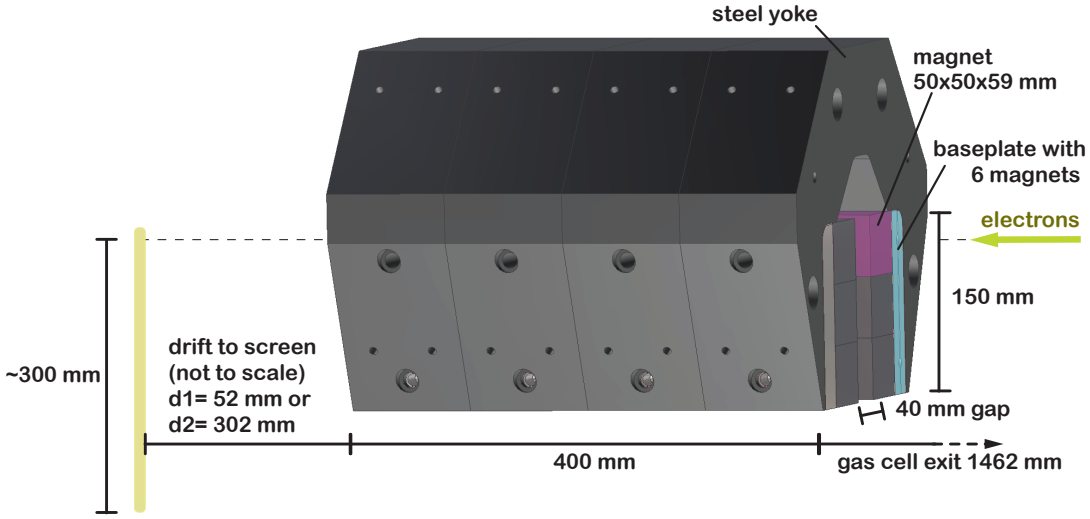

(a) CAD drawing of the spectrometer magnet setup.

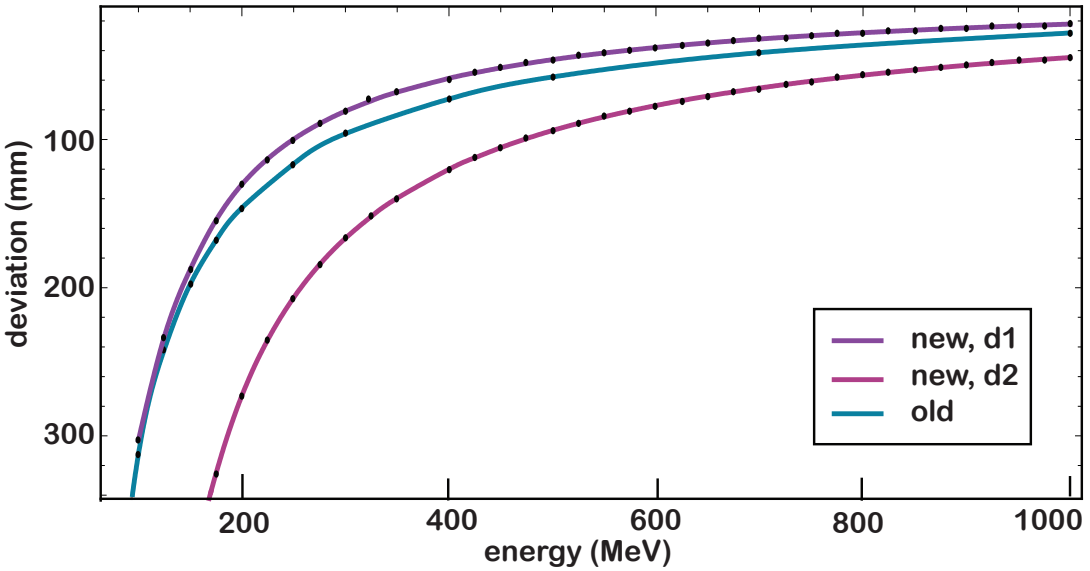

(b) Deviation of the electrons, tracking data courtesy of R. Weingartner (new spectrometer) and B. Hidding (old spectrometer)

Figure V.2.: *Spectrometer setup as used for the gas-cell-length scan*

was slightly changed. In the following this new setup will be described.
The magnetic dipole setup (fig. V.2(a)) has a total length of 400 mm, separable into four 100 mm blocks. Each block consists of a steel yoke, with six single permanent *VACODYM 764 TP* magnets [116] on a baseplate attached to each side. One of these magnets has a size of $50 \times 50 \times 59$ mm. Between the two poles there is a 40 mm gap with a field strength of $\simeq 1$ T.
The entrance of the dipole magnet is 1462 mm behind the exit of the gas cell. The scintillating screen behind the magnet (S2) can be placed either $d1 = 52$ mm or $d2 = 302$ mm

behind the spectrometer exit. It is observed by a CCD-camera. In order to map the camera pixels to an absolute spatial position a second order polynomial is fitted to a ruler placed in the image. The correspondence between spatial deviation and electron energy is obtained by tracking electrons with different energies through the spectrometer setup with the code *GPT* (General Particle Tracker) [117][4]. As an input for this simulation the magnetic field was measured with a Hall sensor in the central plane of the dipole. Also fringe fields outside the magnets were included.
Figure V.2(b) illustrates the simulated spatial deviation of electrons with a certain energy from the original propagation axis for the old and the new spectrometer setup with the two different drift lengths. It can be seen that the resolution for the shorter drift $d1$ is similar to the old setup. Due to geometrical constraints only deviations up to $\approx$ 300 mm can be observed. For $d1$ this means that only energies above $\approx$ 100 MeV are measured. $d2$ gives a higher energy resolution, but only energies higher than $\approx$ 180 MeV are observed. For the gas-cell-length scan the short drift distance $d1$ was chosen.
Currently, this spectrometer can be extended to a length of 800 mm which then deviates 1 GeV-electrons by $\approx$ 100 mm (measured directly at the dipole exit) and thus provides high spectral resolution even for GeV-scale electron beams.

V.3. Charge Calibration

In order to extract information about the charge in the electron bunch by evaluating the intensity of the signal from the scintillating screen, the respective screen together with the imaging system has to be calibrated with a well characterized electron source.
One existent calibration method that can be applied to this problem is the absolute calibration of *Image Plates* (IP) [118, 119] done by Tanaka et al. [120] and Zeil et al. [121]. These photostimulable phosphor plates store energy in metastable color centers (luminescence centers) that is proportional to the energy deposition per area. Since the energy loss for electrons above $\sim$ 10 MeV is nearly constant, the deposited energy corresponds to the charge per area. The stored energy can be read out by a visible-wavelength laser. IPs are very sensitive and can detect even low charge electron bunches, but the read-out takes long and needs a separate scanner, which renders them impractical for permanent use in an electron acceleration experiment. But as their properties are well characterized with conventional accelerators, they can be employed to calibrate a setup consisting of a scintillating screen, imaging optics and a camera. The fact that the calibration is only valid for one geometry and imaging system is a major disadvantage of this method.

In order to obtain a more general calibration for scintillating screens, we introduced an additional constant light source (CLS) as a luminosity reference [115]. Simultaneously, with the scintillator signal the CLS was imaged. By comparing the integrated CLS signal in the final experimental setup at the laser-wakefield accelerator (Fig. V.3) to the signal in

[4] tracking data courtesy of R. Weingartner (new spectrometer) and B. Hidding (old spectrometer)

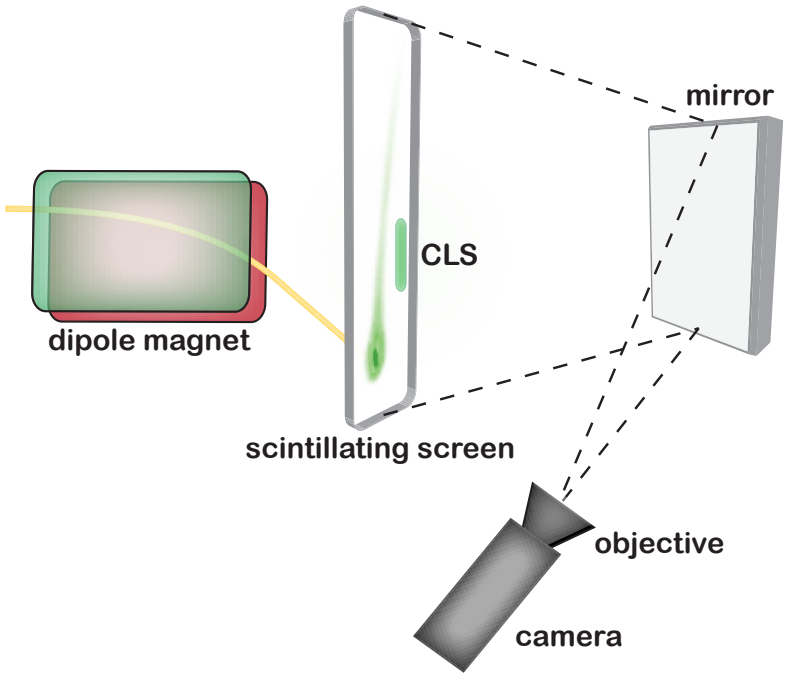

Figure V.3.: *Setup for spectrum and charge acquisition. CLS: constant light source*

the calibration setup, the scaling factor for the scintillator-signal-to-charge conversion can be extracted. Hence, the calibration can be easily transferred to arbitrary imaging systems and geometries, without any additional tools as e.g. an *Image Plate* scanner.
Our CLS are small glass tubes, filled with gaseous tritium and coated with a luminous substance. The electrons emitted by the radioactive tritium permanently activate the luminous substance (radio luminescence), such that a constant photon emission is guaranteed, although of course the half-life of tritium has to be taken into account. These tritium tubes are commercially available from *mb-microtec* [122] and can be easily attached to the scintillating screen. Our CLS-tube is 12 mm long and 2 mm in diameter. If the screen and the CLS together are calibrated at a conventional electron accelerator, the CLS gives a scaling factor for the light intensity versus stimulating charge depending on the imaging setup in the experiment.
The absolute charge calibration is detailed in *'Absolute charge calibration of scintillating screens for relativistic electron detection'* Buck, Zeil, Popp et al.[115]. It was performed at the *ELBE* linear accelerator at *Forschungszentrum Dresden-Rossendorf*, delivering electron bunch trains of variable length. The charge of a single electron bunch can be tuned up to 50 pC. For higher charges up to 100 nC several pulses are summed up with a 154 ns delay between the single pulses, which have a duration of 2 ps. The decay time of the scintillating screens is around one millisecond. Therefore, in order to simulate a higher bunch charge, several bunches can be accumulated. The electron energy was 40 MeV for all measurements. Reference charge measurements were conducted with Faraday Cups and Integrating Current Transformers (ICT), as they are routinely used at conventional accelerators.

Among others the scintillating screen *CAWO OG 16* that was used in the described

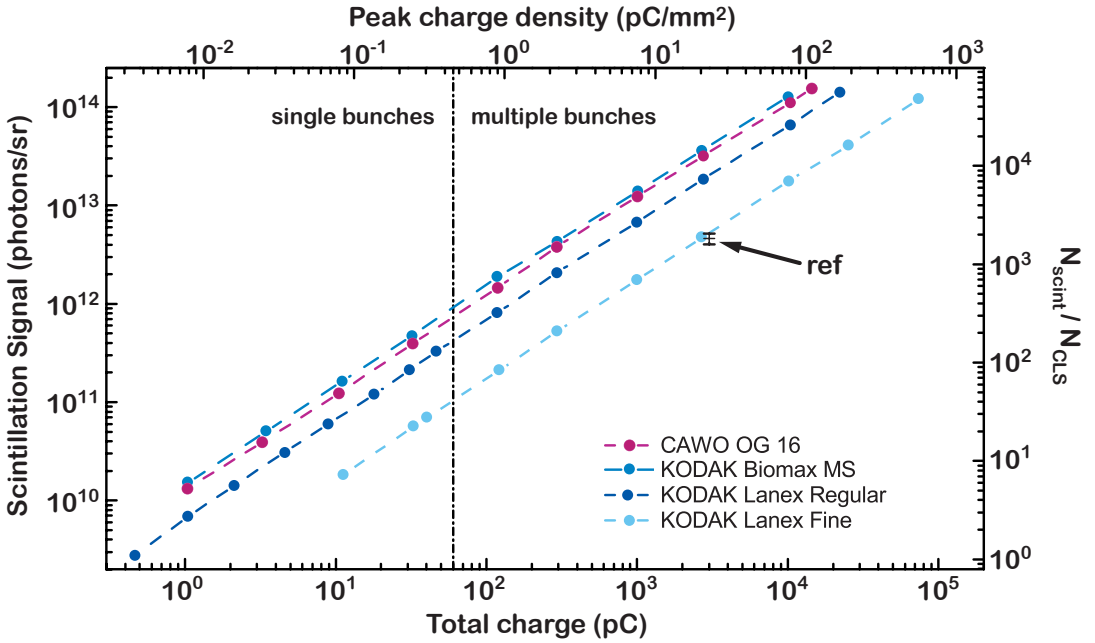

(a) Scintillator signal vs. deposited charge for various commercial screen types, N_{CLS} is the signal of the constant light source recorded with a exposure time of 20 ms. In this work *CAWO OG16* was used. The data point marked "ref" is taken from an independent calibration done by Glinec et al. [114] for the *KODAK* Lanex Fine Screen.

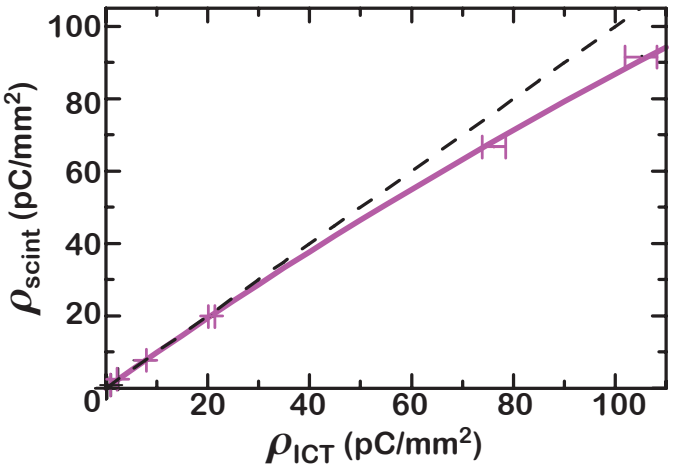

(b) Measured charge density in the peak from the scintillation screen *CAWO OG 16* vs the charge density calculated from an ICT measurement. Dashed line: linear fit (below saturation), solid line: Birks saturation law [123]

Figure V.4.: *Charge calibration of different scintillating screens, original plots and data evaluation by A. Buck, for further details see [115]*

experiments was calibrated. Figure V.4(a) shows the photon signal of the scintillating screen depending on the electron bunch charge. Both the integrated charge is shown as well as the charge per area. In order to extract the charge density a Gaussian was fitted to

the spatial intensity distribution. In addition to the absolute scintillator signal, it is given scaled with the CLS-signal. The important conversion for our experiment is: 1 pC will result in a signal on the *CAWO OG 16* screen that is 4.86 times higher than the spatially integrated signal of the CLS. This holds for images taken with 20 ms exposure time. For longterm calibration a drop in luminosity of the CLS has to be taken into account. This is due to a combination of tritium decay and degradation of the luminous substance. In good approximation an exponential decay with 5 years decay time can be assumed (calibration date: October 2009).
The sensitivity of the *CAWO OG 16* is relatively high, which is advantageous for low-charge electron bunches. The trade-off is the simultaneously reduced spatial resolution. The data point marked "ref" in figure V.4(a) is taken from an independent calibration done by Glinec et al. [114] for one charge density and fits well to our measurement (both done for the *KODAK* Lanex Fine Screen).
Figure V.4(b) shows the measured charge density extracted from the peak of the scintillating screen signal (*CAWO OG 16*) depending on the deposited charge as measured by an ICT. For low charge densities the signal is identical and can be fitted linearly. With higher charge densities the screen signal deviates from the linear fit, the scintillating screen saturates. The fitting curve there is based on Birk's saturation law for scintillators [123]. The charge density that saturates the screen was determined to be 32.9 ± 6.6 pC/mm^2. At this point ρ_{scint} has dropped to 95% of the linear fit. The dispersed charge density (behind the spectrometer magnet) produced in the experiments of this work is still well below that limit.

V.4. Gas Target

The gas target used in all previous experiments described in chapter IV and in the PFT-experiment of chapter VII is a 15 mm-long sapphire capillary with a diameter of $\simeq$ 250 μm. In practice, a groove with a semi-circular transverse profile is laser-machined into a sapphire plate. Two of these plates are pressed together to form the desired channel (figure V.5(a)). Two larger channels are added to one of the plates to serve as gas inlets. The gas cell is filled with hydrogen gas during $\simeq$ 50 ms before the laser arrival. Owing to the large fraction of gas inlet and outlet cross section a steady-state, homogeneous gas density distribution is achieved at the point in time when the interaction starts. It can be assumed that the pressure in the cell corresponds to the applied backing pressure. A detailed characterization of this gas cell, operated with and without external discharge for guiding, can be found in [39].
Other than the widely used super-sonic gas jets this gas cell is operated in a steady-state regime which reduces shot-to-shot fluctuations and supports stable and reproducible electron acceleration [18]. Furthermore, the gas cell length can easily be extended to the centimeter range.
In order to optimize this setup for high-energy electrons, the gas cell length should be adapted to the maximum acceleration length for a given set of laser parameters and electron density. To this end, a variable-length gas cell was designed (figures V.5(b),V.6).

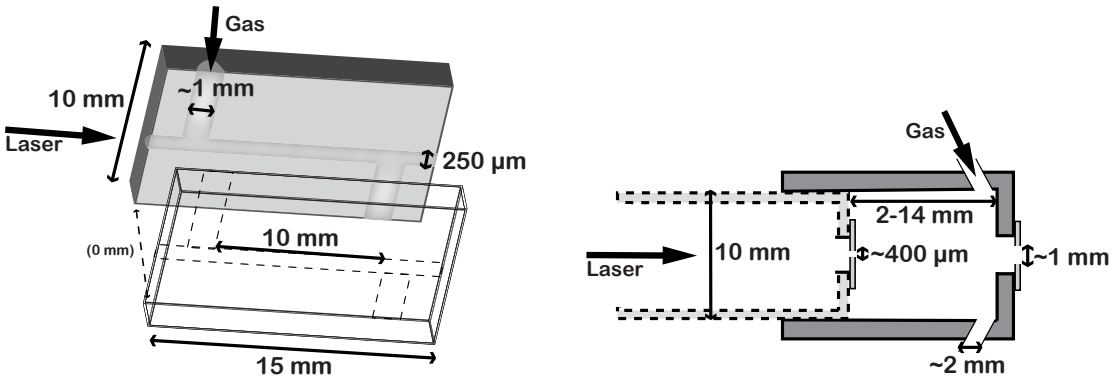

(a) Capillary, consisting of two sapphire plates with a semi-circular groove laser-machined in each plate. The two plates are pressed together to form the full circular channel.

(b) Variable-length gas cell, consisting of two metal cylinders. Sapphire plates with small (several 100 μm) holes are attached to the front sides in order to reduce the gas exit cross section. In total there are six gas inlets distributed rotation-symmetrically (two are shown in the cross section)

Figure V.5.: *Sketch of the two gas targets used for the experiments described in this work. Not drawn to scale.*

This gas cell is used for the experiment described in chapter VI.
In principle, two hollow cylinders with different diameters, that are both open on one end, are fit into each other (figure V.5(b)). The diameter of the hohlraum is 10 mm and the length can be varied between 2 and 14 mm. The length is changed by moving the outer part with an attached translation stage. In the experiment, the front part is fixed and only the rear part moves, such that entrance does not move relative to the longitudinal focus position. The laser can propagate through holes in the base plates of both cylinders with a diameter of $\sim$ 1 mm. In order to reduce the gas flow through the entrance hole a 300 μm thin sapphire plate is attached. The first few full-power laser shots on the sapphire plate drill a small hole with a final diameter of approximately 300 μm. Eight radially arranged holes, each roughly 2 mm in diameter, in the rear cylinder serve as gas inlets.
Figures V.6(b), V.6(c) and V.6(d) show a simulation of the electron density distribution within the variable-length gas cell (at a length of 5 mm), done with the computational fluid dynamics (CFD) modelling software *OpenFoam*. For more details on the simulation parameters and more plots depicting the gas kinetics in the cell see Göppner [125]. The displayed density distribution has developed 1.5 ms after applying a backing pressure of 100 mbar to the gas inlets. In reality this state is probably reached later, as the volume of the gas supply pipe has to be filled, too. In the experiment, if the gas valve opens less than 40 ms before the laser arrival a reduction in electron stability can be observed.
The simulations suggest that also for this gas cell design, just as for the sapphire capillary, the density distribution within the gas cell is very homogeneous. However, in the logarithmically scaled picture V.6(b) and the line-out V.6(d) it can be seen, that, there is a relatively long density gradient outside the gas cell down to vacuum level. The length of this gradient scales with the diameter of the entrance/exit holes. In front of the entrance a long density gradient can pose a problem, if the laser undergoes self-phase modulation

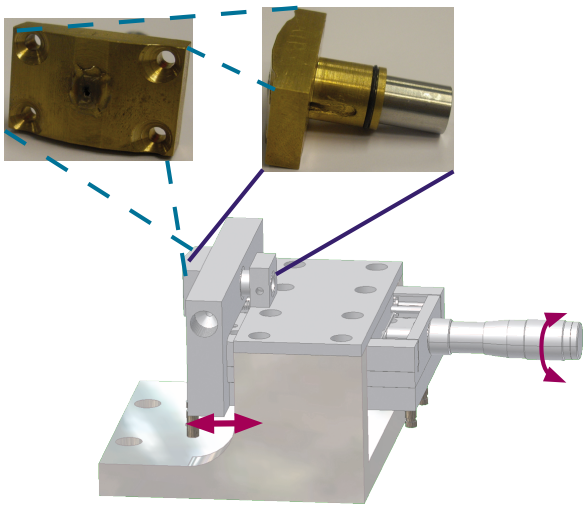

(a) Variable-length gas cell with translation stage for length adjustments

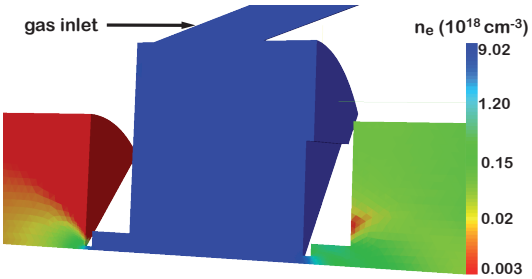

(b) Density distribution, logarithmic scale

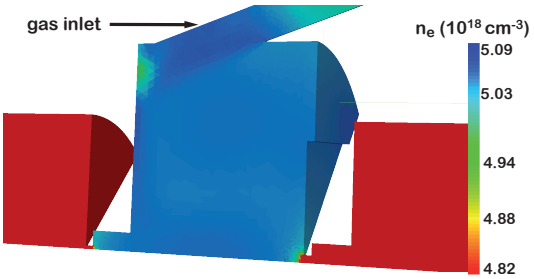

(c) Density distribution, linear scale

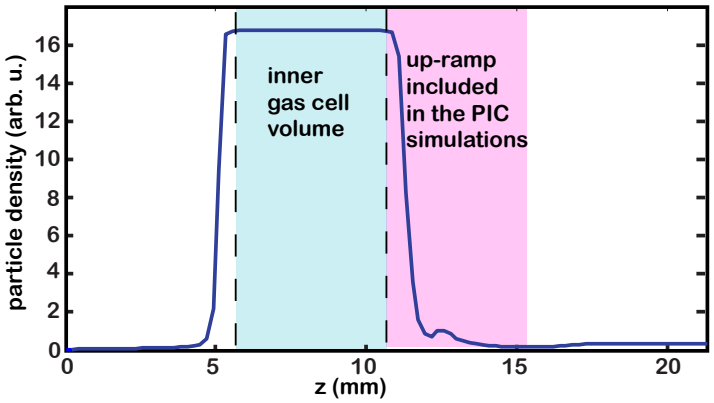

(d) Density profile, longitudinal line-out

Figure V.6.: *Density distribution in the gas cell after* 1.5 ms *simulated with OpenFoam [124]. The gas cell in the simulation has four gas inlets. Using symmetry planes, it is sufficient to simulate a* 45*-degree wedge. Left and right of the gas cell is the vacuum volume included in the simulation box can be seen. In these pictures the laser pulse would propagate from right to left. Simulation data courtesy of B. Göppner (also see [125])*

and self-focusing or even filamentation before it even reaches the geometrical focus. The part of the line-out that is highlighted in pink is therefore included in some of the PIC simulations shown in chapter VI.

V.5. Beam Path Alignment

The laser beam path is defined by two references in the chamber. The first one is a cross-hair that is attached to the rear side of the focusing parabola and observed by a camera. With an iris in the collimated beam before the compressor, the spot size on the parabola can be reduced to approximately 10 mm in diameter and the position of the beam can be reproduced within an accuracy of below 1 mm. The second reference point is the transverse position of the focal spot, which defines the direction of the laser beam. This position can be reproduced within approximately half a focal spot diameter ($< 20\,\mu$m). In practice a flippable uncoated glass wedge approximately 50 mm before the focus reflects the attenuated beam onto a CCD-camera with a 10× magnification microscope objective. The error in the reproducibility of the alignment of the laser beam pointing can thus be estimated to be below ~ 0.6 mrad.

V.6. Diagnostics for Electron Bunch Duration

An additional diagnostics was recently put into operation that allows for a single-shot determination of the electron bunch duration. A short description of the setup is given here, as first measurement results will be used to strengthen some of the claims on electron acceleration mechanisms presented in this work. The setup was co-developed by the author of this thesis before it was taken over by Matthias Heigoldt. A comprehensive characterization will be given in his forthcoming dissertation (at Ludwig-Maximilans-Universität München), some results can also be found in [4].

The physical process exploited for the electron bunch length measurement is the generation of transition radiation. It occurs when a charged particle propagates through a medium with changing optical properties [126]. One easy example is an electron crossing through a metal foil. At both vacuum-metal boundaries transition radiation is generated that is emitted in a $1/\gamma$ cone. The spectrum of this incoherent radiation extends up to the plasma-frequency of the metal foil. If the transition radiation is created by many electrons in a bunch, those spectral parts of the radiation with a wavelength longer than the bunch length add up coherently. Thus for those long wavelengths the spectral intensity increases significantly. The spectral shape of this coherent transition radiation is determined by the Fourier transform of electron bunch profile. The electric field of the transition radiation generated by an electron bunch with N_e electrons and a longitudinal density distribution

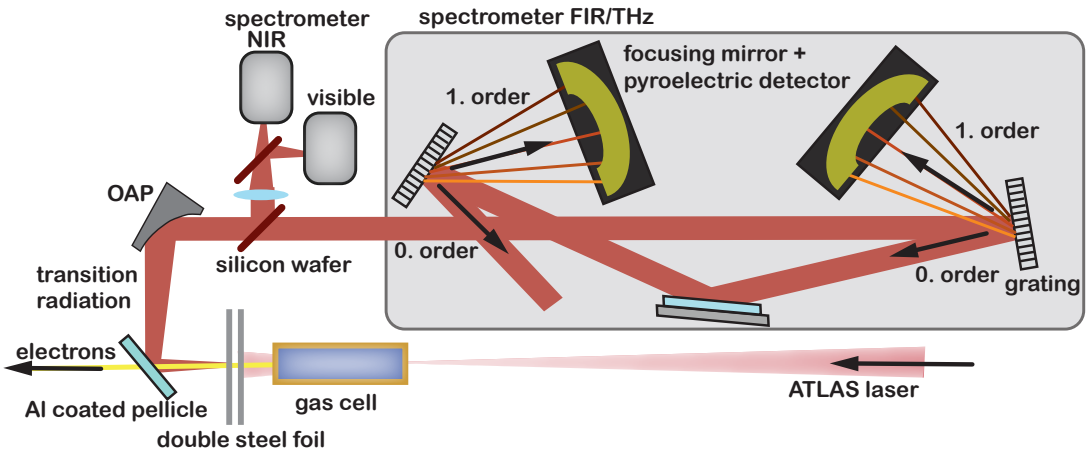

Figure V.7.: *Setup for the detection of transition radiation. OAP: off-axis parabola. Not shown: first filter grating (see text) in the FIR/THz spectrometer. By a thin pellicle the transition radiation is separated from the electron bunches that continue to the electron spectrometer V.2.*

ρ_e is given by

$$E(x,\omega) \propto N_e[\epsilon(\theta,u)D(\omega,u,\theta,\rho)F(\omega,u,\theta)]$$
$$F = \mathscr{F}(\rho_e) \tag{V.1}$$

$\epsilon(\theta,u)$ is the field of a single electron depending on the observation angle θ and the normalized velocity u. $D(\omega,u,\theta,\rho)$ describes the dependence on the transverse size of the bunch. The form factor $F(\omega,u,\theta)$ is the Fourier transform of the electron density distribution. Details on the different factors can be found e.g. in [127].

From simulation and other measurements (e.g. [5, 6]) a duration of < 10 fs is expected for LWF-accelerated electron bunches. This corresponds to transition radiation in the few micrometer wavelength range. Furthermore it is interesting to see also optical wavelengths in order to resolve possible fine structure in the bunch or modulations from double bunches. Thus a combined spectrometer setup was chosen that covers a broad wavelength range from $\sim$ 400nm to 7 μm in a single shot, and in principle can be extended up to several 10 μm.
The electron bunches are sent through a double layer of 20 μm thick steel band, which is advanced by a motorized tape-drive after every laser-shot. The main purpose of the first layer is to block the laser pulse. The transition radiation generated at the backside of the second foil is split up by two 20 μm thick silicon wafers and transported into three different spectrometers. An off-the-shelf optical spectrometer with a CCD-camera and a second commercial grating spectrometer with an InGaAs-array detect wavelengths of 400 – 1100 nm and 1000 – 1800 nm, respectively.
The third spectrometer is based on a design by the *DESY-FLASH* laboratory [128] and can currently cover a wavelength range of 1.7 – 7 μm or 5.5 – 25 mum, depending on the grating configuration. At the entrance to this spectrometer setup the transition radiation is collimated by an off-axis parabola ($F/\# = 7.5$) and sent onto a series of three blazed

gratings. The diffraction into the first order is very efficient (up to ~ 80%) for a certain wavelength range [5]. The radiation with wavelengths outside of this window is mainly specularly reflected (zeroth order). Blazed gratings therefore also act as spectral filters. Also in our setup the first grating is used as a mere filter that diffracts the unwanted part of the spectrum and reflects the wavelength range that is to be analyzed. This light hits a second grating, where the dispersed light in the first diffraction order is refocused on the detector array by a parabolic ring mirror (f = 150 mm, gold coating). If the line spacing of the gratings is adapted correctly its zeroth order light can now be forwarded to a second complementary detection stage (third grating). In the experiment gratings with a ruling of 830 lp/mm (filter), 497 lp/mm (1. detection stage), and 150 lp/mm (2. detection stage) cover the wavelength range from 1.7 to 7 μm. This can be changed to an alternative grating set with 240, 150, 41.85 lp/mm to detect the spectrum between 5.5 and 25 mum.
The detector consists of two arrays of 30 pyroelectric elements each (type *LIM-107-X006* by *InfraTec* [130], $LiTaO_3$ element). The signal of each channel is enhanced by charge-sensitive pre-amplifiers and subsequently fed to shaping amplifiers with 8 μs shaping time. This analog signal is then digitalized by peak-sensing ADCs.
The calibration of the far-IR/THz spectrometer is currently only based on grating efficiency calculations. An absolute calibration of the entire setup including detector response, gratings, beamsplitters and other optics will be done at the *FELBE* infrared free-electron laser (*Forschungszentrum Dresden-Rossendorf*) in the near future. Furthermore, in order to retrieve the electron bunch characteristics, assumptions have to be made about the spectral phase. This can be done for example by adapting the Kramers-Kronig relation [131] or with an interative phase retrieval algorithm as described in [4].
The advantage of this combined spectrometer setup is that the entire interesting wavelength range can be sampled simultaneously, and thus shot-to-shot fluctuations are revealed. From this broad spectrum the length of one electron bunch can be determined, but also possible density distribution substructure within one bunch. Furthermore signal modulations can be detected that come from the interference of several electron bunches that are separated by roughly a plasma wavelength.

V.7. Self-Focusing of the Laser Pulse

The initial laser power of the *ATLAS*-laser is higher than the critical power for self-focusing at most eligible electron densities. For a proper evaluation of the experiment it is therefore necessary to estimate the final laser parameters that prevail while the laser is driving the wakefield. Equation (III.31) describes the evolution of the focal spot size during self-focussing in a certain background electron density. Neglecting energy depletion, the corresponding new vector potential can then be calculated at every point. In theory, self-focusing stops, when complete cavitation is achieved (cf. III.2.4.1). The pulse is

[5] The signal in the first order of a grating blazed for a wavelength λ_B is reduced by ~ 50% at $2/3\lambda_B$ and $3/2\lambda_B$ (e.g. [129])

n_e (10^{18} cm^{-3}/mbar)	a_0	$w(z)$ (μm)	z (μm)
2.47/50	3.6	15.0	446
4.83/100	4.4	12.0	348
6.42/130	4.9	10.9	311

Table V.1.: *Self-focusing parameters: a_0 and waist size w_0 after reaching equilibrium at a distance z. Initial parameters $\tau_0 = 23$ fs, $w_0 = 18.7$ μm and $a_0 = 2.4$*

then self-guided in the cavitated channel with a constant spot size. Therefore, as a rough estimate, the beam radius of a laser pulse with initial parameters as given above was decreased according to (III.31) until the new w_0 and a_0 fulfilled the blowout condition $k_p w_0 = 2\sqrt{a_0}$ (III.36) at a given pressure. A constant electron density was assumed for the whole evolution. From this calculation stable self-guiding should be achieved with the final parameters as shown in table V.1 (after self-focussing over the distance z). For a medium electron density of e.g. $4.8 \cdot 10^{18}$ cm^{-3} the spot size decreases to $w = 12$ μm within $z = 350$ μm, the a_0 simultaneously increases to 4.4. With these parameters, an equilibrium self-guiding state should be maintained.
The self-guiding condition (III.36) is the same correlation that Lu et al. [58] assume for their stable blowout regime. If one also wants to rely on self-injection in addition $w_0 k_p \geq 4$ has to be ensured [58], i.e. with (III.36) $a_0 \geq 4$ after self-focusing. In the experiment this is approximately met for all pressures shown in table V.1 after self-focusing.

Chapter VI

Evolution of Electron Beam Parameters

As it can be seen in figures III.2,III.4 and III.6 the electric field in a non-linear plasma wave has both an electron-accelerating and decelerating phase. As a relativistic electron bunch propagates faster (with $\approx c$) than the plasma wave ($v_{gr,l}$) it will leave the accelerating phase after some time. The maximum distance over which an electron bunch can be accelerated in a single stage is called dephasing length. For a given electron density the final energy of the trapped bunch is determined by the phase in which the acceleration is stopped. The total acceleration/deceleration distance is firstly determined by the plasma length, but also energy depletion or diffraction of the driver laser can be the limiting factor (sections III.2.4.4,III.5.2). In order to exploit the maximum acceleration distance, the laser energy should not deplete before the dephasing point. But to guarantee high efficiency of the process, the depletion length should also not be much longer than the dephasing length. Of course, the plasma length should be adapted accordingly. If no external guiding channel is provided, also self-guiding must be ensured over the same distance. Which process eventually limits the acceleration depends on the relation between laser-parameters and plasma density. Lower densities lead to a longer dephasing and depletion length and but also increase the critical power for self-focussing.
By means of a variable-length gas cell the optimum acceleration distance for given laser parameters can be determined and adopted in future gas target designs. By evaluating the electron parameters at different gas cell lengths their evolution can be reconstructed. From the evolution of the peak energy the respective limiting processes at different pressures can be inferred. Furthermore, the strength and shape of the electric field in the bubble can be estimated and as well as the dephasing length. Another hope was to observe the onset of acceleration, i.e. the self-focusing distance and the beginning of injection. This, however, was not possible, as these processes take place within a distance shorter than the minimum gas cell length.

VI.1. Experimental Scan of the Acceleration Length

VI.1.1 Procedure

In the experiment, the variable-length gas cell as described in section V.4 was employed. Scans of different gas cell lengths under in otherwise constant conditions were conducted at two different electron densities (130 mbar $\equiv 6.42 \cdot 10^{18}$ cm^{-3} and 50 mbar $\equiv 2.47 \cdot 10^{18}$ cm^{-3}). The gas pressure is controlled by a closed-loop electronic regulator and has a maximum deviation of ±4 mbar around the specified value. The reference value is taken from a calibrated pressure gauge at the gas reservoir. As the summed area of the gas cell outlet holes is smaller than the area of the inlet holes and all supply pipes are significantly larger, it can be assumed that the pressure in the gas cell is identical to the pressure in the reservoir. From the ideal gas law the electron density is deduced, taking into account that one H_2 molecule provides two electrons. The gas density inside the opaque gas cell could not be measured directly.
At every length 31 consecutive laser shots were recorded. In order to avoid systematic errors, the length of the gas cell was not changed linearly, but in the following random order: $2, 4, 6, 3, 5, 8, 10, 7, 13$ mm at 130 mbar and $13, 5, 3, 6, 8, 4, 10, 14, 7, 12$ mm at 50 mbar. The length of the gas cell is changed by a differential micrometer screw. The reading accuracy was limited to $\approx 1/16$ mm due to insufficient accessibility.
The *ATLAS 80*-pulse was compressed to be shortest on target, with $\delta t \approx 26$ fs. The focal spot size was $\delta x \approx 22$ μm. A longitudinal position of the gas cell entrance relative to the longitudinal focus position was fixed by optimizing the electron energy at a medium pressure of $\approx$ 80 mbar and a gas cell length of 5 mm. Due to experimental constraints an absolute determination of the offset between longitudinal focus and gas cell entrance position is not easily possible, as the entrance is not accessible to optical probing. The exact dependence is the subject of a different study. For this work an empirically optimized longitudinal gas-cell position is fixed for all scans.

VI.1.2 General Electron Properties

Figure VI.1 shows the false-color charge signal of 31 consecutive shots on the scintillating screen (S2 in fig. V.1) of the electron spectrometer for a small selection of gas cell lengths around the optimum ($2, 4$ and 6 mm), 130 mbar. The signal intensity of all shots is scaled to the same maximum value. It must be noted that the spectral dispersion of the electron spectrometer is not linear. The lower dispersion of higher energies leads to an over-estimation of the spectral peak in these raw pictures. However, from this pictures it can clearly be seen, that the maximum electron energy increases between the measurements at 2 and 4 mm gas cell length. With an even longer gas cell (6 mm) the maximum peak energy only slightly decreases, but the stability is reduced, as can also be seen more quantitatively in the error bars of figure VI.10. All shots exhibit a low energy background, but for the optimized gas cell length of $\sim$ 4 mm the high energy peak is more pronounced.

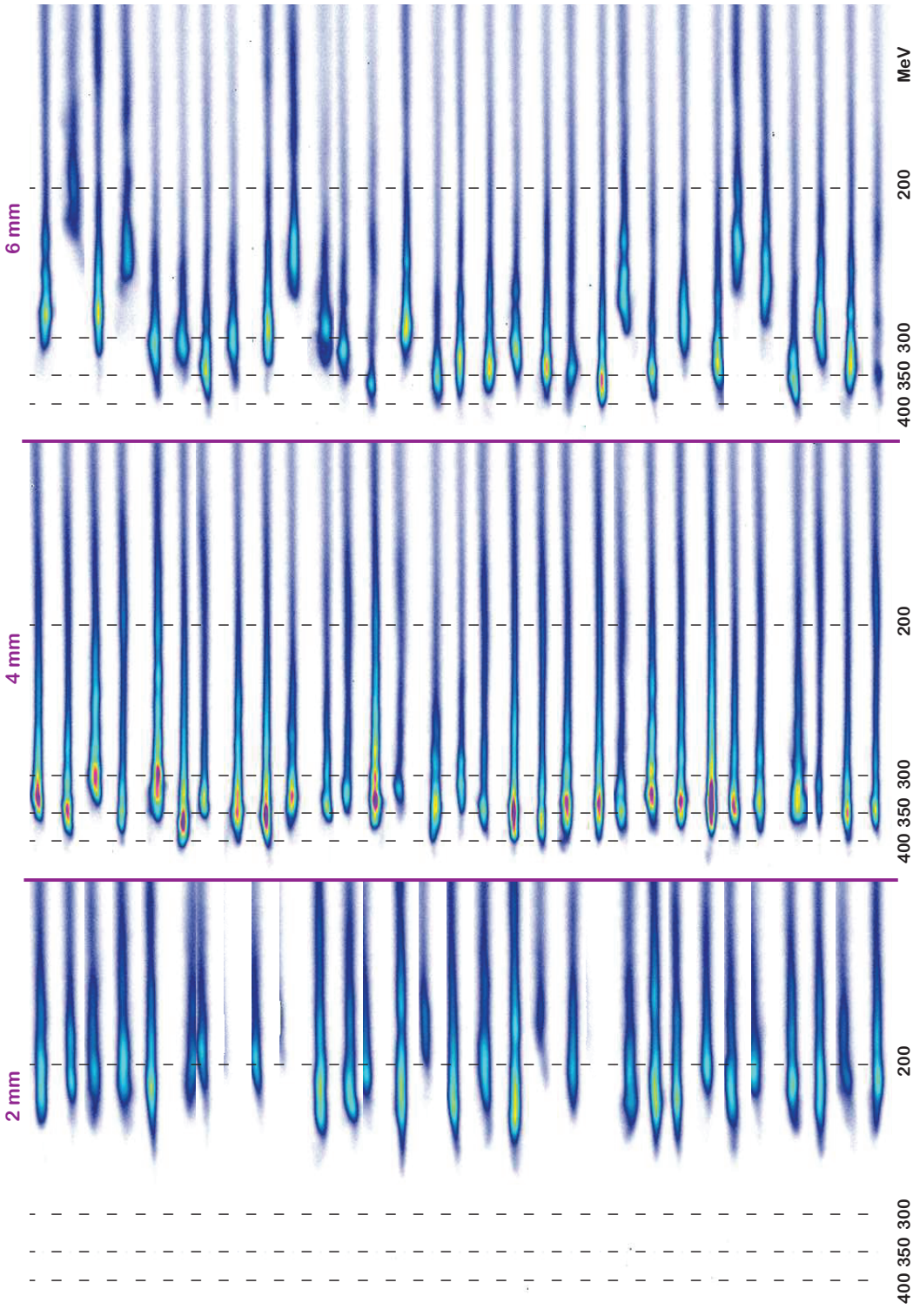

Figure VI.1.: *Images of the scintillating screen behind the permanent dipole magnet for a gas cell length of* 2, 4 and 6 mm *at* 130 mbar

VI.1.2.1 Charge

Figure VI.2 shows some measured sample spectra at a gas cell length of 4 mm (blue line) and a backing pressure of 130 mbar. The signal in the raw pictures of the scintillating screen shown in figure VI.1 was integrated along the axis perpendicular to the spectral dispersion. The integrated signal was re-binned using the spectrometer calibration curve (energy versus spatial deviation) described in section V.2 in order to obtain an equally spaced energy axis. Subsequently, the absolute charge density was extracted by comparing the scintillator signal to the reference light source as discussed in section V.3.

A Gaussian curve was fitted to the high-energy peaks of the spectra (pink curve in fig. VI.2). At this gas cell length this peak contains an average of 14.1 pC (mean of 31 shots) with a standard deviation of 5.9 pC. The highest charge in the peak measured in this series was 26.8 pC. In figure VI.3 the average total measured charge of 31 shots is plotted for every gas cell length. But it has to be noted that due to geometrical constraints only the charge contained in the spectrum above 100 MeV can be evaluated. As the spectra exhibit a broad background presumably continuing to low energies, an increase/decrease of the peak energy naturally results in an increase/decrease of the *measured* integrated charge.

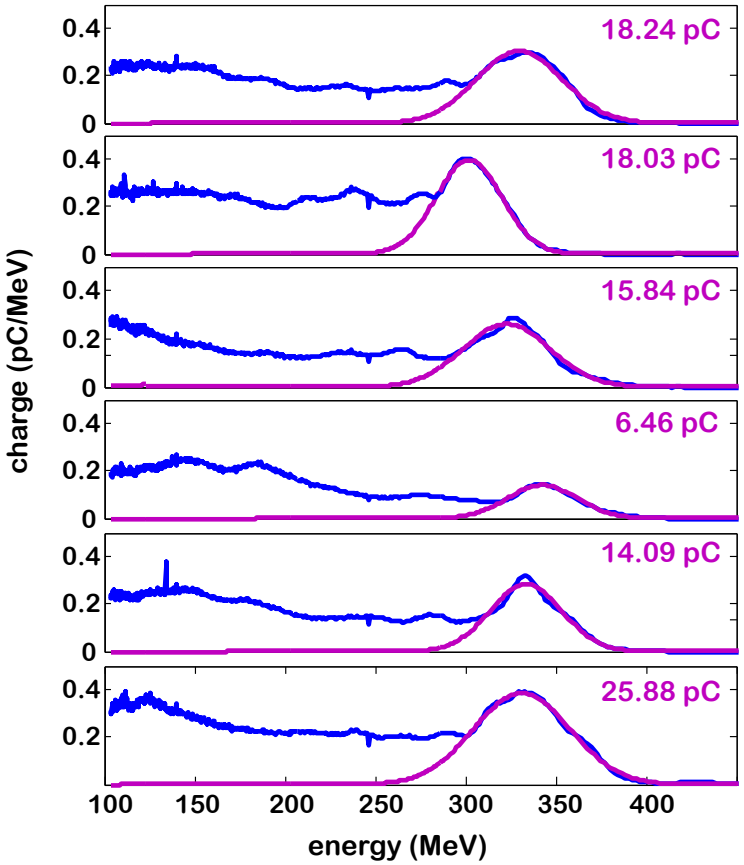

Figure VI.2.: *Sample spectra at a gas cell length of* 4 mm *(blue line),* 130 mbar. *The pink line shows a Gaussian fit to the high-energy peaks. The charge contained in this fit is given on the right.*

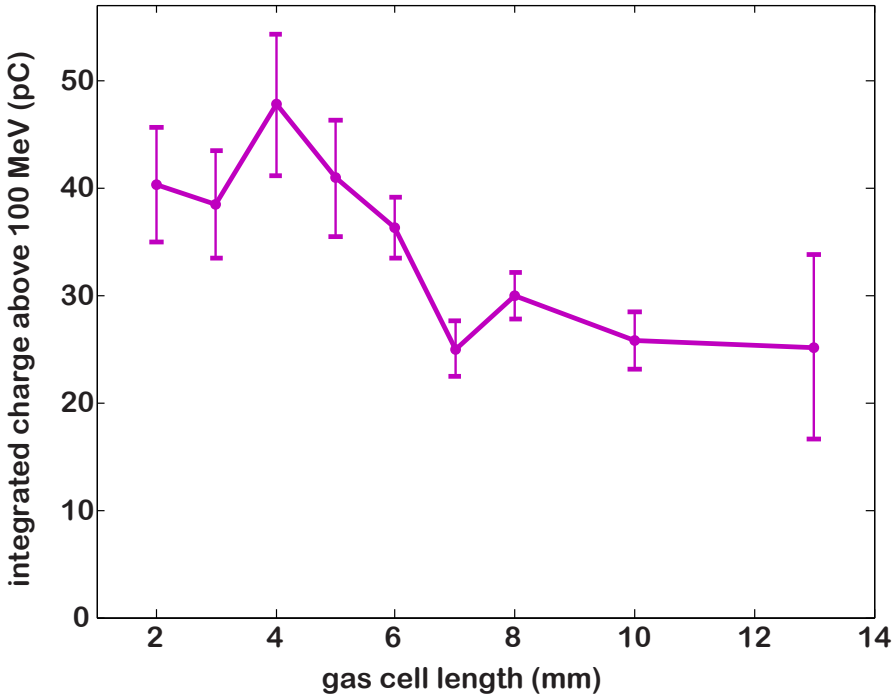

Figure VI.3.: *Evolution of the total charge above* 100 MeV *depending on the gas cell length. Every dot represents the average over 31 shots, the error bars give the corresponding standard deviation.*

The highest charge of 48 pC (above 100 MeV) was measured at a gas cell length of 4 mm.

VI.1.2.2 Divergence

By taking line-outs of the signal on the scintillating screen in the direction perpendicular to the dispersion direction, one can extract the energy resolved divergence Φ of the beam[1]. Figure VI.4 illustrates that the divergence of the electron bunch does not change significantly with for different gas cell lengths between 2 and 10 mm (130 mbar). The filled dots give the energy resolved divergence averaged over 31 shots. The respective standard deviation is represented by the star-shaped dots. The average divergence is below $\Phi \approx 1.4$ mrad FWHM for the spectral peak and increases within the spectrum towards lower energies to ≈ 3.5 mrad FWHM at 100 MeV (figure VI.4).
The third curve in this plot (hollow dots), the normalized divergence, is defined as $\Phi_{norm} = \Phi\gamma\beta$, where γ and β are the relativistic quantities. The normalized divergence takes into account that acceleration inherently decreases the divergence as the longitudinal beam momentum is increased but the transverse momentum stays unaffected (adiabatic divergence damping). In figure VI.4 this is approximately confirmed for low energies; above

[1]For the divergence evaluation a $m \times n$-matrix was considered with the energy resolution along the n-dimension (rows). The spatial divergence was extracted along m (columns). For this each 7 columns were binned into one with the resulting column being the median of the 7. Subsequently the sum of each 5 neighboring columns was taken. From this smoothed curve the FWHM width was evaluated.

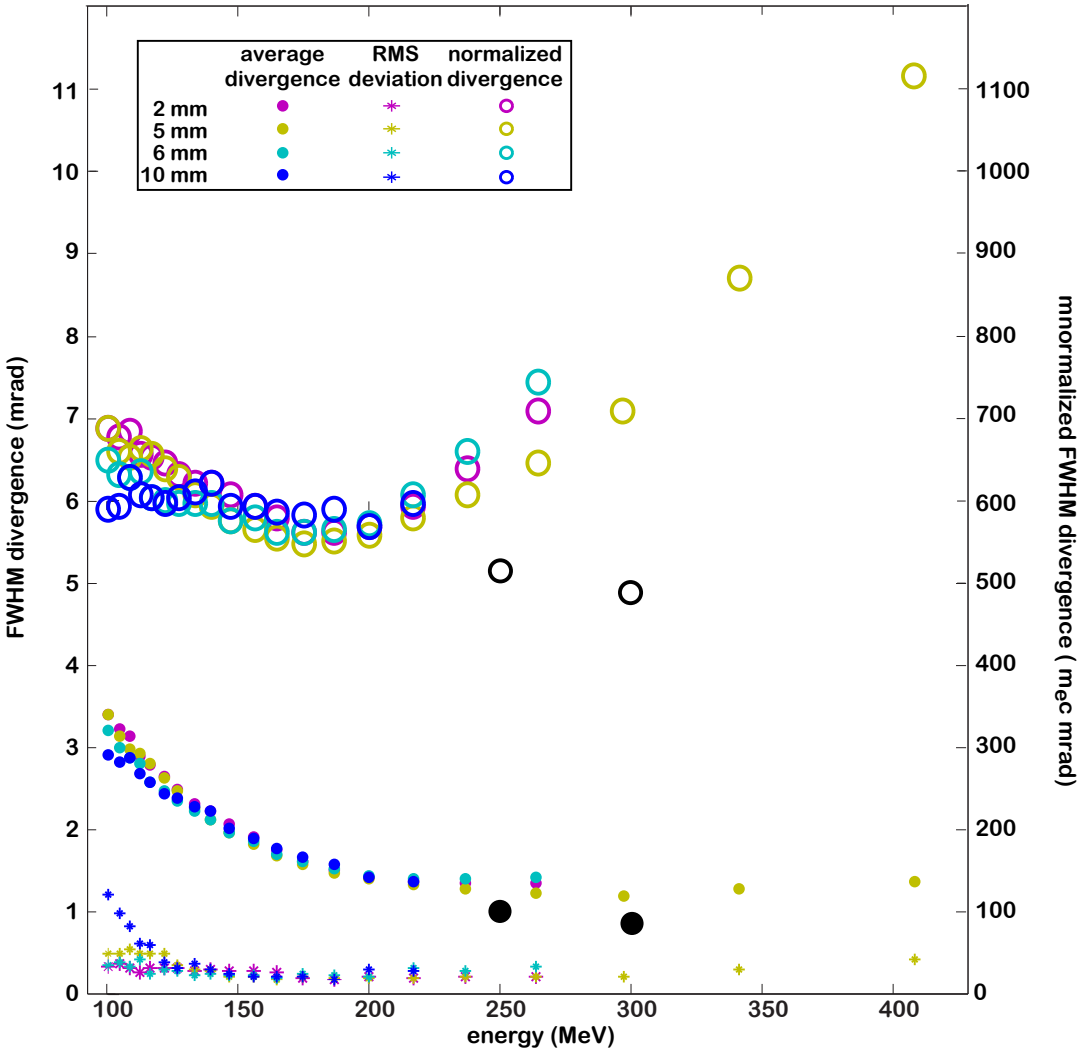

Figure VI.4.: *Divergence evolution of the* 130 mbar*-run, evaluation of the scintillating screen behind the electron spectrometer. Divergence from transverse line-outs, spectrally resolved at different gas cell lengths. For the sake of clarity only a few curves are shown, the divergence for all other curves between* 2 *and* 10 mm *is similar. The middle curves (filled dots) give the FWHM divergence averaged over 31 shots, the lower curves (stars) show the corresponding standard deviation (both cases: left axis). The top set of curves (hollow dots) shows the normalized divergence, which arises from the averaged FWHM divergence multiplied by betaγ (right axis). The black dots belong to a different measurement (see text) indicating the limited resolution of this setup.*

$\approx$ 200 MeV the normalized divergence increases up to twice the low-energy value. However, the measurement of these low divergences is close to the resolution limit of the imaging system [2]. In a different measurement campaign a more elaborate divergence measurement was conducted under very similar conditions (120 mbar instead of 130 mbar, fixed gas cell length of 5 mm): With magnetic quadrupole lenses the electron beam at the gas cell exit was imaged onto a high-resolution scintillating crystal behind the electron spectrometer. From this the transverse size of the electron beam at a certain energy could be determined. In order optimize the electron imaging, the longitudinal position of the magnetic lenses was scanned. During this scan the size of the bunch image on the crystal varied quadratically around a minimum. From the exact shape of this parabola the beam divergence can be extracted. Details on this method and the measurement can be found in [132] and the dissertation of Raphael Weingartner [104]. In this way, the divergence at 250 MeV could be determined to be 1.03 mrad FWHM and at 300 MeV it was 0.87 mrad FWHM corresponding to normalized divergences of 490 $m_e c$ mrad and 517 $m_e c$ mrad, respectively (black dots in figure VI.4). This new measurement with higher resolution indicates a normalized emittance that decreases towards higher energies. This can plausibly be explained by space charge effects that are less dominant for high electron energies. In a next step the imaging of the scintillating screen will be improved, in order to obtain a more accurate single-shot measurement of the energy-resolved divergence at all energies. Simultaneously, a scintillating screen with higher spatial resolution could be used. This, however, would be at the cost of emitted light intensity per incident charge.
The slightly different behavior of the divergence for the longest gas cell length of 14 mm is discussed in the next paragraph.
For the 50 mbar case see appendix D.

In the follow-up measurement that was already mentioned above it was revealed that also the emittance of the electron bunch is independent of the acceleration length. The electron bunch leaving the variable-length gas cell was imaged on a high-resolution YAG crystal behind the electron spectrometer using miniature magnetic quadrupole lenses. From this energy-resolved image of the source both source size and divergence could be determined very precisely. An emittance as small as 0.2 π mm mrad was measured, with the exact value depending on the respective pressure, but not on the gas cell length. Details can be found in [132] and [104].

[2] As extracted from a calibration picture, one pixel corresponds to 340μm, the resolution of the scintillating screen is slightly higher with $\approx$ 200 μm (see chapter V and [39]). But, since at this position of the setup a large range of energies has to be observed, a large field of view is necessary, which limits the resolution of the imaging setup to $\equiv$ 0.7 μm. (At the other scintillating screen S1 in the setup (cf. figure V.1), where the pointing fluctuations and the energy-integrated divergence can be extracted, the spatial resolution is limited by the scintillating screen, not by the imaging setup.)

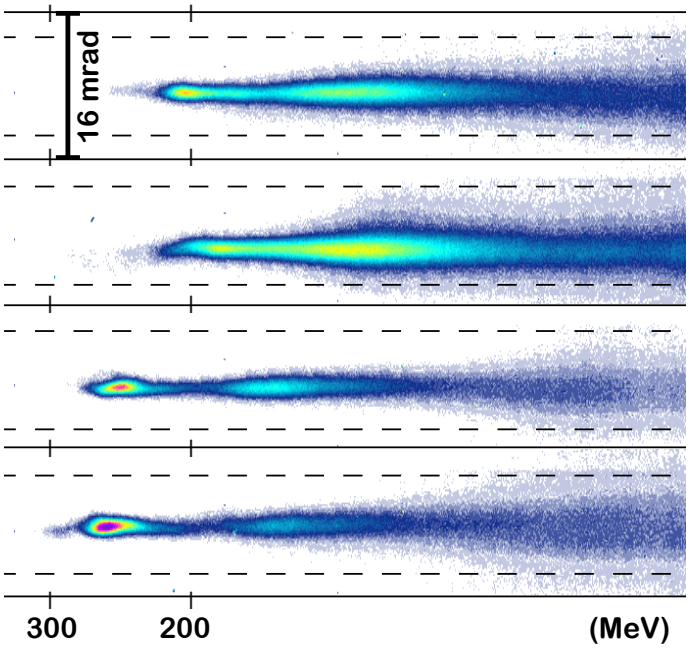

Figure VI.5.: *Sample images from the scintillating screen S2 at a gas cell length of* 14 mm. *(Outside the dashed lines the electrons have to cross* 20 mm *of aluminum before hitting the screen, within those lines the aluminum is only* 2 mm *thick.)*

VI.1.2.3 Double Peaks at 13 mm Gas Cell Length

At a gas cell length of 13 mm the spectrum on the scintillating screen looks different for approximately half of the shots (130 mbar). Figure VI.5 shows the spectrometer screen signal of four example shots. They show a second spectral peak at roughly 150 – 200 MeV with simultaneously increased divergence. A separate measurement with the bunch duration diagnostics described in section V.6 indicates that for similar pressures at gas cell lengths > 10 mm two electron bunches are present. In time, the two bunches are roughly separated by one plasma period. A probable scenario is, that after the laser has depleted, the electron bunch drives its own wakefield and a second electron bunch is trapped. This theory still has to be confirmed by simulations. Details on the measurement and analysis will be available in the dissertation of Matthias Heigoldt (Ludwig-Maximilans-Universität München), partially also in [4].

VI.1.2.4 Spectrum

The evolution of the spectrum with the gas cell length is presented in detail in figure VI.6. It shows the mean spectrum of 31 consecutive shots per gas cell length for 130 mbar (for the corresponding plot of the 50 mbar run see appendix D). It can be clearly seen that the maximum energy increases with increasing gas cell length up to 5 mm. This is merely due to the longer acceleration phase as the total energy gain is determined by $\Delta W = qEL_{acc}$. For a certain average electric field strength E a longer acceleration length L_{acc} will lead to

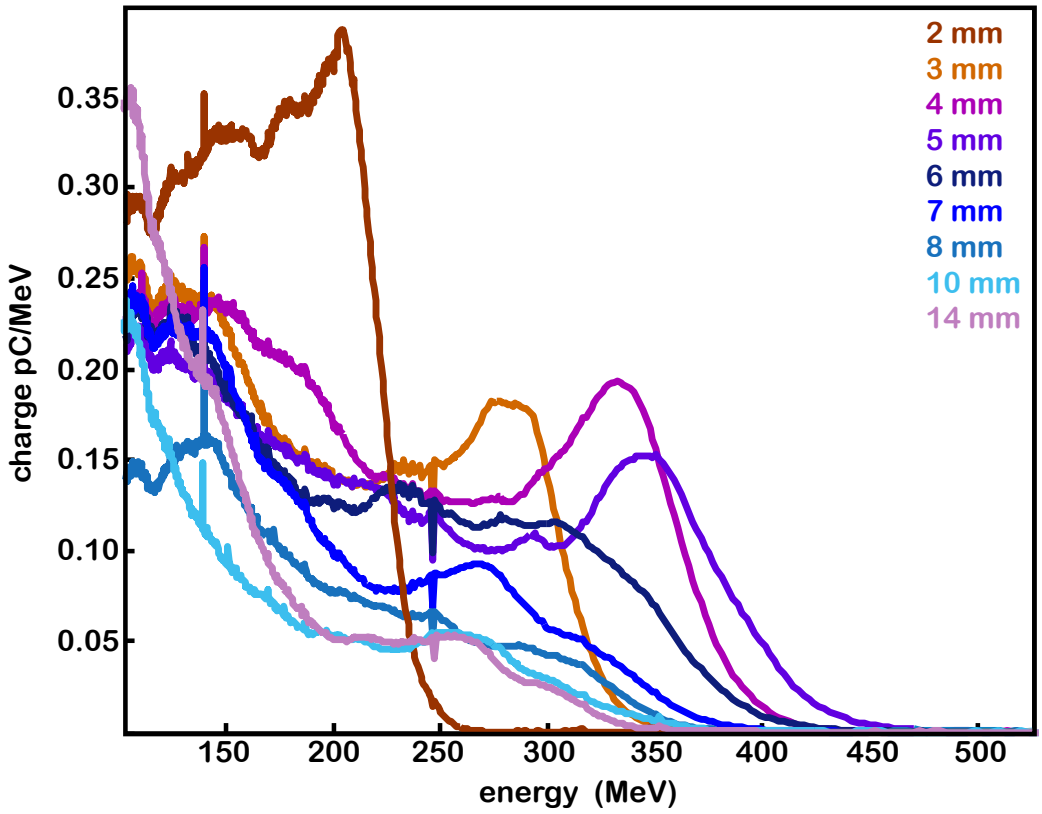

Figure VI.6.: 130 mbar. *Average electron spectrum depending on the gas cell length. Average over 31 consecutively recorded spectra per length.*

higher electron energies. After ≈ 5 mm the maximum energy decreases again, the electrons have reached the dephasing point (also see figure VI.11).
Note that in the averaged spectra narrow peaks are suppressed unless they are reproducible. In figure VI.6 a clear spectral peak only occurs around the dephasing point. There the formation of a peak is also expected as the head of the electron bunch is already in the decelerating phase of the electric field, while the energy of the rear part still increases. The electron density at one intermediate energy is increased and a spectral peak arises. The most pronounced and stable peak forms around the point where the cut-off energy starts to decrease again and subsequently also the energy of the entire peak is reduced. This shows that the laser depletion length is longer than the dephasing length, as after ≈ 5 mm of propagation the electron bunch is significantly decelerated again in the laser-driven wakefield.
Acceleration and subsequent deceleration are quantified in the following section.

VI.1.3 Dephasing Length and Electric Field - 130 mbar

Figure VI.7 depicts the dependency of the high-energy cut-off of the spectra (defined as the energy at which the signal drops to 10% of the peak signal) on the acceleration length at a backing pressure of 130 mbar. Each data point is averaged over 31 consecutive shots,

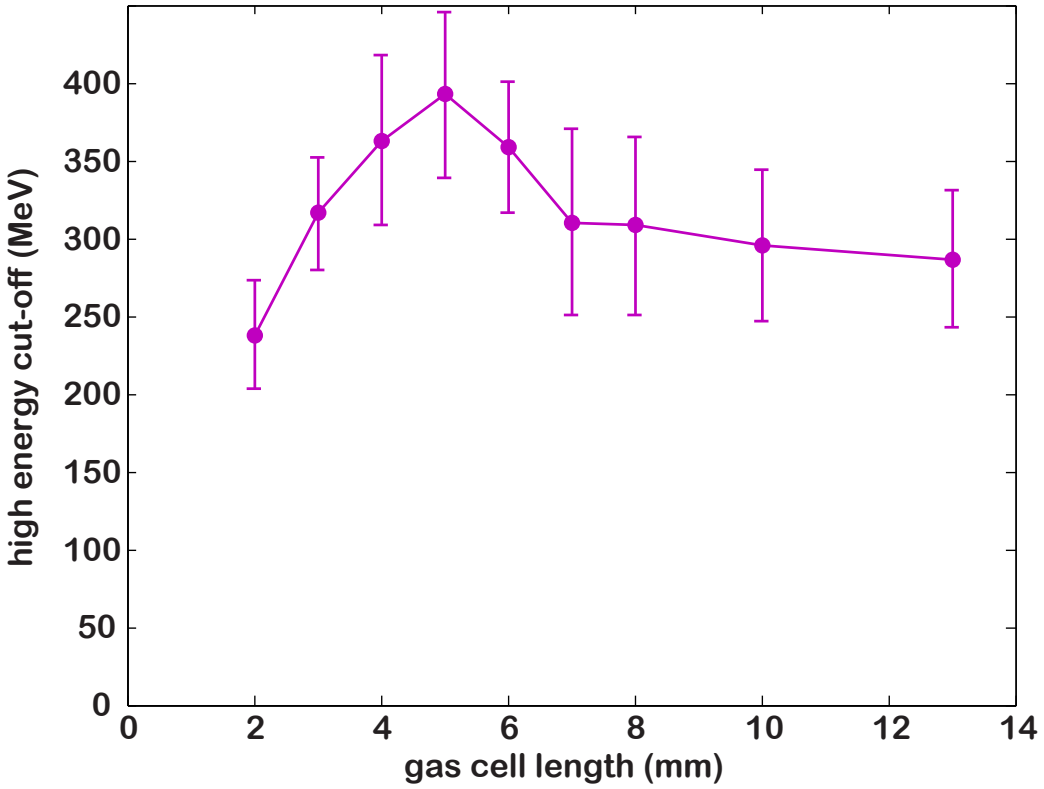

Figure VI.7.: *High-energy cut-off of the electron spectra depending on the gas cell length. Every data point is averaged over 31 consecutive spectra. The error bars indicate the standard deviation.*

the error bars depict the standard deviation.
It can be seen, that in the beginning, a longer acceleration length leads to higher peak energies. After a certain length ($\sim$ 5 mm) the energy decreases again.
Before any further evaluation it will be briefly clarified which functional dependence is expected from theory for the energy gain of the electron on the acceleration distance. The longitudinal electric field E_z within the non-linear wakefield is roughly linear with the maximum accelerating field $-|E_{max}|$ at the rear of the wave bucket, a zero crossing in the middle and a field that acts increasingly decelerating on electrons between the bucket center and the front (cf. e.g. fig. III.2). A relativistic electron injected at the rear propagates forward in this electric field with a velocity $v = c - v_{l,gr}$. The field seen by such an electron is therefore linearly dependent on the acceleration length (= gas cell length) with $z = (c - v_{gr})t$. When the electron reaches the zero-crossing of the electric field it has traveled the dephasing length L_{deph}. After having propagated the distance z in an electric field the electron has gained the energy $\Delta W(z) = e\Phi(z)$ and $\Phi(z) = -\int E_z \mathrm{d}z$. For the linearly increasing electric field (from $-|E_{max}|$ to $+|E_{max}|$) the electron energy should therefore vary as $\Delta W = -1/2e\ dE/dz(z - L_{deph})^2 + W_{max}$. Figure VI.8 shows such a fit to the measured data points. The fit parameters give a dephasing length of $L_{deph} = 4.93$ mm and a electric field gradient of $dE/dz = 34.14$ MV/mm^2. Extrapolating the parabolic fit to an electron energy of zero suggests that injection occurs close to zero ($z = 0.2$ mm), which is expected for these high pressures.

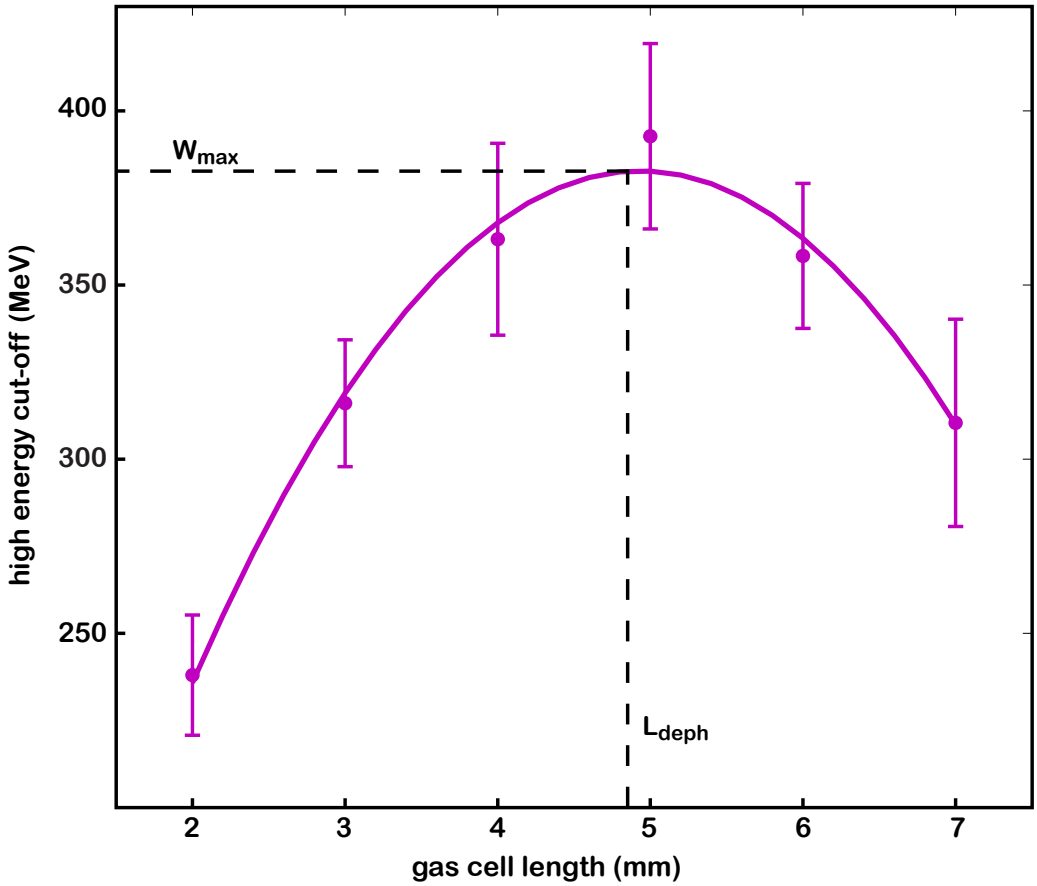

Figure VI.8.: *Fit to the first part of the electron energy evolution:* $\Delta W = -1/2\ e\ dE/dz(z - L_{deph})^2 + W_{max}$. *The fit parameters are:* $dE/dz = 34.14$ MV/mm^2, $L_{deph} = 4.93$ mm, $W_{max} = 382.77$ MeV

The corresponding electric field is $E(z) = -\mathrm{d}\Phi/\mathrm{d}z = 1/e\ \mathrm{d}(\Delta W(z))/\mathrm{d}z$ (also see figure VI.11). Since the data points correspond to the high-energy cut-off of the spectrum, this is the electric field as seen by the electrons with the highest energy. As a result of the injection and acceleration mechanism, these are usually the electrons that constitute the head of the bunch. This is supported by the simulations shown below. They also show that at the position of head of the electron bunch in the bubble distortions of the electric field due to beamloading effects are smallest. The largest electric field acts on the electrons right after injection. At this point ($z = 0.2$ mm) the a field strength of 161.7 GV/m can be extracted from the fit.

VI.1.4 Dephasing Length and Electric Field - 50 mbar

A second length scan was conducted at a backing pressure of 50 mbar $\equiv 2.47 \cdot 10^{18}$ cm^{-3}. Figure VI.9 shows the measured data points together with the 130 mbar run. In the low

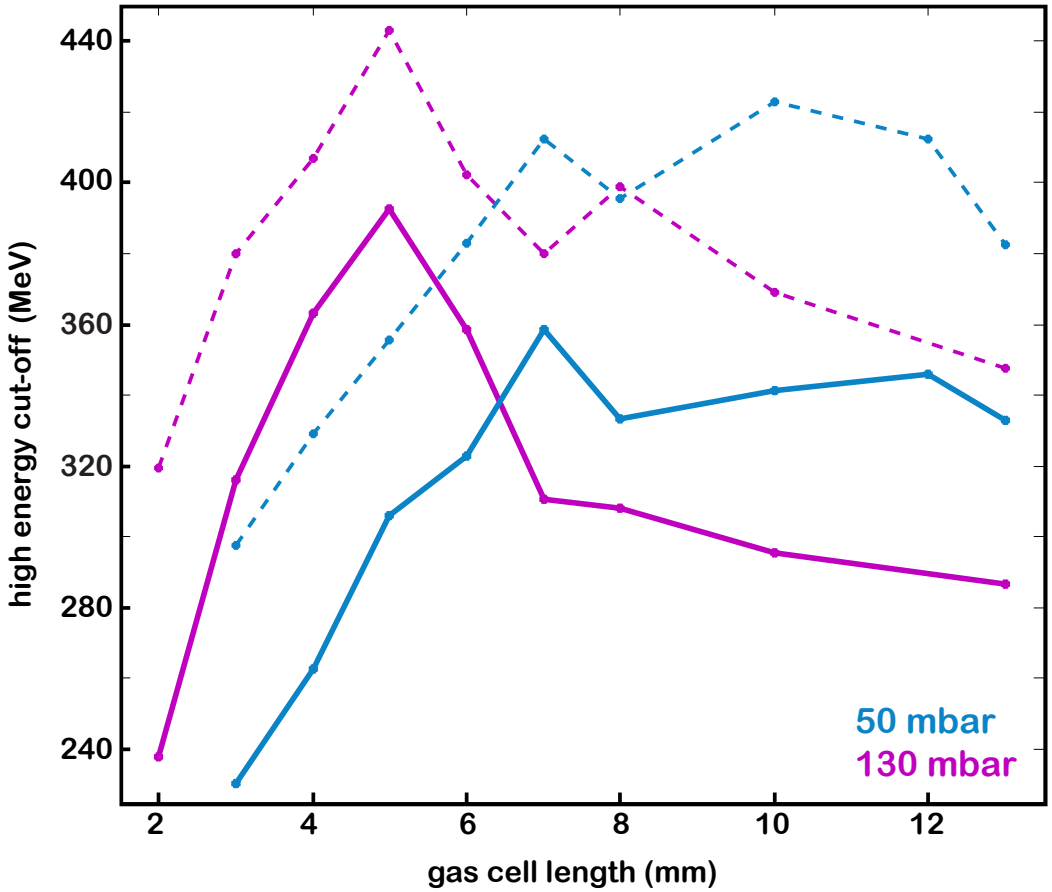

Figure VI.9.: *High-energy cut-off of the electron spectra depending on the gas cell length. Solid lines: average over 31 consecutive spectra per length, dashed lines: average over the 3 shots with the highest energy cut-off.*

density case the energy increases slower with the gas cell length than in the high-density case and the maximum energy is smaller. Theory predicts a lower maximum electric field for lower densities: $E_{max} \propto n_e^{1/2}$. This explains the lower energy gain per gas cell length. However, simultaneously, the dephasing length increases for lower densities with $L_{deph} \propto n_e^{-3/2}$. The maximum energy $W_{max} = eE_{max}L_{deph}$, therefore, is proportional to n_e^{-1} and should thus be higher for lower densities, albeit reached after a longer acceleration distance. This indicates that in the low-density measurement acceleration stops before the electrons have passed the dephasing length. It will be seen below (paragraph VI.1.4.1) that in this run self-guiding can not be sustained long enough, the laser diffracts and ceases driving the wakefield before the maximum electron energy is reached. Still the dephasing length for this density can be extrapolated by applying the same quadratic fit as described above (section VI.1.3). A dephasing length of 16.05 mm and a maximum energy of $W_{max} = 841.27$ MeV are projected. The electric field gradient is $dE/dz = 2.86$ MV/mm^2 and the electric field strength at $z = 0$ mm is $E_0 = 45.9$ GV/m. Figure VI.11 shows the electric field strength that acts on the high-energy part of the electron bunch during propagation. Theses curves are the derivative of the polynomial fit in fig. VI.10.

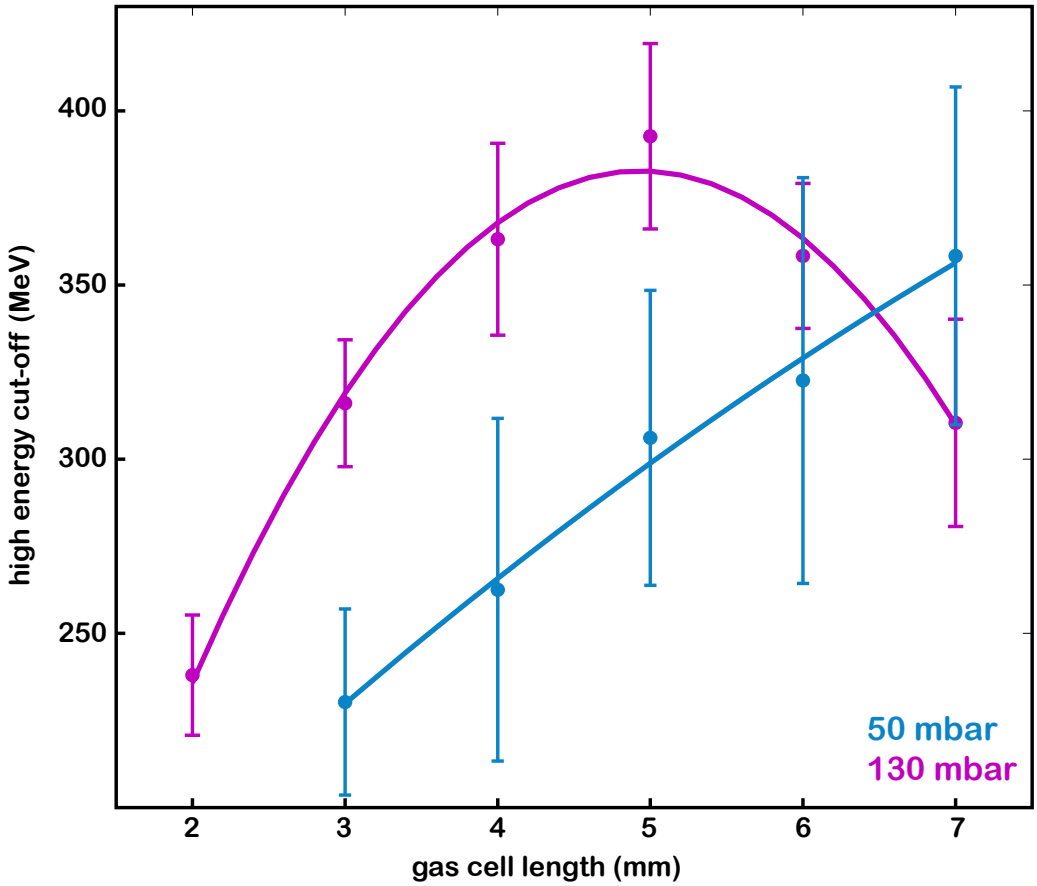

Figure VI.10.: *Measured data as in figure VI.9 with second order polynomial fit* $\Delta W = -1/2\ e\ dE/dz(z - L_{deph})^2 + W_{max}$. *, The error bars are the standard deviation of the cut-off energy of 31 shots. The fit parameters are:*
130 mbar*:* $dE/dz = 34.14$ MV/mm^2, $L_{deph} = 4.93$ mm, $W_{max} = 382.77$ MeV
50 mbar*:* $dE/dz = 2.86$ MV/mm^2, $L_{deph} = 16.05$ mm, $W_{max} = 841.27$ MeV

In the low density case, the dynamics cannot be fully described by the simple second order polynomial as a fitting function. With this fit zero electron energy would only be reached for negative z-values. The real maximum electric field strength and dephasing length, therefore, can deviate from the ones deduced from this fit. One conclusion from that could be that the acceleration gradient in the beginning is actually stronger than indicated by the fit including the data points after longer propagation. This flattening of the acceleration gradient can be caused by beamloading. Electrons are continuously trapped during propagation and the accelerating field is more and more shielded by the field of the electron bunch. This effect is expected to be stronger at lower plasma densities, which explains its strong presence only in the 50 mbar run. But also a second factor probably contributes to this decrease of the electric field. As will be discussed in the next section in this run self-guiding can not be sufficiently sustained over the entire dephasing length. When self-guiding stops the laser diffracts, the transverse spot size increases, which increases the blowout radius and the bubble size, simultaneously the intensity of the driver

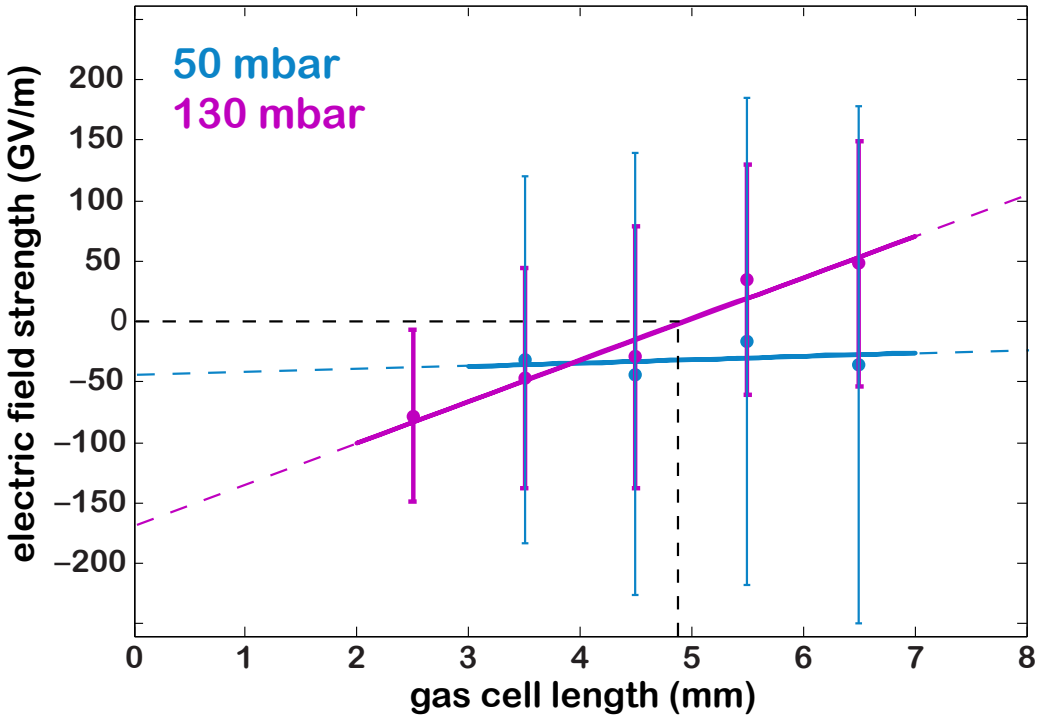

Figure VI.11.: *Deduced instantaneous electric field strength as seen by the highest energy electrons. The dots are obtained from the energy gain between the data points in fig. VI.10. [If the directly measured data points in fig. VI.10 have the coordinates* (x_i, y_i) *then the points* (k_i, j_i) *in this figure have the coordinates* $(k_i, j_i) = (x_i + (x_{i+1} - x_i)/2, y_{i+1} - y_i)$*.] The error bars are the sum of the respective error bars in fig. VI.10, thus assuming the worst case. The straight lines are the derivative of the fitted parabolas in fig. VI.10.*

decreases, both leading to a more and more reduced electric field.

VI.1.4.1 Acceleration Limits

In both measurements, at 50 mbar and 130 mbar, the electron energy does not change significantly after roughly 7 mm of propagation. The gas cell length was extended beyond this length up to 13 mm to verify the stagnation of the cut-off energy. If the energy of the electrons does not change, they are, obviously, not exposed to a longitudinal electric field. In our setting, this happens if the laser stops driving a wakefield. As will be elucidated below, in the 130 mbar case this is well explained by energy depletion of the pulse after $\approx$ 7 mm, in the 50 mbar run, on the contrary, self-guiding cannot be sustained long enough, the laser diffracts.
If the laser does not excite a plasma wave anymore, the electron bunch propagates through the plasma and drives its own wakefield. This interaction is responsible for the low energy decrease that is still observed for gas cell lengths of 7 mm to 13 mm. It has to be noted that, in principle, the energy loss of an electron bunch that is driving its own wakefield can also be large. However, the efficiency of the process depends on the current

and thus on the electron density in the bunch. For an electron bunch with a non-constant density-distribution, for example a Gaussian, only the high-current core will lose energy driving the plasma wake, the low-current front/rear parts stay unaffected [133, 134][3]. In the discussed plot only the high-energy cut-off of the spectrum is considered. Due to the characteristics of the acceleration process and according to simulations, a laser-wakefield accelerated electron bunch is temporally chirped with the high energies in the leading edge. The fact that the energy of these electrons only slowly decreases within the last millimeters of the gas cell suggests, that this leading high-energy part does not contribute notably to the excitation of a plasma wave.

Self-Guiding

In the low-density run acceleration stops after roughly seven millimeters and the achieved electron energies are comparable to the high-density case (fig. VI.9). The two most evident explanations are that the laser pulse driving the wakefield either depletes or diffracts. The power necessary to sustain self-guiding increases with lower densities, yet energy depletion is less severe for lower densities. The parabolic shape of the energy evolution in the high-density run, with acceleration and subsequent deceleration, indicates that in this case the depletion length is much larger than the dephasing length. For the low-density run the laser should deplete even later. Still, clearly, the dephasing point is not reached, indicating that diffraction limits the acceleration.
Without self-focusing the laser diffracts with a Rayleigh length of $l_R = 1.37$ mm. The critical power (III.30) needed for self-focusing to occur is 12 TW in the 50 mbar case and 4.6 TW at 130 mbar. Lu et al. [58] also give an estimate of how much power is needed initially in excess of P_c in order to sustain self-guiding over the entire dephasing length despite of the power loss due to energy depletion during propagation (cf. (III.64); experimental verification in [67]). For this $3.6P_c$ would be needed initially in the high-density case, $10.2P_c$ are available. This confirms the assumption that in that run, self-guiding is not the limiting factor. However, in the low-density case initially $6.3P_c$ would be necessary and only a power of $3.9P_c$ is provided. This means that for the 50 mbar run self-guiding can not be sustained over the entire usable acceleration length. This explains the characteristics of the 50 mbar energy-gain curve. A wakefield is driven and electrons are accelerated over roughly 7 mm. This is less than half the estimated dephasing length (see section VI.1.4) and thus the electrons have not reached the maximum possible energy yet. At longer distances, the laser is diffracted so strongly, due to the lack of self-guiding, that the intensity is not sufficient to drive a plasma wave. From 7 to 14 mm the electron bunch propagates through the plasma and loses some energy due to the interaction with the background electrons and by driving its own plasma wave [135].

[3] Low-current parts of the electron bunch BEHIND the high-current part that is driving a wakefield can also suffer significant energy losses as they sit in the decelerating phase of the electric field in the blowout region.

run	density (10^{18} cm^{-3})	dephasing length (mm)	max. el. field (GV/m)	max. energy (from fit) (MeV)
130 mbar	6.42	4.9	162 GV/m	383
50 mbar	2.47	16.0	46 GV/m	841

Table VI.1.: *Parameters deduced from the experiment*

run	density (10^{18} cm^{-3})	linear deph. length (mm)	wavebreaking field (GV/m)	max. energy (MeV)
130 mbar	6.42	3.6	244 GV/m	439
50 mbar	2.47	14.9	152 GV/m	1132

Table VI.2.: *Parameters predicted by theory*

Energy Depletion

As already indicated above the 130 mbar run is limited by energy depletion of the driver pulse rather than deffraction. This can be deduced from the density scaling of the two processes. Self-focusing is stronger or needs less power at higher densities (III.30), (III.31), however, energy depletion is higher for higher densities (III.51), (III.58). Up to approximately 7 mm the electrons are strongly accelerated and decelerated again. The parabolic course of the acceleration and the high acceleration gradient indicate that also the deceleration still takes place within the high electric field of the laser-driven bubble. Only after 7 mm this curve flattens, as it is expected, when the laser depletes and eventually cannot sustain the wakefield anymore. As in the low density case the electrons then only slowly loose energy to the plasma.
As already described in paragraph III.2.4.4, a high-intensity laser pulse with a Gaussian temporal envelope can well contain half of the energy after propagating the dephasing length. Assuming an initial $a_0 \approx 4$ after self-focussing, the vector potential would then only be decreased to $a_0 \approx 2.8$, which is still enough to sustain a wakefield in the blowout regime. From this consideration and the corresponding measurement that shows that the electron energy indeed is rapidly decreased again beyond the dephasing length it becomes clear that it is important to carefully adjust the acceleration length.

VI.1.5 Comparison to theory

Table VI.2 summarizes different parameters deduced from the measurement and gives the corresponding theoretical values. The linear dephasing length $L_{deph,lin}$ as in (III.49) ($a_0 < 1$) and the cold wavebreaking field E_{max} (III.56) from the 1D non-linear theory are listed. Assuming a linear electric field, the maximum energy is then simply calculated by: $W_{max} = e\, L_{deph}\, 1/2 E_{max}$.

The theoretical linear dephasing length is $L_{deph,lin} = 3.6$ mm for 130 mbar and 14.9 mm for 50 mbar. These values are slightly smaller than the measured values of 4.9 mm and 16.0 mm, respectively. This is expected since for $a_0 > 1$ the plasma wavelength increases,

which consequently leads to a longer dephasing length. Esarey et al. [82] scale the linear dephasing length with $a_0 \cdot \sqrt{2}\pi^{-1}$ for $a_0^2 >> 1$ (III.59) and with $2a_0^{-2}$ for $a_0^2 << 1$. [4] In the presented experiment a_0 is ≈ 2 in the beginning and theoretically close to 4 after self-focusing until energy depletion becomes significant. Assuming the measured dephasing length and applying this non-linear scaling one can extract an average a_0 of 2.9 for the 130 mbar run. The measurement is thus in good agreement with the predictions made by the 1D non-linear theory.

The cold wavebreaking field III.56 from the 1D theory is $E_0 = 244$ GV/m (130 mbar) and 152 GV/m (50 mbar), the measurement yields 162 GV/m and ~ 46 GV/m, respectively. Again the reduced measured field can be explained by beamloading which is not considered in the theory.

VI.1.5.1 Pressure Scan

The same conclusion, i.e. that even in the non-linear regime the laser is not necessarily completely depleted after the dephasing length, can be drawn from a separate measurement: a pressure scan at a fixed gas length. This scan reproduces both regimes seen above, insufficient self-focusing at low pressures and at high pressures a deceleration of the electrons in a wakefield that is driven beyond the dephasing point by a still energetic laser pulse.
At the time this data set was taken, the laser performance had slightly improved compared to the measurement described above. Increased energy (1.5 J on target) and an enhanced focal spot lead to higher absolute electron energies but no qualitatively different behavior. Figure VI.12 shows the electron signal on the scintillating screen S2 behind the dipole magnet. The pressure was set to 200 mbar and then drops slowly for every consecutive shot until it is set back to the highest value again. The gas cell length is kept at 12 mm for all shots, which is longer than the expected dephasing length for all pressures.
In the region with the blue background the electron energy increases with decreasing pressure as the dephasing length and thus the acceleration length increases. For lower pressures highlighted in yellow the same behavior as described above for the 50 mbar run (beyond 7 mm) can be observed. The peak energy stagnates, although the pressure still drops. The laser is no longer self-guided, diffracts and cannot sustain the plasma wave anymore. The most conspicuous shots are those in the pink field. The divergence grows drastically and high-energy electron traces appear.

[4] The scaling theory of Lu et al. [58] (also see section III.5.2) assumes a dephasing length that is the linear one $L_{deph,lin}$ scaled with $\sqrt{a_0} \cdot 2(3\pi)^{-1}$ (III.59). For this to be valid the condition $k_p R = 2\sqrt{a_0}$ (III.36) must be fulfilled, which in simulations leads to a spherical bubble with a radius $R \approx w_0$. For $a_0 < 20$ this leads to a dephasing length (III.59) shorter than $L_{deph,lin}$ as in this case $R < \lambda_p/2$ determines the bubble shape. The simulations with our parameters show that the bubble is not exactly spherical, but elongated in longitudinal direction. This scaling theory is therefore not applicable.

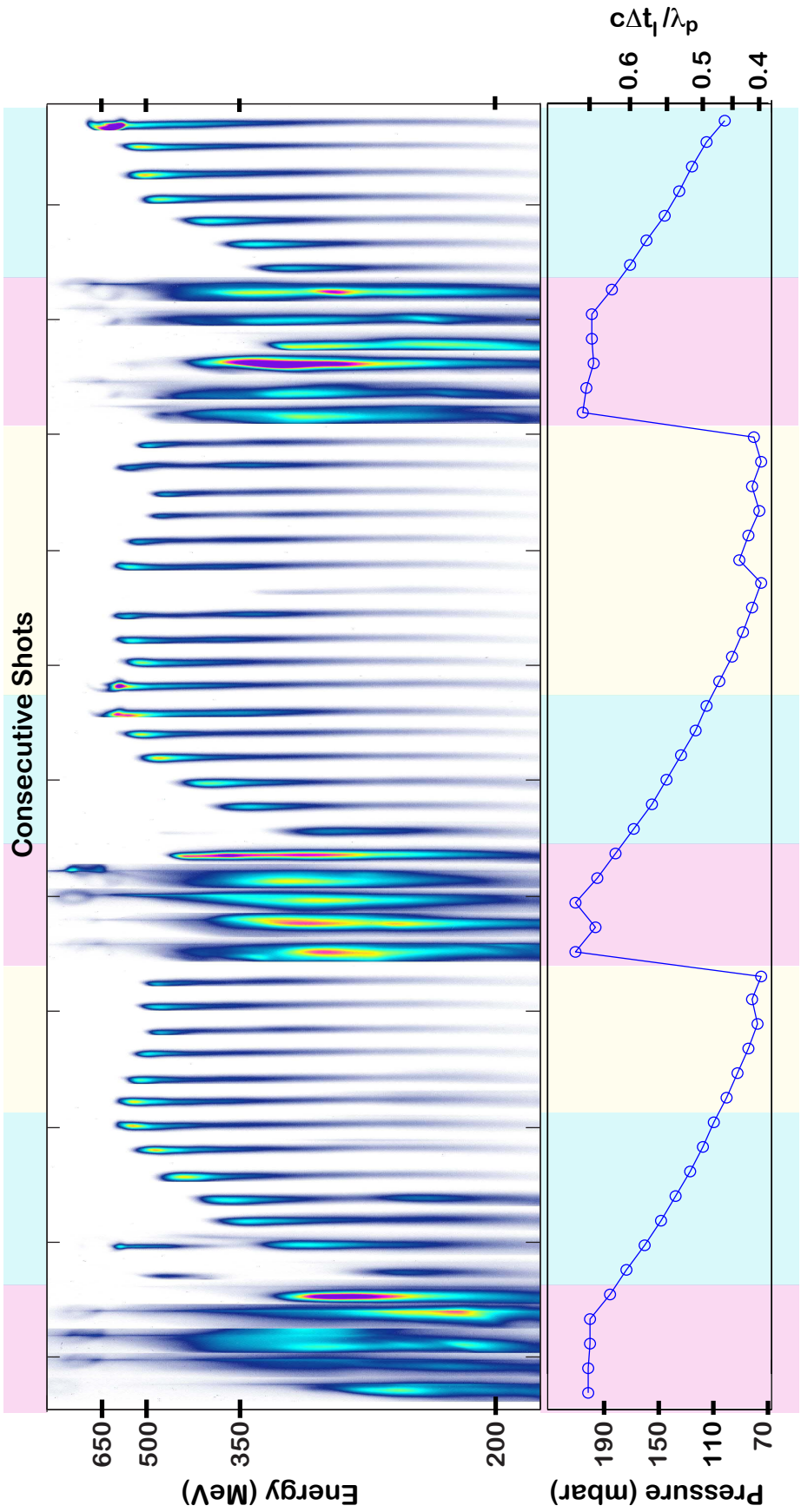

Figure VI.12.: *Pressure scan with consecutive shots at different pressures. The gas cell length is* 12 mm *for all shots. Plotted is the electron signal on a scintillating screen behind a dipole magnet. The lower plot shows the respective pressure for each shot in the upper graph. The right axis on the pressure plot gives the ratio between laser pulse duration and plasma wavelength, illustrating which fraction of the bubble is roughly occupied by the laser pulse.*

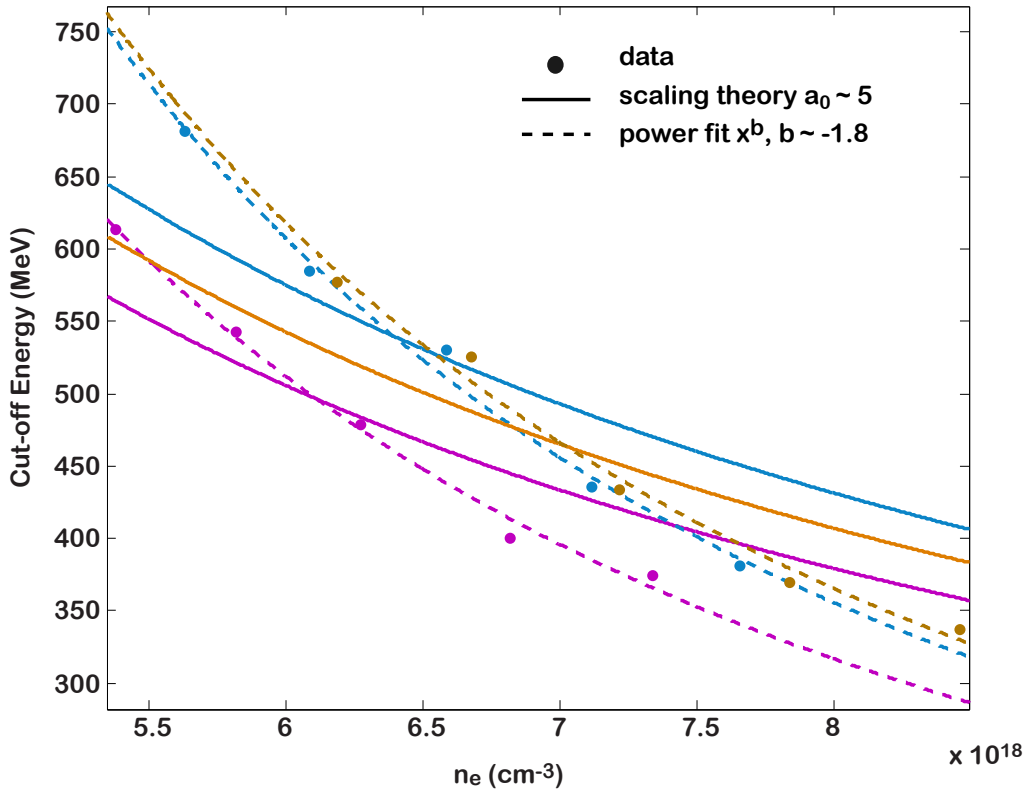

Figure VI.13.: *Fit to the cut-off energy of the shots highlighted in blue in figure VI.12. The three different colors correspond to the three blue regions. The solid line is a fit curve that assumes the validity of formula* (III.62) *and has* a_0 *as free parameter. For the dashed line a power law* ax^b *was assumed.*

The next paragraph is to motivate that these high divergent electron bunches could be the result of direct interaction of the electrons with the ponderomotive potential of the laser pulse.

- As a first step on the way to a possible explanation the exact scaling of the energy cut-off in the blue region will be examined. Figure VI.13 shows fits to the cut-off energies of the those shots. If acceleration takes place exactly over the dephasing length the electron energy should scale proportional to n_e^{-1} (III.62). However, it can be seen, that the best fit to the data rather shows a $n_e^{-1.8}$ dependence. This is best explained by the same argument as in the 130 mbar case above. Even beyond the dephasing length the laser has enough energy to drive a wakefield and the electrons are ”decelerated” again in the long gas cell. So the measured energy in this scan is not the maximum energy that the electrons have reached at the dephasing point, but an energy that has been strongly reduced again in the still existent wakefield. This is equivalent to the second (falling) part of the 130 mbar curve in figure VI.8. In a next step one has to keep in mind that for highly relativistic electrons the term ”deceleration” is actually misleading, as losing energy does not mean that the velocity is notably reduced. Even if the electron bunch sits in the ”decelerating” phase and

constantly loses energy, it still propagates with almost c and eventually catches up with the laser pulse ($v_{gr} < c$). This is of course only possible because the electron has been trapped already with an initial longitudinal momentum and the accelerating and decelerating fields are not exactly symmetrical. The first assumption must be true as only those electrons can be trapped at all. The second assumption is reasonable especially as the wakefield evolves during the acceleration process when the laser intensity decreases and beam loading effects occur.

- The aforementioned fit suggests that there is still a reasonably energetic laser pulse even far beyond the dephasing length. Especially, for high pressures (small bubble size compared to laser pulse length, see right scale on the lower plot in fig. VI.12) this means that the trapped electron bunch can end up in direct interaction with the electro-magnetic field of the laser pulse. There are simulations [107] and measurements [136] demonstrating that the divergence of the electron bunch is increased in the direction of the laser polarization when the electrons inside the bubble interact with the tail of the laser pulse. The electrons are wiggled by the electric field and their momentum in that plane grows. As they still sit within the focusing fields of the bubble the amplitude of the betatron oscillations in laser polarization direction increases and the oscillations are resonantly driven with the laser frequency [107].

- In the presented measurement the polarization axis of the laser is oriented along the dispersion direction of the dipole magnet. Thus, a larger divergence in this direction increases the perceived energy spread in the spectrum. This can be observed for the shots in the pink region, although a real growth in energy spread (also note comment below) can not be excluded, as the divergence in that direction cannot be measured independently[5]. Simultaneously, the width of the electron signal in transverse direction is significantly increased. In this direction the non-dispersed electron profile is observed and thus the pure divergence in the direction perpendicular to the laser polarization. A modulation along this axis cannot be induced directly by the electric field of the laser. But the ponderomotive potential of the laser pulse exhibits a force that acts along the intensity gradients and thus can ”displace” electrons in all directions, i.e. expel electrons in both transverse direction from the high intensity regions and longitudinally accelerate (decelerate) electrons along the temporal envelope of the pulse. That would both increase the energy spread of the electron bunch and the divergence in both spatial directions.

- Assuming that for the shots highlighted in pink the trapped electron bunch has caught up with the main part of the laser pulse thus explains the increased divergence in both directions and an increased energy spread, but can also explain the electron traces at high energies ($\geq$ 650 MeV). As can be seen in the phase-space plot for electrons in laser-driven wakefields (fig. III.3) there exist trajectories, that allow electrons to even overtake the laser pulse. Li et al. [137] show in simulations that electrons can be accelerated by direct laser acceleration (DLA) in the rising edge of an intense laser pulse. The energy transfer is most efficient if the electrons

[5]This will be further investigated in a future measurement by rotating the polarization direction.

are highly relativistic as they then stay in phase with the laser pulse for a long time. In their simulations Li et al. [137] use a very intense ($1.37 \cdot 10^{22}$ Wcm^{-2}) laser pulse and obtain electrons at an energy of almost 3 GeV. The high intensity is necessary to initially accelerate background electrons to relativistic energies very violently, so they get synchronized with the rising edge of the laser pulse and can get further accelerated. In our case the considered electrons already possess highly relativistic energies as they were "pre-accelerated" in the laser-driven wakefield. Therefore it is plausible that even our lower laser intensities could lead to a measurable increase of electron energy by direct laser acceleration. Furthermore, in our case, the ponderomotive force in the front part of the laser pulse is enhanced during the long propagation through plasma as the rising edge is steepened (e.g. [73]) due to self-phase modulation and etching. Li et al. [137] also show that the electron density of the directly accelerated bunch peaks at axial-symmetric off-axis positions with an opening angle that depends on the ratio of the longitudinal and transverse ponderomotive force. Such a ring-like structure can also be noted in the respective shots of the presented pressure scan. Of course, this is one assumption of what is happening in the high density region that has to be confirmed by further experiments.

- In another interpretation one could argue, that the high-energy electron signal comes from particle beam driven wakefield acceleration (PWFA). If the laser-wakefield accelerated electron beam is strongly dephased it will drive its own wakefield. It is possible to either trap new electrons via wavebreaking or accelerate the tail of the driving electron bunch, provided that it reaches into the rear (accelerating) phase of the wakefield. Since in the beam driven case the concept of dephasing does not exist, the trapped electrons in principle can be accelerated to very high energies. However, this explanation does not include the ring-structure seen in many of the high-energy parts of the signals. Also PWFA alone cannot explain the sudden increase in divergence of the main bunch.

VI.1.5.2 Conclusion

The presented experiments show that with a relatively simple tool, the variable-length gas cell, different laser-wakefield regimes can be accessed with the available laser parameters. These regimes can be well characterized and the acceleration process can be optimized for maximum electron energies. The gas cell length scan and the pressure scan demonstrate that in our case at low pressures acceleration is limited by insufficient self-focusing. In order to reach higher electron energies an external guiding channel is necessary. For our laser parameters this is the case below $\approx$ 100 mbar $\equiv 4.8 \cdot 10^{18}$ cm^{-3} (fig. VI.12). At high pressures self-guiding can be sustained over longer distances ($> L_{deph}$) with lower laser powers, but the energy depletion rate of the driver pulse increases. Still a wakefield can be driven over more than the dephasing length (see paragraph III.2.4.4). The electrons are even decelerated again in the wakefield. This and also the evolving shape of the energy spectrum highlight the necessity of a well adapted gas cell length.
The maximum accelerating field in the bubble could be estimated to $\approx$ 160 GV/m for a plasma density of $n_e = 6.42 \cdot 10^{18}$ cm^{-3} (130 mbar) and the corresponding dephasing

length to 4.9 mm, which is in good agreement with theoretical predictions.
While plasma-length scans have been performed by other groups, e.g. [1], to the best of the author's knowledge, this is the first comprehensive scan that covers a wide range of lengths, even beyond the dephasing length. In combination with the meaningful statistics of this measurement this allows for a reliable determination of acceleration parameters.
Especially in combination with further sophisticated diagnostics the variable length gas cell will contribute to a better understanding of the acceleration dynamics. Two follow-up experiments were already mentioned. In a measurement with the transition radiation diagnostics described in section V.6, a decrease of the electron bunch durations with the acceleration length was observed [4, 138]. Possible interpretations of this result have yet to be evaluated. For a gas cell length beyond $\approx$ 10 mm on the interference signal of two or even three electron bunches can be observed. In the second experiment it was shown that the emittance of the electron bunch during the acceleration process is conserved [104].
In further experiments it will be equally interesting to analyze the evolution of the transmitted laser pulse. It should be possible to directly observe e.g. the self-focusing length or the progress of self-compression. Unfortunately, the longitudinal resolution will be restricted by the large Rayleigh length of the laser beam.

The pressure scan at fixed gas cell length supports the findings of the length scan concerning depletion and diffraction of the laser. For high pressures and therefore short dephasing lengths the spectral and spatial shape of the electron bunch changes significantly. This might be explained by interaction of the pre-accelerated electron bunch with the laser pulse and direct laser acceleration of a small part of the electrons. The confirmation of this interpretation will be the subject of further investigations.

One problem of the gas cell design is that a gas "plume" at the entrance/exit holes is unavoidable, as can be seen in figure V.6(d). If there is a long density up-ramp in a region before the geometrical focus the laser will start self-focusing and, if the intensity is too high, potentially break up into several filaments [64, 65] before the bubble regime is reached, thus reducing the stability and reproducibility of the acceleration process. The "soft" focusing used in the experiment probably inhibits strong filamentation in the density up-ramp since the gas plume was shorter than the Rayleigh length, preventing a strong change in beam shape over the density ramp[6]. But at the same time, with these laser parameters self-focusing occurs until the blowout-regime is reached. The simulations discussed in the next section suggest that injection into a wakefield already sets in in the rising edge of the density profile and while the laser spot size is still decreasing. Both continuously varying plasma wavelength and laser beam size change the wakefield shape and injection dynamics.
For optimized electron bunch characteristics it might be advantageous to work with a parameter set that is matched from the beginning. A 1 m focal length setup will lead to to focal spot size of $w_0 = 12.44\ \mu$m, an a_0 of roughly 3.5 (depending on the exact energy available on target). With a backup pressure around 60 mbar $\equiv 3 \cdot 10^{18}$ cm^{-3}, the requirements for complete blowout, self-injection and sufficiently long self-guiding according to

[6] Filamentation only occurs for non-Gaussian near-field profiles, as they are present in a real laser pulse.

run	n_e (10^{18} cm^{-3})	z_1 (mm)	z_2 (mm)	z_3 (mm)	z_4 (mm)
*A*100	5	0	1	2.83	3.73
*A*100(100*mbar*)	4.83	0	4.54	10.3	10.8
*A*100(120*mbar*)	5.80	0	4.54	10.3	10.8
*A*100(150*mbar*)	7.25	0	4.54	10.3	10.8

Table VI.3.: *Simulation parameters. z_{1-4} are the supporting points of the density profile. The laser focus is at z_2. Between z_2 and z_3 the density is constant as given in the second column.*

[58] are approximately met. In this case no prior self-focusing should occur.

VI.2. Simulations of Near-Experimental Parameters

In order to get a better understanding of the acceleration regime that is entered with the available experimental parameter space, several full-scale 3D PIC-simulations were carried out. However, due to the extremely high computational requirements of these simulations, not all parameter combinations can be scanned comprehensively and independently. Currently, only the four simulations shown in table VI.3 with slightly optimistic laser parameters are available. All simulation parameters, including e.g. resolution and box size are listed in appendix C).

In all four simulations the laser pulse has a pulse duration of $\Delta t = 20$ fs, an energy of 1.8 J and is focused to a spot size of $\Delta x = 22\ \mu$m, which results in a normalized vector potential of $a_0 = 2.71$. The longitudinal density profile has a rising edge between $z_1 - z_2$, a plateau between z_2 and z_3 and a linear density roll-off between $z_3 - z_4$. The geometrical focus always lies at z_2. In the first run of the list, *A*100, the profile is trapezoidal. In the other three runs the profile between z_1 and z_2 is taken from the *OpenFoam* density simulation of the gas cell (see fig. V.6). The density profile in the pink area of figure V.6(d) was used as input for the PIC-simulation.

VI.2.1 Self-Focusing

Judging from the initial laser power that lies well above the critical power for self-focusing the laser spot size during a large part of the acceleration process will be smaller than initially and the a_0 correspondingly larger. The calculation summarized in table V.1 already gave a rough idea about the final parameters. But the self-focusing behavior can also be extracted from the simulations, where the density up-ramp in front of the gas-cell is included.

Figure VI.14 shows the evolution of the laser spot size in two different simulations (*A*100 and *A*100(120*mbar*)). In figure VI.14(a) the geometrical focus lies at the end of a 1 mm-long density up-ramp, with a final pressure of 100 mbar. In figure VI.14(b) the longitudinal position of the Gaussian beam focus is $z = 4.54$ mm and the pressure increases from 0 to 120 mbar within these first 4.54 mm. The pink line in both pictures gives the calculated

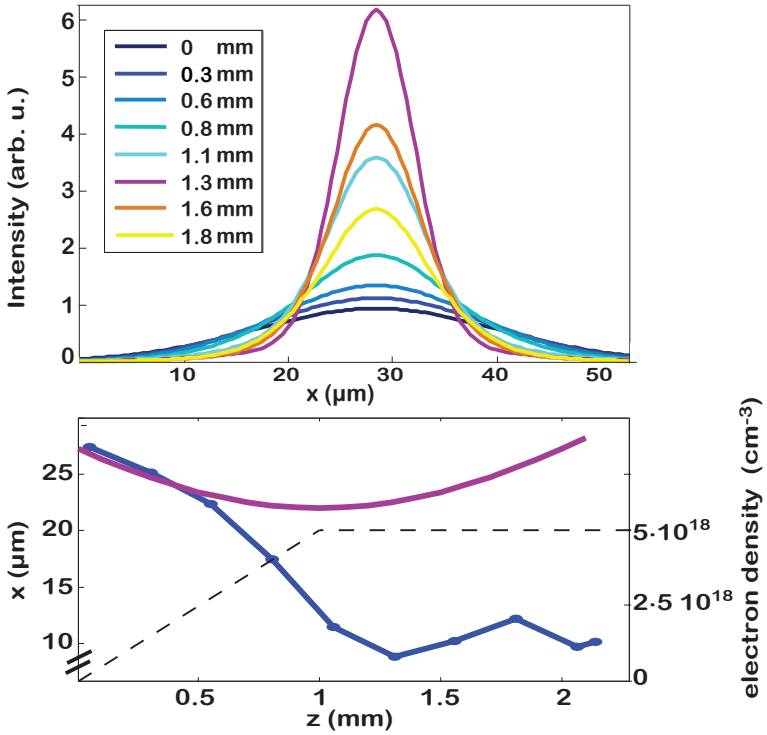

(a) *A*100. The upper picture shows the intensity envelope (from the PIC-simulation) at different longitudinal positions during self-focusing, the lower picture shows the evolution of the FWHM spot size.

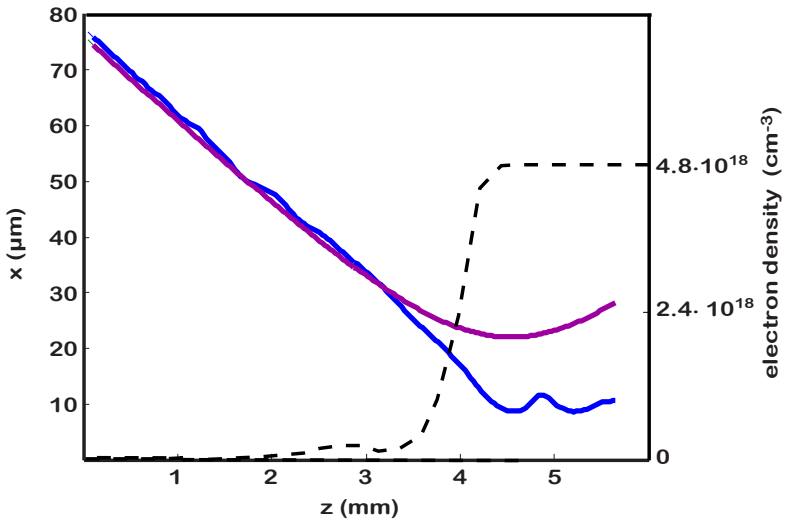

(b) *A*100(120*mbar*), density up-ramp from *OpenFoam* simulation

Figure VI.14.: *Laser spot size evolution during self-focusing. The pink curves in the x-versus-z plots show the calculated evolution of the FWHM focal spot size (Δx) for a Gaussian beam in vacuum with a beam waist of $\Delta x = 22$ µm. The corresponding blue curves depict the evolution in plasma as extracted from PIC-simulations. The dashed lines (right axis) illustrate the longitudinal electron density profile.*

evolution of the focal spot size of a Gaussian beam in vacuum. The small deviation in size between simulation and calculation in the beginning is due to the additional electric field of the plasma that cannot be separated from the laser field in the simulation.
Similar to the calculation, also the simulation shows that the final focal size is reduced by roughly a factor of two compared to the vacuum beam size. Self-focusing starts in the rising edge of the density profile and later on the spot size oscillates during propagation.

VI.2.2 Evolution of the Electron Energy

Figure VI.15(a) shows the evolution of the charge distribution for two different electron densities (corresponding to 100 and 150 mbar backing pressure in the experiment, respectively). Each sub-picture shows the spatial density distribution at one time-step in the frame co-moving at the vacuum speed of light c (cf. appendix B). However, as in the simulation code *OSIRIS* spatial and temporal coordinates are normalized to the plasma-frequency, the n-th time step of simulations with different densities does not show the same progress in the spatial evolution. The connection lines indicate identical longitudinal positions. Figure VI.15(b) shows the corresponding longitudinal phase space. Due to the different velocities of the simulation box (c) and the laser pulse ($v_{gr} < c$), the laser pulse including the trailing bubble slips back in the simulation frame. It is obvious that after the point in time where the injection center leaves the simulation box the simulation becomes unphysical. However, the evolution of the laser pulse and the front part of the electron bunch can still be considered correct as influences from rear electrons are negligible.

In both runs, electrons are injected continuously, thus leading to heavy beamloading effects (section III.4). The blowout region strongly elongates and is also transversely deformed. The electric field of the injected electron bunch deteriorates the accelerating electric field of the bubble. This and the fact that due to the continuous injection all electrons see different phases of the accelerating field, in principle, leads to a broad energy distribution within the electron bunch and consequently no or a very broad energy peak.
It should also be noted that injection starts at a longitudinal position slightly before the electron density plateau, where the laser spot size still decreases. The changing driver size and intensity in the beginning, leading to a different blowout radius, and the varying plasma wavelength further modifies the injection progress.

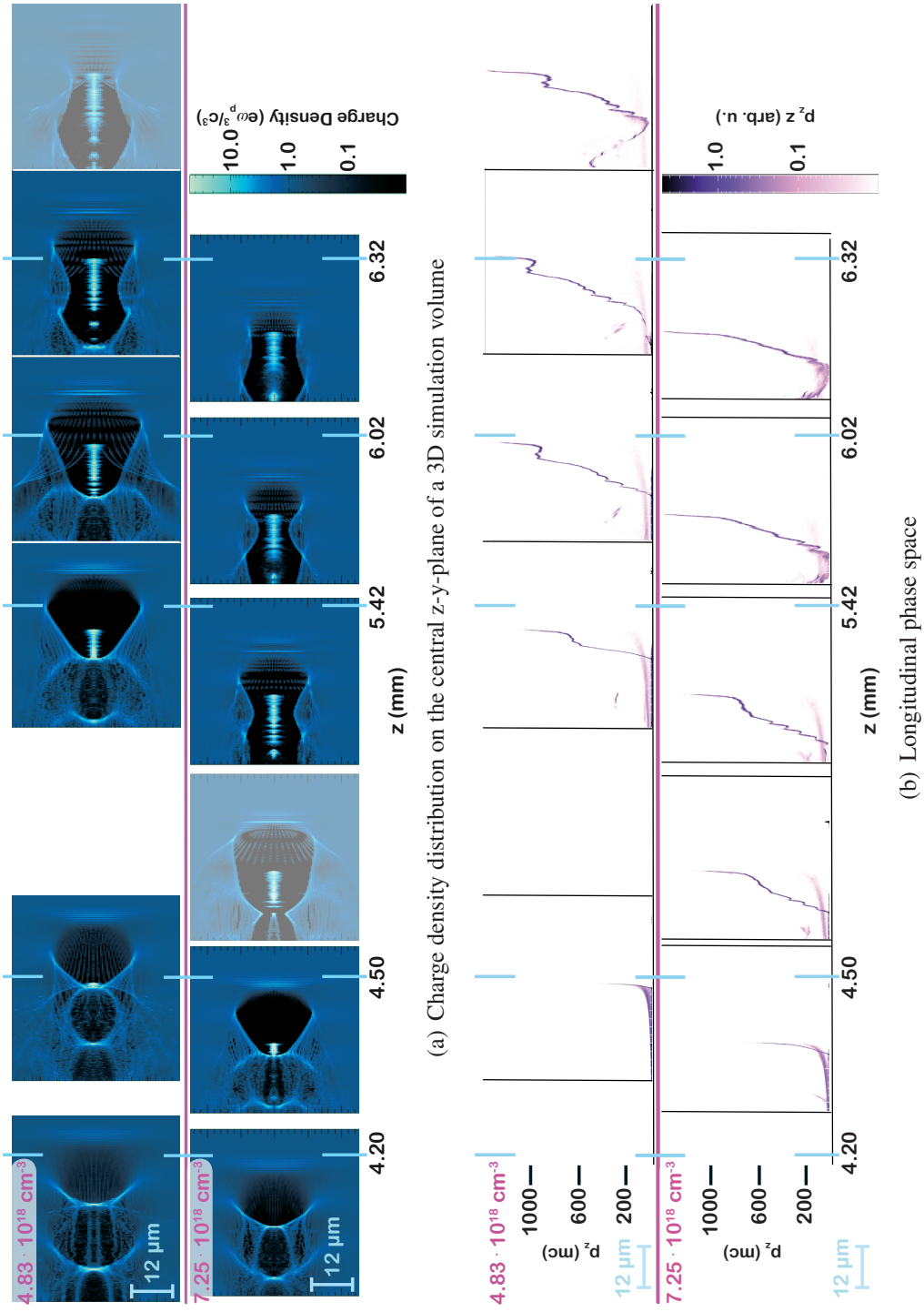

(a) Charge density distribution on the central z-y-plane of a 3D simulation volume

(b) Longitudinal phase space

Figure VI.15: *Charge density and phase space evolution at* 100 *and* 150 mbar.

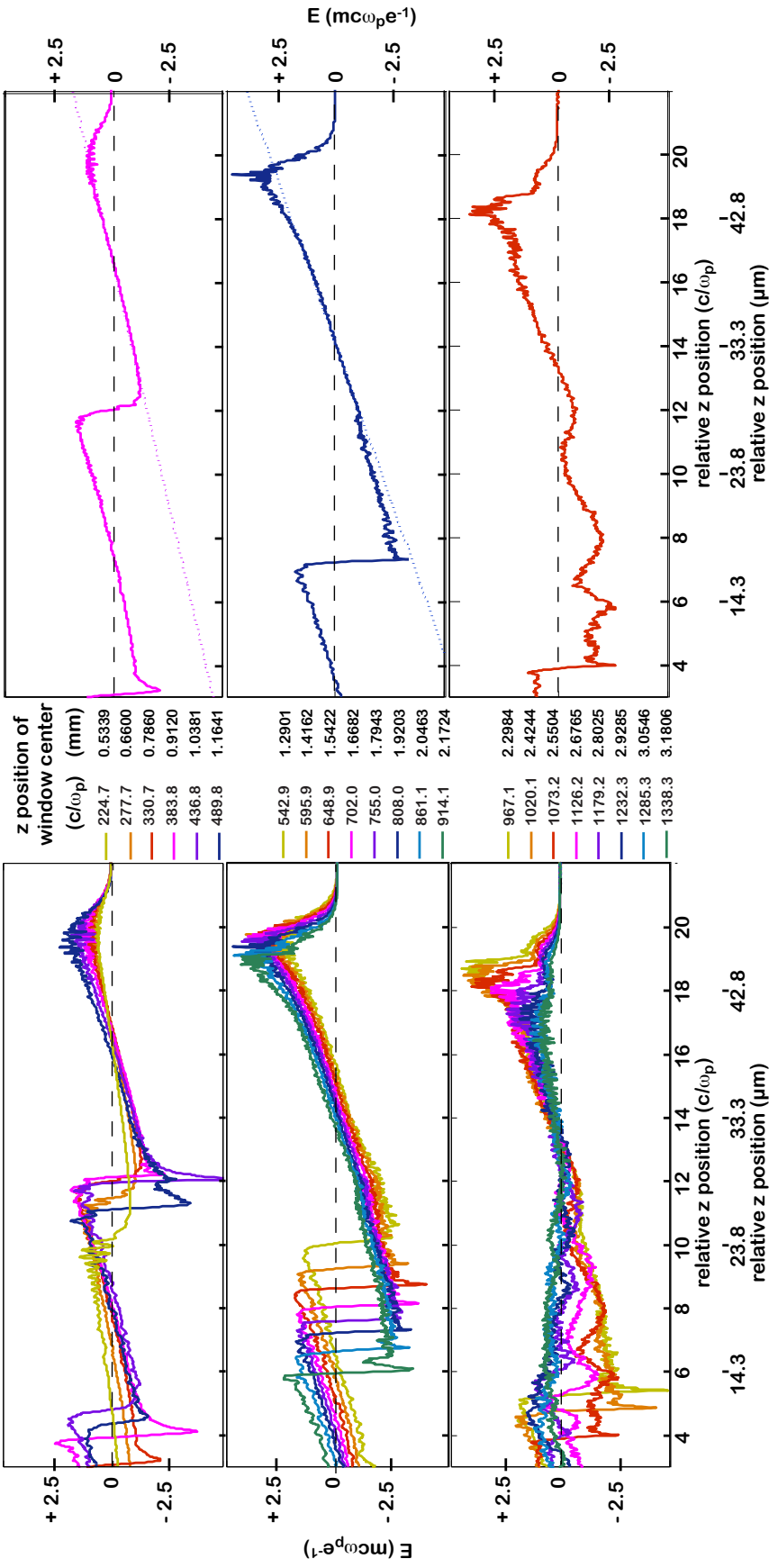

Figure VI.16.: *Longitudinal electric field strength on the central axis of the 3D simulation volume at different time steps (simulation window positions).*

Figure VI.16 shows central line-outs through the longitudinal electric field at subsequent time steps of the *ATLAS100*-run (focal position at $z_2 = 1$ mm, $n_e = 5 \cdot 10^{18}$ cm^{-3})[7]. The plots are loosely grouped into three rough regimes (left column, the right column shows one representative field shape of the respective group). In the first (top) picture a non-linear wakefield evolves and injection starts. The second picture documents the elongation of the blowout region due to beamloading, but the total field within the blowout region is still linear and locally undisturbed. The common feature of the line-outs in the bottom picture are the strong, local modulation of the longitudinal field caused by the intense superimposed field of the trapped electron bunch. As simultaneously the intensity of the laser that drives the wakefield decreases, these beamloading effects dominate.

Figure VI.17 again shows one time step within this third regime. The spatially resolved longitudinal electric field is plotted in the top frame, the respective line-out in the bottom frame. The small inset shows the spatial electron distribution of corresponding electron bunch at the correct longitudinal position, color-coded is the energy of the respective macro-particle from the PIC-simulation. It can be seen, that at this late evolution state the electric field along the entire bunch is positive, i.e. decelerating, but with longitudinally fluctuating strength. As a consequence at this time the entire bunch is decelerated, no "classical" dephasing and subsequent spectral peaking is observed. The local field strength variations lead to minor modulations of the spectrum.

The complete evolution of the energy spectrum is plotted in figure VI.18. The spectrally resolved electron density in the injected bunch ($\gamma > 40$) is shown at densely sampled time-steps (propagation distances) for the different simulation runs. The evolution of the two similar cases of *ATLAS100* (1 mm linear up-ramp) and *ATLAS100(100mbar)* (4.5 mm up-ramp from *OpenFoam* simulation) is plotted to illustrate that the exact length and shape of the density up-ramp does not significantly influence the acceleration dynamics.

It can be clearly seen that new electrons are injected along the entire propagation distance of the bubble. However, the injected electron density varies with time, as the space charge of a trapped electron bunch sitting close to the injection point inhibits further injection until it has propagated far enough towards the bubble center. In figures VI.18(a) and VI.18(b) this causes the distinct stripes. These electrons have different initial momenta and longitudinal injection points and see different acceleration fields, as the field strength locally varies due to beamloading. These trajectories can cross after some propagation and form a spectral peak. The same effect can be observed from a different point of view in the picture series of the longitudinal phase space (fig. VI.15(b)). The injected electrons are spread out in space and have a different longitudinal momentum along the bunch, as they have been accelerated over a different distances depending on their injection time. Only if the slope of the accelerating electric field balances this trend, i.e. faster electrons in the head of the bunch are less accelerated than slower electrons sitting in the tail, a spectral peak can occur (corresponding to a horizontal line in the phase spaces pictures)[8].

[7] Only for this run the electric fields are available. However, the differences between the *ATLAS100* and the *ATLAS100(100mbar)* are negligible. This can also be seen in the spectral evolution in both cases (cf. fig. VI.18)

[8] Mehrling [139] tried to further improve the spectral bunching due to beamloading as seen in this run by tailoring the density profile during injections. But it is still not very practical to rely on this mechanism

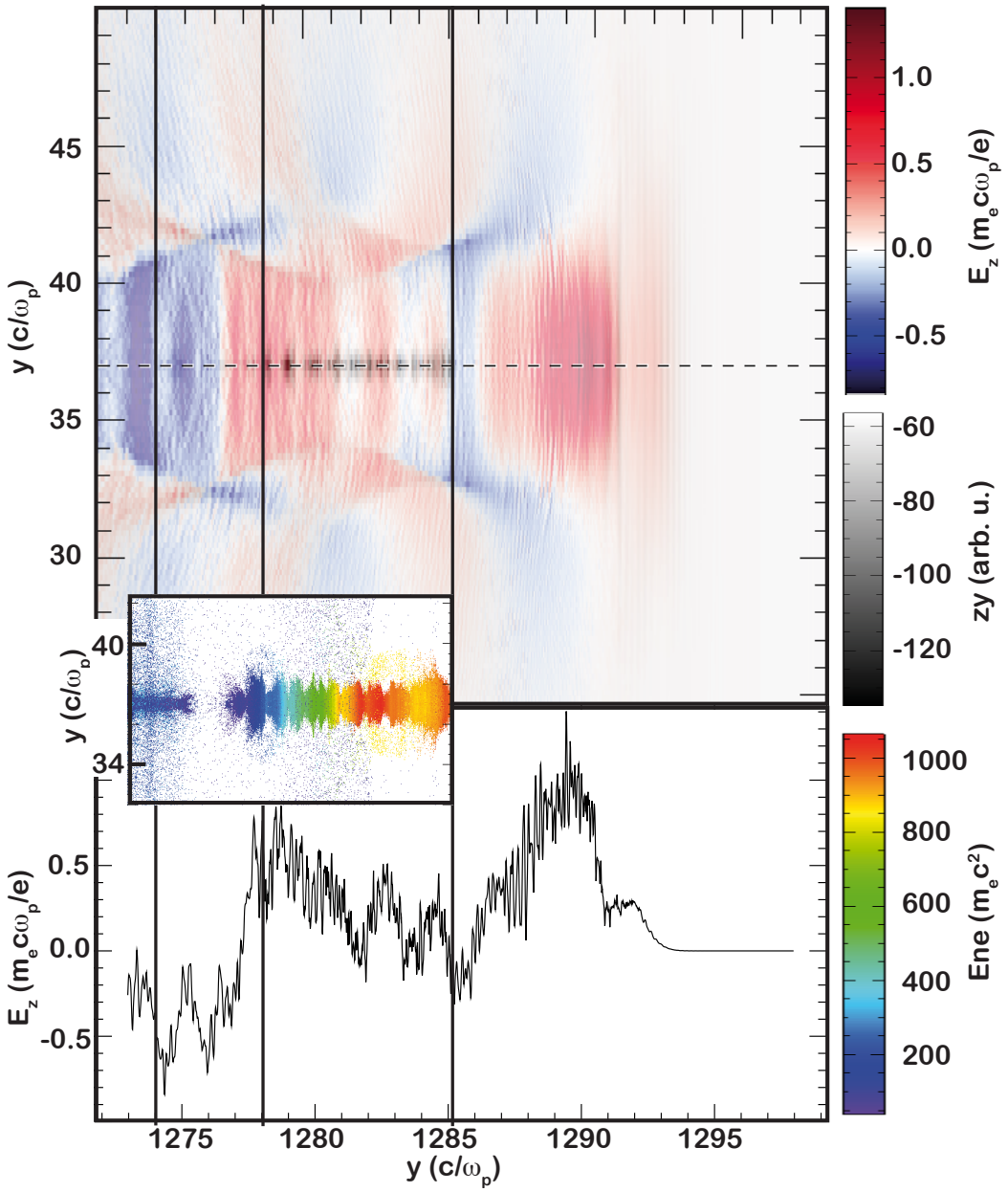

Figure VI.17.: *Longitudinal electric field inside the bubble upper plot: spatial density and field distribution, grey-scale=electron density, blue-white- red-scale=longitudinal electric field lower plot: line-out of E_z along the optical axis*
The inset shows the electron bunch at the correct longitudinal position. Here each dot represents a macro-particle from the PIC-simulation, all particles with $\gamma > 40$ are shown. The color encodes the respective electron (macro-particle) energy.

The same dynamics have also been observed in PIC simulations by [140], where spectral bunching also occurred before the dephasing point due to different accelerating fields for

as shape and position of this peak crucially depend on the initial conditions and the peak is quickly destroyed again during further propagation. Also it is not necessarily background free.

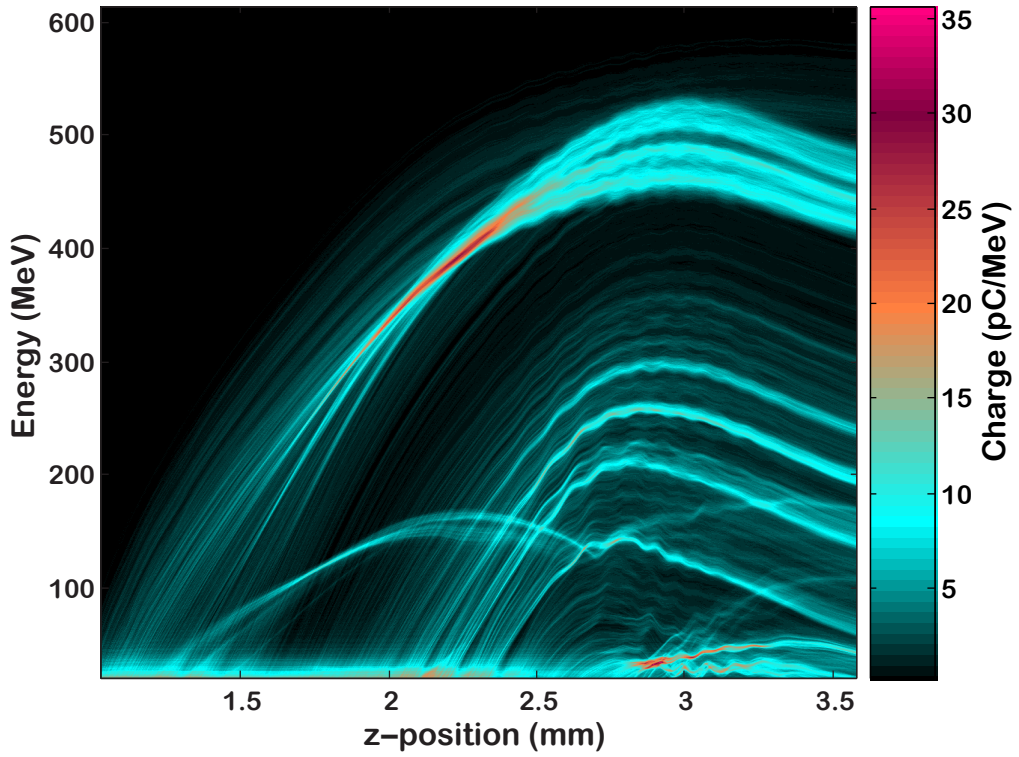

(a) *A100*, $z_2 = 1$ mm

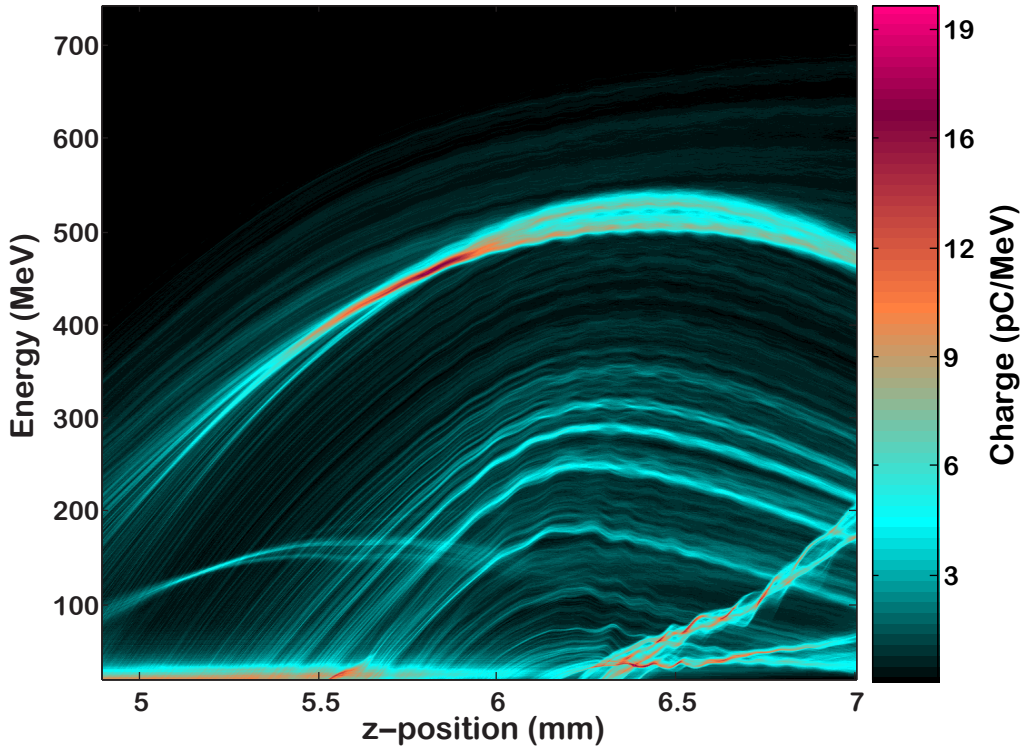

(b) *A100(100mbar)*, $z_2 = 4.54$ mm

Figure VI.18.: *Spectrally resolved evolution of the electron density in the injected bunch ($\gamma > 40$)*

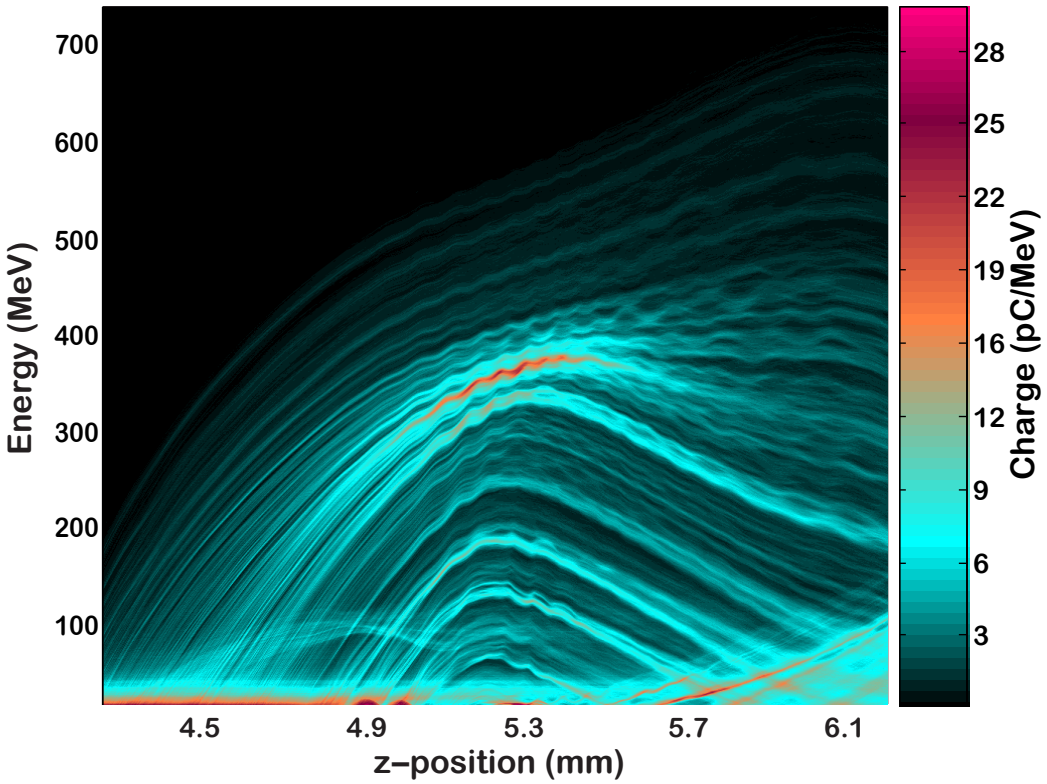

Figure VI.19.: *A100(150mbar), z_2 = 4.54 mm, spectrally resolved evolution of the electron density in the injected bunch ($\gamma > 40$)*

earlier/later trapped electrons.
This energy peak develops at a propagation distance of approximately 2.2 mm after injection in the PIC-runs conducted at a density of roughly $5 \cdot 10^{18}$ cm^{-3} (figs. VI.18(a), VI.18(b)). In this case the spectral bunching is not caused by dephasing, as the entire bunch still sits in the accelerating phase, but is only determined by electric field modulations due to beamloading. All electrons in the bunch are still accelerated but different parts of the bunch see different field strength. The occurrence of this peak is temporally extremely confined and the acceleration distance (i.e. length of the gas cell) must be adapted very accurately for its successful extraction. In figures VI.18(a), VI.18(b) shortly after the peak the spectrum spreads out again and approximately 0.8 mm further most parts of the bunch are uniformly decelerated, no significant additional spectral bunching, as would be expected at the undisturbed dephasing point, occurs. This corresponds to the case of figure VI.17, where due to laser depletion and beamloading effects, the electric field is positive and thus decelerating everywhere along the electron bunch.
In the simulation with the higher background electron density of $7.25 \cdot 10^1 8$ cm^{-3} VI.19 a less distinct peak forms with higher surrounding background. Beyond the peak position, the high energy part is further accelerated, lower energies are decelerated.
In all cases, the formation of the spectral peak is not determined by injection or dephasing, but by beamloading effects, that heavily distort the accelerating fields. Although the peak in the simulation exhibits desirable characteristics, such as low energy spread, the

peak energy	347 MeV
energy spread	16 MeV, 0.046%
charge	459 pC
RMS pulse duration	11 fs

Table VI.4.: *Parameters of the energy peak at* $z = 2$ mm *in the ATLAS100 run.*

process that leads to its generation is very unstable and hardly controllable. Furthermore the plasma length has to be adopted very accurately, in order to extract the bunch at the wanted evolution stage.
Table VI.4 gives the result of a quantitative evaluation of the spectral peak at $z = 2$ mm in the *ATLAS100* run. The charge contained only in the peak is more than 20 times higher than in the spectral peak of the experimental measurement[9]. In the simulation the longitudinal extent (pulse duration) of the part of the electron bunch constituting the spectral peak is roughly twice the length determined experimentally. From a measurement with the bunch duration diagnostics described in section V.6 a bunch duration of ~ 5 fs was deduced ([4] and dissertation of M. Heigoldt). These discrepancies already indicate that the simulations strongly overestimate the trapped charge and thus heavily suffer beamloading-induced distortions.

VI.3. Comparability of Simulation and Experiment

While some results are similar in simulation (section VI.2) and experiment (section VI.1), it is obvious that major features of the acceleration dynamics differ strongly.
One aspect that is well modeled by the simulation is the maximum electron energy of 350 MeV (sim) vs. 380 MeV (exp). Furthermore the simulations predict a regime where electrons are continuously trapped. From the high background in the experimental electron spectra it can be concluded that there the injection is continuous as well. The simulation shows that a plasma wave is driven already during self-focusing in the density up-ramp and injection into the wakefield starts before the minimum laser spot size is reached. During further acceleration the spot size oscillates (cf. fig. VI.14). The, especially in the beginning, strongly varying focal size influences the injection dynamics. This effect is enhanced by the changing plasma wavelength in the rising edge of the density profile.
However, not all elements of the simulation can be found in the experiment. Especially, the amount of trapped charge and its effects on the wakefield structure seems to be overestimated in the simulations. The bunch charge of > 450 pC is more than 10 times the

[9] The total bunch charge can not be compared since in the simulation the injection center at the rear of the bubble leaves the simulation box before the acceleration ends. This does not influence the characteristics of the spectral peak sitting in the front of the trapped bunch, but the total bunch charge is underestimated. Still, the peak in the simulation contains roughly 10 times the charge of the entire electron bunch in the experiment (above 100 MeV)

experimentally measured charge. In the simulation beamloading heavily distorts the electric field within the blowout region. Even before the head of the electron bunch can reach the zero-crossing of the electric field strength (dephasing) the entire electric field is deteriorated and decelerates the bunch as a whole. However, in the experiment the beamloading effects seem to be less severe. Electrons are accelerated (and even decelerated again) over a length that corresponds well to the theoretical dephasing length for this pressure. The spectral electron density peaks around the dephasing point, as one would expect if the head of the bunch is decelerated while the tail is still in the accelerating phase. The high-energy cut-off of the electron spectrum changes in good approximation quadratically with the propagation distance suggesting an undisturbed linear acceleration field.
Another difference is seen in the scale of the evolution: in the simulation the high-energy peak forms after only 2.2 mm of propagation, in the experiment it takes roughly twice this distance.

These discrepancies can be partially explained by the slightly differing parameters:
The duration of the driver pulse in the simulation is almost 30% shorter than in the experiment. According to (III.58) this will also decrease the energy depletion length by 30%. In the simulation the laser therefore is more intense in the beginning, thus driving a wakefield with a higher electric field. More electrons are trappped until the beamloading field cancels the electric field of the bubble (cf. sections III.4 and III.5.3 or e.g. [141]). At the same time it depletes faster than in the experiment, leading to an eventually weaker electric field facing the initial high amount of trapped charge. This can explain both the shorter acceleration length in the simulation and the strongly distorted electric field.
In the simulation a Gaussian spatial beam profile is assumed before the focus, while the real beam profile exhibits hot-spots and irregular intensity variations outside the Rayleigh range. The simulations show, that self-focusing already starts in the density up-ramp before the geometrical focus position. As well known from high-power laser systems in that case small-scale self-focusing can occur [142], where the pulse breaks into several filaments. It is not obvious whether this really could be completely avoided in the experiment by choosing a long focal length. M.D. Feit [66] claim that, if the power in these filaments is still above P_{cr} they will eventually coalesce and form a single (cavitated) channel that contains most of the initial beam power. Even if there is no filamentation, the final beam profile can be asymmetric or otherwise distorted from inhomogeneous self-focusing.

A large fraction of the differences between simulation and experiment, however, could result from numerical errors. Cormier-Michel et al. [143] state that ”[n]umerical errors can lead to errors in the macro-particle orbits in both phase and momentum. These errors [...] can be large enough to result in unphysical trapping in the plasma wake. The resulting numerical heating in intense short-pulse laser-plasma interactions grows much faster and to a higher level than the known numerical grid heating of an initially warm plasma in an undriven system.” This numerical heating is caused by the discretization of the fields and the small number of macro-particles (in our case 1 per cell). To a certain degree it can be reduced by appropriate smoothing and increasing the number of macro-particles, if computationally possible. Additionally, it must considered that the transverse size of

the trapped electron beam is small and only marginally resolved by the grid. According to Cowan et al. [144] this leads to artificial emittance growth. They also mention that a low transverse grid resolution results in wrong numerical dispersion leading to a too low group velocity of the laser pulse and thus too rapid dephasing.
Ideally, a warm plasma (few tens of eV) is initialized with both longitudinal and transverse resolutions of the same order and such that high that numerical heating is well below the physical temperature. However, with conventional PIC codes, this is not possible with the currently available computational power. With the availability of Lorentz-boosted-frame codes (e.g. [145]) and adaptive mesh refinement approaches (e.g. [146]) for laser-wakefield acceleration this kind of simulation will be easier in the future.

Chapter VII

Wakefields from Tilted Driver Pulses

The experiment described in this chapter is dedicated to the analysis of the impact of a laser pulse front tilt (PFT) or (equivalently) angular chirp (section II.1.4.2) on the accelerated electron bunch. The necessity to pay more attention to this laser parameter arose when, unexpectedly, in the experiment the electron pointing direction was stable but reproducibly deviated from the laser axis by a few mrad. This was especially problematic as further devices, such as magnetic lenses, an undulator and X-ray diagnostics, were carefully aligned to the laser axis. As this steering hinted to an asymmetry in the setup, several possible causes were analyzed and a non-vanishing PFT in the laser pulse was detected. After removing the PFT the electron bunch propagated along the laser axis again. These deviations in electron pointing could be observed only due to the excellent stability and reproducibility of the electron bunch parameters in a steady-state flow gas cell [18]. It, consequently, also allowed for a systematic study of laser-wakefield acceleration with a tilted driver pulse with meaningful statistics.

This comprehensive measurement with different intentionally introduced pulse front tilts will be described in this chapter. It is structured as follows: For a better understanding of the experimental problems and measurement results, first the basic characteristics and evolution of an angularly chirped laser pulse are analyzed. In the second section the measurement details and results will be shown. The last section supports the interpretation of the experiment by 3D PIC simulations.

VII.1. Characteristics of an Angularly Chirped Laser Pulse

The presence of an angular chirp in the near-field of an ultra-short pulse has important implications on the properties of the laser far-field during transition into focus. Using the Kostenbauder matrix formalism appendix E the evolution of an angularly chirped pulse was traced. An angularly chirped beam is focused by a 1.5 m-focal length curved mirror. Figure VII.1 shows the intensity envelope of the pulse ±3 mm ≈ ±5l_r around the focus for

the *ATLAS 25*-pulse with an angular chirp of 0.05 μrad/nm and without angular chirp. Figure VII.2 depicts the evolution of the corresponding pulse front tilt angle around the focus. The following observations can be made:

- Up to several Rayleigh lengths before the geometrical focus, the PFT angle increases, while the beam is focused down (fig. VII.2). This is mainly due to the fact that the transverse beam size is reduced, while the group delay difference between the two outermost parts of the beam stays constant (cf. (II.25)).
- Within several Rayleigh lengths around the focus, the PFT angle decreases, is zero in the focus, flips and further evolves in a point-symmetric fashion.
- The transverse and longitudinal (temporal) dimensions of the pulse in the focus are considerably increased if an angular chirp is present compared to the unchirped pulse (fig.VII.1), leading to a reduction in focused intensity.

The last two points are easily explained, if one considers that for an angularly chirped beam different laser wavelengths are incident onto the focusing optic under different angles. Different wavelengths will therefore be focused to different spatially separated focal spots, that all have the same (longitudinal) z-position but are next to each other in the transverse plane. In other words, the near-field angular chirp is converted to a spatial chirp in the far-field. This directly explains the absence of a pulse front tilt in the focus and the increase of the focal spot size in the chirp direction. In addition, the spatial wavelength separation locally reduces the spectral bandwidth of the pulse, which in turn leads to an increased pulse duration. This pulse lengthening due to the onset of the spatial chirp becomes significant a few Rayleigh lengths before the focus. This is also roughly the point where the pulse front tilt angle begins to decrease again.

The reduced spectral bandwidth σ'_ω and the enlarged transverse size w'_0 of the spatially chirped focal spot is given by (II.19) as a function of the bandwidth σ_ω and size w_0 of the unchirped pulse and the spatial chirp in the focus. Assuming that the pulse is transform-limited, the new pulse duration is then $\tau'_0 = 2/\sigma'_\omega$ (see section II.1.2). The focal intensity is reduced by a factor: $w_0\tau_0/(w'_0\tau'_0)$.

The spatial chirp ξ in the focus that is caused by an angular chirp in the collimated beam is given by

$$\xi = \frac{dx_0}{d\omega} = f \cdot \frac{dk_x}{d\omega} = f \cdot \frac{d\alpha}{d\lambda}\frac{\lambda_0}{c} \tag{VII.1}$$

where f is the focal length of the focusing optic (also cf. equations (II.21),(E.5) and section II.1.4.1) [1]. This correlation can be easily reconstructed by multiplying the Kostenbauder matrices for *reflection from a diffraction grating* and *focusing* and subsequently evaluating the matrix element E that describes the spatial chirp E.

[1] It must be noted, that for the implementation of the spatial chirp in the simulation code *OSIRIS* the wave vector is expanded: $k = k_0 + \kappa(x - x_0)$. That means, that the spatial chirp is given as $dk/dx \propto d\omega/dx = \upsilon$. This frequency gradient, however, is NOT simply the reciprocal of $\xi = dx_0/d\omega$, but also depends on the input pulse parameters w_0, σ_ω (see (II.18)). Due to this non-trivial relation it can even happen, that for certain input pulse parameters the spatial chirp (and ξ) increases, but υ decreases.

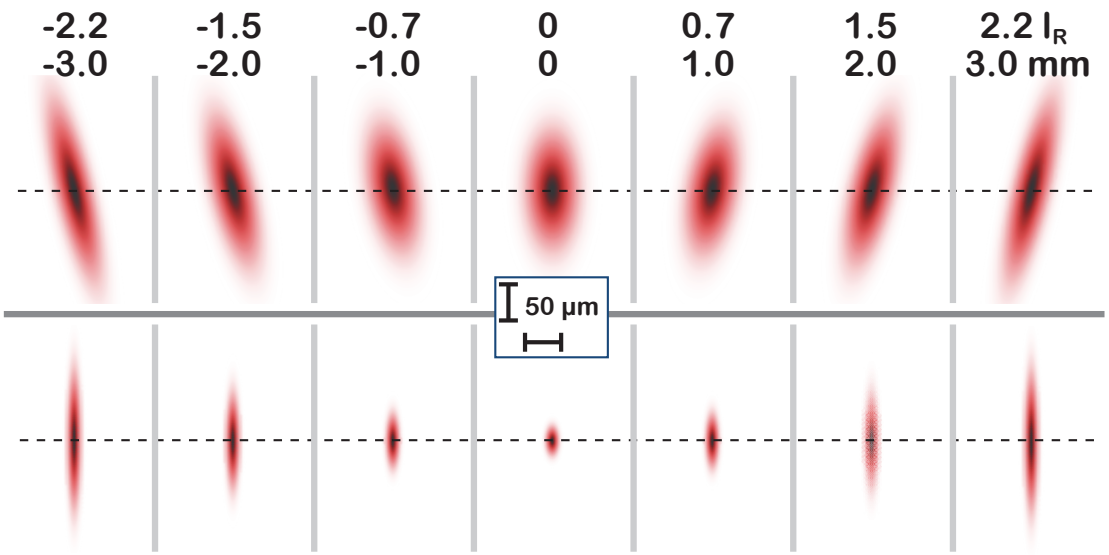

Figure VII.1.: *Evolution of the pulse intensity envelope around the focus for ATLAS parameters with an angular chirp of* 0.05 μrad/nm *(upper row) and without angular chirp (lower row).*

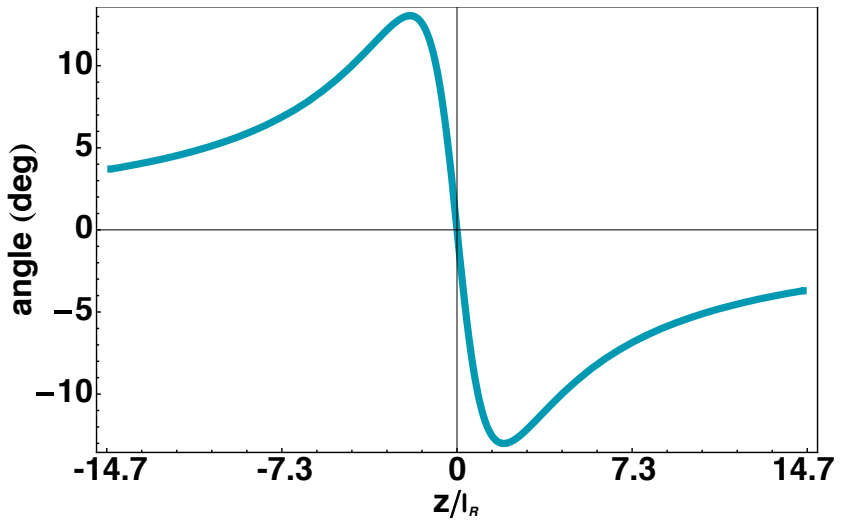

Figure VII.2.: *PFT angle evolution around the geometrical focus for ATLAS parameters and an angular chirp of* 0.05 μrad/nm

Focusing the *ATLAS 25*-beam with an angular chirp of 1 μrad/nm over $f = 1.5$ m results in an elliptical focus with only a factor of 1.15 between the major axis (in direction of the chirp) and the minor axis (unchirped direction). It is not possible to reliably infer the presence of this chirp just from observing the shape of the focal spot, due to other geometrical aberrations that might be present in the beam. As will be seen later, an angular chirp of that amount, noticeably influences the electron bunch characteristics. Hence, it is necessary to set up proper diagnostics for detecting and quantifying angular chirp/pulse front tilt in the laser pulse (see section VII.2.2).

It must be noted that the evolution of the pulse front tilt in plasma is different from the vacuum evolution. The index of refraction varies over the transverse pulse extent, as it is differently modulated by the pulse itself, depending on the local intensity. This even leads to a deviation of the laser pulse from the initial propagation axis, as will be seen in the simulations. Simultaneously, the pulse is usually self-guided beyond the Rayleigh length. The self-guiding characteristics will be altered by the presence of a PFT, but in any case, the pulse diffracts differently than in vacuum, which in turn changes the PFT evolution. The proper evolution is indicated by the PIC simulations described below.

VII.2. Experiment

In order to study the influence of a pulse front tilt in the driver laser on the acceleration process, different an angular chirps were intentionally introduced by rotating one of the compressor gratings. The amount of angular chirp was quantified with an spectrally resolved interferometer. Pointing and spectrum of the electron bunches that were accelerated with a tilted driver pulse were analyzed. The separate components of the setup and the measurement results will be characterized in this section.

VII.2.1 Setup and Measurement Procedure

The general experimental setup used for these measurements is detailed in chapter V. The gas target is the 15 mm-long sapphire capillary as illustrated in figure V.5(a) (also see [39]). It was filled with hydrogen at 155 mbar backing pressure corresponding to an electron density of $n_e = 7.7 \times 10^{18}$ cm^{-3}. Due to its evolutionary status at the time of the experiment, the driver laser, *ATLAS25*, delivered an energy of $\approx$ 850 mJ on target and a pulse duration of either $\Delta\tau \approx 37$ fs in a focal spot size of $\Delta x = 22$ μm. The shot-to-shot variations in laser energy were measured to be $\sim$ 2% RMS. Figure VII.3 displays the measurement geometry. For this experiment, the PFT is introduced in the plane parallel to the chamber floor and consequently deviations in electron pointing occur in this plane. Also the laser polarization axis lies in the same plane. The direction of energy dispersion in the electron spectrometer is oriented perpendicular to the chamber floor. The electron pointing was measured on a scintillating screen (S1 in figs. V.1,VII.3) that was situated 1.12 m behind the gas cell exit.

In order to systematically measure the influence of different angular chirps on the point-

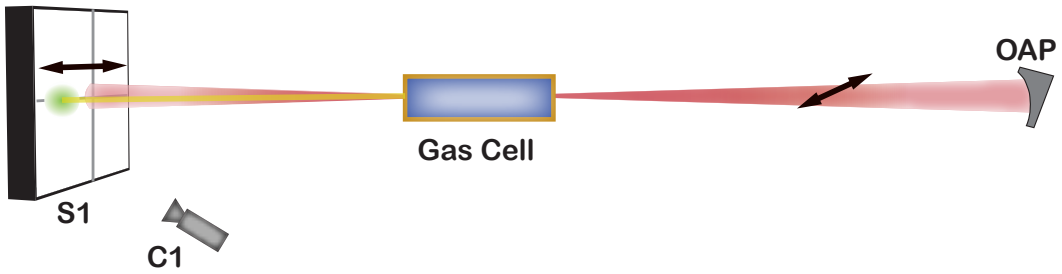

Figure VII.3.: *Scheme of the measurement geometry.*

ing of the wakefield-accelerated electrons the following steps were carried out for each angular chirp setting:

- The angular chirp was introduced by rotating one compressor grating in the *ATLAS*-laser around the axis parallel to the grooves (cf. figure II.6). The amount of angular chirp is related to the grating rotation angle ϵ by

$$\mathrm{d}\varphi/\mathrm{d}\lambda = 2\epsilon \tan\beta_0/(s\cos\beta(\omega_0)) \tag{VII.2}$$

  Here β_0 denotes the angle of incidence, $\beta(\omega_0)$ the reflection angle for the central frequency and s the groove density. For an angular chirp of up to 1.5 μrad/nm we thus had to detune the grating by up to 0.17 mrad.

- The beam path through the compressor was realigned by turning the compressor end mirror, such that the position and direction of the laser pulse out of the compressor was identical for all different measurement series. The alignment of the remaining beamline to and the way through the experimental chamber was checked as described in section V.5. Thereby it could be ensured that any pointing deviation of the electron beam measured on $S1$ was not due to a changed beam path of the laser after modifying the angular chirp.

- An acousto-optic spectral filtering device (*DAZZLER*) ([37, 38] and section II.2.1.2) was used to adapt the amount of dispersion in the amplifier chain to the misaligned compressor. Thereby the temporal chirp from the laser system could be removed. However, in the focus of an angularly chirped beam, due to the spatial separation of different frequencies, the bandwidth is reduced locally leading to an increased pulse duration compared to a pulse without angular chirp.

- The angular chirp was measured as described in section VII.2.2

- Electrons were accelerated under identical conditions except for the amount of pulse front tilt in the driver pulse and the consequences hereof as increased focal spot size, increased pulse duration and therefore reduced intensity. (Only for the highest measured angular chirp the pressure had to be increased slightly to maintain self-injection.)

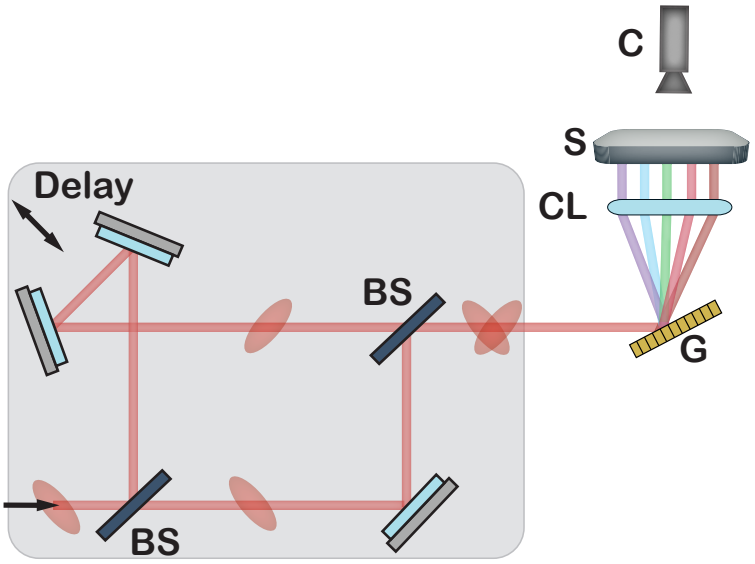

Figure VII.4.: *Spectrally Resolved Inverted Field Autocorrelator (SRI). BS: Beamsplitter, G: Grating, CL: Cylindrical Lens, S: Screen, C: Camera. Gray box: Inverted Field Autocorrelator (IFA).*

VII.2.2 Measuring the Pulse Front Tilt

A coarse, qualitative determination of a pulse front tilt can be done by means of an inverted field autocorrelator (IFA) [31]. The setup is shown in the gray shaded box of figure VII.4. An ultra-short collimated laser pulse with a pulse front tilt can be imagined as a pancake-shaped pulse that is tilted with respect to the propagation direction. It is sent into a Michelson interferometer, of which one arm includes a delay stage with two mirrors that flip the orientation of the pulse. When the two replicas are brought together again, interference fringes will only appear within a small stripe of the beam profile where the two oppositely tilted pulses cross. By changing the delay this stripe can be moved across the beam profile. The smaller the pulse front tilt, the wider this stripe. When interference fringes are observed across the entire beam profile, no pulse front tilt is present. For this method, the interference fringes should be oriented parallel to the PFT-plane.
In order to obtain a quantitative measurement of the pulse front tilt/angular chirp, the described inverted field interferometer can be complemented by a diffraction grating setup that spectrally resolves the fringes (SRI=spectrally resolved interferometer, figure VII.4)[31, 147]. For broadband pulses the interference fringes in an autocorrelator will blur. Spectrally resolving this interference pattern yields a fringe spacing that depends on $\Lambda = \lambda/\epsilon$, where ϵ is the angle between the two beams. Any deviation from that linear dependence is an indication of an angular chirp and thus a pulse front tilt in the beam.
Figure VII.5 shows the raw picture as seen by the camera C in the SRI setup on the screen S (cf. fig. VII.4). The interference fringes are spectrally resolved along the horizontal axis. From a Fourier transform along the vertical axis the fringe spacing Λ can be obtained for every wavelength. The spatial calibration for a quantitative analysis of this image is done by imaging a known spatial grid on the screen S. For the spectral calibration a thin

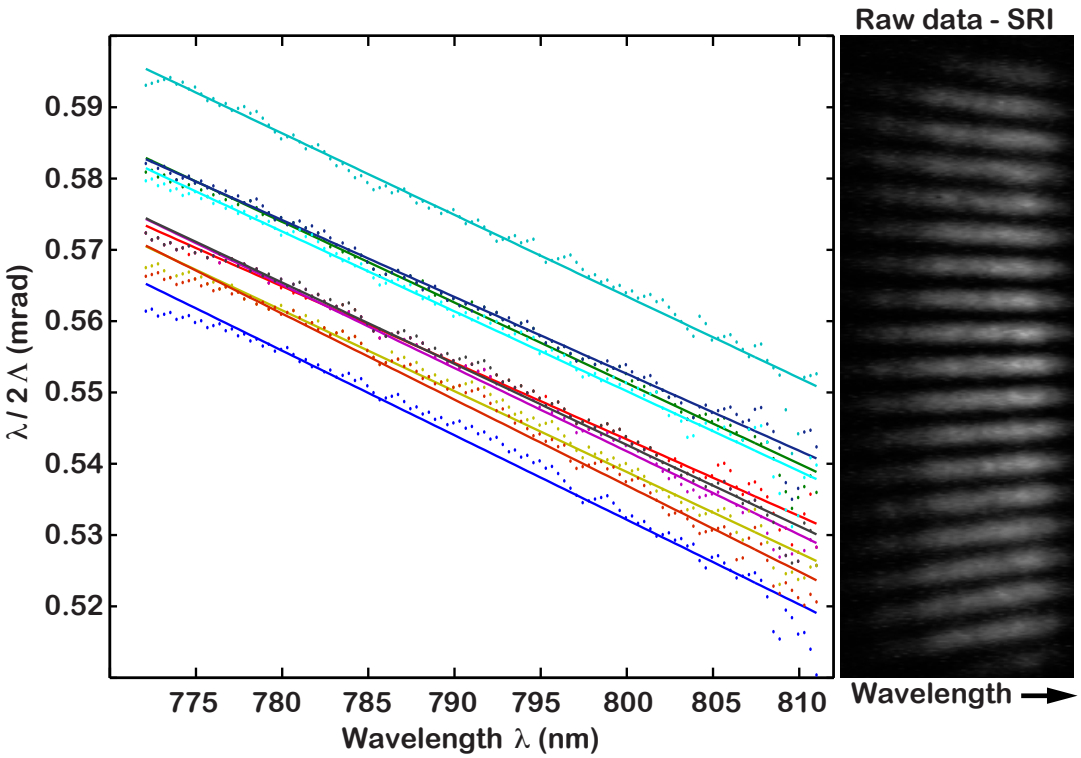

Figure VII.5.: *On the right a raw image is shown as it is seen on the screen S by the camera C of the SRI illustrated in figure VII.4.* Λ *is the fringe spacing as deduced from the raw image. The different colors represent the analysis of different subsequently taken pictures of the same angular chirp. The average slope in this case is* 1.1379 ± 0.054 μrad/nm. *The factor 2 in the scaling of the vertical axis comes from the fact that one interferometer arm is inverted and thus twice the angular chirp is measured.*

metal post was placed in the spectrally dispersed beam in the stretcher at subsequently three different positions. Observing the resulting spectral dip with a calibrated spectrometer and simultaneously on the screen in the SRI setup defines the spatial position of the respective wavelength. For the final evaluation the interference fringe width Λ is scaled with the wavelength as $\lambda/\Lambda(\lambda)$ and plotted versus the wavelength λ. An example is shown on the left in figure VII.5. In this plot zero angular chirp would give a horizontal line, a linear angular chirp will create a straight line, where the slope corresponds to the angular chirp. Due to the inversion of the one interferometer arm, twice the angular chirp is measured. Other than in the IFA, here the interference fringes must be perpendicular to the plane of the angular chirp.
The linear fit to the $\lambda/\Lambda(\lambda)$ versus λ -curve is the dominating error source (cf. [31]). For our setup it is given as ± 0.1 μrad/nm, considering error bars that include at least 50% of the data points. The measurement error calculated from the RMS deviation of 12 individual angular chirp measurements per compressor setting amounts to 0.05 μrad/nm.

The SRI method also delivers the correct result for the angular chirp if the pulse is temporally not fully compressed.

It should be noted that IFA measures the PFT, as the information is inferred from a signal variation at the position where the two inverted replica of the tilted pulse cross. This PFT can be caused by an angular chirp or by a combination of spatial and temporal chirp. The SRI directly measures the angular chirp, the PFT can be deduced from geometrical considerations. A PFT from spatial plus temporal chirp will not be detected by an SRI.

VII.2.3 Measurement Results

In the following the electron properties after acceleration with a tilted driver pulse are summarized as deduced from the scintillating screens S1 and S2 (see figure V.1).

VII.2.3.1 General electron properties

As described in [18], electron acceleration in the steady state flow gas cell is extremely stable and reproducible. Shot-to-shot pointing fluctuations are only 1.7 mrad RMS. This reproducibility in combination with an electron-injection rate of close to 100% allowed for the observation of small deviations in the pointing direction with meaningful statistics. The recorded spectra typically displayed a broad electron background with a quasi-monoenergetic feature with a high-energy cut-off at 170 ± 7 MeV RMS independent of PFT, similar to the results shown in [18][2]. However, for the largest measured PFT only those shots of the pointing distribution with lower angular deviations could be evaluated given the limited acceptance angle of the spectrometer. The accelerated charge above 100 MeV is 23 ± 6 pC RMS as deduced from the signal on the scintillating screen S2.

VII.2.3.2 Pointing Deviation

Figure VII.6 displays the detected electron pointing for different amounts of angular chirp. Both the respective peak positions (centroid) of a series of shots and their summed signal are shown. Clearly, the center of mass of the distribution shifts along the y-axis as a function of angular chirp. In all these measurements electron injection occurred at every shot for a background electron density of $7.7 \cdot 10^{18}$ cm^{-3} with the exception of the largest measured angular chirp of ~ 1.6 μrad/nm, for which the electron density had to be increased to $9.9 \cdot 10^{18}$ cm^{-3}. This was necessary in order to sustain a high trapping probability despite the reduction of laser intensity at focus due to the increase in angular chirp. For an angular chirp of 2.3 μrad/nm (corresponding to a reduction of a_0 by a factor of 1.8) and above no injection could be achieved. In $\sim$ 50% of all shots with angular chirp ≥ 1 μrad/nm two or more electron bunches were recorded simultaneously on the screen. Laser shots that produced two or more electron beams simultaneously were omitted from the analysis and are not shown in figure VII.6.
The bunch-pointing fluctuations increased from 1.7 mrad RMS at no angular chirp to 4.8 mrad RMS for the highest angular chirp value. This can be seen from the error bars in figure VII.6(b) which give the RMS pointing fluctuation over all shots for each angular

[2] In this experiment the laser power was lower than in the measurements described in the previous chapter. This explains the lower electron energies.

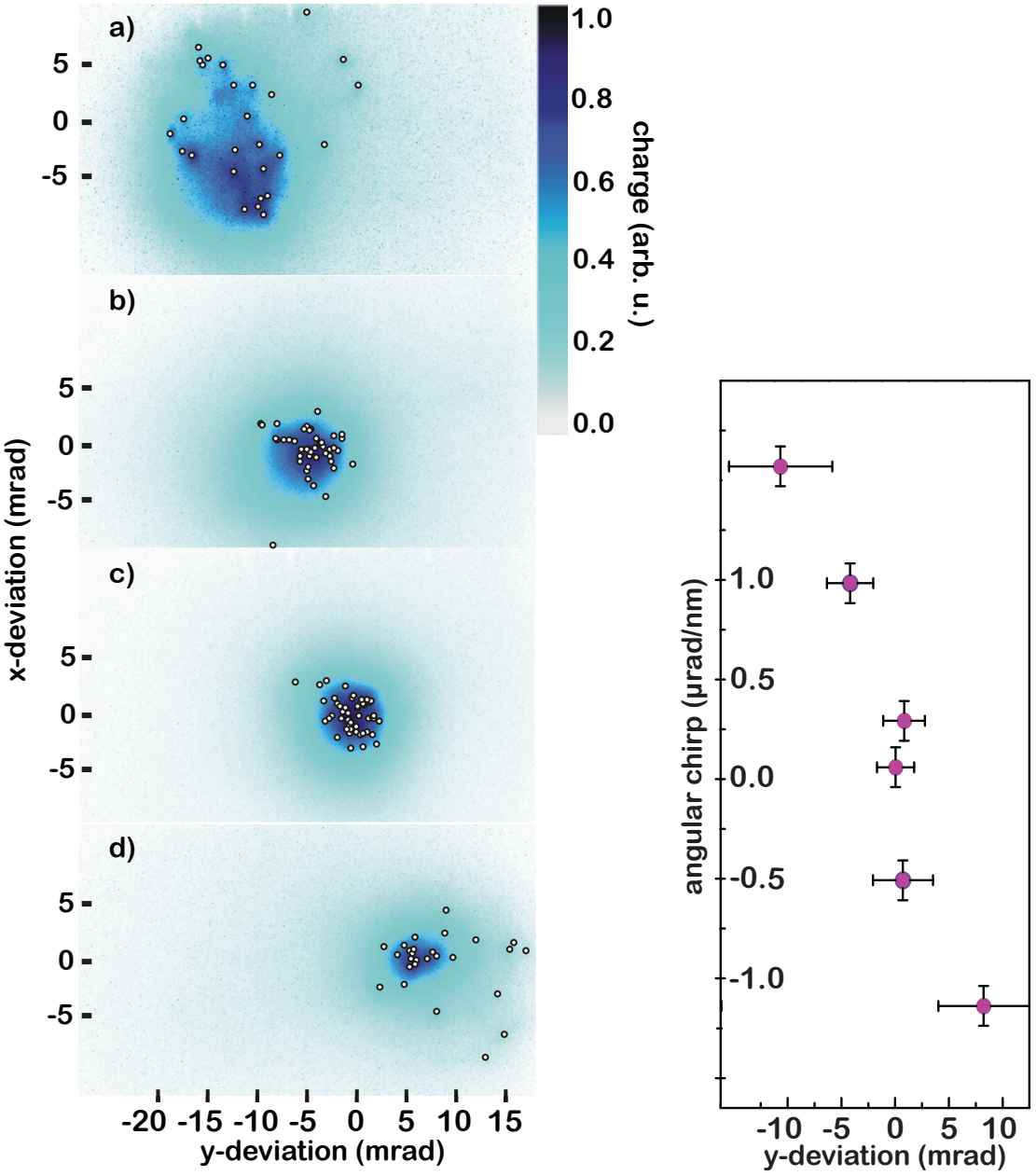

Figure VII.6.: *Steering of the electron beam pointing by changing the PFT/angular chirp. For the highest angular chirp, the initial electron density had to be increased in order to achieve injection.* ***left:*** *Individual peak positions (dots) and the summed signal of electron beams hitting screen S1. Each series of shots was generated with a different angular chirp. Angular chirp in* µrad/nm*: a)* 1.57 *b)* 0.98 *c)* 0.06 *d)* −1.13

right: *The dots represent the center of mass of the electron-beam-pointing distributions as shown in the left plot (plus two more measurements at different angular chirps). The vertical error bars result from the RMS pointing fluctuations, the horizontal error bars from the error of the angular chirp measurement.*

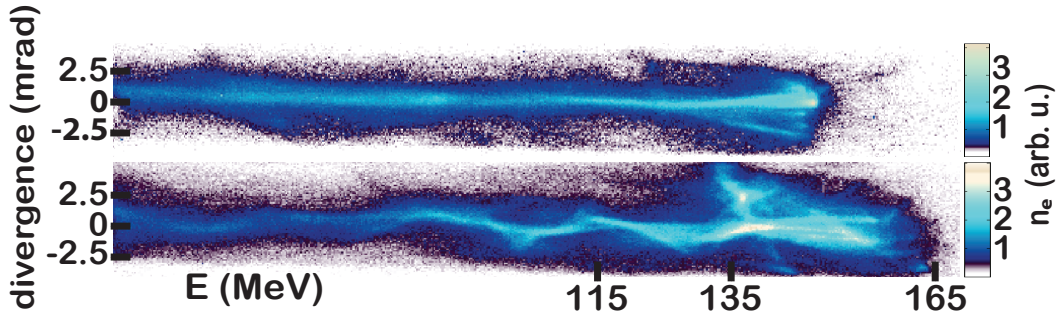

Figure VII.7.: *Measured electron spectra on scintillating screen S2, top: no PFT in the driver laser, bottom: PFT present*

chirp value. The reduced stability can partially be attributed to the less reliable injection process for higher PFTs, i.e. lower laser intensities. In addition, it can be seen from the simulations described below, that the presence of a PFT in the driver pulse results in an asymmetric wakefield. This facilitates electron injection at off-axis positions. The increased betatron oscillations induced in this way (see section III.5.4) may also deteriorate the electron-pulse quality.

However, already small angular chirps ($\sim$ 1 μrad/nm) result in a deflection of the electron beam from the optical axis of up to ±4 mrad while the pointing fluctuations remain still small (< 2.5 mrad RMS). This effect can therefore be exploited to steer the electron bunches. In contrast to beam-direction control with magnetic devices there is no chromaticity.
From these numbers it also becomes clear that the influence of the laser PFT on laser-wakefield acceleration is significant and has been underestimated to date. An angular chirp of 1 μrad/nm is only detectable with proper diagnostics, but causes a 4 mrad deflection of the electron beam (for our focusing conditions). Hence, this parameter must be monitored carefully, especially if alignment sensitive devices such as undulators need to be positioned relative to the electron beam trajectory.

VII.2.3.3 Betatron Motion

In addition to the angular deviation of the electron bunch measured on screen S1 another effect was observed in the experiment. On screen S2 the electron bunches are spectrally resolved in one dimension, whereas the perpendicular axis gives spatial information, which in our case corresponds to the plane in which the laser-pulse symmetry is broken by PFT. Some of the electron beams generated from tilted-pulse driven LWFA leave a corrugated trace on this screen, corresponding to a variation of beam pointing with electron energy. One example shot is shown in figure VII.7. This wiggled electron trace may be experimental evidence of collective betatron oscillations performed by the electrons trapped in the wake. These can occur when, e.g. caused by an asymmetry in the wakefield, the electron bunch is injected at one localized off-axis position (see section III.5.4). This theory is confirmed by the simulations in section VII.3.

Glinec et al. [148] have explained similar observations by the presence of higher-order asymmetric modes in the driving laser. Mangles et al. [149] created a wavefront with coma to achieve similar results. Our experiments, however, suggest that the observed oscillations can also be a result of the tilted intensity-front of the laser beam. If the off-axis injection should be exploited to generate enhanced betatron radiation from the electron bunch oscillations within the bubble our concept to introduce the asymmetry is by far better determinable and controllable. The simulations show that the amount of PFT influences the off-axis injection distance. According to (III.72) this changes the critical wavelength of the betatron radiation. An experimental test of this correlation is still outstanding.

VII.3. LWFA Simulations with a Tilted Driver Pulse

In order to understand how the LWFA process changes when the intensity front of the driver pulse is tilted we conducted full 3D PIC simulations using the *OSIRIS* code. Some of the insights gained from these simulations will generally be true for asymmetric laser pulses. Asymmetries can be caused by imaging aberrations as coma [149] or higher order Gaussian modes [148].

In the simulations the laser pulse was initialized at focus without PFT, but with a spatial chirp and an accordingly increased pulse width and length and hence a decreased pulse intensity. As seen in section VII.1 from this a PFT will evolve behind the focus. The pulse propagates in the z-direction, the spatial and angular chirps are oriented along the x-axis and the pulse is linearly polarized along the y-axis. Details of all simulations presented in this chapter can be found in appendix C.

First an ”extreme” case will be presented, where the different characteristics of LWFA with a tilted driver pulse are very pronounced. Subsequently, a simulation will be discussed that was conducted with laser and plasma parameters as they are used in the experiment. A very intense laser with $a_0 = 3$, $\Delta t = 17$ fs and $\Delta x = 5\ \mu$m is assumed, the electron density was chosen to match the transverse beam size: $n_e = 17 \cdot 10^{18}$ cm^3. With these parameters the bubble regime is entered without any further non-linear pulse modifications, the bubble is spherical. Due the small beam size and large spectral bandwidth the impact of the angular chirp on the laser can be well observed.

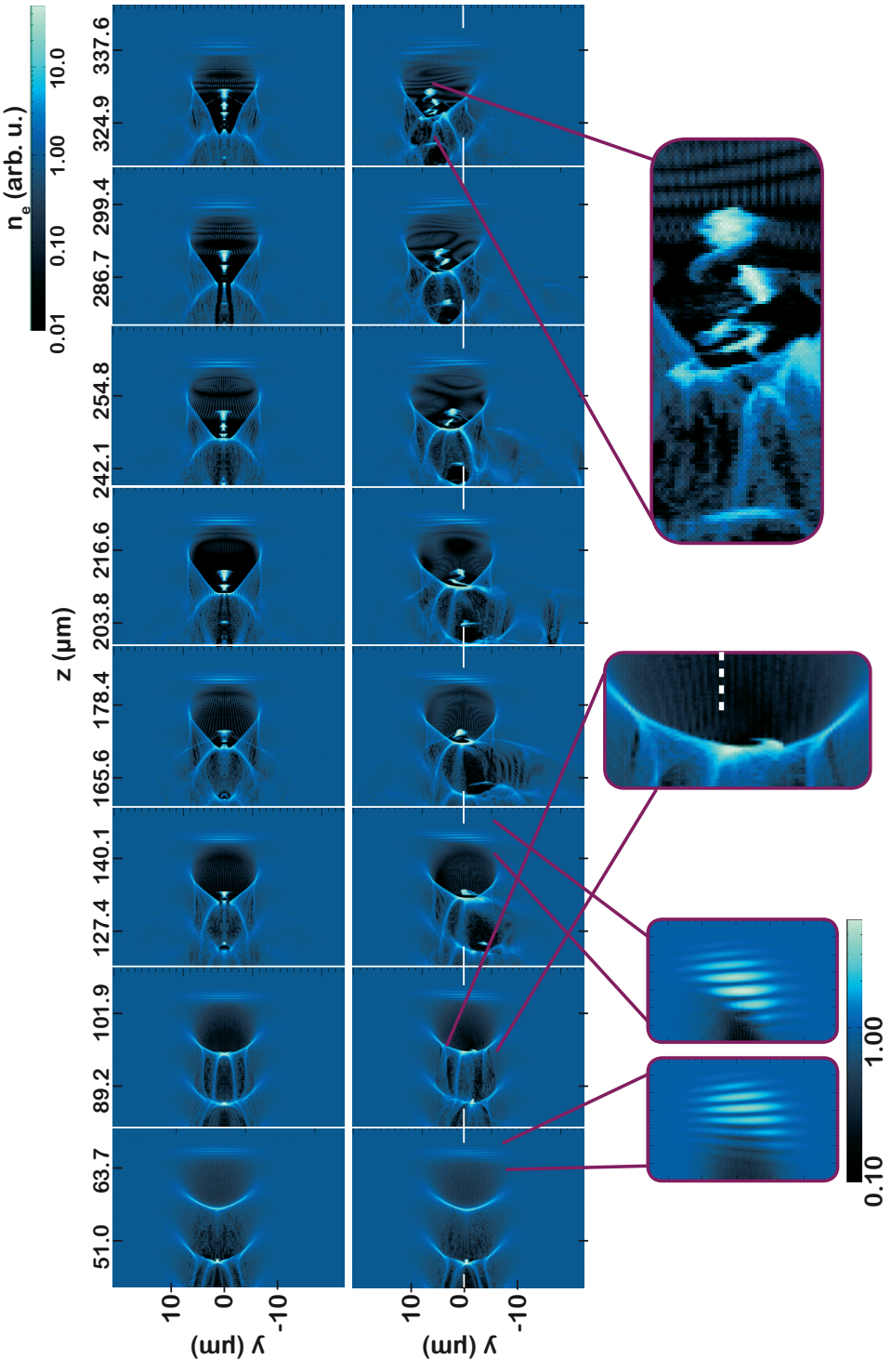

Figure VII.8.: *3D simulation of an extreme case showing deviation of the bubble, off-axis injection of electrons into the wakefield and collective electron-betatron oscillations. (Δt = 17 fs, Δx = 5 µm, a_0 = 3, $n_e = 17 \cdot 10^{18}$ cm^3, top row: no PFT, bottom row: $d\alpha/d\lambda$ = 0.008 µrad/nm assuming a focal length of f = 50 cm, run E(PFT) in appendix C). The laser pulse is initialized with a spatial chirp in focus that subsequently evolves to an angular chirp (zoomed images).*

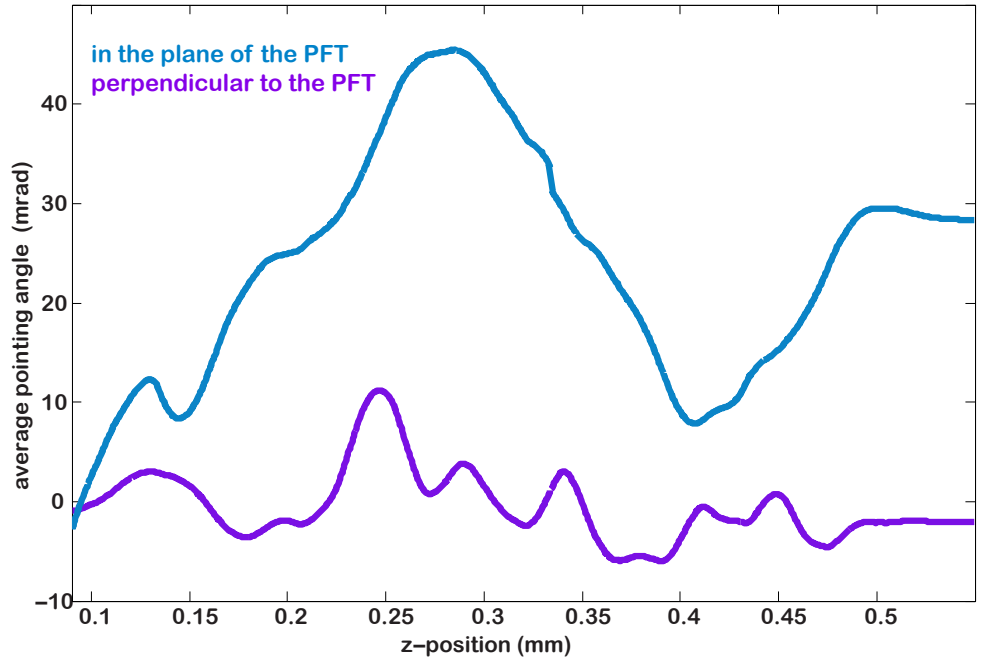

Figure VII.9.: *Summed average pointing angle, plasma-vacuum transition at* 0.5 mm*, run E(PFT)*

Figure VII.8 shows the spatial electron-density plot of the extreme case. For comparison the run in the upper row was done without pulse front tilt, in the lower row the pulse was initialized with a spatial chirp in focus that subsequently evolves into a PFT (note the zoomed regions of the laser pulse in fig. VII.8). The consequences of the tilted intensity front of the driver pulse can be observed very clearly. It is evident that as soon as the PFT develops after the focus, the laser pulse is deflected away from the initial laser-propagation axis. This can be attributed to the transverse plasma-density gradient caused by the tilted pulse front, which corresponds to a varying refractive index perpendicular to the laser-propagation direction. The wakefield excited by this tilted pulse naturally follows the deviated driver and becomes asymmetric. In addition, these asymmetrically deformed wakefields favor self-injection at off-axis positions. This can be observed in frame two and three of the bottom row in figure VII.8. In the focusing field of the bubble the trapped bunch performs strong betatron oscillations (see zoomed image on the right), with an amplitude that is proportional to the off-axis distance of the injection point (cf. III.5.4).
The transverse motion of the laser pulse due to the PFT subsequently increases the offset between the bubble and the self-injected beam. As a result, the transverse electric field pushes the electron beam towards the bubble center. Thus, the average perpendicular velocity of the electron beam approaches the corresponding transverse bubble velocity.
Figure VII.9 shows the mean deviation angle of all trapped electrons ($\gamma > 40$) extracted from the ratio of transverse and longitudinal momentum. In the plane of the PFT (blue curve), the injected electron bunch performs large-amplitude oscillations around an axis that is determined by the propagation direction of the tilted laser pulse. In the plane perpendicular to the PFT (purple curve), the betatron oscillations are centered around zero

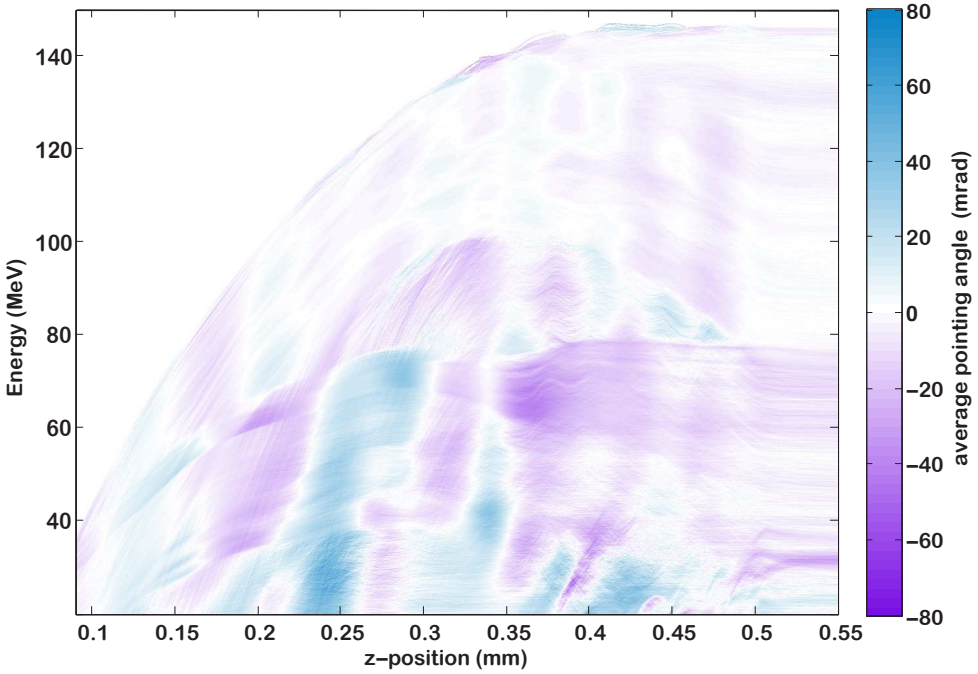

(a) perpendicular to PFT direction, in polarization direction

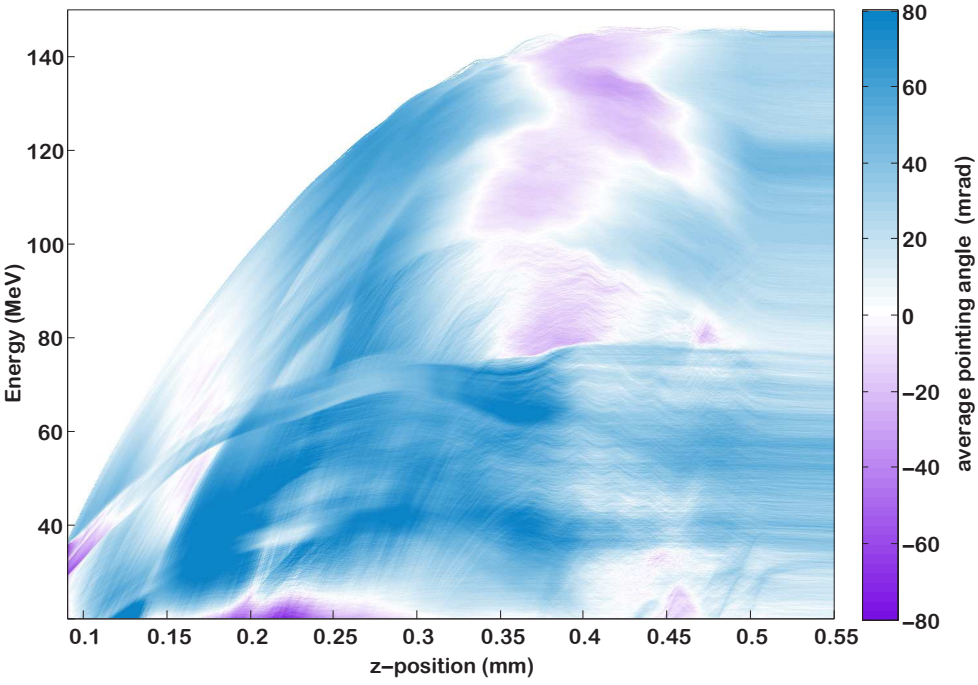

(b) in the plane where the PFT is present

Figure VII.10.: *Spectrally resolved average pointing angle, run E(PFT) in appendix C, plasma-vacuum transition at* 0.5 mm

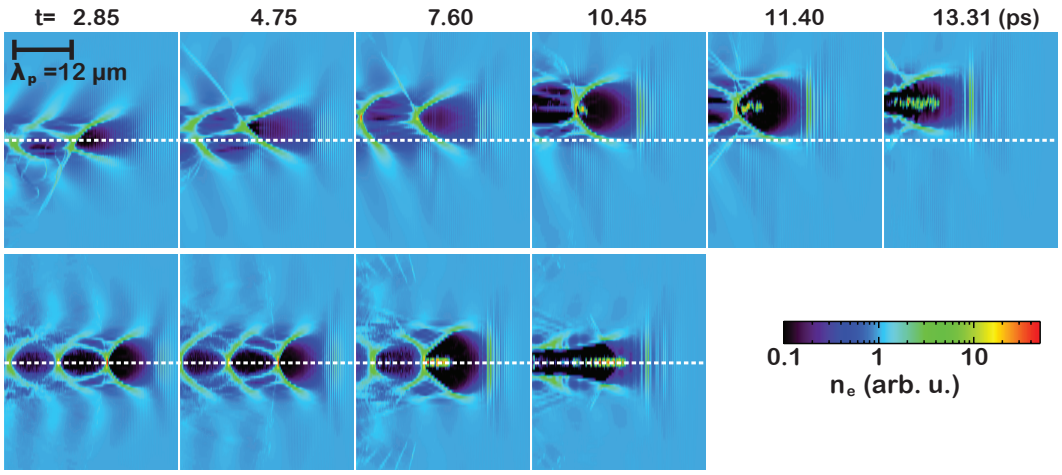

Figure VII.11.: *Cross-section through the central x-z plane of a 3D LWFA-simulation volume with (top) and without (bottom) a pulse-front-tilted driver laser* ($\Delta\tau$ = 37 fs, Δx = 22μm, a_0 = 1.0, $n_e = 7.7 \cdot 10^{18}$ cm^3, $d\phi/d\lambda$ = 1 μrad/nm, *assuming a focal length of* 1.5 m*)*

and significantly smaller. Figure VII.10 shows the deviation angle as in figure VII.9 but spectrally resolved (again in the plane of the PFT, fig. VII.10(a), and in the perpendicular plane, where there is no asymmetry present, fig. VII.10(b)). In this figure and also in the electron density plot (fig. VII.8, zoomed image, bottom right) it can be seen that simultaneously injected sub-bunches perform collective betatron motion. All electrons trapped at a similar localized off-axis position on a time scale Δt shorter than the characteristic evolution time of the PFT ($\Delta t \ll l_R/c$) acquire about the same transverse momentum when oscillating in the transverse and focusing electric-field potential of the wake. In the case of a driver pulse without PFT the plasma wave and therefore the injection region is cylindrically symmetric.

Before discussing the full consequences of those characteristics, the second set of simulations should be introduced. These 3D-simulations, shown in fig. VII.11, are done with parameters closely resembling the actual experiment and will therefore allow for a more quantitative comparison. The same basic features as in the extreme case discussed above are present, but less pronounced. In the run without PFT (second row, fig. VII.11), a pulse length of Δt = 37 fs was used, focused to a spot size of Δx = 22 μm, with a peak normalized vector potential a_0 = 1. The preformed plasma has a uniform electron density of 7.7×10^{18} cm^{-3}. The angular chirp is dφ/dλ = 1 μrad/nm, assuming a focal length of 1.5 m. Figure VII.11 shows the spatial electron density distribution, figure VII.12 illustrates the evolution of the mean angular deviation ϕ_s of the self-injected electron bunch (all particles with $\gamma > 40$).

As long as the transverse focusing fields of the wakefield are present, ϕ_s is mainly determined by the betatron motion of the electron bunch within the bubble and oscillates from $\sim$ 3 to $\sim$ 36 mrad. The fact that the *average* electron propagation angle ϕ_s oscillates at all, reflects the broken symmetry during injection and the in-phase oscillation of electrons in

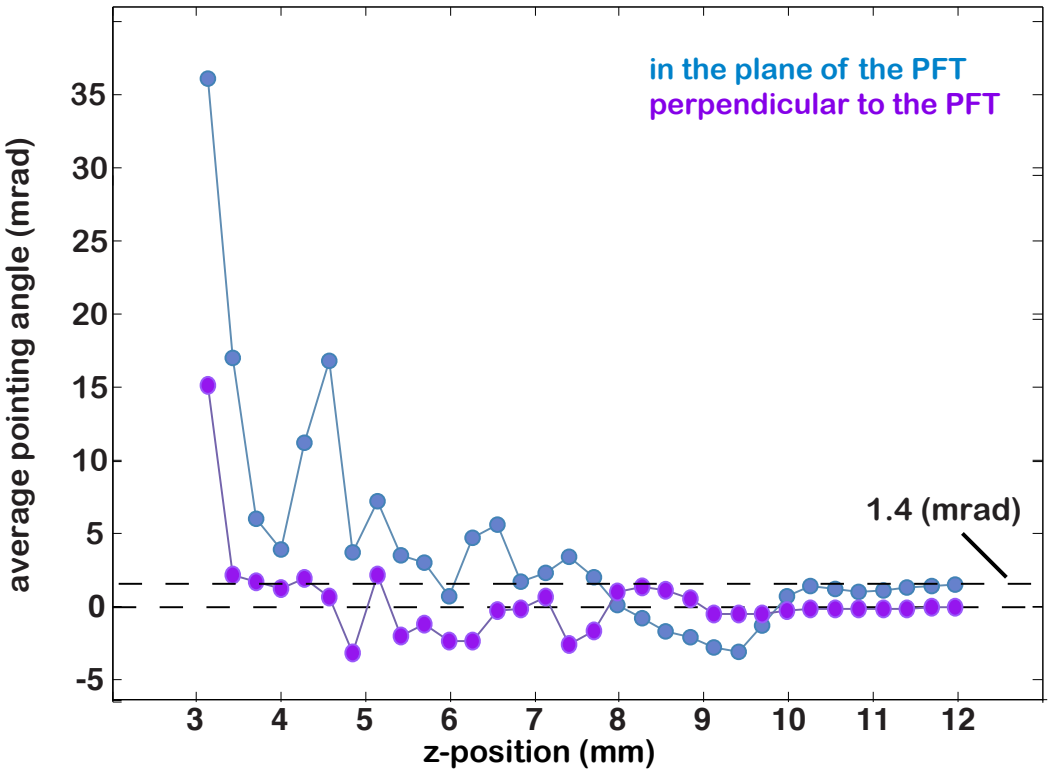

Figure VII.12.: *Angular deviation of the electron bunch (average over all electrons with $\gamma > 40$)*

the bunch. The fact that ϕ_s does not oscillate symmetrically around zero can be attributed to the shifting wakefield structure. As soon as the laser starts to deplete, these oscillations are damped to −3-7 mrad as the transverse focusing fields in the bubble decrease. At the very end of the gas cell, when in our case the laser is entirely depleted and the wakefield is no longer driven, the mean angular deviation of the electron bunch stabilizes at 1.4 mrad, consistent with the deviation of the bubble. Shortly before laser energy depletion becomes significant and the bubble structure starts dissolving, the bubble has an angular offset of 2.6 mrad. The final net deviation of 1.4 mrad of the electron bunch, after the betatron oscillations were damped during the propagation through the residual plasma, is associated with the transverse deviation of the blowout region. Therefore, as indicated by the experimental results, the electron beam, eventually, leaves the plasma under an angle that is mainly determined by the wakefield direction. For further comments on these dynamics see the next section VII.4

Both simulations with a tilted driver pulse, the extreme case and the run with parameters close to the experiment, show: An intensity front tilt in the driver pulse may be used to excite axially asymmetric plasma-wakes, which can steer electron bunches away from the initial laser-propagation axis. However, if the acceleration distance ends before the betatron oscillations are damped, the bunch direction will not only be determined by the deviated wakefield, but mainly by the large instantaneous transverse momentum of the betatron motion.

VII.4. Comparison of Simulation and Experiment

The simulation (figure VII.12) was carried out with an angular chirp of 1 μrad/nm and results in an angular deviation of the electron bunch of 1.4 mrad. The bubble structure was deviated by 2.6 mrad. In the experiment an angular chirp of 0.98 μrad/nm and a deviation of 4.2 mrad were measured. For a similar angular chirp the extracted deviations lie well within one order of magnitude.
However, it must be noted that PIC-simulations of laser-driven non-linear wakefields suffer from numerical heating which, in the worst case, changes the injection dynamics and leads to increased trapping of electrons (see discussion at the end of section VI.3). Furthermore the trapped electron bunch is only poorly resolved in transverse direction, which leads to inaccurate treatment of the beam self-fields and induces artificial emittance growth [144]. As we want to evaluate betatron oscillations and a transverse angular deviation of the bunch, the low transverse resolution might be an issue, at least if it comes to quantitative analysis.
Although it is difficult to detect and extract such numerical errors, the huge discrepancy between the simulated and measured divergence might indicate that such problems exist: In the simulation the divergence decreases from 90 mrad RMS to 13 mrad RMS during the propagation (considering all particles with $\gamma > 40$). Experimentally, the electron beam divergence inside the bubble cannot be measured directly, but the divergence of the generated betatron radiation can give a hint. The divergence of the betatron radiation of a single electron is given by K/γ, where K is mainly determined by the maximum excursion (cf. end of section III.5.4). The divergence of the betatron radiation of an electron *bunch* is obtained by convolution with the electron beam divergence. In a recently conducted measurement with our setup the divergence of the betatron radiation from electron oscillations in the wakefield was determined to be $5 - 10$ mrad RMS [150]. This is still lower than the final simulated divergence and far below the divergence of the electron bunch during acceleration.
It can therefore be assumed that the dynamics of the trapped electrons is not modeled correctly to a quantitatively reliable extent. However, the motion of the laser pulse and the trailing wakefield is not subject to the numerical problems mentioned above. As the trapped electron bunch follows this bubble structure, this deviation is the important parameter to be considered.

Discrepancies can also result from the following experimental properties and uncertainties that cannot be fully reproduced in the simulations.

- The exact longitudinal position of the geometric laser focus in the plasma is unknown. As can be seen from figure VII.1, the PFT angle strongly changes during propagation. Certainly, this evolution is different for propagation in plasma and in vacuum. Thus, depending on where exactly the plasma starts relative to the geometrical focus position the final deviation angle will be different.

- Additional asymmetries that amplify the effect can be present in the laser pulse or in the gas target (e.g. higher order Gaussian modes in the laser transverse profile,

cf. [148]

- The self-focussing and self-compression of the laser pulse that is necessary for driving a wakefield with these laser parameters is a highly non-linear process. Small variations in the initial experimental laser parameters compared to simulation can lead to large difference in the exact properties of the laser, when it starts to drive the wakefield and thus of the wakefield itself.

VII.5. Conclusion

The benefits of the a driving a wakefield with a tilted laser pulse are on one hand the possibility of all-optical electron bunch steering and on the other hand the enhancement and control of betatron oscillations and therefore the generated high-energy radiation. If the steering effect is exploited, using an external injection scheme might be advantageous, as the asymmetry of the wakefield also influences the injection dynamics in an for this application unwanted way. For instance, the combination of counter-propagating pulse injection (section III.3.3,[91]) and PFT-steering could be desirable. The complexity and geometry of the setup with two or more pulses does not allow for arbitrary positioning of magnetic lenses that otherwise have to be used for steering.
For many applications, however, it is important to avoid any deviation of the electron bunch from the original laser-propagation axis. Especially, when further devices as an undulator and subsequent X-ray diagnostics have to be aligned, reliable electron pointing along the predetermined axis is indispensable. Thus the angular chirp in the laser system, but also other possible asymmetries in the spatial intensity distribution, have to be carefully monitored. Recent experiments, that have to be further evaluated, also indicate that even a distorted near-field can be fatal, although the focal spot in vacuum itself is symmetric. If the longitudinal focus position of a high-intensity laser is not exactly at a sharp rising edge of the electron density profile, but further downstream, a wakefield can be driven already before the focus, where the beam profile is still inhomogeneous and thus can lead to asymmetric wakefields.
In other respects, the asymmetry causes off-axis self-injection into the wakefield. Esarey et al. [106] lists this as an important feature on the way to X-ray ion channel lasers, where eventually the betatron radiation should be coherently amplified in a laser-generated wakefield or plasma channel. But also the incoherent betatron radiation from a bubble, sometimes called ”bubbletron radiation”, can be useful for a variety of applications. The collectively oscillating electrons emit radiation, which may be coherent and in the keV-energy range (cf. e.g. [106, 151]). It is radiated into a small opening angle of $1/\gamma$, and thus spatially coherent. In *phase contrast imaging* ([3] and e.g. [152]) images especially from biological tissue are taken and the introduced phase rather than the intensity variation is evaluated. As the imaginary part of the refractive index usually is much larger than the real part for X-rays, more information can be extracted from these pictures albeit lower dose deposition. However, in order to be able to extract the phase information a spatially coherent X-ray source is advantageous. Bubbletron radiation in principle are a good can-

didate for low-cost, relatively compact (compared to conventional synchrotrons) X-ray sources for phase contrast imaging. Furthermore a potential knob to tune the radiation wavelength is available, as the strength of PFT changes the off-axis distances for injection (see [149, 153]). The drawbacks currently are the lower photon count per shot and the low repetition rate.
Another advantage of X-ray pulses from laser-wakefield accelerated electrons is that they are ultra-short, as their length is mainly determined by the electron bunch length [154]. As has been shown by e.g. [5] the electron bunch length is well below 10 fs. Preliminary measurements with the transition radiation diagnostics described in section V.6 indicated similar bunch lengths for our setup.

Chapter VIII

Outlook

In this work different aspects of the dynamics in laser-wakefield acceleration have been studied. Plasma-based acceleration is a promising concept for future generations of particle accelerators, since a plasma wave can sustain extremely high field strengths (for our setup $\sim$ 160 GV/m) and thus accelerate electrons within short distances to relativistic energies. However, if the plasma wave is excited by a high-intensity laser pulse, the laser group velocity $v_{gr,l} < c$ determines the phase velocity of the wave and the faster relativistic electrons can move from the accelerating to the decelerating phase of the electric field. Thus, in order to maximize the final electron energy, it is important to adapt all possible limitations of the acceleration distance to this dephasing length. With the gas cell length scan described in this work the importance of different factors, such as plasma length, energy depletion/diffraction length of the laser, at two different pressures was analyzed. Most importantly it was found that for lower densities, theoretically leading to higher energies, the maximum energy could not be reached as the laser diffracts before the dephasing length. Therefore, an external guiding channel is advisable if the main goal is to maximize the achievable energy for given laser parameters.
In a second measurement with a tilted driver pulse it was shown that up to now the impact of residual angular chirp in the laser pulse was underestimated. Already small angular chirps (1 μrad/nm) result in a deflection of the electron beam from the optical axis of up to 4 mrad (in our setup).
Both experiments of this work did not only contribute to a better understanding of the physical process and the dynamics during acceleration, but they also identified some tolerable error margins for different parameters of the accelerator, such as laser pulse distortions and gas target length. This is essential for the step from proof-of-principle experiments to user facilities that run stably on a daily basis.
As eventually such user facilities are supposed to provide brilliant X-ray radiation to biologists and medics, it is legitimate to ask how suited currently available LWFA-electron bunches already are for this purpose.

The most ambitious goal in this context is the table-top free-electron-laser. Grüner et al. [22] give an example scenario for a possible XUV- and X-ray FEL seeded with LWF-accelerated electrons and using a novel short-period undulator. For radiation at 32 nm

electrons with a peak energy of 150 MeV with 200 pC charge and a relative energy spread of 0.5% are necessary, for 2.5 Å-radiation electron bunches at 1.74 GeV with 640 pC charge and an energy spread of 0.1% have to be provided. For both cases an electron bunch duration of 4 fs and an undulator period of 5 mm was assumed.
The necessary energy is well within the scope of stat-of-art plasma accelerators. 1 GeV has already been demonstrated by Leemans et al. [15]. For the recently commissioned, more powerful *Texas Petawatt* laser (200 J in 150 fs) Kalmykov et al. [155] predict $2.6 - 7$GeV, 1.3 nC in 10cm-long plasmas with $2 \cdot 10^{18}$ cm^{-3}. These energies would even reduce the X-ray wavelength down to 0.15 Å.
Also the assumed electron bunch duration of 4 fs has been confirmed experimentally. Lundh et al. [6] measured a 3 fs-bunch, with our transition radiation diagnostics a bunch duration of $\approx$ 5 fs was extracted. This electron bunch length is approximately transferred onto the X-ray pulse allowing for pump-probe experiments of ultra-short processes.
The great challenge, however, lies in the last two parameters, energy spread and charge. The smallest energy spread so far was demonstrated by Rechatin et al. [17]. They achieved 1% FWHM relative energy spread, which is still an order of magnitude too high for the hard X-ray FEL. But even worse, this bunch only contained 10 pC of charge. On the other hand, bunch charges of up to $\approx$ 700 pC have been measured, but distributed over a broad broad range of energies (e.g. 300 pC with 8.4% FWHM energy spread [15], $500 - 700$ pC integrated in the entire spectrum between 30 and $\approx$ 125 MeV [156]). In laser wakefield acceleration energy spread and bunch charge are strongly coupled and depend mainly on the injection scheme, i.e. by which mechanism electrons are trapped in the wakefield, and on beamloading dynamics. Only if injection takes place localized in time and space, all electrons see the same longitudinal electric field during the acceleration process and are accelerated for the same period of time, leading to a background-free, narrow energy peak. This can only be ensured with an external injection method, as self-injection due to wavebreaking often leads to continuous injection. In section III.3 different possible approaches were listed. One concept that is currently under investigation is injection in a shock-front that is generated by a transverse electric discharge at the entrance of the gas cell. Shock-front injection has already been successfully demonstrated by [93] by means of a razor blade in a super-sonic gas jet.
In addition, in order to keep the energy spread small, the electric field of the trapped bunch,ideally, balances the accelerating field such that the field strength along the entire bunch is constant (cf. III.4).
From these considerations, it becomes clear, that for the near future intense investigations on a sophisticated injection scheme are crucial on the way to a laser-driven X-ray FEL.

On the other hand, while in most schemes for *temporally incoherent* X-ray generation (spontaneous undulator radiation, betatron radiation, Thomson backscattering) a small electron energy spread leads to a desirable narrow-band X-ray spectrum, it is not essential for the mechanism to work. Already now such X-rays from laser-accelerated electrons can - in many aspects- compete with conventional synchrotron sources. Figure VIII.1 shows the peak brilliance of several conventional second and third generation synchrotron X-ray sources at *DESY* (Hamburg, Germany), *BESSY* (Berlin, Germany), *ESRF* (Grenoble,

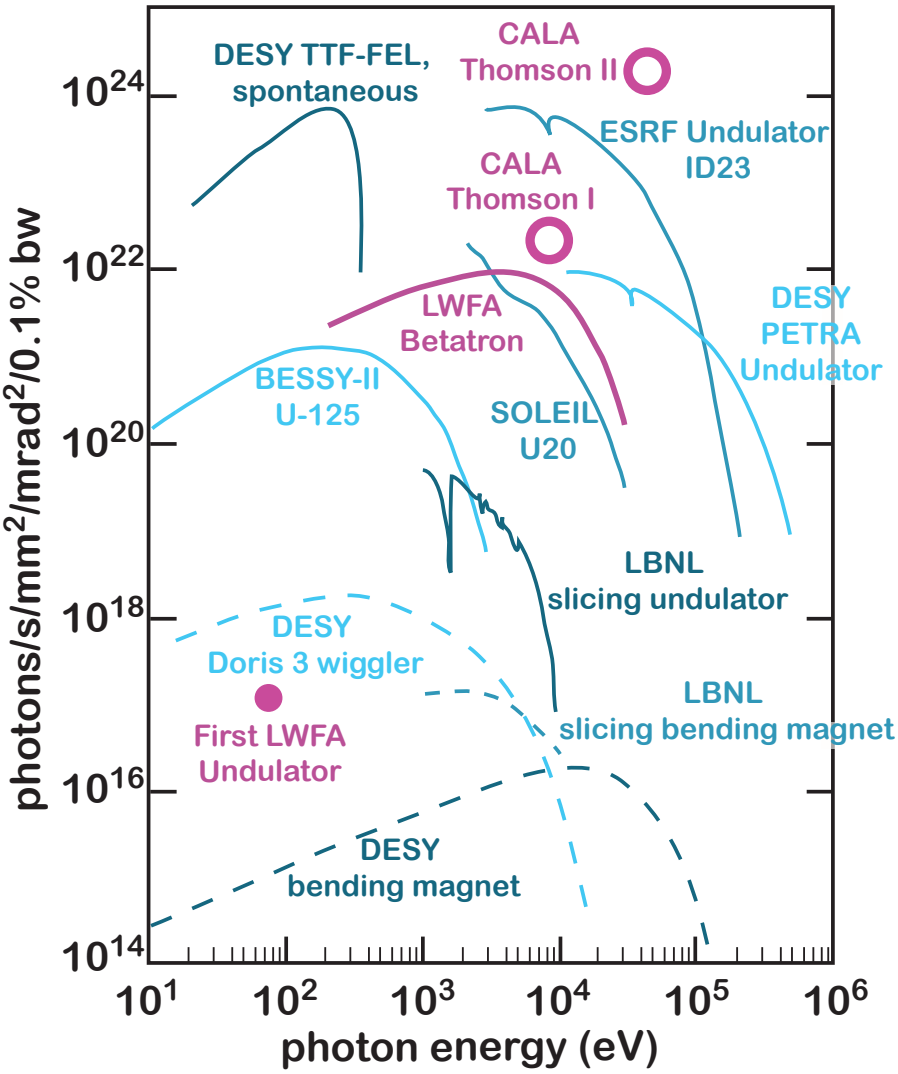

Figure VIII.1.: *Plot adapted from [157, 158, 159]*
Peak brilliance of conventional 2nd (dashed lines, blue) and 3rd (straight lines, blue) generation synchrotron sources. The pink line shows the brightness of a LWFA-betatron source as measured by Matsuoka et al. [157]. The authors assumed that the X-ray pulse duration equals the laser pulse duration of 30 fs. *The filled pink dot is the peak brilliance of the first undulator source that was seeded with our LWFA-accelerated electron bunches [21]. For the undulator radiation a pulse duration of* 10 fs *and source size of* 2 µm *was assumed. The hollow dots represent the expected peak brilliance of CALA Thomson scattering sources (see text).*

France), *LBNL* (Berkeley, USA), *SOLEIL* (Paris, France). The filled pink dot marks the peak brilliance deduced from the first proof-of-principle experiment that realized a laser-driven soft-X-ray undulator source [21]. The pink line is the peak brilliance of the betatron radiation from a laser-wakefield accelerator measured by Matsuoka et al. [157]. Both cases are already in the same region as conventional synchrotrons, and fast progress can be expected, as every increase in electron bunch charge or reduction in energy spread due to improved injection schemes will increase the peak brilliance. While even the first

	I	II
driver laser	5 kHz 100 mJ,5 fs	1 kHz, 500 mJ,5 fs
electron bunches	30 MeV, 10 pC	50 MeV, 10 pC
probe pulse	1 J, 1 ps, 1 μm, $a_0 = 0.5$	2 J, 1 ps, 1 μm, $a_0 = 0.74$
X-rays (energy)	7.5 keV	37 keV
X-rays (brilliance)	peak $3.27 \cdot 10^{22}$, av. $4 \cdot 10^{12}$	peak $2.69 \cdot 10^{24}$, av. $6.75 \cdot 10^{13}$

Table VIII.1.: *Expected X-ray parameters for Thomson scattering at the CALA-facility. Brilliances are given in units of* photons/mm^2/mrad^2/s/0 1%bandwidth. *For the focal spot size of the counter-propagating probe pulse and the electron bunch diameter* 22 μm *were assumed.*

proof-of-principle experiment delivered impressive results, especially the undulator radiation brilliance will benefit from better electron beam quality. Furthermore, betatron radiation might be enhanced by off-axis injection caused by a tilted driver pulse as described in this work.
The two hollow dots are peak brilliances as they are expected from a novel laser-driven Thomson-scattering source as it is planned in the framework of the *CALA* project[1]. With the pursued concept, a so-far-neglected problem of the above mentioned laser-driven X-ray sources is tackled: High-intensity Titanium-Sapphire lasers run at a maximum repetition rate of $\approx$ 10 Hz, larger systems like the *Texas Petawatt* cannot exceed one shot per hour due to heat problems. The conventional accelerator *SOLEIL*, on the other hand, runs at a few hundred Hertz. Thus the average flux/brilliance of synchrotrons still exceeds laser-driven X-ray sources by several orders of magnitude. Considerable progress in the development of high-power diode-pumped OPCPA or disc lasers must be made before the high-intensities needed for the acceleleration of electrons to GeV energies will be available at those high-repetition rates. However, the advantage of Thomson scattering is that electron energies as low as $\approx$ 30 MeV are sufficient to generate hard X-rays, as the wavelength of the scattered laser pulse ($\sim$ 1 μm), not the undulator period $\sim 5 - 20$ mm, determines the X-ray wavelength. Such low energy electron bunches (up to 25 MeV) have already been demonstrated with only 65 mJ (8 fs) driver pulses relying on shockfront injection [93]. Although still challenging, laser systems at these energies can be scaled to high repetition rates more easily. Therefore *SPECTRE*, the high-flux X-ray generation at *CALA*, is based on the following concept (also see table VIII.1):
The planned diode-pumped OPCPA laser system *PFS Pro*[2] will deliver 500 mJ, 5 fs-pulses at a repetition rate of 1 kHz, resulting in wakefield-accelerated electron bunches of $\sim$ 70 MeV, 100 pC. The pump pulses of *PFS Pro* will be recycled and used as the counter-propagating scattering laser pulse (2 J, 1 ps, 1 μm). From this configuration 37 keV-radiation can be generated with an average brilliance of $6.75 \cdot 10^{13}$ and a peak brilliance of $2.69 \cdot 10^{24}$ photons/mm^2/mrad^2/s/0 1%bandwidth. Table VIII.1 summarizes

[1] The "Centre for Advanced Laser Applications" will be a research and eventually user facility situated in Garching (Germany), dedicated to laser-driven particle acceleration (electrons and protons), secondary X-ray sources and their application in biology and medicine.
[2] based on technology that is currently being developed for *PFS*[160]

those parameters (II) and also lists the corresponding numbers for an intermediate stage (I). With the availability of these advanced laser sources *SPECTRE* will provide X-rays with an average brilliance that is approaching conventional synchrotrons while maintaining the high temporal resolution of $<$ 5fs-pulses originating from the laser-wakefield-accelerated electron bunches.
In the long run also an X-ray FEL is planned for *CALA* with several orders of magnitude higher brilliances. As a comparison, the X-ray FEL *LCLS* (Stanford, USA) based on a linear radio-frequency-accelerator provides a peak brilliance above
10^{32} photons/mm^2/mrad^2/s/0 1%bandwidth. But, as discussed above, for this ambitious goal further advances have to be made both in laser development and laser-wakefield acceleration.

In conclusion it can be said that LWFA-based, table-top, ultra-short-pulse X-ray sources that provide brilliant radiation will come into reach in the near future. Fast progress is being made at improving the quality of the electron beam and its stability and reproducibility. First experiments proved that brilliant, spatially coherent X-rays beams can be generated with different methods. Finally, even first phase-contrast images have been created (e.g.[161]), pointing the way towards a variety of medical and biological applications.

Chapter A

Gaussian Parameters

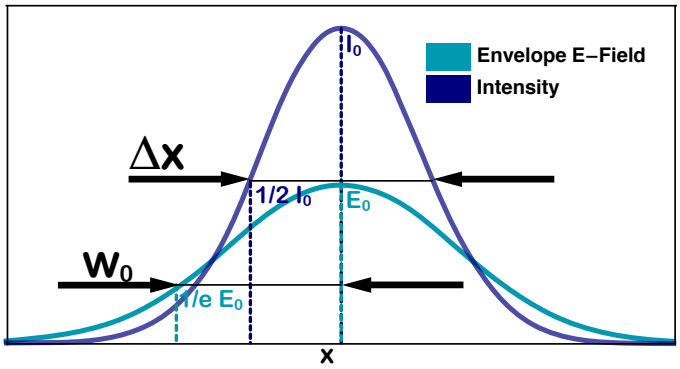

Figure A.1.: *Gaussian quantities for electric field and intensity envelope*

Throughout this work the laser pulses are assumed to be Gaussian in time and space. Pulse duration and spot size are defined in two ways:

the half width at $1/e$ of the maximum height of the electric field envelope
τ_0 and w_0 (and σ_ω in frequency space)

the full width at half maximum of the intensity envelope
Δt and Δx.

Therefore the field envelope is (example for the spatial dependence)

$$E(x) = E_0\, e^{-(x/w_0)^2} \tag{A.1}$$

The intensity envelope then is

$$\begin{aligned} I(x) \propto E(x)^2 = E_0^2\, e^{-2(x/w_0)^2} = \\ = I_0\, e^{-4\ln(2)(x/\Delta_x)^2} \end{aligned} \tag{A.2}$$

and

$$\Delta x = \sqrt{2\ln(2)}w_0 \tag{A.3}$$

Chapter B

Particle-in-Cell Simulations

Owing to the high complexity of a many-particle system and the extreme non-linearities that can occur during the interaction of a high-intensity laser pulse with plasma most problems cannot be solved analytically. The numerical approach that is suitable to simulate these physical processes is called "particle-in-cell" (PIC) method [162],[163], [164],[165]. The assumptions that are usually made in this context are:

- The process of ionization can be neglected as the involved peak laser intensities are several orders of magnitude above the ionization level. A fully ionized quasi-neutral plasma is used at initialization.

- Electron-ion collisions can be neglected. The time scale τ_{int} of the interaction is much smaller than the mean free time between collisions τ_c. Even for solid state plasma densities $\tau_c/\tau_{int} \approx 40$ [52].

The particles in PIC-simulations are so-called macro-particles each representing a certain amount of real plasma particles[1]. In simulations of the laser-wakefield acceleration process, usually only the dynamics of the electron population is simulated, the protons form an immobile neutralizing background. This is valid as the laser intensity is too low to influence the approximately 2000 times heavier protons.
In order to simulate the dynamics of the macro-particles at the presence of external electro-magnetic fields, the following set of equations is solved: The Vlasov equation [166] models the plasma dynamics

$$\frac{\partial f}{\partial t} + \frac{\boldsymbol{p}}{m\not{c}\gamma} \cdot \nabla f + \boldsymbol{F}\frac{\partial f}{\partial \boldsymbol{p}} = 0 \tag{B.1}$$

where $f(t, \boldsymbol{x}, \boldsymbol{p})$ is the charge distribution function and $\boldsymbol{F} = q(\boldsymbol{E} + \boldsymbol{v} \times \boldsymbol{B})$ is the Lorentz force
The Maxwell equations describe the evolution of the fields (external fields + fields of the

[1] In the 3D simulations shown in this work one macro-particle typically corresponds to $\sim 10^4$ electrons

charged particles)

$$\frac{\partial \boldsymbol{E}}{\partial t} = c^2 \nabla \times \boldsymbol{B} - \frac{1}{c^2 \epsilon_0} \boldsymbol{j}$$
$$\frac{\partial \boldsymbol{B}}{\partial t} = -\nabla \times \boldsymbol{E} \tag{B.2}$$

where the current density $\boldsymbol{j}$ can be found via $\boldsymbol{j} = q \int \boldsymbol{v}(\boldsymbol{p}) f(t, \boldsymbol{x}, \boldsymbol{p}) d\boldsymbol{p}$ and $\boldsymbol{v}(\boldsymbol{p}) = \boldsymbol{p}/(m\gamma)$. Numerically, the spatial positions of the particles and their momenta are continuous coordinates, whereas the fields are only defined on a discrete 3-dimensional grid. The equations above are then solved for discrete subsequent time steps. Figure B.1 illustrates the algorithm. For each time step, the summed up fields (external fields+ fields of the charged particles) are computed on the spatial grid and then interpolated to the continuous particle positions. The particles are moved according to the Vlasov equation, the generated currents are extracted and distributed on the spatial grid. Finally, new field distribution is calculated.

The resolution of the grid must be chosen such that the important structures are well

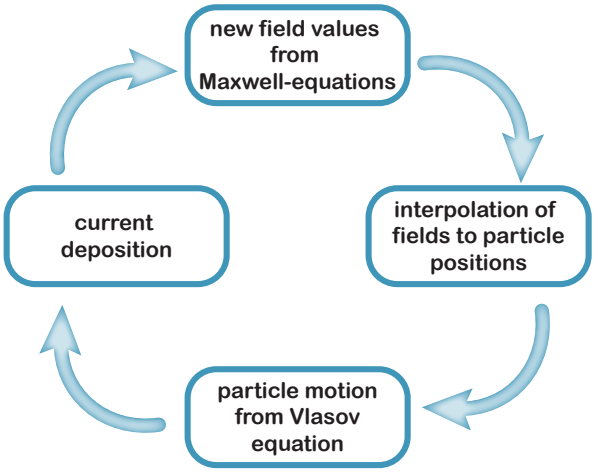

Figure B.1.: *Scheme of the PIC algorithm*

sampled. In the case of LWFA simulations that usually means, that in laser propagation direction the laser wavelength must be resolved. In the transverse direction it is sufficient to resolve the plasma wavelength. In order to correctly include all dispersion effects in the simulation the so-called Courant condition [167] has to be fulfilled: The delay Δt between two simulation steps must be around the same time as a light wave needs to cross one spatial cell in the grid.

The PIC-code used for the simulations shown in this thesis is *OSIRIS* [163]. *OSIRIS* is a massively parallel code (as all PIC codes) and provides a "co-moving" simulation box, that moves with the speed of light in laser propagation direction. For long laser propagation distances as they are necessary in LWFA-simulations, this concept considerably reduces the size of the simulation volume. *OSIRIS* uses units that are normalized to the plasma frequency $\omega_p = 1$ and also $n_e = 1$. It follows: $\lambda_p = 2\pi$, all lengths are scaled to

c/ω_p, time is scaled to $1/\omega_p$. The input parameter, that eventually determines the plasma density is the normalized laser frequency ω_l/ω_p. In real-world parameters the absolute plasma density is only defined for a certain laser wavelength.
In the shown LWFA-simulations the laser pulse was modeled with a Gaussian transverse profile and a symmetric polynomial temporal profile.

Chapter C

Simulation Details

For the simulations presented in this thesis we employed the massively parallel particle-in-cell code *OSIRIS* [163]. All runs are fully three-dimensional. We used a Gaussian transverse profile and a symmetric polynomial temporal profile, with a central wavelength $\lambda_0 = 800$ nm.
Below the input parameters for the simulations included in this work are shown, in real-world units under the assumption that $\lambda_0 = 800$ nm and in the *OSIRIS* unit system. The normalized parameters (second table) are named and defined as the respective *OSIRIS* input variables. The simulation box size in each spatial direction divided by the respective number of cells gives the resolution. It should be noted that the pictures shown in the previous chapters are mostly cropped in transverse direction to magnify the interaction region. The original simulation boxes are larger in order to avoid unphysical behavior at the borders.
In all runs, the initial longitudinal electron density profile has a rising edge of a certain length R before it reaches the plateau of maximum homogeneous density. Except for the $A100(100mbar)/(150mbar)$-runs, this rising edge is on the order of the plasma wavelength. In the $A100(100mbar)/(150mbar)$-runs the entire gas density profile of the gas cell as shown in V.6 was modeled, with a 4.5 mm low-density gas plume in front gas cell entrance. The longitudinal focal position, however, is at the entrance, i.e. at the beginning of the plateau.
The runs with an angularly chirped driver pulse were initialized at focus with a certain spatial chirp that corresponds to an angular chirp in the collimated beam. Pulse length and transverse focal size were adapted accordingly (see (II.19)), while pulse energy and spectral content were kept constant.

Table C.1.: *Spatial chirp in the focus and corresponding angular chirp in the collimated beam for* $f = 50$ cm *(*$E1$,$E2$*) and* $f = 150$ cm *(*$ATLAS(PFT)$*)*

run	angular chirp (μrad/nm)	spatial chirp ($2\pi\ dx/d\omega$) (m · s)	*OSIRIS* chirp parameter
$E(0)$	0	0	0
$E(PFT)$	0.008	$8.54518 \cdot 10^{-21}$	0.202321
$ATLAS(0)$	0	0	0
$ATLAS(PFT)$	1	$3.2 \cdot 10^{-18}$	0.00644222

Table C.2.: *Angular chirp runs in SI units*

run	n_e (cm^{-3})	a_0	Δt (fs)	Δx (μm)	long. focus pos. (mm)	box size (x_1, x_2, x_3) (μm)	charge/MP (C)
$E(0)$	$17.4195 \cdot 10^{19}$	3	8.4961	9.00707	0	(31.85,61.15,61.15)	$1.60093 \cdot 10^{-15}$
$E(PFT)$	$17.4195 \cdot 10^{19}$	2.8881	8.7220	9.2341	0	(31.85,61.15,61.15)	$1.60093 \cdot 10^{-15}$
$ATLAS(0)$	$7.735 \cdot 10^{18}$	1.085	37	22	0	(57.32,133.75,133.75)	$2.654668 \cdot 10^{-15}$
$ATLAS(PFT)$	$7.735 \cdot 10^{18}$	0.801	59.3	25.2	0	(57.32,133.75,133.75)	$2.654668 \cdot 10^{-15}$

Table C.3.: *Angular chirp runs, normalized units (OSIRIS)*

run	ω_0	a_0	$long.rise/fall$	$per.w0$	$long.focus$	box size (x_1, x_2, x_3)	cells (x_1, x_2, x_3)
$E(0)$	10	3	2	6	0	(25,48,48)	(1600,360,360)
$E(PFT)$	10	2.8881	2.05323	6.151218	0	(25,48,48)	(1600,360,360)
$ATLAS(0)$	15	1.085	8.1781	10.2143	0	(30,70,70)	(2000,350,350)
$ATLAS(PFT)$	15	0.801	13.1	11.7	0	(30,70,70)	(2000,350,350)

Table C.4.: *Lengthscans, SI units*

run	n_e (cm^{-3})	a_0	Δt (fs)	Δx (μm)	long. focus pos. (mm)	box size (x_1, x_2, x_3) (μm)	charge/MP (C)
$A100$	$5 \cdot 10^{18}$	2.71	20	22	1	(59.41,175.86,175.86)	$4.57506 \cdot 10^{-15}$
$A100(100mbar)$	$4.83 \cdot 10^{18}$	2.71	20	22	4.54	(60.45,181.35,181.35)	$4.60588 \cdot 10^{-15}$
$A100(120mbar)$	$5.8 \cdot 10^{18}$	2.71	20	22	4.54	(55.2,199,199)	$5.15 \cdot 10^{-15}$
$A100(150mbar)$	$7.25 \cdot 10^{18}$	2.71	20	22	4.54	(49.34,177.62,177.62)	$4.60234 \cdot 10^{-15}$

Table C.5.: *Lengthscans, normalized units (OSIRIS)*

run	ω_0	a_0	$long.rise/fall$	$per.w0$	$long.focus$	box size (x_1, x_2, x_3)	cells (x_1, x_2, x_3)
$A100$	18.66	2.71	2.52	7.862	-425	(25,74,74)	(2350,370,370)
$A100(100mbar)$	18.991	2.71	2.48	7.728	-1877	(25,75,75)	(2375,375,375)
$A100(120mbar)$	17.33	2.71	2.717	8.468	-2100	(25,90,90)	(1940,450,450)
$A100(150mbar)$	15.501	2.71	3.038	9.467	-2300	(25,90,90)	(1940,450,450)

Table C.6.: *LWFA theory, SI units*

run	n_e (cm^{-3})	a_0	Δt (fs)	Δx (μm)	long. focus pos. (mm)	box size (x_1, x_2, x_3) (μm)	charge/MP (C)
$a_0 = 1$	$7 \cdot 10^{18}$	1	15	14.84	0.042	(50,100,100)	$4.7 \cdot 10^{-15}$
$a_0 = 3$	$7 \cdot 10^{18}$	3	15	14.84	0.042	(50,100,100)	$4.7 \cdot 10^{-15}$

Table C.7.: *LWFA theory, normalized units (OSIRIS)*

run	ω_0	a_0	$long.rise/fall$	$per.w0$	$long.focus$	box size (x_1, x_2, x_3)	cells (x_1, x_2, x_3)
$a_0 = 1$	15.775	1	2.239	6.273	4	(25,50,50)	(1963, 248,248)
$a_0 = 3$	15.775	3	2.239	6.273	4	(25,50,50)	(1963, 248,248)

Chapter D

Experimental Length Scan - Low Density Spectra

Figure D.1 shows the summed spectra at different gas cell lengths in the 50 mbar case. As expected, and discussed in detail in VI.1, the cut-off energy increases with increasing gas-cell length. But as the dephasing point is not reached due to insufficient self-focussing also no noticeable high-energy spectral peak forms.
Instead, in this case a low energy peak around 150 MeV can be observed, which develops after approximately 5 mm. From the signal on the scintillating screen shown in figure D.2 it can be seen that this spectral peak features an extremely high (spatial) divergence[1].
This could come from injection into a second bubble behind the laser pulse or from injections into a wakefield that is driven by the first electron bunch after the laser has diffracted. However, the curve of the cut-off energy suggests that at this gas cell length the laser is still present. Also a later measurement of coherent transition radiation generated by the electron bunch could not confirm a signal from two separate bunches at these gas cell lengths ([4], [138]). Another interpretation could then be that the peak formation is owed to a similar process as seen in the simulations in section VI.2.2. Beamloading deforms the electric field in the rear part of the bubble as the laser spot size increases, the blowout radius increases and the driver intensity is reduced. A resulting ”flipped” electric field that is (locally) higher closer to the injection point can lead to spectral bunching. The simultaneously increased bubble size and equally, or even more, disturbed focusing field of the bubble explain the increased divergence.
An appropriate simulation will be needed to confirm this assumption.

[1] The signal of some shots is transversely cut in the picture, but not in the original data.

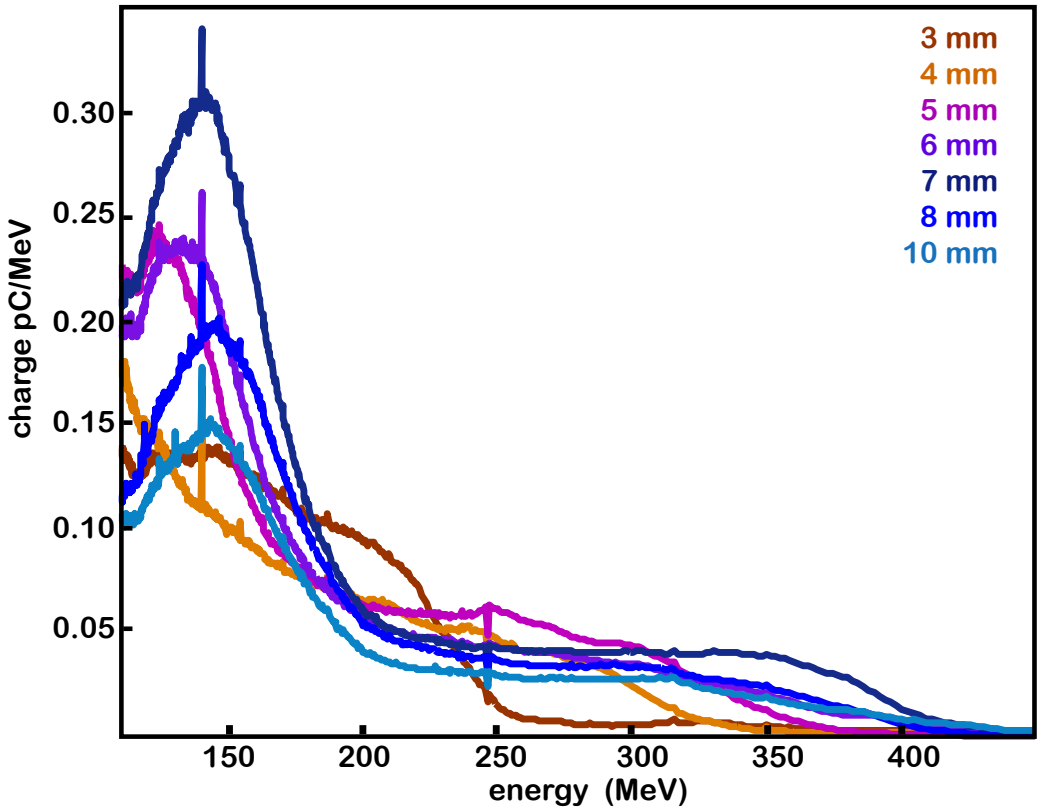

Figure D.1.: 50 mbar. *Average electron spectrum depending on the gas cell length. Average over 31 consecutively recorded spectra per length.*

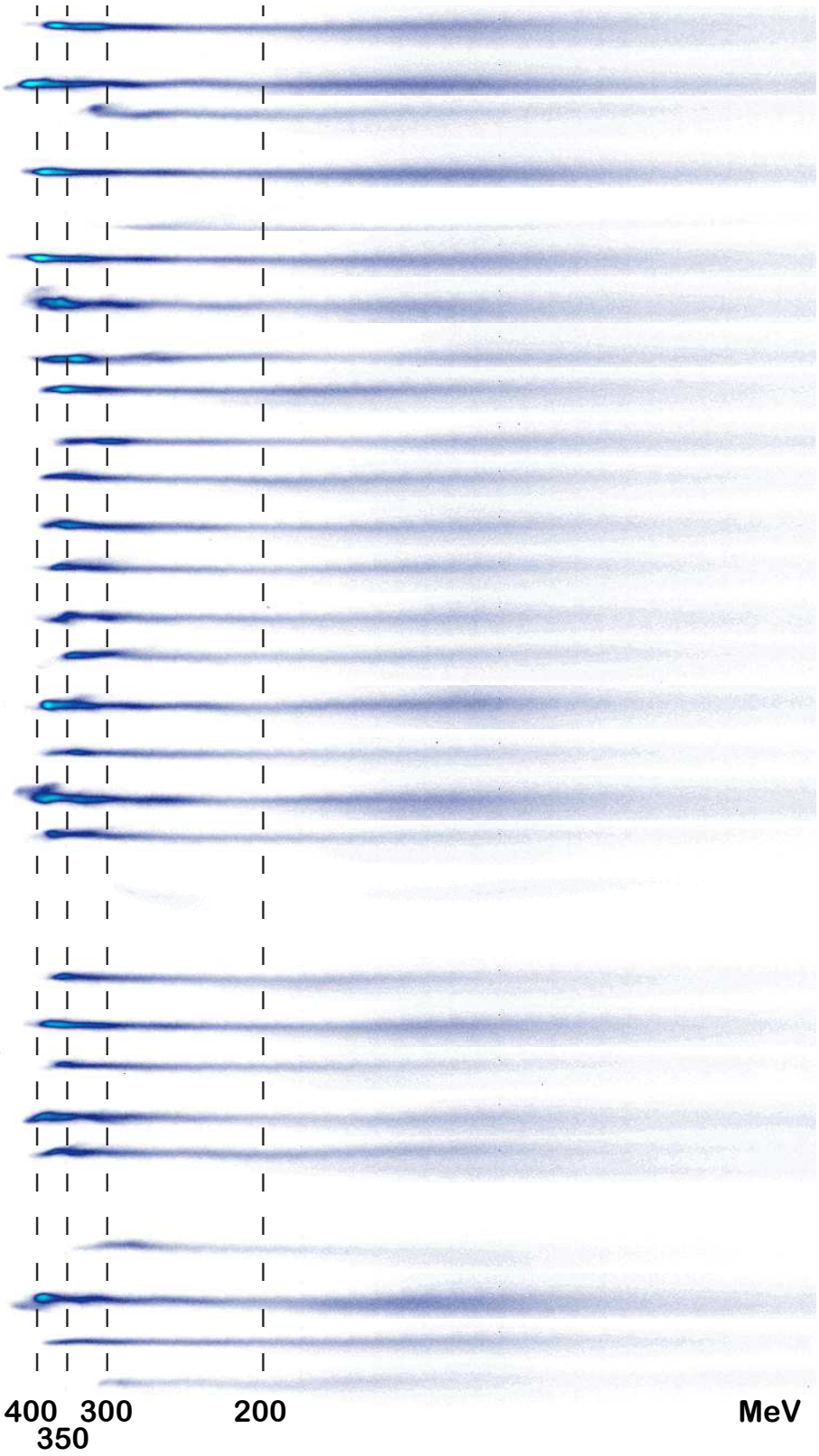

Figure D.2.: *Images of the scintillating screen behind the permanent dipole magnet for a gas cell length of* 7 mm *at* 50 mbar. *The color scale is set to the same maximum as in VI.1*

Chapter E

Pulse Propagation with Kostenbauder Matrices

In some of the experiments presented in this work an angularly chirped pulse was used to drive a plasma wakefield. In order to comprehend the properties and also the evolution of such spatio-temporally distorted pulses a formalism for Gaussian pulse propagation was used that includes these effects. The extension of the ABCD-matrix approach (linear ray tracing) to so-called Kostenbauder matrices will be described in this section. A more detailed overview over the description of Gaussian pulse propagation can also be found in [29] and in the original publication [168].
A Gaussian pulse has a Gaussian spatial (c.f. II.1.3) and a Gaussian temporal electric field strength profile:

$$E(x,y,t) \propto \exp\left[-\left(\frac{1}{w^2}+i\frac{\pi}{\lambda R}\right)(x^2+y^2)-\left(\frac{1}{\tau_0^2}+i\beta\right)t^2\right] \tag{E.1}$$

where w is the Gaussian beam width, R the radius of curvature as given in section II.1.3, and τ_0 is the Gaussian pulse duration with $\tau_0 = \Delta t/(4\ln 2)$ if Δt defines the FWHM pulse duration on the intensity envelope. β characterizes a temporal chirp.
If one considers only one of the spatial dimensions, the exponent can be written as a quadratic form in x and t:

$$E(x,t) \propto \exp\left(\begin{bmatrix} x & t \end{bmatrix}\begin{bmatrix} Q_{xx} & Q_{xt} \\ Q_{tx} & Q_{tt} \end{bmatrix}\begin{bmatrix} x \\ t \end{bmatrix}\right) \tag{E.2}$$

$$= \exp\left(\left[Q_{xx}x^2 + 2Q_{xt}xt - Q_{tt}t^2\right]\right) \tag{E.3}$$

From this representation it follows that

- $Q_{xt} = Q_{tx}$
- The matrix $\boldsymbol{Q} = \left[\begin{smallmatrix} Q_{xx} & Q_{xt} \\ Q_{tx} & Q_{tt} \end{smallmatrix}\right]$ completely characterizes a Gaussian pulse.
- if the off-axis elements are zero, expression (E.1) is reproduced, which is a perfect undisturbed Gaussian pulse. It follows $Q_{xx} = -\frac{1}{w(z)^2} - i\frac{\pi}{\lambda R(z)}$ and $Q_{tt} = \frac{1}{\tau_0^2} - i\beta$

- if $Q_{xt} \neq 0$ a pulse front tilt is present and the angle is given by $\psi = \dfrac{\mathrm{Re}\,(Q_{xt})}{\mathrm{Re}\,(Q_{tt})}$.

In order to propagate such a Gaussian pulse through an optical system, including lenses, gratings, prisms etc., the standard ABCD-matrix formalism (e.g. [169]) can be extended to the time domain. The structure of these extended 4×4 so-called Kostenbauder-matrices $\mathscr{K}$ [168] is best understood if - for the beginning - one characterizes a pulse by a vector, similar to ray propagation, that includes a transverse spatial coordinate x, a propagation angle θ, time t and frequency ν. Then the 4×4 propagation matrices can be introduced, where the matrix elements describe the differential change of the output parameters depending on the different input parameter changes as imposed by one specific optical component.

$$\begin{bmatrix} x_{out} \\ \theta_{out} \\ t_{out} \\ \nu_{out} \end{bmatrix} = \begin{bmatrix} A & B & 0 & E \\ C & D & 0 & F \\ G & H & 1 & I \\ 0 & 0 & 0 & 1 \end{bmatrix} \begin{bmatrix} x_{in} \\ \theta_{in} \\ t_{in} \\ \nu_{in} \end{bmatrix} \tag{E.4}$$

with

A	spatial magnification	$\partial x_{out}/\partial x_{in}$
B	”free space propagation”	$\partial x_{out}/\partial \theta_{in}$
C	”refraction”	$\partial \theta_{out}/\partial x_{in}$
D	angular magnification	$\partial \theta_{out}/\partial \theta_{in}$
E	spatial chirp	$\partial x_{out}/\partial \nu_{in}$
F	angular chirp	$\partial \theta_{out}/\partial \nu_{in}$
G	pulse front tilt	$\partial t_{out}/\partial x_{in}$
H	time versus angle	$\partial t_{out}/\partial \theta_{in}$
I	group delay dispersion	$\partial t_{out}/\partial \nu_{in}$

The 2x2 sub-matrix consisting of the elements A, B, C, D, is the ”normal” ray propagation matrix. Optical elements that do not affect the temporal pulse properties such as focusing mirrors, free space propagation …, are fully described by this sub-matrix (see e.g.[169]), all other off-axis elements of the Kostenbauder matrix in these cases are 0.
However the Kostenbauder matrix of, for example, a diffraction grating mixes spatial and temporal coordinates:

$$\mathscr{K}_{grating} = \begin{bmatrix} -\frac{\cos\beta}{\cos\beta_0} & 0 & 0 & 0 \\ 0 & -\frac{\cos\beta_0}{\cos\beta} & 0 & \frac{\lambda_0}{c}\frac{(\sin\beta-\sin\beta_0)}{\cos\beta} \\ \frac{1}{c}\frac{\sin\beta_0-\sin\beta}{\cos\beta_0} & 0 & 1 & 0 \\ 0 & 0 & 0 & 1 \end{bmatrix} \tag{E.5}$$

Here, β_0 is the incidence angle and β the diffraction angle as also illustrated in Figure II.6. Entry $F = \mathscr{K}^{(2,4)}_{grating}$ describes the angular chirp introduced by the grating. This expression is equivalent to (II.21), taking into account the grating equation $s(\sin\beta - \sin\beta_0) = m\lambda_0$ with groove spacing s, angle of incidence β_0, diffraction angle β and diffraction order m.

In order obtain the propagation matrix through an entire setup of different optical components one simply has to multiply the Kostenbauder matrices of each element and then apply the resulting matrix to the input vector.
Going back to the $\boldsymbol{Q}$-matrix (E.2) to characterize the input pulse and considering a general Kostenbauder-matrix $\mathscr{K}$ (E.4) to describe the effects of an optical system, the matrix $\boldsymbol{Q}_{out}$ defining the resulting output pulse is obtained via

$$\boldsymbol{Q}_{out} = \frac{\begin{bmatrix} A & 0 \\ G & 1 \end{bmatrix} \boldsymbol{Q}_{in} + \begin{bmatrix} B & \frac{1}{\lambda}E \\ H & \frac{1}{\lambda}I \end{bmatrix}}{\begin{bmatrix} i\frac{\lambda}{\pi}C & 0 \\ 0 & 0 \end{bmatrix} \boldsymbol{Q}_{in} + \begin{bmatrix} D & \frac{1}{\lambda}F \\ 0 & 1 \end{bmatrix}} \tag{E.6}$$

As already indicated in E certain spatio-temporal distortions that are *added* by the optical system can be directly retrieved from the Kostenbauder-matrix of the system: E gives the added spatial chirp, F the angular chirp and I the group delay dispersion, that is added during the propagation through the respective optics. However, as already described in II.1.4.2, the pulse front tilt is not exactly determined by the matrix element $G = \partial t_{out}/\partial x_{in}$ of the optical system, as dx_{out} might not be identical to dx_{in}. As mentioned above the pulse front tilt therefore must be extracted from the off-axis Q_{out}-element. The pulse front tilt angle is $\psi = \mathrm{Re}\,(Q_{xt})/\,\mathrm{Re}\,(Q_{tt})$.
Of course, in order to obtain the total spatio-temporal distortions in the final pulse, not only the fraction added by a certain optical system, one always has to analyze the output Q-matrix. A Fourier transform with respect to time t of expression (E.3) delivers $E(x,\omega) = \exp\left(S_{xx}x^2 + 2S_{x\omega}x\omega - S_{\omega\omega}\omega^2\right)$ and the real part of the off-diagonal element $S_{x\omega}$ is the spatial chirp. Similarly, the off-diagonal element of the Fourier transform with respect to t and x, leading to $E(k_x,\omega)$ describes the angular dispersion.

This extended matrix approach for Gaussian pulses can also be useful to retrieve e.g. the total dispersion and pulse elongation introduced by different prism or grating stretcher/-compressor geometries.

Bibliography

[1] S. Kneip, S. R. Nagel, S. F. Martins, S. P. D. Mangles, C. Bellei, O. Chekhlov, R. J. Clarke, N. Delerue, E. J. Divall, G. Doucas, K. Ertel, F. Fiuza, R. Fonseca, P. Foster, S. J. Hawkes, C. J. Hooker, K. Krushelnick, W. B. Mori, C. A. J. Palmer, K. Ta Phuoc, P. P. Rajeev, J. Schreiber, M. J. V. Streeter, D. Urner, J. Vieira, L. O. Silva, and Z. Najmudin1. Near-gev acceleration of electrons by a nonlinear plasma wave driven by a self-guided laser pulse. *Phys. Rev. Lett.*, 103(3), 2009.

[2] Dr. Wilhelm Konrad Röntgen. Eine neue Art von Strahlen - II. Mittheilung. In *Sonderdruck aus den Sitzungsberichten der Würzburger Physik.-medic. Gesellschaft 1895*. Stahel'sche K. Hof- und Universitätsbuch- und Kunsthandlung, 1896.

[3] U. Bonse and M. Hart. An x-ray interferometer. *Applied Physics Letters*, 6(8), 1965.

[4] Sevtoslav Bajlekov. *Towards a free-electron laser driven by electrons from a laser-wakefield accelerator: electron bunch diagnostics and simulations*. PhD thesis, University of Oxford, 2011.

[5] A. Buck, M. Nicolai, K. Schmid, C. M. S. Sears, A. Sävert, J. M. Mikhailova, Ferenc Krausz, M. C. Kaluza, and L. Veisz. Real-time observation of laser-driven electron acceleration. *Nature Physics*, 7:543, 2011.

[6] O. Lundh, J. Lim, C. Rechatin, L. Ammoura, A. Ben-Ismaïl, X. Davoine, G. Gallot, J-P. Goddet, E. Lefebvre, V. Malka, and J. Faure. Few femtosecond, few kiloampere electron bunch produced by a laser–plasma accelerator. *Nature Physics*, 7: 219–222, 2011.

[7] T. Tajima and J. M. Dawson. Laser electron accelerator. *Phys. Rev. Lett.*, 43(4): 267–270, 1979.

[8] D. Strickland and G. Mourou. Compression of amplified chirped optical pulses. *Optics Communications*, 55:447, 1985.

[9] C. E. Clayton, K. A. Marsh, A. Dyson, M. Everett, A. Lal, W. P. Leemans, R. Williams, and C. Joshi. Ultrahigh-gradient acceleration of injected electrons by laser- excited relativistic electron plasma waves. *Phys. Rev. Lett.*, 70(1):37–40, 1993.

[10] A. Modena, Z. Najmudin A., A. E. Dangor, C. E. Clayton, K. A. Marsh, C. Joshi, V. Malka, C. B. Darrow, C. Danson, D. Neely, and F. N. Walsh. Electron acceleration from the breaking of relativistic plasma waves. *Nature*, 377(606-608), 1995.

[11] A. Pukhov and J. Meyer-ter-Vehn. Laser wake field acceleration: the highly nonlinear broken-wave regime. *Appl. Phys. B*, 74:355–361, 2002.

[12] J. Faure, Y. Glinec, A. Pukhov, S. Kiselev, S. Gordienko, E. Lefebvre, J.-P. Rousseau, F. Burgy, and V. Malka. A laser–plasma accelerator producing monoenergetic electron beams. *Nature*, 431:541–544, 2004.

[13] C. G. R. Geddes, Cs. Toth, J. van Tilborg, E. Esarey, C. B. Schroeder, D. Bruhwiler, C. Nieter, J. Cary, and W. P. Leemans. High-quality electron beams from a laser wakefield accelerator using plasma-channel guiding. In *Nature* Faure et al. [12], pages 538–541.

[14] S. P. D. Mangles, C. D. Murphy, Z. Najmudin, A. G. R. Thomas, J. L. Collier, A. E. Dangor, E. J. Divall, P. S. Foster, J. G. Gallacher, C. J. Hooker, D. A. Jaroszynski, A. J. Langley, W. B. Mori, P. A. Norreys, F. S. Tsung, R. Viskup, B. R. Walton, and K. Krushelnick. Monoenergetic beams of relativistic electrons from intense laser–plasma interactions. *Nature*, 431:535–538, 2004.

[15] W. P. Leemans, B. Nagler, A. J. Gonsalves, Cs. Toth, K. Nakamura, C. G. R. Geddes, E. Esarey, C. B. Schroeder, and S. M. Hooker. Gev electron beams from a centimetre-scale accelerator. *Nature Physics*, 2(10):696–699, 2006.

[16] S. Karsch, J. Osterhoff, A. Popp, T. P. Rowlands-Rees, Zs. Major, M. Fuchs, B. Marx, R. Hörlein, K. Schmid, L. Veisz, S. Becker, U. Schramm, B. Hidding, G. Pretzler, D. Habs, F. Grüner, F. Krausz, and S. M. Hooker. Gev-scale electron acceleration in a gas-filled capillary discharge waveguide. *New Journal of Physics*, 9(11):415, 2007.

[17] C. Rechatin, J. Faure, A. Ben-Ismail, J. Lim, R. Fitour, A. Specka, H. Videau, A. Tafzi, F. Burgy, and V. Malka. Controlling the phase-space volume of injected electrons in a laser-plasma accelerator. *Phys. Rev. Lett.*, 102:164801, 2009.

[18] J. Osterhoff, A. Popp, Zs. Major, B. Marx, T. P. Rowlands-Rees, M. Fuchs, M. Geissler, R. Hörlein, B. Hidding, S. Becker, E. A. Peralta, U. Schramm, F. Grüner, D. Habs, F. Krausz, S. M. Hooker, and S. Karsch. Generation of stable, low-divergence electron beams by laser-wakefield acceleration in a steady-state-flow gas cell. *Physical Review Letters*, 101(8):085002, 2008.

[19] ILC, . URL `http://www.linearcollider.org/`.

[20] S. Kneip, C. McGuffey, J. L. Martins, S. F. Martins, C. Bellei, V. Chvykov, F. Dollar, R. Fonseca, C. Huntington, G. Kalintchenko, A. Maksimchuk, S. P. D. Mangles, T. Matsuoka, S. R. Nagel, C. A. J. Palmer, J. Schreiber, K. Ta Phuoc, A. G. R.

Thomas, V. Yanovsky, L. O. Silva, K. Krushelnick, and Z. Najmudin. Bright spatially coherent synchrotron x-rays from a table-top source. *Nature Physics*, 6:980–983, 2011.

[21] M. Fuchs, R. Weingartner, A. Popp, Zs. Major, S. Becker, J. Osterhoff, I. Cortrie, B. Zeitler, R. Hörlein, G. Tsakiris, U. Schramm, T. P. Rowlands-Rees, S. M. Hooker, D. Habs, F. Krausz, S. Karsch, and F. Grüner. Laser-driven soft-x-ray undulator source. *Nature Physics*, 5(11):826, 2009.

[22] F. Grüner, S. Becker, U. Schramm, T. Eichner, M. Fuchs, R. Weingartner, D. Habs, J. Meyer ter Vehn, M. Geissler, M. Ferrario, L. Serafini, B. van der Geer, H. Backe, W. Lauth, and S. Reiche. Design considerations for table-top, laser-based VUV and X-ray free electron lasers. *Appl. Phys. B*, (3):431–435, 2007.

[23] E. Esarey, S. K. Ride, and P. Sprangle. Nonlinear thomson scattering of intense laser pulses from beams and plasmas. *Phys. Rev. E*, 48:3003–3021, 1993.

[24] H. Schwoerer, B. Liesfeld, H.-P. Schlenvoigt, K.-U. Amthor, and R. Sauerbrey. Thomson-backscattered X-rays from laser-accelerated electrons. *Phys. Rev. Lett.*, 96(014802), 2006.

[25] J.D. Jackson. *Classical Electrodynamics*. Wiley, New York, 2006.

[26] C. Rulliere, editor. *Femtosecond Laser Pulses - Principles and Experiments*. Springer, 1998.

[27] G. Pretzler. Höchstleistungskurzpulslaser. lecture notes (unpublished), 2000.

[28] M. Wollenhaupt, A. Assion, and T. Baumert. Femtosecond laser pulses: Linear properties, manipulation, generation and measurement. URL `http://www.physik.uni-kassel.de/fileadmin/typo3home/groups/11/Downloads/Sonstiges/Skript-Version30.pdf`. lecture notes.

[29] R. Trebino. Spatio-temporal optics (lecture notes). URL `https://public.me.com/ricktrebinoorhttp://www.physics.gatech.edu/gcuo/lectures/UltrafastOptics/lectures/UFO-06-Spatio-temporal-optics.ppt`.

[30] X. Gu, S. Akturk, and R. Trebino. Spatial chirp in ultrafast optics. *Optics Communications*, 242:599, 2004.

[31] G. Pretzler, A. Kasper, and K.J. Witte. Angular chirp and tilted light pulses in cpa lasers. *Appl. Phys. B*, 70:1, 2000.

[32] O. E. Martinez. Pulse distortions in tilted pulse schemes for ultrashort pulses. *Optics Communications*, 59(3):229, 1986.

[33] S. Akturk, X. Gu, E. Zeek, and R. Trebino. Pulse-front tilt caused by spatial and temporal chirp. *Optics Express*, 12(19):4399, 2004.

[34] J.W. Goodman. *Introduction to Fourier Optics*. The McGraw-Hill Companies, Inc., 1996.

[35] J. Hebling. Derivation of the pulse front tilt caused by angular dispersion. *Optical and Quantum Electronics*, 28:1759, 1996.

[36] J.-C. Diels and W. Rudolph. *Ultrashort Laser Pulse Phenomena: Fundamentals, Techniques, and Applications on a Femtosecond Time Scale*. Academic Press (Optics and Photonics Series), 1996.

[37] F. Verluise, V. Laude, J.-P Huignard, P. Tournois, and A. Migus. Arbitrary dispersion control of ultrashort optical pulses with acoustic waves. *J. Opt. Soc. Am. B*, 17(1), 2000.

[38] P. Tournois. Acousto-optic programmable dispersive filter for adaptive compensation of group delay time dispersion in laser systems. *Optics Communications*, 140 (4-6):245, 1997.

[39] J. Osterhoff. *Stable, ultra-relativistic electron beams by laser-wakefield acceleration*. PhD thesis, Ludwig-Maximilans-Universität München, 2009.

[40] Rainer Hörlein. *Investigation of the XUV Emission from the Interaction of Intense Femtosecond Laser Pulses with Solid Targets*. PhD thesis, Ludwig-Maximilans-Universität München, 2008.

[41] K. Strehl. Aplanatische und fehlerhafte Abbildung im Fernrohr. *Zeitschrift für Instrumentenkunde*, 15:362, 1895.

[42] R. J. Goldston and P.H. Rutherford. *Introduction to Plasma Physics*. In Gibbon [43], 1995.

[43] Paul Gibbon. *Short Pulse Laser Interactions with Matter*. Imperial College Press, 2007.

[44] W.L. Kruer. *Physic sof laser plasma interactions*. Addison Wesley Publishing Company, 1988.

[45] J. Meyer-ter-Vehn and A. Pukhov. Relativistic laser-plasma interactions: I. analytical tools. lecture notes.

[46] C. I. Moore, J. P. Knauer, and D. D. Meyerhofer. Observation of the transition from thomson to compton scattering in multiphoton interactions with low-energy electrons. *Physical Review Letters*, 74(13):2439–2442, 1995.

[47] D. Bauer. Theory of intense laser-matter interaction. lecture notes, http://www.physik.uni-rostock.de/fileadmin/Physik/Bauer/tilmi.pdf.

[48] M. V. Ammosov, N. B. Delone, and V. P. Krainov. Tunnel ionization of complex atoms and of atomic ions in an alternating electromagnetic field. *Soviet Physics, Journal of Experimental and Theoretical Physics*, 64(6):1191, 1986.

[49] N. B. Delone and V. P. Krainov. *Multiphoton processes in atoms*. Springer Verlag, Heidelberg, 2nd edition, 1994.

[50] G. Mainfray and G. Manus. Multiphoton ionization of atoms. *Reports on Progress in Physics*, 54(10):1333, 1991.

[51] G. Leuchs. Multiphoton ionization of atoms. In J. Harvey and D. Walls, editors, *Laser Physics*, volume 182 of *Lecture Notes in Physics*, pages 174–194. Springer Berlin, Heidelberg, 1983. ISBN 978-3-540-12305-7.

[52] L. Landau and L. Pitaevskii. *Course of Theoretical Physics, Physical Kinetics*, volume 10. Pergamon Press, Oxford, 1981.

[53] P. Kaw and J. Dawson. Relativistic nonlinear propagation of laser beams in cold overdense plasmas. *Physics of Fluids*, 13(2):472–481, 1970.

[54] N. A. Bobrova, A. A. Esaulov, J.-I. Sakai, P. V. Sasorov, D. J. Spence, A. Butler, S. M. Hooker, and S. V. Bulanov. Simulations of a hydrogen-filled capillary discharge waveguide. *PHYSICAL REVIEW E*, 65:016407, 2001.

[55] E. Esarey, P. Sprangle, J. Krall, and A. Ting. Overview of plasma-based accelerator concepts. *IEEE Transactions on Plasma Science*, 24(2):252–288, 1996.

[56] W. B. Mori. The physics of the nonlinear optics of plasmas at relativistic intensities for short-pulse lasers. *IEEE Journal of Quantum Electronics*, 33(11):1942, 1997.

[57] P. Sprangle, E. Esarey, J. Krall, and G. Joyce. Propagation and guiding of intense laser pulses in plasmas. *Phys. Rev. Lett.*, 69(15):2200–2203, 1992. doi: 10.1103/PhysRevLett.69.2200.

[58] W. Lu, M. Tsoufras, C. Joshi, F.S. Tsung, W.B. Mori, J. Vieira, R. A. Fonseca, and L. O. Silva. Generating multi-gev electron bunches using single stage laser wakefield acceleration in a 3d nonlinear regime. *Phys. Rev. ST Accel. Beams*, 10:061301, 2007.

[59] H.S. Brandi, C. Manus, and G. Mainfray. Relativistic self-focusing of ultraintense laser pulses in inhomogeneous underdense plasmas. *Phys. Rev. E*, 47(5), 1993.

[60] E. Esarey, C. B. Schroeder, and W. P. Leemans. Physics of laser-driven plasma-based electron accelerators. *Reviews of Modern Physics*, 81:1229–1280, 2009.

[61] G. Z. Sun, E. Ott, Y. C. Lee, and P. Guzdar. Self-focusing of short intense pulses in plasmas. *Phys. Fluids*, 30:526, 1987.

[62] B. Hafizi, A. Ting, P. Sprangle, and R. F. Hubbard. Relativistic focusing and ponderomotive channeling of intense laser beams. In *Phys. Rev. E* Sun et al. [61], page 4120.

[63] C. D. Decker, W. B. Mori, K.-C. Tzeng, and T. Katsouleas. The evolution of ultra-intense, short-pulse lasers in underdense plasmas. *Phys. Plasmas*, 3:2047, 1996.

[64] A.G.R. Thomas, Z. Najmudin, S. P.D. Mangles, C.D. Murphy, A. E. Dangor, C. Kamperidis, K. L. Lancaster, W.B. Mori, P.A. Norreys, W. Rozmus, and K. Krushelnick. Effect of laser-focusing conditions on propagation and monoenergetic electron production in laser-wakefield accelerators. *Physical Review Letters*, 98:095004, 2007.

[65] M. D. Feit, A. M. Komashko, S. L. Musher, A. M. Rubenchik, and S. K. Turitsyn. Electron cavitation and relativistic self-focusing in underdense plasma. *Phys. Rev. E*, 57(6):7122–7125, 1998.

[66] A.M. Rubenchik M.D. Feit, A.M. Komashko. Relativistic self-focusing in underdense plasma. *Physica D*, 152–153:705–713, 2001.

[67] T. P. A. Ibbotson, N. Bourgeois, T. P. Rowlands-Rees, L. S. Caballero, S. I. Bajlekov, P. A. Walker, S. Kneip, S. P. D. Mangles, S. R. Nagel, C. A. J. Palmer, N. Delerue, G. Doucas, D. Urner, O. Chekhlov, R. J. Clarke, E. Divall, K. Ertel, P. Foster, S. J. Hawkes, C. J. Hooker, B. Parry, P. P. Rajeev, M. J. V. Streeter, and S. M. Hooker. Investigation of the role of plasma channels as waveguides for laser-wakefield accelerators. *New Journal of Physics*, 12(045008), 2010.

[68] A. Butler, D. J. Spence, and S. M. Hooker. Guiding of high-intensity laser pulses with a hydrogen-filled capillary dischargewaveguide. *Phys. Rev. Lett.*, 89:185003, 2002.

[69] P. Volfbeyn, E. Esarey, and W. P. Leemans. Guiding of laser pulses in plasma channels created by the ignitor-heater technique. *Phys. Plasmas*, 6(5):2269, 1999.

[70] D. F. Gordon, B. Hafizi, R. F. Hubbard, J. R. Penano, P. Sprangle, and A. Ting. Asymmetric self-phase modulation and compression of short laser pulses in plasma channels. *Phys. Rev. Lett.*, 90(21), 2003.

[71] B. Hidding, K.-U. Amthor, B. Liesfeld, H. Schwoerer, S. Karsch, M. Geissler, L. Veisz, K. Schmid, J. G. Gallacher, S. P. Jamison, D. Jaroszynski, G. Pretzler, and R Sauerbrey. Generation of quasimonoenergetic electron bunches with 80-fs laser pulses. *Phys. Rev. Lett.*, 96:105004, 2006.

[72] J. Faure, Y. Glinec, J. J. Santos, F. Ewald, J.-P. Rousseau, S. Kiselev, A. Pukhov, T. Hosokai, and V. Malka. Observation of laser-pulse shortening in nonlinear plasma waves. 95:205003, 2005.

[73] J. Schreiber, C. Bellei, S. P. D. Mangles, C. Kamperidis, S. Kneip, S. R. Nagel, C. A. J. Palmer, P. P. Rajeev, M. J. V. Streeter, and Z. Najmudin. Complete temporal characterization of asymmetric pulse compression in a laser wakefield. *Phys. Rev. Lett.*, 105:235003, 2010.

[74] V. N. Tsytovich, U. De Angelis, and R. Bingham. Beat-wave-wake acceleration by short high intensity laser pulses. *Comments on Plasma Physics and Controlled Fusion*, 12:249, 1989.

[75] V. I. Berezhiani and I. G. Murusidze. Relativistic wake-field generation by an intense laser pulse in a plasma. *Physics Letters A*, 148(6–7):338, 1990.

[76] S. V. Bulanov, V. I. Kirsanov, and A. S. Sakharov. Excitation of ultra-relativistic langmuir waves by electromagnetic pulses. *Physica Scripta*, T30:208, 1990.

[77] P. Sprangle, E. Esarey, and A. Ting. Nonlinear theory of intense laser-plasma interactions. *Physical Review Letters*, 64(17):2011, 1990.

[78] S. Dalla and M. Lontano. On the maximum longitudinal electric field of a large amplitude electron plasma wave excited by a short electromagnetic radiation pulse. *Physics Letters A*, 173(6):456, 1993.

[79] E. Esarey, P. Sprangle, J. Krall, and A. Ting. Self-focusing and guiding of short laser pulses in ionizing gases and plasmas. *IEEE Journal of Quantum Electronics*, 33(11):1879, 1997.

[80] R.J. Kingham and A. R. Bell. Enhanced wakefields for the 1d laser wakefield accelerator. *Physical Review Letters*, 79(24):4810, 1997.

[81] T. Esirkepov, S. V. Bulanov, M. Yamagiwa, and T. Tajima. Electron, positron, and photon wakefield acceleration: trapping, wake overtaking, and ponderomotive acceleration. *Physical Review Letters*, 96(1):014803, 2006.

[82] E. Esarey, B. A. Shadwick, C. B. Schroeder, and W. P. Leemans. Nonlinear pump depletion and electron dephasing in laser wakefield accelerators. volume 737, pages 578–584, 2004.

[83] A. Ting, E. Esarey, and P.Sprangle. Nonlinear wake-field generation and relativistic focusing of intense laser pulses in plasmas. *Physics of Fluids B: Plasma Physics*, 2(6):1390–1394, 1990.

[84] S. V. Bulanov, I. N. Inovenkov, V. I. Kirsanov, N. M. Naumova, and A. S. Sakharov. Nonlinear depletion of ultrashort and relativistically strong laser pulses in an underdense plasma. *Physics of Fluids B: Plasma Physics*, 4(7):1935–1942, 1992.

[85] D. Teychenné, G. Bonnaud, and J.-L. Bobin. Electrostatic and kinetic energies in the wake wave of a short laser pulse. *Physics of Plasmas*, 1(6):1771–1773, 1994.

[86] B. A. Shadwick, C. B. Schroeder, and E. Esarey. Nonlinear laser energy depletion in laser-plasma accelerators. *Phys. Plasmas*, 16(056704), 2009.

[87] C. B. Schroeder, E. Esarey, B. A. Shadwick, and W. P. Leemans. Trapping, dark current, and wave breaking in nonlinear plasma waves. *Phys. Plasmas*, 13:033103, 2006.

[88] S. V. Bulanov, F. Pegoraro, A. M. Pukhov, and A. S. Sakharov. Transverse-wake wave breaking. *Phys. Rev. Lett.*, 78(22):4205, 1997.

[89] D. Umstadter, J.K. Kim, and E. Dodd. Laser injection of ultrashort electron pulses into wake-field plasma waves. *Phys. Rev. Lett.*, 76:2073, 1996.

[90] C. B. Schroeder, P. B. Lee, J. S. Wurtele, E. Esarey, and W. P. Leemans. Generation of ultrashort electron bunches by colliding laser pulses. *Phys. Rev. E*, (59):6037–6047, 1999 (and references herein).

[91] J. Faure, C. Rechatin, A. Norlin, A. Lifschitz, Y. Glinec, and V. Malka. Controlled injection and acceleration of electrons in plasma wakefields by colliding laser pulses. *Nature*, 444:737–739, 2006.

[92] H. Suk, N. Barov, J. B. Rosenzweig, and E. Esarey. Plasma electron trapping and acceleration in a plasma wake field using a density transition. *Phys. Rev. Lett.*, 86: 1011–1014, 2001.

[93] K. Schmid, A. Buck, C. M. S. Sears, J. M. Mikhailova, R. Tautz, D. Herrmann, M. Geissler, F. Krausz, and L. Veisz. Density-transition based electron injector for laser driven wakefield accelerators. *Physical Review Special Topics - Accelerators and Beams*, 13:091301, 2010.

[94] T. Katsouleas, S. Wilks, P. Chen, J.M. Dawson, and J.J. Su. Beam loading in plasma accelerators. *Particle Accelerators*, 22:81–99, 1987.

[95] M. Tzoufras, W. Lu, F. S. Tsung, C. Huang, W. B. Mori, T. Katsouleas, J. Vieira, R. A. Fonseca, and L. O. Silva. Beam loading in the nonlinear regime of plasma-based acceleration. *Physical Review Letters*, 101(145002), 2008.

[96] S. Masuda, E. Miura, K. Koyama, S. Kato, M. Adachi, T. Watanabe, K. Torii, and M. Tanimoto. Energy scaling of monoenergetic electron beams generated by the laser-driven plasma based accelerator. *Physics of Plasmas*, 14(2):023103, 2007.

[97] A. Maksimchuk, S. Reed, N. Naumova, V. Chvykov, B. Hou, G. Kalintchenko, T. Matsuoka, J. Nees, P. Rousseau, G. Mourou, and V. Yanovsky. Energy scaling of quasi-monoenergetic electron beams from laser wakefields driven by 40-tw ultrashort pulses. *Applied Physics B: Lasers and Optics*, 89:201–207, 2007.

[98] A. J. W. Reitsma, R. A. Cairns, R. Bingham, and D. A. Jaroszynski. Efficiency and energy spread in laser-wakefield acceleration. *Phys. Rev. Lett.*, 94(8):085004, 2005.

[99] K. V. Lotov. Blowout regimes of plasma wakefield acceleration. *Phys. Rev. E*, 69 (4):046405, 2004.

[100] S. Gordienko and A. Pukhov. Scalings for ultrarelativistic laser plasmas and quasi-monoenergetic electrons. *Physics of Plasmas*, 12:043109, 2005.

[101] W. Lu, C. Huang, M. Zhou, W. B. Mori, and T. Katsouleas. Nonlinear theory for relativistic plasma wakefields in the blowout regime. *Phys. Rev. Lett.*, 96:165002, 2006.

[102] K. H. Pankofsky and W. A. Wenzel. Some considerations concerning the transverse deflection of charged particles in radio-frequency fields. *Review of Scientific Instruments*, 27:967, 1956.

[103] A. G. Khachatryan, A. Irman, F. A. van Goor, and K.-J. Boller. Femtosecond electron-bunch dynamics in laser wakefields and vacuum. *Phys. Rev. ST Accel. Beams*, 10:121301, 2007.

[104] R. Weingartner. *Characterization of the transverse slice emittance of laser-wakefield-accelerated electrons*. PhD thesis, Ludwig-Maximilans-Universität München, 2011.

[105] A.G.R. Thomas. Scalings for radiation from plasma bubbles. *Physics of Plasmas*, 17:056708, 2010.

[106] E. Esarey, B. A. Shadwick, P. Catravas, and W. P. Leemans. Synchrotron radiation from electron beams in plasma-focusing channels. *Phys. Rev. E*, 65:056505, 2002.

[107] K. Nemeth, B. Shen, Y. Li, H. Shang, R. Crowell, K. C. Harkay, and J. R. Cary. Laser-driven coherent betatron oscillation in a laser-wakefield cavity. *Phys. Rev. Lett.*, 100:095002, 2008.

[108] A. Popp, J. Osterhoff, T. P. Rowlands-Rees, Zs. Major, M. Fuchs, B. Marx, R. Hörlein, K. Schmid, B. Hidding, L. Veisz, F. Grüner, U. Schramm, F. Krausz, S.M. Hooker, and S. Karsch. Electron acceleration in a gas-discharge capillary. In Pawel Gasior and Jerzy Wolowski, editors, *34th EPS Conference on Plasma Phys. Warsaw*, volume 31F of *europhysics conference abstracts*, pages O–3.002. European Physical Society, 2007.

[109] T. P. Rowlands-Rees, C. Kamperidis, S. Kneip, A. J. Gonsalves, S. P. D. Mangles, J. G. Gallacher, E. Brunetti, T. Ibbotson, C. D. Murphy, P. S. Foster, M. J. V. Streeter, F. Budde, P. A. Norreys, D. A. Jaroszynski, K. Krushelnick, Z. Najmudin, and S. M. Hooker. Laser-driven acceleration of electrons in a partially ionized plasma channel. *Phys. Rev. Lett.*, 100(105005), 2008.

[110] J. Osterhoff, A. Popp, Zs. Major, B. Marx, T. P. Rowlands-Rees, M. Fuchs, R. Hörlein, F. Grüner, D. Habs, F. Krausz, S. M. Hooker, and S. Karsch. Stable laser-driven electron beams from a steady-state-flow gas cell. In *ADVANCED ACCELERATOR CONCEPTS: Proceedings of the Thirteenth Advanced Accelerator Concepts Workshop*, volume 1086 of *AIP Conf. Proc.*, page 125, 2009.

[111] R. Trebino. *Frequency-Resolved Optical Gating: The Measurement of Ultrashort Laser Pulses*. Springer, 2002.

[112] R. Trebino, P. Bowlan, P. Gabolde, X. Gu, S. Akturk, and M. Kimmel. Simple devices for measuring complex ultrashort pulses. *Laser and Photonics Reviews*, 3 (3):314, 2009.

[113] Cawo scintillating screens, . URL http://www.cawo.com/.

[114] Y. Glinec, J. Faure, A. Guemnie-Tafo, V. Malka, H. Monard, J. P. Larbre, V. De Waele, J. L. Marignier, and M. Mostafavi. Absolute calibration for a broad range single shot electron spectrometer. *Review of Scientific Instruments*, 77(10):103301, 2006.

[115] A. Buck, K. Zeil, A. Popp, K. Schmid, A. Jochmann, S. D. Kraft, B. Hidding, T. Kudyakov, C. M. S. Sears, L. Veisz, S. Karsch, J. Pawelke, R. Sauerbrey, T. Cowan, F. Krausz, and U. Schramm. Absolute charge calibration of scintillating screens for relativistic electron detection. *Review of Scientific Instruments*, 81(3):033301, 2010.

[116] Vacuumschmelze, . URL http://www.vacuumschmelze.de/.

[117] General partickle tracking code, . URL http://www.pulsar.nl/gpt/index.html.

[118] M. Sonoda, M. Takano, J. Miyahara, and H. Kato. Computed radiography utilizing scanning laser stimulated luminescence. *Radiology*, 148:833, 1983.

[119] K. Takahashi. Kijinsei keikotai o mochita imeijingu shisutemu - imaging systems using photostimulable phosphors. In *240th Meeting Technical Digest*, page 1. Phosphor Research Society of Japan, 1992.

[120] Kazuo A. Tanaka, Toshinori Yabuuchi, Takashi Sato, Ryosuke Kodama, Yoneyoshi Kitagawa, Teruyoshi Takahashi, Toshiji Ikeda, Yoshihide Honda, and Shuuichi Okuda. Calibration of imaging plate for high energy electron spectrometer. *Review of Scientific Instruments*, 76(1):013507, 2005.

[121] K. Zeil, S. D. Kraft, A. Jochmann, F. Kroll, W. Jahr, U. Schramm, L. Karsch, J. Pawelke, B. Hidding, and G. Pretzler. Absolute response of fuji imaging plate detectors to picosecond-electron bunches. *Review of Scientific Instruments*, 81(1): 013307, 2010.

[122] mb-microtec, . URL http://www.mbmicrotec.com.

[123] J. B. Birks. *The Theory and Practice of Scintillation Counting*. Pergamon, Oxford, 1964.

[124] . URL http://www.openfoam.com/.

[125] Thomas Benedikt Göppner. Density gradients in discharge capillary waveguides. Master's thesis, Ludwig-Maximilans-Universität München, 2011.

[126] V. L. Ginzburg and I. M. Frank. Radiation of uniformly moving electron at transition from one media into another one. *Sov. Phys. JETP*, 16(15), 1946.

[127] J. van Tilborg, C.B. Schroeder, E. Esarey, and W.P. Leemans. Pulse shape and spectrum of coherent diffraction-limited transition radiation from electron beams. *Laser and Particle Beams, Cambridge University Press*, 22:415–422, 2004.

[128] Hossein Delsim-Hashemi. *Infrared Single Shot Diagnostics for the Longitudinal Profile of the Electron Bunches at FLASH*. PhD thesis, DESY, 2008. URL `http://www-library.desy.de/preparch/desy/thesis/desy-thesis-08-024.pdf`.

[129] Erwin Loewen and Christopher Palmer. *Diffraction Grating Handbook*. Newport Corporation, 6th edition.

[130] InfraTec, . URL `http://www.infratec.de/`.

[131] R.Lai and A.J. Sievers. On using the coherent far ir radiation produced by a charged-particle bunch to determine its shape: I analysis. *Nuclear Instruments and Methods in Physics Research A*, 397:221–231, 1997.

[132] R. Weingartner, S. Raith, A. Popp, S. Chou, J. Wenz, K. Khrennikov, M. Heigoldt, A. R. Maier, N. Kajumba, M. Fuchs, F. Krausz, S. Karsch, and F. Grüner. preliminary title: Ultra-low slice emittance electron beams from a laser-wakefield accelerator. *in preparation*, 2011.

[133] M. J. Hogan, C. D. Barnes, C. E. Clayton, F. J. Decker, S. Deng, P. Emma, C. Huang, R. H. Iverson, D. K. Johnson, C. Joshi, T. Katsouleas, P. Krejcik, W. Lu, K. A. Marsh, W. B. Mori, P. Muggli, C. L. O'Connell, E. Oz, R. H. Siemann, and D. Walz. Multi-gev energy gain in a plasma-wakefield accelerator. *Phys. Rev. Lett.*, 95(054802), 2005.

[134] P Muggli, I Blumenfeld, C E Clayton, F J Decker, M J Hogan, C Huang, R Ischebeck, R H Iverson, C Joshi, T Katsouleas, N Kirby, W Lu, K A Marsh, W B Mori, E Oz, R H Siemann, D R Walz, and M Zhou. Energy gain scaling with plasma length and density in the plasma wakefield accelerator. *New Journal of Physics*, 12(045022), 2010.

[135] K. H. Pae, I. W. Choi, and J. Leea. Self-mode-transition from laser wakefield accelerator to plasma wakefield accelerator of laser-driven plasma-based electron acceleration. *Phys. Plasmas*, 17(123104), 2010.

[136] S. P. D. Mangles, A. G. R. Thomas, M. C. Kaluza, O. Lundh, F. Lindau, A. Persson, F. S. Tsung, Z. Najmudin, W.B. Mori, C.-G. Wahlström, and K. Krushelnick. Laser-wakefield acceleration of monoenergetic electron beams in the first plasma-wave period. *Phys. Rev. Lett.*, 96(215001), 2006.

[137] Y. Y. Li, Y. J. Gu, Z. Zhu, X. F. Li, H. Y. Ban, Q. Kong, and S. Kawata. Direct laser acceleration of electron by an ultra intense and short-pulsed laser in under-dense plasma. *Phys. Plasmas*, 18(053104), 2011.

[138] M. Heigoldt, S. Bajlekov, A. Popp, K. Khrennikov, J. Wenz, S.-W. Chou, F. Krausz, S. Hooker, and S. Karsch. perlimiary title: Evolution of electron bunch duration and observation of double bunch acceleration. in preparation.

[139] Timon Mehrling. Studying laser wakefield acceleration of relativistic electron bunches in inhomogeneous plasma with pic simulations. Master's thesis, Technische Universität Muñchen, 2011.

[140] M. Geissler, J. Schreiber, and J. Meyer-ter-Vehn. Bubble acceleration of electrons with few-cycle laser pulses. *New Journal of Physics*, 8(186), 2006.

[141] C.G.R. Geddes, D. Bruhwiler, J.R. Cary, E. Cormier-Michel, E.Esarey, C.B. Schroeder, W.A. Isaacs, N. Stinus, P. Messmer, A. Hakim, K. Nakamura, A.J. Gonsalves, D. Panasenko, G.R. Plateau, Cs. Toth, B.Nagler, J. van Tilborg, T. Cowan, S. M. Hooker, and W.P. Leemans. Laser wakefield simulations towards development of compact particle accelerators. *Journal of Physics: Conference Series (SciDAC 2007)*, 78(012021), 2007.

[142] Anthony J. Campillo. *Self-focusing: Past and Present (Topics in Applied Physics)*, volume 114, chapter 6 (Small-Scale Self-focusing). Springer Berlin / Heidelberg, 2009.

[143] E. Cormier-Michel, B. A. Shadwick, C. G. R. Geddes, E. Esarey, C. B. Schroeder, and W. P. Leemans. Unphysical kinetic effects in particle-in-cell modeling of laser wakefield accelerators. *Phys. Rev. E*, 78(1):016404, 2008.

[144] B. M. Cowan, D. L. Bruhwiler, E. Cormier J. R. Cary, E. Esarey, C. G. R. Geddes, W. P. Leemans, and C. B. Schroeder. Advanced models for simulation of laser plasma accelerator stages. In *Laser and Plasma Accelerators Workshop, Shanghai*, 2011.

[145] S. F. Martins, R. A. Fonseca, J. Vieira, L. O. Silva, W. Lu, and W. B. Mori. Modeling laser wakefield accelerator experiments with ultrafast particle-in-cell simulations in boosted frames. *Phys. Plasmas*, 17(056705), 2010.

[146] J.-L. Vaya, P. Colella, A. Friedman, D.P. Grote, P. McCorquodale, and D.B. Serafini. Implementations of mesh refinement schemes for particle-in-cell plasma simulations. *Comput. Phys. Commun*, 164:297–305, 2004.

[147] K. Varju, A.P. Kovacs, G. Kurdi, and K. Osvay. High-precision measurement of angular dispersion in a cpa laser. *Appl. Phys. B*, 74([Suppl.]):S259–S263, 2002.

[148] Y. Glinec, J. Faure, A. Lifschitz, J. M. Vieira, R A. Fonseca, L. O. Silva, and V. Malka. Direct observation of betatron oscillations in a laser-plasma electron accelerator. *EPL (Europhysics Letters)*, 81(6):64001, 2008.

[149] S. P. D. Mangles, G. Genoud, S. Kneip, M. Burza, K. Cassou, B. Cros, N. P. Dover, C. Kamperidis, Z. Najmudin, A. Persson, J. Schreiber, F. Wojda, and C.-G. Wahlström. Controlling the spectrum of x-rays generated in a laser-plasma accelerator by tailoring the laser wavefront. *Applied Physics Letters*, 95(18), 2009.

[150] J. Wenz, K. Khrennikov S. Schleede, M. Heigoldt, J. Xu, F. Krausz, F. Pfeiffer, and S. Karsch. peliminary title: Phase contrast imaging with betatron radiation from laser-plasma accelerators. *in preparation*, 2011.

[151] F Albert, K Ta Phuoc, R Shah, S Corde, R Fitour, A Tafzi, F Burgy, D Douillet, T Lefrou, and A Rousse. Full characterization of a laser-produced kev x-ray betatron source. *Plasma Physics and Controlled Fusion*, 50(12):124008, 2008.

[152] S. Fourmaux, S. Corde, K. Ta Phuoc, P. Lassonde, G. Lebrun, S. Payeur, F. Martin, S. Sebban, V. Malka, A. Rousse, and J. C. Kieffer. Single shot phase contrast imaging using laser-produced betatron x-ray beams. *Optics Letters*, 36(13):2425, 2011.

[153] S. W. Hwang and H. J. Lee. Betatron radiation of an off-axis injected electron in a laser wakefield accelerator. *Journal of the Optical Society of Korea*, 13(1):86–91, 2009.

[154] K. Ta Phuoc, R. Fitour, A. Tafzi, T. Garl, N. Artemiev, R. Shah, F. Albert, D. Boschetto, A. Rousse, D-E. Kim, A. Pukhov, V. Seredov, and I. Kostyukov. Demonstration of the ultrafast nature of laser produced betatron radiation. *Phys. Plasmas*, 14(080701), 2007.

[155] S.Y. Kalmykov, S.A. Reed, S.A. Yi, A. Beck, A.F. Lifschitz, X. Davoine, E. Lefebvre, V. Khudik, G. Shvets, P. Dong, X. Wang, D. Du, S. Bedacht, Y. Zhao, W. Henderson, A. Bernstein, G. Dyer, M. Martinez, E. Gaul, T. Ditmire, and M.C. Downer. Laser wakefield electron acceleration on texas petawatt facility: Towards multi-gev electron energy in a single self-guided stage. *High Energy Density Physics*, 6(2): 200–206, 2010.

[156] C. McGuffey, A. G. R. Thomas, W. Schumaker, T. Matsuoka, V. Chvykov, F. J. Dollar, G. Kalintchenko, V. Yanovsky, A. Maksimchuk, and K. Krushelnick. Ionization induced trapping in a laser wakefield accelerator. *Phys. Rev. Lett.*, 104(2), 2010.

[157] T. Matsuoka, S. Kneip, C. McGuffey, C. Palmer, J. Schreiber, C. Huntington, Y. Horovitz, F. Dollar, V. Chvykov, G. Kalintchenko, A.G.R. Thomas, V. Yanovsky, K. Ta Phuoc, S. P. D. Mangles, Z. Najmudin, A. Maksimchuk, and K. Krushelnick. Synchrotron x-ray radiation from laser wakefield accelerated electron beams in a plasma channel. *Journal of Physics: Conference Series (The Sixth International Conference on Inertial Fusion Sciences and Applications)*, 244(042026), 2010.

[158] DESY - HASYLAB, spectral characterstics of x-ray sources, . URL http://hasylab.desy.de/facilities/sr_and_fel_basics/fel_basics/tdr_spectral_characteristics/index_eng.html.

[159] A. Roussea, K. Ta Phuoc, R. Shah, R. Fitour, and F. Albert. Scaling of betatron x-ray radiation. *Eur. Phys. J. D*, 45:391–398, 2007.

[160] Zs. Major, S. Trushin, I. Ahmad, M. Siebold, C. Wandt, S. Klingebiel, T.-J. Wang, J. A. Fülöp, A. Henig, S. Kruber, R. Weingartner, A. Popp, J. Osterhoff, R. Hörlein, J. Hein, V. Pervak, A. Apolonski, F. Krausz, and S. Karsch. Basic concepts and current status of the petawatt field synthesizer — a new approach to ultrahigh field generation. *Review of Laser Engineering*, 37(6):431, 2009.

[161] S. Kneip, C. McGuffey, F. Dollar, M.S. Bloom, V. Chvykov, G. Kalintchenko, K. Krushelnick, A. Maksimchuk, S.P.D. Mangles, T. Matsuoka, Z. Najmudin, C.A.J. Palmer, J. Schreiber, W. Schumaker, A.G.R. Thomas, and V. Yanovsky. X-ray phase contrast imaging of biological specimens with tabletop synchrotron radiation. *Nature Precedings*, npre.2011.5946.1, 2011.

[162] V. A. Vshivkov Y. N. Grigoryev and M. P. Fedoruk. *Numerical Particle-In-Cell Methods: Theory and Applications*. Walter de Gruyter Inc, 2002.

[163] R.A. Fonseca, L.O. Silva, F.S. Tsung, V.K. Decyk, W. Lu, C. Ren, W.B. Mori, S. Deng, S. Lee, T. Katsouleas, and J.C. Adam. Osiris: A three-dimensional, fully relativistic particle in cell code for modeling plasma based accelerators. In Sloot P; Tan CJK; Dongarra JJ; Hoekstra AG, editor, *Lecture Notes in Computer Science*, volume 2331, page 342, 2002.

[164] C Huang, W An, V K Decyk, W Lu, W B Mori, F S Tsung, M Tzoufras, S Morshed, T Antonsen, B Feng, T Katsouleas, R A Fonseca, S F Martins, J Vieira, L O Silva, E Esarey, C G R Geddes, W P Leemans, E Cormier-Michel, J-L Vay, D L Bruhwiler, B Cowan, J R Cary, and K Paul. Recent results and future challenges for large scale particle-in-cell simulations of plasma-based accelerator concepts. *Journal of Physics: Conference Series*, 180(1):012005, 2009.

[165] T Umeda, Y Omura, T Tominaga, and H Matsumoto. A new charge conservation method in electromagnetic particle-in-cell simulations. *Computer Physics Communications*, 156(1):73, 2003.

[166] A.A. Vlasov. On vibration properties of electron gas (in russian). *Zhurnal Eksperimentalnoi i Teoreticheskoi Fiziki*, 8:291, 1938.

[167] R. Courant, K. Friedrichs, and H. Lewy. Über die partiellen Differenzengleichungen der mathematischen Physik. *Mathematische Annalen*, 100(1):32–74, 1928.

[168] A.G. Kostenbauder. Ray-pulse matrices: A rational treatment for dispersive optical systems. *IEEE Journal of Quantum Electronics*, 26(6):1148, 1990.

[169] E. Hecht and A. Zajac. *Optics*. In Hecht and Zajac [169], 3rd edition, 1997.

Publications by the author

R. Weingartner, M. Fuchs, ***A. Popp***, S. Raith, S. Becker, S. Chou, M. Heigoldt, K. Khrennikov, J. Wenz, T. Seggebrock, B. Zeitler, Zs. Major, J. Osterhoff, F. Krausz, S. Karsch, and F. Grüner. **Imaging laser-wakefield-accelerated electrons using miniature magnetic quadrupole lenses** *Phys. Rev. ST Accel. Beams,*14:052801, 2011.

A. Popp, J. Vieira, J. Osterhoff, Zs. Major, R. Hörlein, M. Fuchs, R. Weingartner, T. P. Rowlands-Rees, M. Marti, R. A. Fonseca, S. F. Martins, L. O. Silva, S. M. Hooker, F. Krausz, F. Grüner, and S. Karsch. **All-Optical Steering of Laser-Wakefield-Accelerated Electron Beams** *Physical Review Letters,* 105(21):215001, 2010.

A. Buck, K. Zeil, ***A. Popp***, K. Schmid, A. Jochmann, S. D. Kraft, B. Hidding, T. Kudyakov, C. M. S. Sears, L. Veisz, S. Karsch, J. Pawelke, R. Sauerbrey, T. Cowan, F. Krausz, and U. Schramm. **Absolute charge calibration of scintillating screens for relativistic electron detection** *Review of Scientific Instruments* 81(3) 033301, 2010.

M. Fuchs, R. Weingartner, ***A. Popp***, Zs. Major, S. Becker, J. Osterhoff, I. Cortrie, B. Zeitler, R. Hörlein, G. Tsakiris, U. Schramm, T. P. Rowlands-Rees, S. M. Hooker, D. Habs, F. Krausz, S. Karsch, and F. Grüner. **Laser-driven soft-X-ray undulator source.** *Nature Physics,* 5(11):826, 2009.

J. Osterhoff, ***A. Popp***, Zs. Major, B. Marx, T. P. Rowlands-Rees, M. Fuchs, M. Geissler, R. Hörlein, B. Hidding, S. Becker, E. A. Peralta, U. Schramm, F. Grüner, D. Habs, F. Krausz, S. M. Hooker, and S. Karsch. **Generation of stable, low-divergence electron beams by laser-wakefield acceleration in a steady-state-flow gas cell.** *Physical Review Letters,* 101(8):085002, 2008.

S. Karsch, J. Osterhoff, ***A. Popp***, T. P. Rowlands-Rees, Zs. Major, M. Fuchs, B. Marx, R. Hörlein, K. Schmid, L. Veisz, S. Becker, U. Schramm, B. Hidding, G. Pretzler, D. Habs, F. Grüner, F. Krausz, and S. M. Hooker. **Gev-scale electron acceleration in a gas-filled capillary discharge waveguide.** *New Journal of Physics,* 9(11):415, 2007.

Conference Proceedings

J. Osterhoff, , ***A. Popp***, Zs. Major, B. Marx, T. P. Rowlands-Rees, M. Fuchs, R. Hörlein, F. Grüner, D. Habs, F. Krausz, S. M. Hooker, and S. Karsch. **Stable laser-driven electron beams from a steady-state-flow gas cell** *In ADVANCED ACCELERATOR CONCEPTS: Proceedings of the Thirteenth Advanced Accelerator Concepts Workshop,* volume 1086 of AIP Conf. Proc., page 125, 2009.

A. Popp, J. Osterhoff, T. P. Rowlands-Rees, Zs. Major, M. Fuchs, B. Marx, R. Hörlein, K. Schmid, B. Hidding, L. Veisz, F. Gruñer, U. Schramm, F. Krausz, S.M. Hooker, and S. Karsch. **Electron acceleration in a gas-discharge capillary.** *In 34th EPS Conference on Plasma Phys.*Warsaw, volume 31F of europhysics conference abstracts, pages O3.002. European Physical Society, 2007.

Laser Development

Zs. Major, S. Trushin, I. Ahmad, M. Siebold, C. Wandt, S. Klingebiel, T.-J. Wang, J. A. Fülöp, A. Henig, S. Kruber, R. Weingartner, ***A. Popp***, J. Osterhoff, R. Hörlein, J. Hein, V. Pervak, A. Apolonski, F. Krausz, and S. Karsch. **Basic concepts and current status of the petawatt field synthesizer a new approach to ultrahigh field generation.** *Review of Laser Engineering,* 37(6):431, 2009.

I. Ahmad, S. A. Trushin, Zs. Major, C. Wandt, S. Klingebiel, T.-J. Wang, V. Pervak, ***A. Popp***, M. Siebold, F. Krausz, and S. Karsch. **Frontend light source for short-pulse pumped OPCPA system.** *Applied Physics B: Lasers and Optics,* 2009.

M. Siebold, S. Klingebiel, C. Wandt, Zs. Major, ***A. Popp***, I. Ahmad, T.-J. Wang, J. Hein, F. Krausz, and S. Karsch. **High energy diode-pumped Yb:YAG laser for ns-pulses.** In *Advanced Solid-State Photonics*, OSA Technical Digest Series (CD), page MF3. Optical Society of America, 2008.

Acknowledegements

> Was die Wissenschaften am meisten retadiert, ist, daß diejenigen, die sich damit beschäftigen, ungleiche Geister sind.
>
> Johann Wolfgang von Goethe

- First of all, I want to thank my doctoral advisor, **Prof. Dr. Stefan Karsch**, for accepting me as his PhD student and guiding me to this interesting field of research. With his great ideas, helpful discussions and incredible skills and support in the lab he was a superb supervisor.
- Equally, I want to express my thanks to **Prof. Dr. Ferenc Krausz**, head of the Laboratory for Attosecond and Highfield Physics, for giving me the opportunity to work in this excellent environment.
- Furthermore, I would like to thank **Prof. Dr. Malte C. Kaluza** for reviewing this thesis.
- Special thanks go to all my colleagues, who were directly involved in the experiments. Especially in the beginning, I could learn a lot from **Dr. Jens Osterhoff** and **Dr. Zsuzsanna Major** while setting up and conducting the first LWFA experiments in a gas cell. The latest experiments were carried out with patient support from **Konstantin Khrennikov**, **Johannes Wenz**, **Matthias Heigoldt** and **Shao-Wei Chou**. **Raphael Weingartner** helped whenever he was needed and was always the motivating force that kept us working until the bakery opened. Without the incredible effort of these people and their creative way of quickly fixing things during long nights in the lab, this work would not have been possible.
- I also want to thank **Jorge Vieira** and the entire ***OSIRIS*-team** for their endless support with the PIC simulations and discussions of the results. Also **Timon Mehrling** ran and analyzed several simulations during his diploma thesis that contributed to this work.
- I could also spend some time in the lab with **Matthias Fuchs** and **Tom Rowlands-Rees**, which was always a pleasure. The work eventually resulted in a great experiment, the first LWFA-driven undulator radiation, which provided great motivation for the subsequent measurements.

- **Rainer Hörlein** was always available for discussions, that helped to get my mental chaos sorted, a simple coffee break or questions regarding all kinds of technical and CAD-problems.
- Of course, none of the experiments would have been possible without the technical support from **Manfred Fischer**, **Alois Boswald**, **Anton Horn**, **Harald Haas**, and **Hans-Peter Schönauer**.
- Many thanks go to **Tom Strobl**, **Michael Rogg**, and their team at the **MPQ-Werkstatt** for patiently dealing with my imperfect CAD skills.
- Also **Frau Wild** had a great share in making my stay at the institute enjoyable. THANK YOU!
- Last, but not least, I want to thank all other colleagues of the high-field group, especially **Alexander Buck**, **Patrick Heißler**,**Christoph Skrobol**, **Christoph Wandt**, **Sandro Klingebiel** for outstanding coffee and lunch breaks, X-mas film sessions, nightly photo projects, and enhanced Wiesn experiences.
- Finally: Thanks to Petra Electric for many stimulating sessions, to Cindy for the space she offered, to the Grenouille for persistent, encouraging dancing and to Timon, for his Ocean.